Nano- and Micro- Electrodes:

Applications in the Biosensing Field

Claudio Zuliani

Ph.D. **2010**

Nano- and Micro- Electrodes:
Applications in the Biosensing Field

Claudio Zuliani

A thesis presented at the Dublin City University
for the degree of Doctor of Philosophy

Supervisors: Pr. Robert J. Forster, Pr. Tia E. Keyes
School of Chemical Sciences,
Dublin City University.

January 2010

I hereby certify that this material, which I now submit for assessment on the programme of study leading to the award of Doctor of Philosophy is entirely my own work, that I have exercised reasonable care to ensure that the work is original, and does not to the best of my knowledge breach any law of copyright, and has not been taken from the work of others save and to the extent that such work has been cited and acknowledged within the text of my work.

Signed: _____ ID No.: 56104821

(Candidate)

Date: _____

Acknowledgements

In first instance I would like to thank my supervisors Pr. Robert Forster and Pr. Tia Keys to embark me in this project and providing the funding. In particular, I have to thank Robert for his support, ideas and enlightening discussions throughout the years of my Ph.D. at the Dublin City University. For my visiting period at the Newcastle upon Tyne University I thank Dr. Darren Walsh, who introduced me to nanoelectrodes and SECM in a very simple way.

I have also to thank my large family back in Italy for the long distance support: mum&dad, sisters, nephews and nieces especially Gaia, because the time she was here it reminds me a bit the time in Padova.

During these three years and half I have shared labs, offices or houses with several people and I met many others inside and outside the university. It is hard to remember everybody but I thank all of them for the friendship they showed me and for the cheerful moments we lived together. About my days back in Newcastle I remember Paola, Lara and Francesco who have been the few Italians that I spent so much time with since I have been being abroad. Then Jon, for the tandem English-Italian course we set up, Miguel and Lee as lab-mates.

For my days in Dublin, first of all, I have to thank the entire Irish community in the Forster's group because of their very cheerful and warming welcoming. And I happily remember all those lunch breaks sitting on the DCU green with the April sunshine when, just arrived, all my concentration was focused to figure out what the hell people around me were talking about. Fortunately, my English slightly improved since then (or at least I'd like to think so) but not that much as I can understand only half of Stephen's stories. Well I guess the Balbriggan accent does not help. Then I'd like to mention Linda and Elaine for their chatting and entertaining skills, Emmet for his catch phrase "you'll be grant, man" that he says for whatever occasion, Colm as he did not prosecute me despite I copied the majority of his music, Eoin for the tennis-badminton-bowling challenges which I've always won, Andrea for her kindness. Then moving to the "foreigner side" of the group: Bincy because of all the pranks we played each other and Anitha because she cooks well and she will make a good housewife. And about the rest of the people I met during this time: Katya for providing cookies at the tea breaks, Qiang, Jie, Giovanni, Lynn, Nicoletta for her shouting at me if I was 5 minutes late, Kieran, Zoe and the rest of the soccer mates, Vlado for the organic chemistry suggestions, Elena, Marcello, Brian, Paolo, Silvia&Giuseppe, the ginger Kieran, Emma, Nikki, James, Karthika as she managed to become less annoying to me, Maurice for the Faraday Box construction and Barry for technical assistance. Finally, a big thank to Anita: we got along since we first met; she has been part of almost every trip I took inside Ireland and outside and, despite the inconvenient accommodations that she sometimes booked, I have been pleased to share "the walk of life" of these years with her.

Table of Contents

Nano- and Micro- Electrodes: Applications in the Biosensing Field

Claudio Zuliani

Abstract

Platinum and gold inlaid disk micro- and nano-sized electrodes were prepared using a laser puller. It is the very first time that a similar procedure is fully described for the preparation of gold microelectrodes. Scanning Electron Microscopy, Cyclic Voltammetry, High Speed Chronoamperometry and Scanning Electrochemical Microscopy were used to characterize the electrodes. Radius of platinum and gold tips ranged from 7 nm and 500 nm up to several micrometers, respectively. Platinum probes with radius < 200 nm were employed in high resolution SECM imaging of an array of nanocavities (600–700 nm wide and 400-500 nm deep) prepared by means of nanosphere lithography. The small size of the probe employed in the study allowed resolving the features of the sample, showing the significant capability to do electrochemistry with submicrometer spatial resolution.

The small size of these electrodes allowed their application as immunosensors using the steady-state current of a redox probe as transducing principle. In fact, an object having larger size than the electrode blocks the diffusing of the redox probe towards the electrochemical active surface. Indeed, platinum UMEs were coated with Goat-Human Immunoglobulin (hIgG) while anti-hIgG labelled polystyrene microspheres were injected into the electrochemical cell and let settle. Stable step like decreases (~ 2- 5 %) in the UME current were interpreted as binding of a single bead on the electrode surface due to the immunological reaction between hIgG and anti-hIgG. When the microelectrodes are uncoated, no immunological reaction can occur and then no stable step-like decrease should be observed. However, it was noticed that the electrostatic attraction between the electrode and the microspheres could cause the stabilization of the beads on the electrode surface and produce similar stable step-like drops in the current.

Finally, UMEs were employed in the preparation of glucose microsensors which were based on the glucose oxidase immobilization and in the anodic oxidation of the enzymatically produced hydrogen peroxide. Indeed, a comparative study of the results obtained with four enzyme immobilization procedures was carried out. The work highlighted that the high concentration of glucose oxidase necessary to have sensitive microsensors hampered the polymerization of pyrrole. On the other hand, the microsensors prepared by entrapment of the enzyme in a polyphenol matrix showed good sensitivity (~ 1 - 2 $mAM^{-1}cm^{-2}$) and very fast response time (< 4 seconds). Direct glucose oxidase deposition induced by applied potential did not improve the performances compared to the latter case. Finally, sensors prepared by ruthenium electrodeposition in presence of the enzyme showed encouraging results in terms of enhanced sensitivity (~ 10 - 20 $mAM^{-1}cm^{-2}$) However, a drift in the amperometric signal prevents its analytical use at the moment.

Abbreviations and Symbols

Chemicals

BSA	albumin from bovine serum
FcMeOH	ferrocenemethanol
hIgG	human immunoglobulin G
HEPES	N-(2-Hydroxyethyl)piperazine-N′-(2-ethanesulfonic acid)
$K_4Fe(CN)_6$	hexacyanoferrate(II) trihydrate
PBS	phosphate buffer solution
$Ru(NH_3)_6Cl_3$	ruthenium hexamine chloride

Acronyms

AFM	Atomic Force Microscopy
CV	Cyclic Voltammetry
ET	Electron Transfer
PZC	Potential of Zero Charge
rpm	rotation per minute
SAMs	Self Assemble Monolayers
SECM	Scanning Electrochemical Microscopy
SEM	Scanning Electron Microscopy
STM	Scanning Tunneling Microscopy
UME	ultramicroelectrode

Symbols

a	radius of the disk electrode	m
a_S	radius of the substrate	m
A_g	electrode geometric area	cm^2
A_m	electrode microscopic area	cm^2
C^*	bulk concentration	M
C_d	double layer capacitance	F
C_d^0	specific interfacial capacitance	F cm^{-2}
C_O^*	bulk concentration of the oxidised species	M
C_R^*	bulk concentration of the reduced species	M

$C_{spheres}$	concentration of microparticles	$Num*mL^{-1}$
C_{stray}	stray capacitance	F
d	tip-substrate distance	m
d_s	diameter of the solid spheres	m
D	diffusion coefficient	$cm^2\ s^{-1}$
D_O	diffusion coefficient of the oxidised species	$cm^2\ s^{-1}$
D_R	diffusion coefficient of the reduced species	$cm^2\ s^{-1}$
e^-	electron	-
E	electrochemical potential	V
$E_{1/2}$	half wave potential	V
$E°$	standard electrochemical potential	V
F	Faraday constant	C
h	recess depth	m
H	normalized recessed microelectrode depth	-
i	current	A
i_b	background current	A
i_c	capacitive current	A
i_{ss}	steady state current	A
i_T	current at the SECM tip	A
$i_{T,\infty}$	current at the tip at infinitively large distance	A
i.d.	inner diameter	mm
I_T	normalized current in SECM	A
k^o	standard heterogeneous electron transfer rate constant	$cm^2\ s^{-1}$
K_M^{app}	Michaelis-Menten apparent constant	M
L	normalised distance	-
m	diffusion mass transport coefficient	$cm\ s^{-1}$
n	number of electrons exchanged	-
o.d.	outer diameter	mm
Ox	oxidised species	-
pI	isoelectric point	-
pK_a	negative log of the acid dissociation constant	-
Q	charge passed in an electrochemical experiment	C
r_g	radius of the glass shield of an electrode	m

R	gas constant	J K^{-1} mol^{-1}
RC	cell time constant	s
Red	reduced species	-
R_G	UME glass shield factor	-
R_{SE}	ratio between the size of microspheres and UME	-
R_u	uncompensated resistance	Ω
t	time	s
T	temperature	°C
U	enzyme units	g^{-1}
v	scan rate in a cyclic voltammetry experiment	V s^{-1}
v_s	settling velocity	μm s^{-1}

Greek Symbols

ΔE	potential bias	V
ΔE_p	peak potential separation	V
Δi_{max}	saturation current in an enzyme based sensor	A
Δi_{ss}	difference between i_{ss} and i_b after glucose addition	A
κ	solution conductivity	Ω^{-1} cm^{-1}
ρ	roughness factor	-
ρ_s	density solid spheres	g cm^{-3}

Publications and Presentations

Zuliani, C.; Walsh, D.; Keys, T.E.; Forster, R.J.: "Nanometer-Dimensioned Platinum and Gold Electrodes: Properties and High-Resolution Scanning Electrochemical Microscopy." To be submitted.

4th ECHEMS Meeting, June 25-28, 2008, Cameret sur Mer, France. *Poster presentation*: "Nanoelectrodes and SECM applications."

216th ECS Conference, October 4-9, Vienna, Austria. *Oral presentation*: "Fabrication and characterisation of nano- and micro- electrodes and their use in immuno- and glucose- sensor applications."

The reasonable man adapts himself to the world; the unreasonable one persists in trying to adapt the world to himself. Therefore all progress depends on the unreasonable man.

George Bernard Shaw

Chapter 1

Literature Survey

1.1 Introduction

Electrochemistry at electrodes with micro and nanoscopic dimensions is one of the most important frontiers in modern electrochemical science[1-4] but this area can be still considered in its infancy[5] as the construction of microelectrodes with radii smaller than 1 μm is still far from routine. Development of standard procedures, with possibly high yield and high reproducibility, for the preparation of the nanometer sized electrodes is a key point to fulfil the scientific research at these small scales. Besides, establishment of a defined characterization protocol for the identification of the defective nanodes is also needed. The thesis addresses these two preliminary steps and then moves to the area of biosensing research.

Immunoassays relay mostly on the use of labels *e.g.*, radioactive compounds, fluorescent dyes, enzymes and ECL-based labels[6] to probe whether the immunochemical reaction has occurred or not. However, the major drawback is that these methods are often expensive and require long preparation, *e.g.* labelling and washing steps in order to remove the unbound labelled molecules.[7] Gorschluter *et al.*[7] proposed a simple principle for an amperometric detection of the immuno reaction. Specifically, when an object, *e.g.*, a microsphere, covers the microelectrode surface it causes the steady state current of a redox mediator to drop to a lower value because its diffusion towards the electrode is blocked by the sphere. However, the authors did not show any result of an immunosensor based on this principle. In this thesis, human immunoglobulin G (hIgG) coated microelectrodes and anti-hIgG labelled latex microspheres were employed to evaluate the feasibility of such immunosensor design. Indeed, hIgG is the most abundant immunoglobulin in human beings and it has been considered as model protein in several studies for the development of immunosensors.[8-11]

Miniaturized amperometric glucose biosensors offer some intrinsic advantages including a steady state response achieved in a short time, implantation feasibility and smaller quantity of biomaterials and reagents.[12] In particular, the thesis presents a comparative study of several procedures for the immobilization of glucose oxidase on electrodes with radius smaller than 5 μm. The small scales of these sensors were aimed in order to have fast response time which might allow their use “on the fly” glucose

measurement with the probe having the double function of being both the lancet and the sensor. Point-of-care would tremendously benefit from a top-down process leading to introduction of these devices.[13-16] Besides, this work aims also the development of sub-micrometer sensors which are extremely important for the measurements of metabolites in biological microenvironments with high spatial and temporal resolution.[17,18]

The thesis is divided into several sections. Chapter 1 is a survey of the relevant literature. After a brief description of the main electrochemical techniques employed in this work, the properties of microelectrodes and the two most common procedures for the fabrication of nanodes are reviewed. This chapter introduces also the concept of biosensors. Particular attention is given to the glucose sensors based on the glucose oxidase immobilization and anodic detection of enzymatically generated hydrogen peroxide. From this point of view, the most suitable and reproducible immobilization procedures for the modification of electrodes were outlined. The concept of an immunosensor based on the redox steady state current of a microelectrode as transducing principle was presented.

Chapter 2 deals with the preparation of platinum and gold microelectrodes and special care concerns the description of the sealing and pulling steps *i.e.*, parameters in the laser puller, type and size of the glass capillaries, size and temper of the wire in relation to the resulting probes. The characterization of the probes is here described with special care in correlating these results to the geometrical and electrochemical properties of the probes. The last part of the chapter describes the use of nanometer sized platinum electrodes in high resolution SECM imaging.

Chapter 3 presents the use of the redox steady state current of a UME as transducing principle. Indeed, the chapter outlines the role of size and of charge of a microsphere settling on the UME in relation to the blocking of the diffusion of the redox probe towards the electroactive surface. The latter part of the chapter deals with the statistical recognition of the specifically bound anti hIgG labelled beads on the hIgG coated UMEs from the non-specifically bound anti hIgG labelled beads on uncoated UMEs. The effect of the electrode potential is also investigated in the latter cases.

Finally, Chapter 4 deals with the preparation of glucose microsensors using four enzyme immobilization procedures. Indeed, the work presents a comparative study of

their performances in term of sensitivity, response time and reliability. The investigation addresses also the preparation of sub-micrometer glucose sensors.

1.2 Electrochemical Techniques

1.2.1 Scanning Electrochemical Microscopy

1.2.1.1 Overview

Scanning Electrochemical Microscopy was developed in the middle of '80s by Bard and Engstrom.[19] They showed that an amperometric ultramicroelectrode could be used as a local probe to map concentration profiles at a larger active electrode.[20] Several reviews can give an overview of the SECM applications.[19-22] Indeed, investigations of modified electrodes,[23-27] light induced conversion efficiency,[28] studies of electrogenerated species,[29-31] single molecule detection,[32,33] patterning of microstructures on surfaces,[34] and imaging of biological targets[35-43] have been reported in the literature. As a probe microscopy, SECM offers the advantage of a rigorous electrochemical theory[35] combined with the contemporaneous electrochemical/topography patterning of a surface and nanometer positioning resolution.[35] In terms of topography, SECM encounters significant competition from other scanning probe techniques such as Atomic Force Microscopy (AFM) and Scanning Tunneling Microscopy (STM), which provide better resolution in favourable cases even to the single atom scale.[38] However, SECM gives different information because it probes the surface electrochemical reactivity of a substrate and assesses the electron transfer at the interfaces.[35,38,44-47] The decrease of the probe size has allowed the resolution to be increased. However, SECM investigations with tips smaller than 1 μm are very difficult because the challenge of the probe fabrication and use.[5] Finally, SECM itself is an excellent technique which allows the properties of the nanoelectrodes themselves to be probed and has been successfully employed to characterize those.[21,22]

1.2.1.2 Experimental SECM Set-Up

Figure 1.1 shows the standard SECM set-up which is a 3 or 4 electrode cell configuration. The working electrode is referred to as the tip or probe.[35] The sample, usually called the substrate, is at the bottom of cell, perpendicular to the direction of the tip which then scans above it.[35] Tip and substrate potentials are controlled at the same time using a bipotentiostat. Reference and counter electrode complete the configuration. The microelectrode is held in a vertical position in a Teflon block mounted on a shaft attached to the z piezo-motor.[35] Two other motors provide for lateral displacement in the *x*-*y* plane.[35]

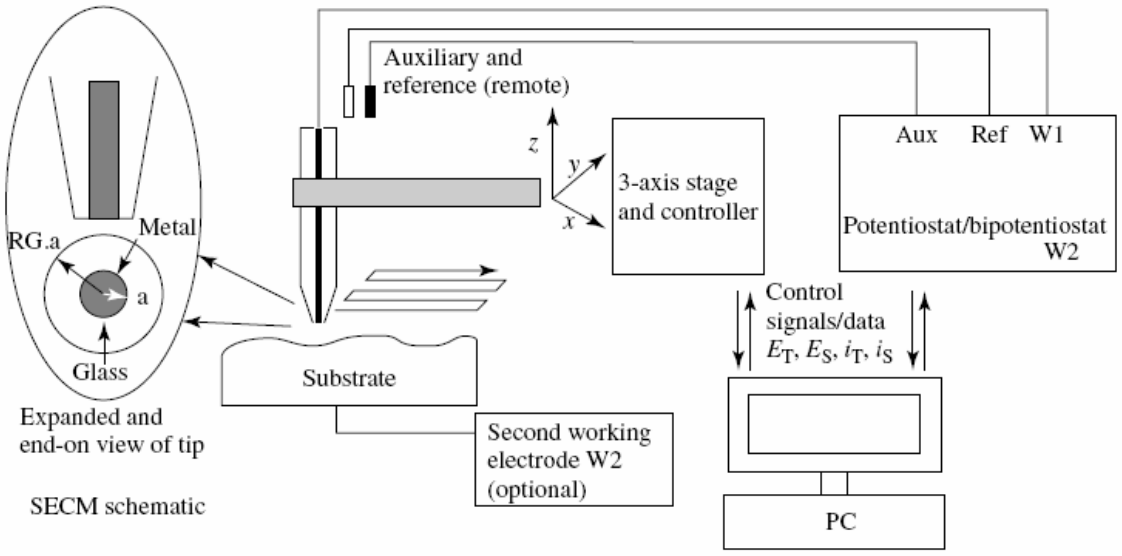

Figure 1.1 A diagram of the SECM cell configuration. Adapted from Horrocks.[48]

1.2.1.3 SECM Feedback Mode

The instrument can operate in several modes[20-22,35] but here only a brief description of the feedback mode is presented because the latter is employed in the characterization of the microelectrodes reported in the next chapter. Indeed, in the feedback mode the tip is immersed in solution in the presence of a redox mediator and its potential held so that the current is controlled by diffusion. Assuming that *Ox* is the species initially present, then it is converted at the electrode surface to *Red* as shown in Equation 1.1.

$$Ox + e^- \rightarrow Red \qquad (1.1)$$

When conductor substrate is not biased, as the concentration of *Red* in the bulk, C_R^*, is ~ 0, it follows from the Nernst equation that (E_S - $E°$) >> 0, where E_S is potential of the substrate and $E°$ the standard potential of the mediator.[19,21,22,35] So, all the reduced species which diffuse from the tip are oxidized at the substrate because of this driving force.[22] The latter behaviour is at the base of the so called positive feedback in SECM. In fact, this additional flux of *Ox* from the substrate increases the steady state current at the probe. In reality, the validity of this discussion depends on substrate area and the heterogeneous constant rate of the mediator at the substrate interface.[49,50]

Figure 1.2 shows the typical behaviour of the probe current when the latter approaches a surface. Indeed, in the condition of Equation 1.1, a typical steady-state current, $i_{T,\infty}$, characterizes the tip response when it is far away from the substrate, $d \geq 10\ a$, where d is the tip-substrate distance and a is the probe radius. Figure 1.2a shows that, when the electrode is moved toward an insulator substrate the tip current, i_T, decreases because the probe shield blocks the diffusion of *Ox* from the bulk solution to the electrode.[19,21,22,35] The closer the tip gets to the substrate, the smaller i_T becomes. On the other hand, when the tip approaches a conductor at $d \leq a$, an increase of i_T is observed because of the additional flux of *Ox* to the tip.[35] The smaller the value of d, the larger i_T is, with $i_T \rightarrow \infty$ as $d \rightarrow 0$, assuming the oxidation of *Red* on the substrate is diffusion-limited.[19,21,22,35] In both cases (approach on conductor or insulator) the amount of the "feedback" depends on the distance tip-substrate and on the geometrical factors of the tip.[35] The plot of the normalized current I_T (= $i_T/i_{T,\infty}$) versus the normalised distance L (= d/a) is called negative, Figure 1.2a, or positive, Figure 1.2b, feedback approach curve depending if the tip approaches respectively an insulator or a conductor substrate.[35] As rule of thumb, when L is between 4 and 5, the decrease (due to the negative feedback) or the increase (due to the positive feedback) of the tip current is approximately 10 % of $i_{T,\infty}$.

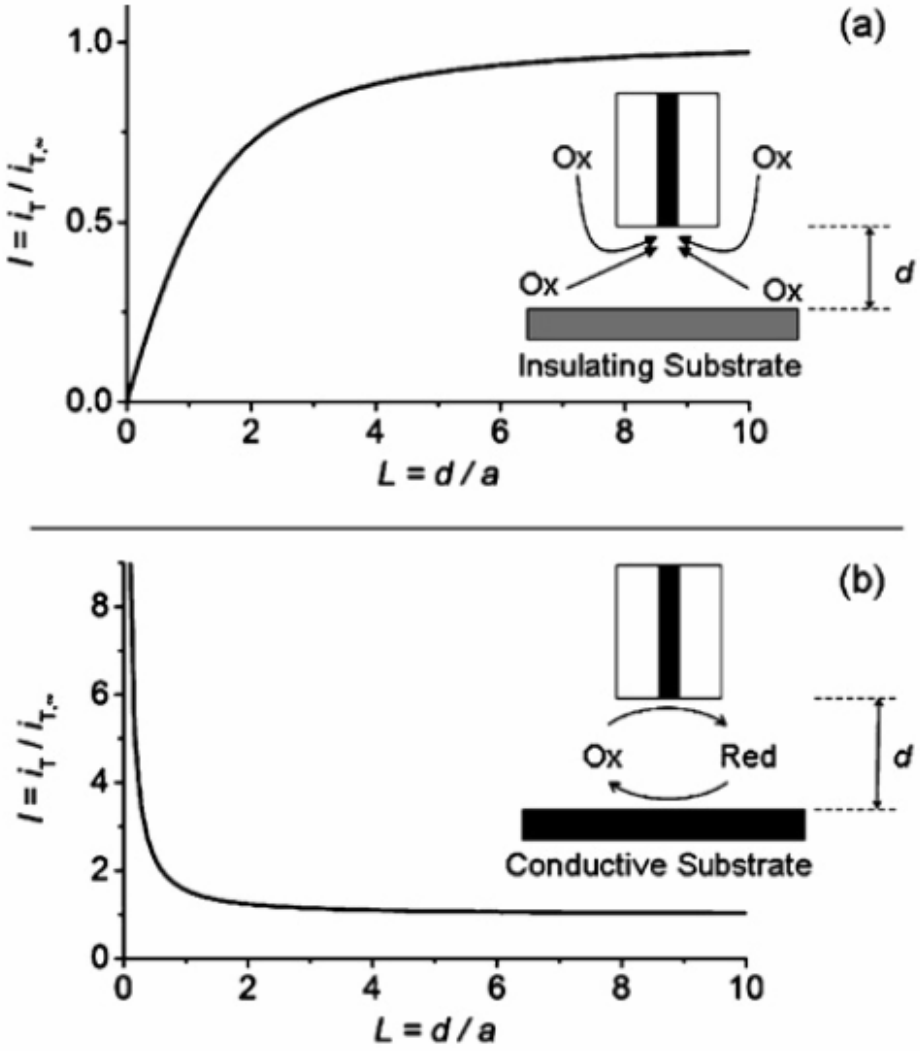

Figure 1.2 SECM approach curves on (a) insulator and (b) conductor substrates. Negative feedback is observed on an insulator substrate and positive feedback is observed on a conductor substrate. Adapted from Fan *et al*..[34]

1.2.1.4 Theoretical Fitting of the SECM Response

A brief overview of the analytical expressions present in the literature which model the positive and negative feedback response is presented here. Only the analytical equations valid for a completely insulator or conductor substrate with fast heterogeneous electron transfer for the redox species are considered. Finally, all the expressions here reported describe dimensionless current-distance curves and they are

valid only for a inlaid disk tip, equal diffusion coefficients of *Ox* and *Red* and an infinitely large substrate, *i.e.*:[21]

$$a_S \geq a + 1.5d \tag{1.2}$$

where a_S is the radius of the substrate.

The first to provide a theoretical description of approach curves over a conductor and an insulator were Kwak and Bard.[51] A better solution was formulated by Amphlett and Denuault[35] because the simulation space was expanded beyond the edge of the insulator sheath and diffusion from behind that was taken into account. Their expression for the diffusion-controlled positive feedback is:

$$I_T[L] = k_1' + \frac{k_2'}{L} + k_3' \exp\left(\frac{k_4'}{L}\right) \tag{1.3}$$

and for negative one is:

$$I_T[L] = \frac{1}{k_1 + \frac{k_2}{L} + k_3 \exp\left(\frac{k_4}{L}\right)} \tag{1.4}$$

where k_1', k_2', k_3', k_4' and k_1, k_2, k_3, k_4 are the constants listed in Table 1.1 and 1.2, respectively.[35]

Table 1.1 Constants listed for Equation 1.3 in function of the glass shield factor, R_G, with the corresponding relative error (%) and range of validity for the normalized distance. Adapted from Amphlett *et al.*.[52]

R_G	k_1'	k_2'	k_3'	k_4'	Error (%)	L validity range
1002	0.7314	0.77957	0.26298	-1.29017	< 0.2	0.1-200
10.2	0.72627	0.76651	0.26015	-1.41332	< 0.3	0.1-200
5.09	0.72035	0.75128	0.26651	-1.62091	< 0.5	0.1-20
1.51	0.63349	0.67476	0.36509	-1.42897	< 0.2	0.1-200

Table 1.2 Constants listed for Equation 1.4 in function of the glass shield factor, R_G, with corresponding relative error (%) and range of validity for the normalized distance. Adapted from Amphlett *et al.*.[52]

R_G	k_1	k_2	k_3	k_4	Error (%)	L validity range
1002	0.13219	3.37167	0.8218	-2.34719	< 1	0.3-20
100	0.27997	3.05419	0.68612	-2.7596	< 1	0.4-20
50.9	0.30512	2.6208	0.66724	-2.6698	< 1	0.4-20
20.1	0.35541	2.0259	0.62832	-2.55622	< 1	0.4-20
15.2	0.37377	1.85113	0.61385	-2.49554	< 1	0.4-20
10.2	0.40472	1.60185	0.58819	-2.37294	< 1	0.4-20
8.13	0.42676	1.46081	0.56874	-2.28548	< 1	0.4-20
5.09	0.48678	1.17706	0.51241	-2.07873	< 1	0.2-20
3.04	0.60478	0.86083	0.39569	-1.89455	< 0.2	0.2-20
2.03	0.76179	0.60983	0.23866	-2.03267	< 0.15	0.2-20
1.51	0.90404	0.42761	0.09743	-3.23064	< 0.7	0.2-20
1.11	-1.46539	0.27293	2.45648	8.995E-7	< 1	2-20

Lefrou[53] introduced an analytical expression describing the positive feedback with R_G parameter which can be continuously varied. The author used conformal mapping transformations to derive an expression made of a combination of mathematical functions containing arctan(L) and arcos($1/R_G$). The final analytical expression is:

$$I_T[L, R_G] = \alpha[R_G] + \frac{\pi}{4\beta[R_G]\arctan(L)} + \left(1 - \alpha[R_G] - \frac{1}{2\beta[R_G]}\right)\frac{2}{\pi}\arctan(L) \tag{1.5}$$

where

$$\alpha[R_G] = \ln 2 + \ln 2\left(1 - \frac{2}{\pi}\arccos\left(\frac{1}{R_G}\right)\right) - \ln 2\left(1 - \left(\frac{2}{\pi}\arccos\left(\frac{1}{R_G}\right)\right)^2\right) \tag{1.6}$$

and

$$\beta[R_G] = 1 + 0.639\left(1 - \frac{2}{\pi}\arccos\left(\frac{1}{R_G}\right)\right) - 0.186\left(1 - \left(\frac{2}{\pi}\arccos\left(\frac{1}{R_G}\right)\right)^2\right) \quad (1.7)$$

Equation 1.5 describes the system within the 2% of error for all the values of L and R_G. Moreover, β gives an estimation of the ratio $\frac{i_{T,\infty}}{4nFDC^*a}$ *i.e.*, the effect of the finite insulator shield size on the steady state current.[53]

Cornut and Lefrou[54] using conformal mapping transformation studied also the case of the negative feedback for a microdisk electrode. The analytical expression which was proposed for values of R_G ranging between 57 and 1000 is:

$$I_T[L, R_G] = \frac{1}{\left(1 + \frac{4.9}{L^{1.48}}\right)^{0.69} + \frac{2}{\pi L}\ln\left(\frac{R_G}{100}\right)} \quad (1.8)$$

On the other hand, for R_G values ranging from 1.3 to 62 the authors fitted simultaneously approach curves with different R_G values and the expression of this fitting is here reported:

$$I_T[L, R_G] = \left(1 + \frac{2.3\ln(R_G + 6.65) - 4.2}{L^{(0.34 + 0.81\arctan(R_G{}^2))}}\right)^{-0.6} \quad (1.9)$$

The new fit is less accurate than others present in the literature but, the reduction of the number of adjustable parameters and an acceptable error (always largely lower than experimental errors) make this new expression very useful.[54] Recently, Cornut and Lefrou[55] demonstrated by simulation that it is possible to consider an uncentred electrode as a centred one having an apparent R_G progressively smaller as much as the metal disk is shifted far from the axis.

Equations 1.5 and 1.9 are used in the Chapter 2 in order to fit the experimental positive and negative feedback approach curves of the microelectrodes characterized by SECM. These expressions were preferred to others in the literature because of their simplicity of use.

1.2.1.5 SECM Imaging in Feedback Mode

Scanning the SECM tip above the substrate in the *x*-*y* plane as shown in Figure 1.3 allows a three-dimensional image to be obtained. Indeed, the tip current changes reflect the changes in the substrate topography and then the current image obtained can be converted into a plot of *Z*-height.[34,35] The assumption is that the substrate does not contain areas which have different values of the rate constant of the heterogeneous electron transfer of the redox probe otherwise the current changes are related also to those and then the topography and the electro-activity features are convoluted in the SECM image.[19,21,35] In conclusion, the SECM image represents the surface topography when the reactivity of the substrate can be considered uniform and vice versa it represents correctly the surface reactivity when the surface is not very rough.[22]

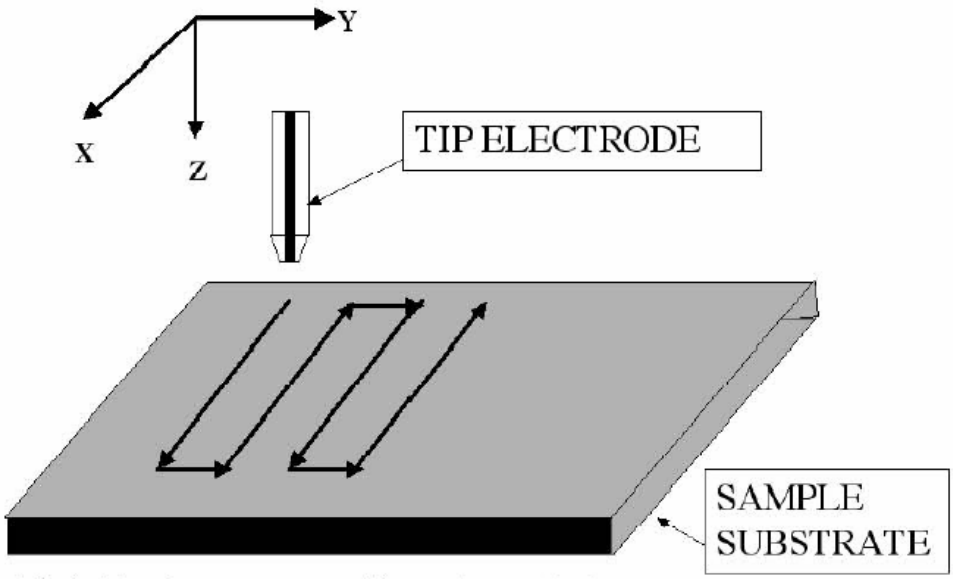

Figure 1.3 The SECM probe is scanned in the *x*-*y* plane at constant height above the substrate. The current of the probe is recorded and it can be converted in a Z-height map of the substrate topography when the electrochemical reactivity of the latter is uniform. Adapted from Bard *et al.*.[35]

In a standard experiment, the tip is scanned at constant height above the substrate. The likelihood of a probe crash against the surface protrusions increases with decreasing electrode size.[56] Indeed, as the tip has to scan over the sample within a few probe radii in order to have a good resolution, roughness or tilt of the substrate become significantly important factors when seeking to reduce the tip size.[35] *x*-*y* line

calibration, although time consuming, can minimize the problem of the substrate tilt, but it is not practically applicable at the very small scales where fine, *i.e.*, submicrometer, adjustment cannot be easily delivered manually. Several strategies have been investigated to sort these issues *e.g.*, constant current mode,[35] tip position modulation,[35] shear force feedback loop,[57-65] impedance feedback loop[45,66-68] and hybrid AFM-SECM technique[69,70] but their description is beyond the scope of this thesis.

1.2.2 Cyclic Voltammetry

Among the several electroanalytical methods developed, cyclic voltammetry is still one of the most popular. In cyclic voltammetry a chosen potential window is scanned and the current response arising from the reactions occurring at the electrode surface is monitored in function of the potential.[71] The experiments are generally performed using a stationary working electrode in a quiescent solution.[71] The term cyclic depends on the fact that the voltage is scanned in a triangular fashion, as shown in Figure 1.4. At the initial potential, E_1, no faradic process occurs at the electrode. Then a linear potential sweep is applied in either a positive or negative direction.[71] When the faradic process occurs, the current starts to increase.[71] This reaction creates a concentration gradient and electro-active species diffuse towards the electrode until depletion effects set in and the current begins to decrease towards the baseline.[34,48,71] After the final potential, E_2, is reached, the sweep is reversed and the potential is returned to its initial value. Useful scan rates range from few mVs^{-1} to thousands of Vs^{-1} when microelectrodes are employed.[34,48,71,72] Further details on the behaviour at microelectrodes will be given in the following sections.

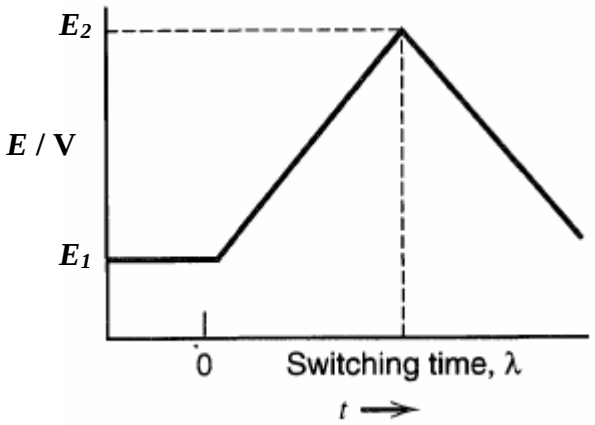

Figure 1.4 Potential waveform for a cyclic voltammetry experiment. The potential is initially set at E_1 where no faradic reaction occurs. Then the potential is scanned linearly both in a positive or negative direction with a characteristic scan rate, v. At $E = E_2$ the potential is inverted and the experiment is stopped when E_1 is reached. Adapted from Bard.[71]

1.2.3 Chronoamperometry

Chronoamperometry is a potential step technique, in which the potential of the working electrode is changed abruptly from an initial potential E_1, where no faradic process occurs, to a final potential E_2 where the redox species is active, Figure 1.5. A double exponential decay can be observed corresponding to the double layer charging and the faradic processes. However, the possibility that the two decays are time-resolved depends on the electrode dimension and the kinetic of the electron transfer.[34,48,71]

The capacitive current due to the charging of the double layer, i_c, decays as:[34,48,71]

$$i_c[t] = \left(\frac{\Delta E}{R_u}\right)\exp\left(\frac{-t}{R_u C_d}\right) \tag{1.10}$$

where R_u, C_d and ΔE are respectively the uncompensated resistance, the double layer capacitance and the difference between E_2 and E_1, (= $|E_2 - E_1|$). The rate constant of the heterogeneous electron transfer of a surface bound species, k, is calculated from:[73,74]

$$i_f[t] = kQ\exp(-kt) \tag{1.11}$$

where i_f is the faradic current, Q is the total charge passed in the reaction and t is the time. Then, a plot of the logarithm of the current in function of the time should be fitting with two linear trends if the two contributes are time-resolved.[3,75]

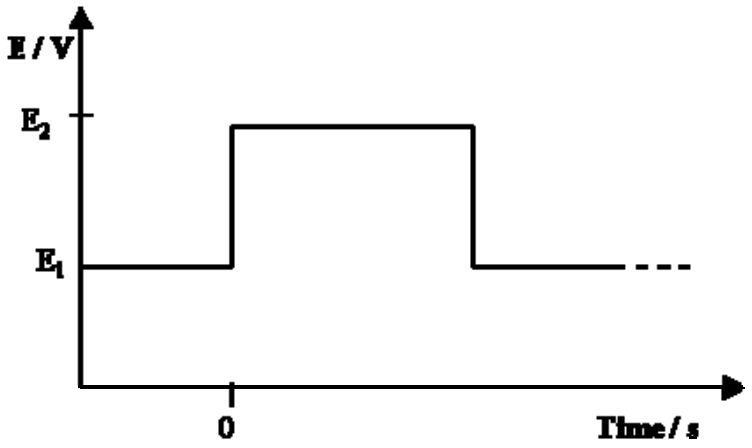

Figure 1.5 Potential waveform for chronoamperometry. E_1 is the initial potential and E_2 the final potential.

1.3 Microelectrodes and Nanoelectrodes

1.3.1 Overview

Historically, understanding the dynamics of electrochemical systems was sometimes limited by the lack of experimental tools with adequate sensitivity and range of timescale.[4,5,34] Introduction of microelectrodes at the end of the 1970s allowed overcoming several of these limitations.[3] Reviews on their characteristics and applications were published by Pons and Fleishmann, Forster and Zoski to mention few.[2-4] Electrochemistry at electrodes with microscopic dimensions constitutes one of the most important frontiers in modern electrochemical science.[5]

Microelectrodes and ultramicroelectrodes (UMEs) have been fabricated with several different shapes and the most common are illustrated as cross sections in Figure 1.6. The most popular geometry is the microdisk which is employed in approximately 50 % of all investigations[76] because of the ease of the construction and polishing procedure. A wide range of materials have been employed in the construction of microelectrodes

especially platinum, gold and carbon fibres, although mercury, iridium, nickel, silver, and superconducting ceramics have been also used.[76]

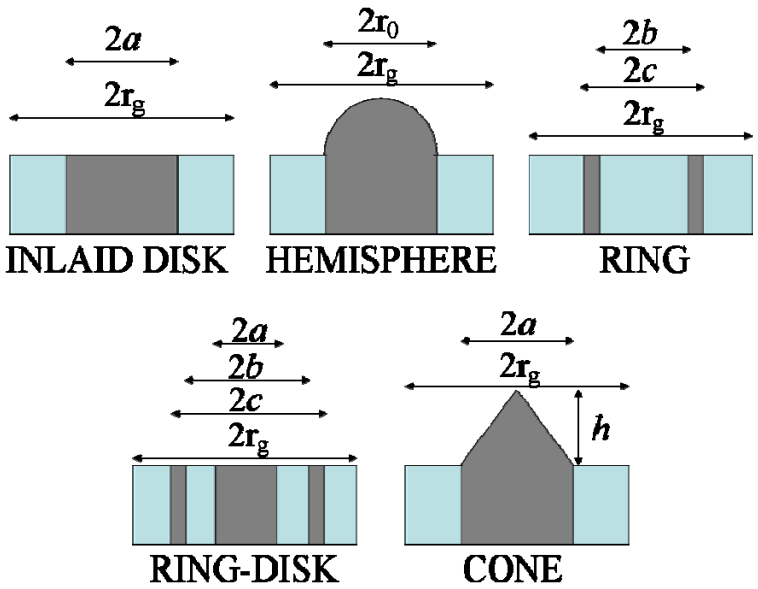

Figure 1.6 Popular microelectrodes geometries. *a*: radius of the disk or conical electrode; *b*: inner radius of the ring electrode; *c*: outer radius of the ring electrode; *h*: height of the conical electrode; r_0: radius of the hemispherical electrode; r_g: radius of the glass shield. Adapted from Zoski.[4]

Microelectrodes can be defined operationally as electrodes having at least one of the critical dimensions smaller than 25 μm.[4] There is not a unanimous agreement about the definition of nanodes. Generally, when the electrode critical dimension becomes comparable to the thickness of the double layer or to the size of the molecules, the experimental behaviour starts to deviate from the theoretical expectations valid for microelectrodes.[4,5,77,78] Operationally, electrodes with critical dimensions smaller than 10 nm are referred to as nanodes.[4]

The success of UMEs arises because of their attributes: small currents, steady-state current, short response times and increased faradic/charging current ratio under steady state conditions.[5] Microelectrodes opened new domains of space (single molecule detection), time (steady-state, fast-sweep up to megavolts/s), chemical medium (non aqueous solvents, unsupported electrolyte, air) and methodology (Atomic Force Microscopy, Scanning Electrochemical Microscopy, Scanning Tunneling Microscopy) within the electrochemical techniques.[4,32-35,72,79,80] Moreover, thanks to their high

penetrating capacity, the minute quantities of materials electrolyzed and the feasibility of implantation they have been used for *in vivo* analysis.[81,82] Despite that, this area can be still considered in its infancy.[5] In fact, at the moment the construction of platinum and gold disk microelectrodes with radii smaller than 1 μm is still far from being routine. However, preparation of electrodes in the nanometer and even in the angstrom range has been reported.[56,83-85]

1.3.2 Mass Transport

In electrochemical systems, three types of mass transport have to be considered: diffusion, migration and convection. Migration, which is the movement of charged species due to a potential gradient, can be neglected in this work because supporting electrolyte was always present in excess.[71] Baltes *et al.*[86] showed how natural convection disturbed the concentration profile at a 40 μm microelectrode generator using Scanning Electrochemical Microscopy in the generator-collector mode. However, for short time experiments, natural convection can usually be neglected.

Diffusion is the movement of species under the influence of a gradient of chemical potential *i.e.*, a concentration gradient.[71] For example, as shown in Figure 1.7, considering the reduction reaction $Ox + e^- \rightarrow Red$ occurring at an electrode under the application of the potential E_2, a depletion layer will form near by the electrode surface.[71] Qualitatively, it is possible to say that the oxidized species diffuses towards the electrode surface and the reduced species diffuses away from it.[71] The diffusion mass transport coefficient, m, it is proportional to D/a where D and a are respectively the diffusion coefficient of the species and the electrode disk radius.[3,34,71,72] Considering that D is in the order of ~ 10^{-6} cm^2s^{-1} in aqueous solution, and a is in the range 10^{-3} – 10^{-6} cm, this means m is ~ 10^{-3} – 1 cm s^{-1}. So UME's mass transport coefficient is similar to the ones observed at the dropping mercury electrode or a rotating disk electrode, but under entirely quiescent conditions.[3]

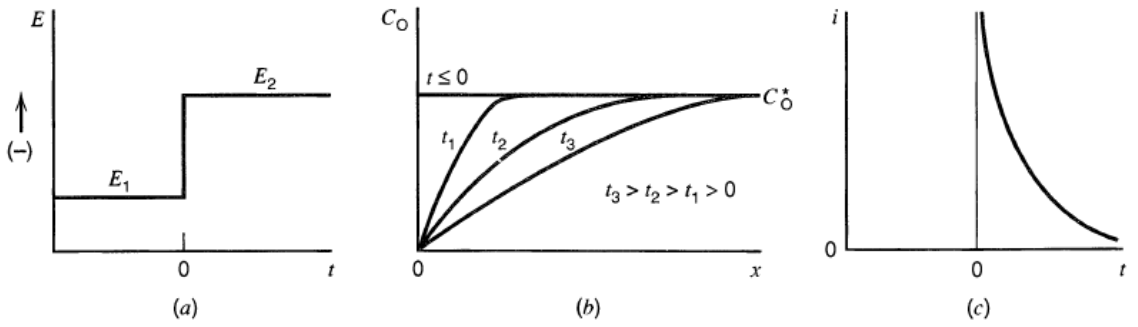

Figure 1.7 (a) Waveform for a step experiment in which the species *Ox* is electrochemical inactive at E_1, but is reduced at the diffusion controlled rate at E_2. (b) Concentration profiles for various times into the experiment. (c) Current flow *vs.* time. Adapted from Bard.[71]

1.3.3 Diffusion Regimes at the Disk Microelectrode

The concentration gradient at the electrode surface, under the application of the potential step in Figure 1.7a, is obtained by solving Fick's second law.[71] Figure 1.8 shows that diffusion occurs in two dimensions at a disk electrode: radially with respect to the axis of symmetry and normal to the plane of the electrode.[71] The current density is not uniform across the face of the disk, *i.e.* it is greater at the edge, and no exact solution is available.[71] However, the problem was approached by Aoki and Osteryoung[71] in terms of a dimensionless parameter, $\tau = 4D_O t/a^2$ where D_O is the diffusion coefficient for the *Ox* species and *t* is the time. According to this approach the current, *i*, depends on the time according to:[71]

$$i = \frac{4nFAD_O C_O^*}{\pi a} f(\tau) \qquad (1.12)$$

where *n*, *F*, *A* and C_O^* are, respectively, the number of electrons exchanged, the Faraday constant, the area of the electrode and the bulk concentration of *Ox*.

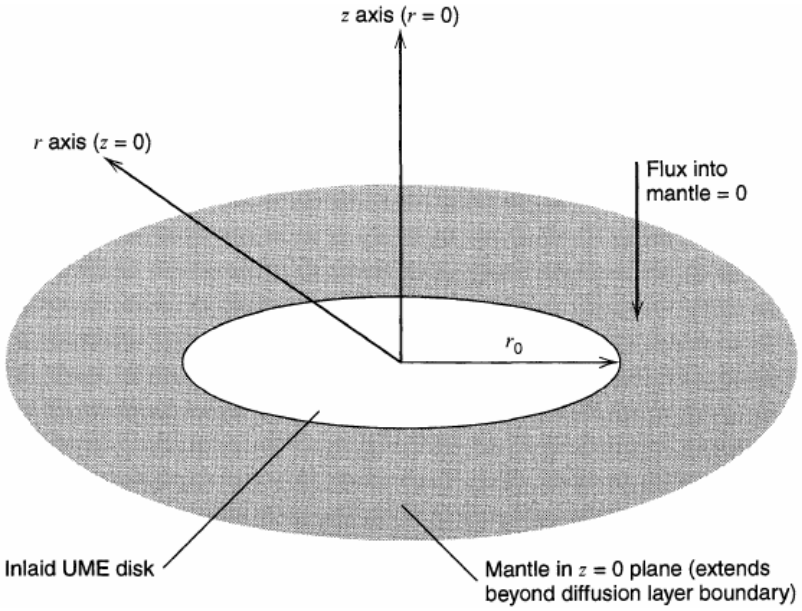

Figure 1.8 Geometry of the diffusion at the ultramicroelectrode disk. Adapted from Bard.[71]

Details about the τ function, $f(\tau)$, can be found elsewhere,[87] however, their discussion is beyond the scope of this review. Figure 1.9 shows that three regimes characterize the current-time curve for a disk-UME. At short time scale the diffusion layer remains thin compared to a and the diffusion has a semi-infinite linear character.[3,34,71] The current flowing at this stage decays following the Cottrell trend:[3,34,71]

$$i = \frac{nFAD_{\mathrm{O}}^{1/2}C_{\mathrm{O}}^{*}}{\pi^{1/2}t^{1/2}} \tag{1.13}$$

Then, the diffusion layer thickness becomes comparable to a and the radial diffusion starts to become more important. Finally, at still longer times, when the diffusion field grows to a size >> a, it resembles the hemispherical or spherical case and the current approaches a steady state. Indeed, for an inlaid disk microelectrode, the steady state current, i_{ss}, is given by:[3,34,71,88]

$$i_{ss} = 4nFD_{\mathrm{O}}C_{\mathrm{O}}^{*}a \tag{1.14}$$

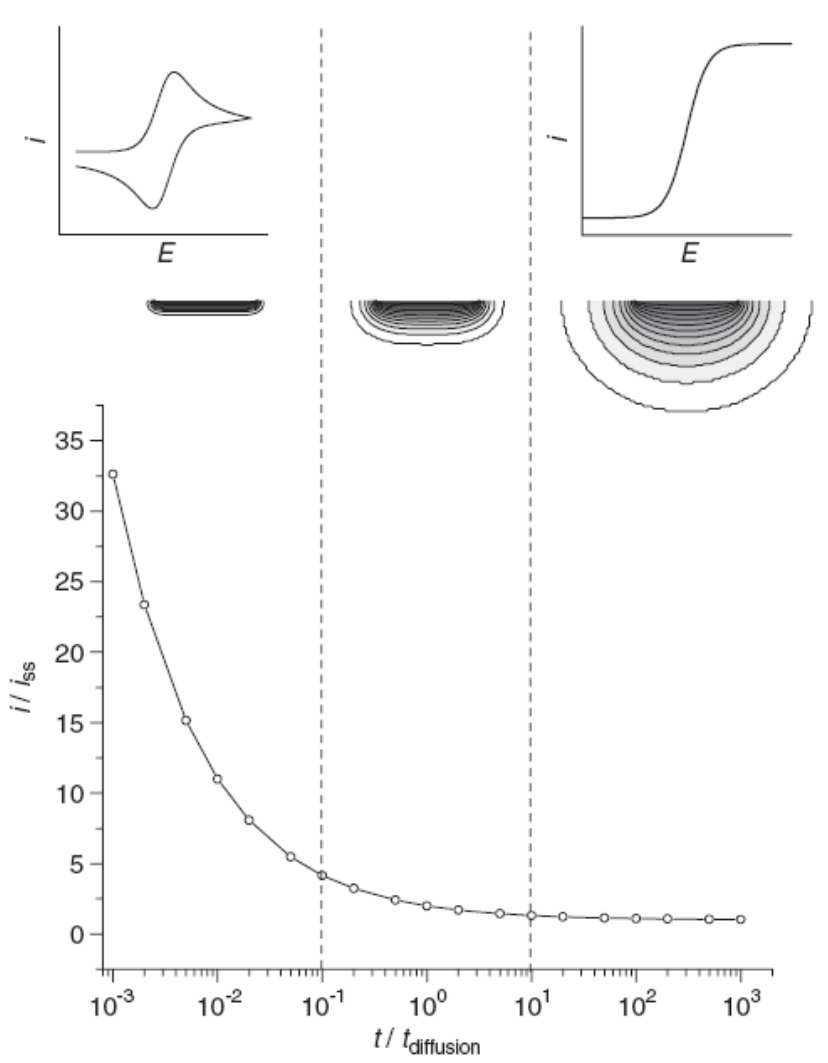

Figure 1.9 The current transient (bottom) and the three diffusion regimes at the microdisk *i.e.* linear, transient and (hemi)spherical. The dashed lines have been arbitrarily drawn at $t_{planar} = t_{diffusion}/10$ and $t_{spherical} = 10t_{diffusion}$ where $t_{diffusion} \approx a^2/D$. The grey scale contour lines are the simulated concentration maps and illustrate the shape of the diffusion layer for each regime. The corresponding transient and steady-state voltammetric responses (upper) are also indicated. Adapted from Denuault *et al.*.[34]

As rule of thumb (derived from the spherical UME case) it is possible to estimate that the steady state current would be observed in cyclic voltammetry if $v << RTD/nFa^2$, where v, R, T, D are respectively the scan rate, the gas constant, the temperature and the diffusion coefficient of the species.[71,88] Similarly, Fang and Leddy[88] introduced a scan rate parameter, δ, which is = $(RTD/nFv)^{0.5}$ and has the dimension of a length. Indeed, when $\delta << a$ the system is characterized by linear regime while when $\delta >> a$ but $< r_g$ radial diffusion with hemispherical character occurs.[88] Spherical diffusion (from above

and below the glass shield) occurs when $\delta >> a$ and $> r_g$.[88] Using Equation 1.14, any effect of the finite size of the glass shield is neglected instead diffusion from behind the plane of the electrode enhances the flux of species to the electrode,[88] but this aspect will be discussed further in Section 1.3.10.

In the case of a recessed microdisk, Equation 1.14 does not hold as the edge effects due to the spherical diffusion are delayed.[89] The steady state current profile at such microelectrode was derived by Bond et *al.*[81] and it is here reported:

$$i_{ss} = 4nFD_O C_O^* a \frac{\pi}{4H + \pi} \tag{1.15}$$

where $H = h/a$ and h is the depth of the recess. It is important to notice that Equation 1.15 should be used only when $H > 1$ while other expressions have been proposed to model the current at shallow recessed electrodes[89-91] but they are not here reported.

1.3.4 Ohmic Drop

When the current, i, flows through a solution due to the application of a certain potential, it generates an ohmic drop, given by iR_u where R_u is the uncompensated resistance between the reference and the working electrode.[34,71] An error is then introduced in any potentiostatic experiment as the true potential at the working electrode differs from the apparent (or applied) potential.[34,71] It is important to minimize the iR_u drop as it can cause separation of the peak potentials and inaccurate results. The uncompensated resistance for a disk microelectrode with radius a is given by:[71,72]

$$R_u = \frac{1}{4\kappa a} \tag{1.16}$$

Equation 1.16 establishes that the uncompensated resistance increases decreasing the radius of the electrode but, as the steady state current is proportional to the radius, iR_u is constant. Besides, as the faradaic current observed at microelectrodes is typically 4 - 6 orders of magnitude smaller than that at macroelectrodes, the ohmic drop is dramatically lower.[3,34] Under these conditions, positioning the reference electrode near the working electrode does not produce any gain and there is no danger of polarizing the

reference by passing the cell current through it.[34,71] Thus, two-electrode cells are often used, especially in high-speed experiments.[87]

1.3.5 Double Layer

When an electrode comes into contact with an electrolytic solution, a double layer is formed at the interface, in which the charge present on the metal electrode is compensated by a layer of oppositely charged ions in the solution.[71,72] A number of theories have been proposed to describe the electrode/solution interface and their description can be found elsewhere.[87] According to Stern and Graham model[87] the interface is split into three regions: the metal layer, the inner layer and the diffuse layer.[71] Any time the applied potential is altered, reorganization of the ions and solvent dipoles in the double layer on the solution side of the interface occurs.[34,71,78] As the capacitive current must flow through the uncompensated resistance then the electrochemical cell can be then simply depicted as shown in Figure 1.10.[87]

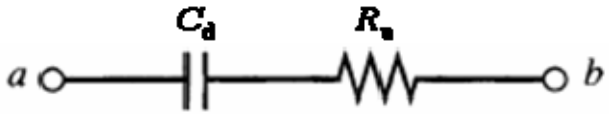

Figure 1.10 Equivalent circuit for an electrochemical cell in the absence of any faradaic process. C_d is the capacitance of the double layer and R_u the uncompensated resistance of the solution. Adapted from Bard.[71]

The potential at the interface does not attain the applied potential until this charging process is complete.[71] The product R_uC_d is the so called cell time constant and for a microdisk it is given by:[71,72]

$$R_uC_d = \frac{aC_d^0}{4\kappa} \tag{1.17}$$

where C_d^0 is the specific interfacial capacitance *i.e.* capacitance per unit area.

95% of the current to charge the double layer passes in 3 times the R_uC_d value.[71,72] As any faradic current before this time is convolved with the charging current, meaningful

measurements of the faradaic current can be made only when the capacitive current is over, typically when $t > 5\ R_u C_d$.[3] From Equation 1.17, a decrease of the electrode radius causes a proportional drop in the $R_u C_d$ value. The small double layer capacitance at ultramicroelectrodes facilitates rapid changes in the electrode potential (fast response times). Figure 1.11 shows the expected behaviour is obtained experimentally with platinum microelectrodes with $1 < a < 25$ μm.[72]

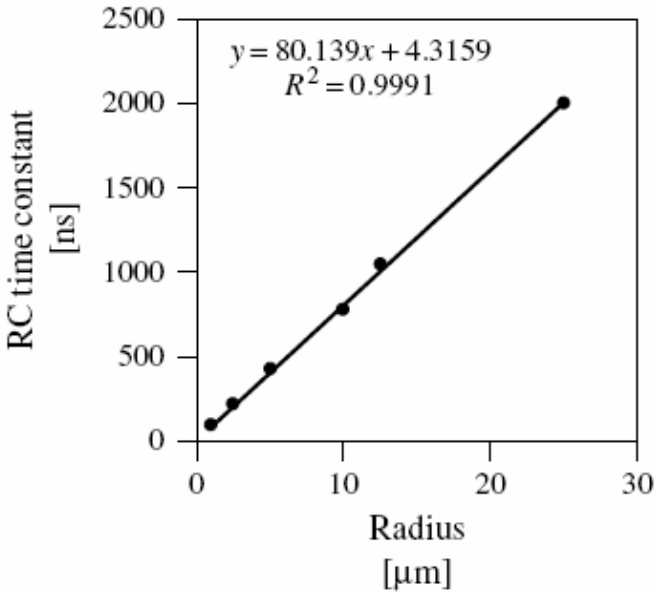

Figure 1.11 Relationship between the $R_u C_d$ cell time constant and the radius of platinum microdisk where the supporting electrolyte was 0.1 M HCl. Cell time constants were measured using chronoamperometry conducted on a microsecond to sub-microsecond timescale by stepping the potential from 0.200 to 0.250 *vs.* Ag/AgCl. Adapted from Forster.[34]

UMEs are employed in fast scan voltammetry because the small charging current results in distortion at values of the sweep rate that are approximately a thousand times larger than those used with a macroelectrode.[71,80] In fact, the charging current, i_c, is present in a voltammogram as the baseline and it depends on the scan rate v according to Equation 1.18.[71]

$$i_c = vC_d \tag{1.18}$$

Using this equation it is also possible to calculate the value of the electrode capacitance. Indeed, in a cyclic voltammogram the difference in the current, Δi, between the

oxidative and reductive branches in a non faradic region should be equal to $2vC_d$.[71] Plotting these Δi values against the scan rate and fitting the data to a linear regression, gives a trend line with slope equal to $2C_d$.[71]

1.3.6 Electrochemical Area

Gold and platinum metals can be electrochemically cleaned by cycling them in 1 M H_2SO_4 between the oxygen and the hydrogen evolution regimes.[34] The two metals form stable oxide layers on the anodic sweep prior to oxygen evolution, which triggers desorption of adventitious impurities, and they can be fully reduced to the bare metal during the cathodic sweep.[34] Assuming that oxygen forms a monatomic layer on the surface, *i.e.*, each metal atom is thought to be bound to a single oxygen atom, the charge under the voltammetric peak for the oxide reduction can be related to the electrochemical area:[71]

$$Q_O = 2eN_A\Gamma_O A_m \tag{1.19}$$

where e is the electron charge, N_A is Avogadro's constant, Γ_O is the surface concentration of atomic oxygen (assumed to be equal to the surface density of metal atoms) and A_m is the electrode area. The reference charge Q_O^S is calculated from the number of metal atoms per unit surface area and then it follows that:[71]

$$A_m = \frac{Q_O}{Q_O^S} \tag{1.20}$$

420 and 390 μC cm^{-2} have been accepted as values of Q_O^S for polycrystalline platinum and gold, respectively.[71] The peak for the oxide reduction is at potentials of approximately 0.45 and 0.94 V *vs.* Ag/AgCl in the case of platinum and gold, respectively.[71] A_m is typically larger than the geometric area, A_g, and the roughness factor, ρ, is the ratio of the two:[71]

$$\rho = \frac{A_m}{A_g} \tag{1.21}$$

Routinely polished metal electrodes typically have roughness factors of 2 - 3, but single crystal faces of high quality can have roughness factors below 1.5.[71]

1.3.7 Towards Nanode Dimensions

As fabrication procedures become more advanced, electrodes with nanometer dimensions and below have been fabricated.[56,83-85] When an electrode approaches molecular dimensions, approximately 10 - 100 Å, corrections for the double-layer effects have to be considered.[5] In fact, the electrochemical properties change as the diffuse layer becomes equal to or greater than the dimension of the electrode, *i.e.* molecules experience solution characteristics, *e.g.* potential and viscosity, different from the bulk.[72,78] Some reports observed anomalous properties in the migration transport[44,77] or violation of the electroneutrality at nanodes[92] and, in light of this, the validity of using nanodes to measure ET process was questioned.[21,84] Nanosized electrodes, because of their small size, are particularly sensitive to adsorption which can cover up the active disk.[85]

As described in Section 1.3.5, $R_u C_d$ should decrease with the electrode size but, experimentally, when the electrode approaches the nanometer dimension, the cell time constant no longer decreases and reaches a limiting value.[72] This is due to what is known as stray capacitance, C_{stray}, which arises from the imperfect sealing of such small electrodes within the glass shield, the leads and the electrical connections.[72] An increase in the cell time constant occurs according to the following equation:[72]

$$R_u C_d = \frac{1}{4\kappa a}(\pi a^2 C_d^0 + C_{stray}) \qquad (1.22)$$

with the symbols given in Equation 1.17. Depending on the quality of the electrode produced and the experimental setup, the stray capacitance is typically between a few pF and several tens of pF.[34] Figure 1.12 shows that the stray and double layer capacitances might become comparable at nanometer-sized tips and that an increase of the cell time constant beyond the value dictated by the double-layer charging itself might occur.[34] Therefore, particular care of the seal between the insulator and the microwire is recommended.[34] Besides, contributions from leads and cables should be

minimized *i.e.*, length of the cables, corrosion on the clip, resistance of the connection between the microscopic electrode and the external macroscopic hook up wire.[34]

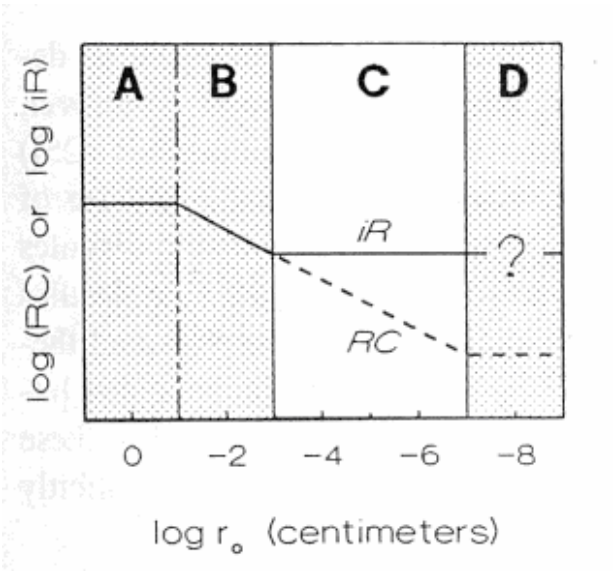

Figure 1.12 Schematic representation of the ohmic drop and cell time constant of an electrochemical cell as a function of the radius of the working electrode. The various zones may be defined as A, macroelectrodes, B, microelectrodes, C, ultramicroelectrodes and D, nanoelectrodes or smaller. The scales are arbitrary. Adapted from Amatore.[78]

Figure 1.13 shows that a perfect microdisk electrode is challenging to produce and faults in the fabrication are depicted. Microelectrodes with non ideal geometries possess anomalous properties which are detailed elsewhere.[34,84] Faulty UMEs should be characterized and removed in order to avoid misinterpretation of the data.[34,84]

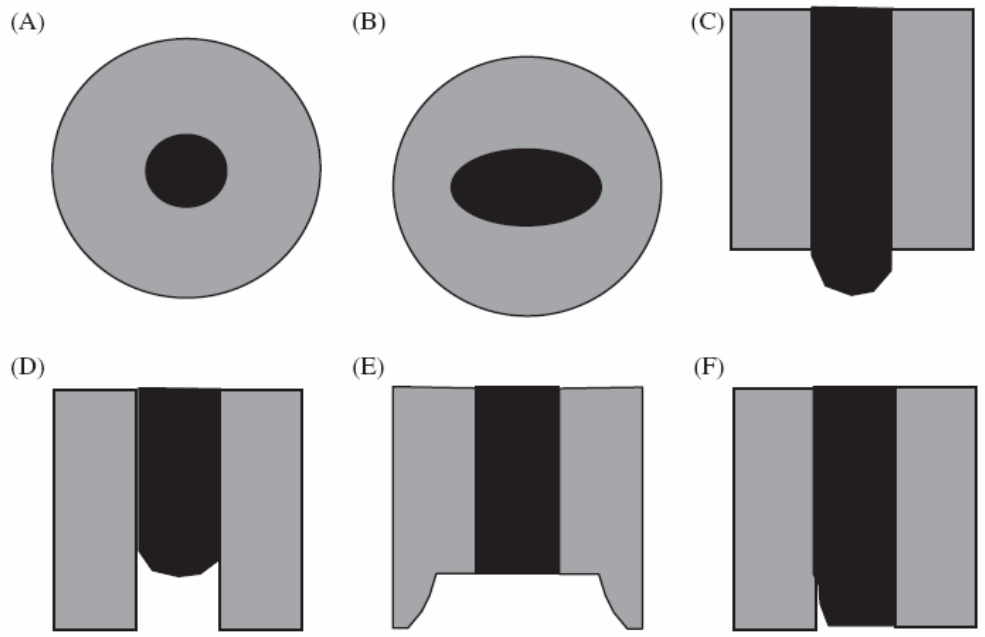

Figure 1.13 Ultramicroelectrodes with different shapes: (A) a perfect inlaid microdisk, (B) a planar elliptical shaped UME, (C) a convex UME with the metal wire protruding from the glass sheath, (D) a recessed UME, (E) a lagooned UME in which the cavity in the insulator is large than the microwire, (F) a leaky UME. Adapted from Forster *et al.*.[34]

1.3.8 Fabrication Procedures of Nano- and Micro- Electrodes

The literature survey here presented deals mainly with the procedures for the construction of platinum inlaid disk microelectrodes which is doubtless the most popular geometry among all the electrode designs due to the mechanical stability and the ease of construction.[49,56,83,84,93-95] Sealing a metallic wire (or a carbon fibre) in a glass capillary, followed by manual polishing and eventual sharpening step to reduce the thickness of the insulator was the traditional way to fabricate disk ultramicroelectrodes.[34] However, handling wires smaller than 10 μm in diameter is difficult. A lower limit, down to 1 μm, can be reached using Wollaston wires, but again the procedure is complicated and time consuming.[34]

To overcome these problems and to reach finer size, different solutions were proposed. A very common one is the electrochemically etching of the wire followed by an insulation step and a heat treatment which shrinks the insulating layer and exposes only

the fine tip.[34] This method was introduced by Penner *et al.*[96] allowing the preparation of conical ultramicroelectrodes. The dimensions of the microelectrode can be controlled at some extent by the number of applications of the insulating material.[32,34,94,97-100] The main problems of electrodes prepared in this way are that they are conically shaped and not easily polishable.[34] Besides, several coatings are necessary before to have a probe in the micrometer scale and the electrochemical stability of the coating might be a significant issue to consider.[34]

1.3.8.1 Laser Puller Fabrication: Introduction

Nanometer-sized platinum electrodes were prepared successfully according to a procedure elaborated first by Pendley *et al.*[83] and optimized by Shao *et al.*[84], Schuhmann[56] and Heinze[85] groups. This manufacture seems to offer a more automated and reliable long-term approach to the nanodes fabrication and it might be adapted for the preparation of microelectrodes employing different metals than platinum.[5,83] Figure 1.14 summarizes the steps involved in the preparation of platinum microelectrodes according to this method. Indeed, it consists of two steps where a platinum wire is sealed inside a capillary and the assembly pulled to a fine tip with the metal insulated by the glass.[34] Pulling of commercial available glass-platinum fibers proved to be successful as well.[101] Many glass/metal combinations are possible *e.g.*, glass type, inner and outer diameter of the capillary, temper and diameter of the platinum wire.[34,56,84,85]

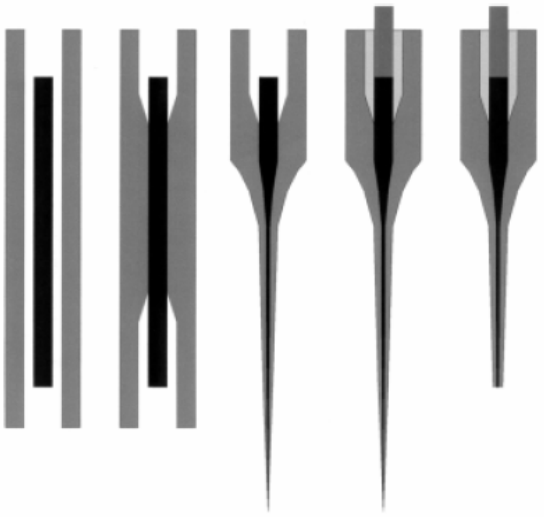

Figure 1.14 Sketch of the two-steps manufacture of the nanoelectrodes using a laser puller. From left to right: insertion of the wire into the capillary, sealing of the wire within the glass, pulling of the wire/capillary assembly, contacting at the back of the microwire and sharpening of the electrode. Adapted from Katemann *et al.*.[56]

The parameters of a laser pipette puller, which has to be used in order to pull a quartz pipette to a fine point in the nanometer scale, are here reported and briefly described:

1. HEAT – output power of the laser.

2. FILAMENT – scanning pattern of the laser beam, which controls the length of the capillary heated.

3. VELOCITY – the velocity at which the glass carriage must be moving before the hard pull is executed.

4. DELAY – controls the timing of the activation of the hard pull relative to the deactivation of the laser.

5. PULL – controls the force of the hard pull.

The role of these parameters is described in more detail in the Sutter P-2000 manual. Moreover, an extensive study of the parameters in pulling optical fibers can be found elsewhere.[102,103] Nevertheless, the main concepts presented there can be adapted to the pulling of quartz and borosilicate capillaries as done in Chapter 2.

The advantages of this procedure are that it is a quick and potentially reproducible. The resulting microelectrodes range from few nanometers up to micrometers and have smooth and long tapers with a lot of mechanical strength (limited damages occurring in a SECM approach crash).[34,56,84,85] On the other hand, the main notable disadvantage is that the wire is covered by the glass after the pulling step and needs to be exposed in order to make a connection to a contacting solution.[5,34]

1.3.8.2 Laser Puller Fabrication: Wire Tempers

Pt wire can be purchased in two tempers: annealed or hard. Pendley and Abruna[83] noted that to ensure success in their microelectrode preparation it was essential using annealed platinum wire. According to them, hard drawn wire did not decrease in diameter when pulled while annealed platinum wire was more ductile and could be drawn to much smaller diameters. This result contrasts with the conclusions presented by Katemann *et al.*[56] who employed the hard temper in the fabrication of platinum microelectrodes. Recently, Maurezoll and LeSuer[34] considering that both tempers could be used as long as conditions set in the laser puller were optimized.

1.3.8.3 Laser Puller Fabrication: Glass Capillaries

Quartz and borosilicate glass soften at temperature above ~ 1600 °C and 800 °C, respectively. As platinum melts at 1772 °C, borosilicate[83,84] or quartz[56] can be both employed with that metal in the preparation of microelectrodes with the laser puller. A vacuum pump is recommended because it enables using lower working temperature, *i.e.* with the same filament a lower heat value, removes dust and moisture from the capillary and improves the quality of the sealing.[34,56] The ratio o.d./i.d. of the glass capillary influences the thickness of the insulating glass sheath surrounding the metal surface of the UME and then the ability to position the wire properly in the centre.[34] As the wire is sealed into the glass prior to pulling, there is no obvious consideration on the influence of the o.d/i.d ratio on the pulling step.[34]

Quartz is an excellent insulation material and its dielectric constant is 3.8 which is larger than the borosilicate glass *i.e.*, 4.6.[104] Moreover, it offers a better mechanical support as the flexibility and strength of the resulting taper is significantly improved compared to other glasses.[34] From the above considerations, only quartz capillaries have been employed in this work for the fabrication of the platinum microelectrodes with the laser puller. However, for the preparation of the gold probes, the consideration that gold melts at 1064.4°C, suggested only borosilicate or aluminosilicate could be used. At this moment, there are very limited applications of laser puller procedure to prepare gold probes and no characterization data has been reported.[83]

1.3.8.4 Laser Puller Fabrication: Wire Exposition

The metal wire after the pulling step is completely covered by the glass and so a way to expose it has to be found. In the literature, two main procedures have been reported: micro-polishing or dipping in hydrofluoric acid.[34,56,84,105] The latter is done by submerging the electrode in a 40 % hydrogen fluoride bath.[84] The etching procedure has the significant feature that it does not require mechanical pretreatment, *i.e.* the metal undergoes an effective electro-polishing process during the etching and it is microscopically smooth.[84] However, a conical shaped microelectrode results from this procedure and the metal surface of the electrodes so prepared cannot be renewed or polished.[84] From this point of view micro-polishing offers better reproducibility and control and it can also be repeated at will.[56] Figure 1.15 shows that the polishing is achieved by rotation of the microelectrode which is then slowly lowered down onto a stationary grinding plate covered with a diamond or an alumina particles suspension.[34,56,106] Once polished, the tip of the electrode should be smooth and free from cracks.

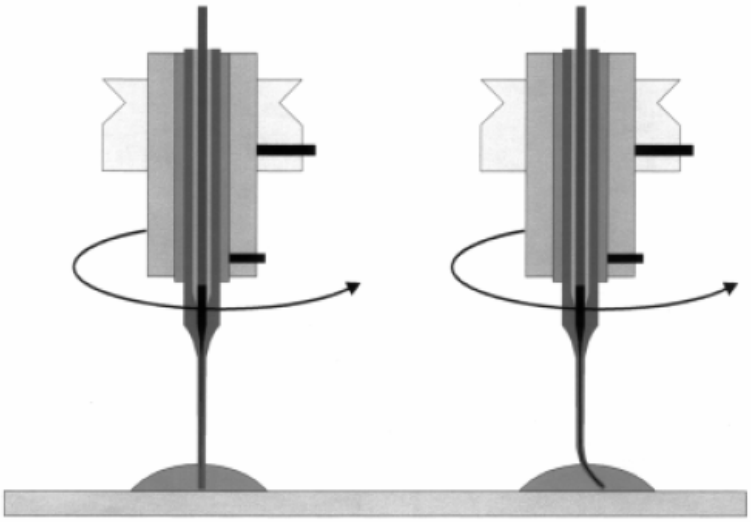

Figure 1.15 Schematic presentation of the set-up for nanoelectrodes polishing. On the left, the electrode is rotated on a polishing plate in a water-alumina suspension, and on the right, rotation of the electrode tip as it touches the polishing surface. Adapted from Katemann.[56]

1.3.9 Dual Electrodes

Dual tips were introduced in the 1990's by Kirchhoff's and Matsue's groups[101] but micrometer thermocouples were produced earlier by Fish *et al.*[95] and they were very similar to the design of the former. Two different designs can be found in the literature. The first one is a disk-disk ultramicroelectrode prepared sealing two Pt wires in a double barrelled capillary.[107] The second geometry is the disk-ring UME shown in Figure 1.16 and it consists of an inlaid disk metal microelectrode coated with gold and then insulated with commercial nail polish.[101,108,109] This probe can be considered the static equivalent of the rotating ring-disk electrode with the species transported by diffusion instead of convection.[101,108,109] The disk-ring geometry offers two advantages when compared to the other. First, completely theoretical treatment for the SECM approach curves which might help the characterization and second, innate symmetry of the design, *i.e.* no dependence on the SECM scan direction, which is important if the probe has to be employed in SECM investigations.[101] It is important to note that the metal coating of the glass of the microelectrodes could also be opportunely set in order

to electromagnetically shield those and reduce the environmental noise, see Section 1.3.11.

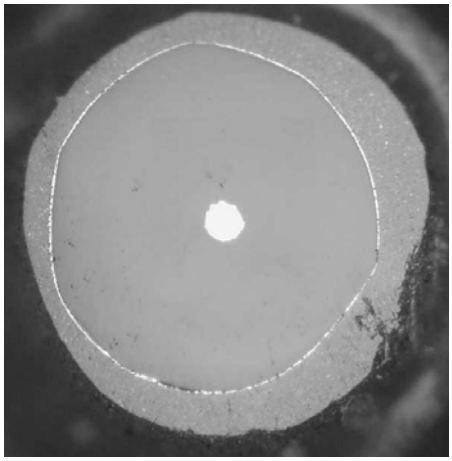

Figure 1.16 A photograph of the ring-disk microelectrode. The diameter of the disk is 25 μm while the thickness of the ring coated layer is ~ 500 nm. Adapted from Liljeroth.[108]

1.3.10 UMEs Characterization

The microelectrode geometry has to be well characterized otherwise errors can be made in interpreting the experimental data.[84] SEM has been employed to check the quality of the seal between the metal wire and the insulating material by Caruana and Bannister.[110] The authors noted that the main factors affecting its reproducibility are the cleanliness of the wire and the method of the sealing. Scanning Electron Microscopy provides also an insight of the morphology of the tip *i.e.* whether the metal is recessed within or protruding from the insulator.[34,84] However, SEM imaging of probes smaller than 0.5 - 1 μm in radius is really difficult because of the glass which can be charged by the electron beam causing a drift in the image focus.[56,84,111] Better results can be obtained when a field emission source is used or by coating the sample with a conductor.[112]

From the steady state current in a cyclic voltammetry of a redox mediator it is possible to derive the tip radius using Equation 1.14 and assuming a inlaid disk geometry. Besides, CV can test the quality of the seal between the wire and the glass *e.g.*, slow achievement of a steady state and sloping of the current branches are signs of a leaking

microelectrode.[34,84] Moreover, capacitance and resistance can be measured from a non faradic region of the CV as explained in Section 1.3.5.[71] For example, Figure 1.17 shows the comparison between two voltammograms which proved that the capacitive contribution to the total current was decreased after thermal treatment of the probe.[113] It is important to notice that a slight overestimation of the radius from Equation 1.14 might occur because of the glass shield *i.e.*, when $R_G \leq 2$ the error in the radius estimation becomes > 10 %. Corrections of the measured radius based on the separation between the forward and reverse branches measured at half the steady state current, $\Delta E_{1/2}$, which is scan rate and R_G dependent, were proposed[88,98] but their use is not very practical and they are not described here.

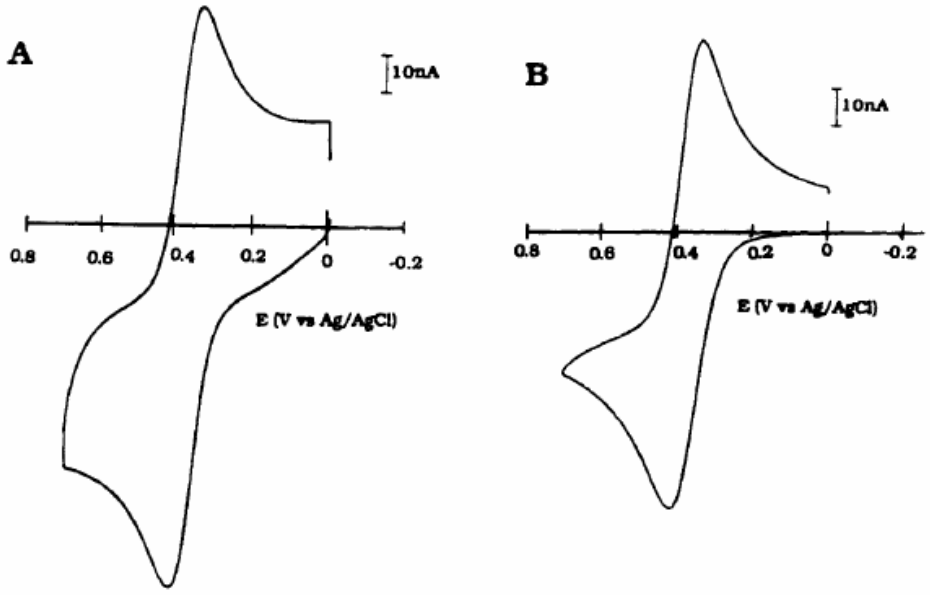

Figure 1.17 Cyclic voltammograms at 100 mV s^{-1} at a 10 nm gold disk nanoelectrode ensemble in 5 μM aqueous $TMAFc^+$ and 1 mM $NaNO_3$ (A) before thermal treatment and (B) after thermal treatment to seal the nanoelectrode tip. Adapted from Menon *et al.*.[113].

The radius calculated by SECM takes in account the finite size of the insulator and the R_G factor is calculated simultaneously in the fitting of the approach curves.[35] Besides, when SEM suffers from charging effects, Scanning Electrochemical Microscopy is the only method able to discriminate microelectrodes having different defective geometries.[19,21,22,35]

The properties of the microelectrodes should be corroborated by several techniques in order to improve consistency and avoid artefacts in the measurement of other data. A mixture of SEM, redox mediator CVs and SECM seems to offer a reliable platform of techniques for a reasonably complete characterization of the geometrical and electrochemical properties of micro- and nano-probes.[56,84,85] Indeed, these three techniques are employed in Chapter 2 to characterise the nano- and micro-electrodes prepared in this work. Besides, cell time constants and roughness factor of the probes are also determined respectively from chronoamperometric decays of the capacitive current, as explained in the Section 1.2.3, and from the voltammograms in 1 M H_2SO_4, as explained in Section 1.3.6.

1.3.11 Environmental Noise

Mains interference is generally due to the capacitive coupling between the experimental cell and mains supply. This involves an unshielded resistance (as the microelectrode body) acting as one plate of the capacitor and a nearby lighting or power circuit as the other.[114] A value of 0.2 pF as stray capacitance between the microelectrode and the mains can induce an unwanted current of 10 nA which is enough to swamp the measurement of the faradaic current.[114] The issue becomes detrimental especially at the higher scan rates because of Equation 1.18.

Different solutions have been proposed to tackle interferences in the measurements associated with a current reading. As the concentration of the electroactive species is proportional to the faradic current, increasing its concentration is the simplest solution when practicable. In potentiostatic circuits a platinum wire or other noble metal can be inserted along the interior length of a Luggin capillary to provide low-impedance pathway for the error signal.[114] The use of a faraday cage is of pivotal importance. Electromagnetic shielding of the electrode body itself proved to reduce stray capacitance though it might complicate the design of the electrode.[115-117]

1.4 Biosensors

1.4.1 Introduction

A biosensor is a device that detects, transmits and records information regarding a physiological or biochemical change. The key component is the integration of the biomaterial onto a suitable transducer thereby converting a biochemical signal into a quantifiable electrical response.[12,118,119] Biosensors have high selectivity towards the substrate molecule (analyte) thanks to the high specificity.[12] In the metabolism sensors, this specificity arises from a binding site for the analyte molecule on the biomolecule (immobilized at the transducer) and in the following catalysed reaction.[12] On the other hand, in the affinity sensors the specificity arises from the recognition site with a characteristic binding constant.[12] The metabolism sensors, *e.g.*, enzyme based sensors, can be used in repeated measurements while the affinity sensors, *e.g.*, immunosensors, have to be regenerated prior to a second measurement.[12] The biosensor specificity has allowed analysis of complex media such as blood, food or water without a separation step or expensive instrumentation.[12,120,121]

Biosensors can be tracked back to the 1960s when Clark and Lyons[122] pioneered the development of oxygen based enzyme electrodes. Since that, research topic for medicine and biochemistry has received more and more attention in the last twenty years in an attempt to monitor biomarkers of chronic diseases.[123] However, applications of biosensors include other areas *i.e.*, agriculture, food analysis and environmental monitoring.[124] Biosensors advantages over the conventional analytical instruments are that they are low cost, fast-response, portable, miniaturized and simple-to-operate analytical tools.[12,123,125] On the other hand, they have some limitations which hampers their routine use.[126] Particularly, insufficient long term stability, electrochemically active interferences in the sample and difficult calibration, especially for the enzyme based sensors.[12,127]

1.4.2 Enzyme-based Biosensor Overview

In the enzyme sensors, the selectivity towards a certain substrate arises from the specificity of the catalytic enzymatic reaction with the substrate.[12] Moreover, thanks to

the high turnover rates of the biocatalysts, they offer high sensitivity being able to accelerate the chemical reactions of a factor 10^8-10^{20} as compared with the uncatalyzed reactions.[119,121] The major drawbacks of these sensors are the thermal and chemical stability of the enzyme which then affects this catalytic function.[119,121]

The immobilization of the biomolecule is one of the key factors in developing a reliable sensor[127,128] because it has a significant impact on the diffusion of the analyte to the catalytic site and on its local concentration.[12] Several methods for the enzyme immobilization have been developed: adsorption,[121] microencapsulation,[12,121,129] entrapment in gels or polymer matrices,[12,121,129,130] crosslinking,[12,121,129,131,132] and covalent coupling on SAMs[12,119,121,127-129,133] to mention the main ones. However, generally speaking, adsorption and encapsulation methods may not offer good adhesion of the biomolecules on the transducer surface, they suffer from a low reproducibility and have a poor spatially controlled deposition.[12,121,123,134] On the other hand, crosslinking and covalent coupling methods require specific functional groups to link together and this may compromise the properties of the biomolecules *e.g.*, catalytic efficiency.[12,121,123,134]

1.4.3 Diabetes

Academic and commercial interest in the development of stable and reliable glucose sensors is especially associated with the increase of diabetes,[127,128,134-136] but other fields, *e.g.* food and alcohol industry, might benefit from the output of this research.[134] Diabetes mellitus is a metabolic disorder resulting from insulin deficiency and hyperglycaemia *i.e.*, blood glucose concentrations higher than the normal range of ~ 4-6 mM with values that can reach 30 mM.[121,123,127,128,134] Stringent personal control of blood glucose is recommended to avoid severe medical pathologies.[128] The worldwide market for glucose monitoring is estimated in about $7 billion[136,137] with glucose biosensors accounting for about 85% of the entire biosensor market.[128]

Non-invasive continuous glucose monitoring methods can be done only in hospital and no such electronic device operated by the consumer have been actually manufactured or entered in the market.[136,137] Subcutaneous implantation of electrochemical glucose

sensors is still one of the most promising techniques for continuous glucose monitoring in the short term but biocompatibility and biofouling, which suppresses the glucose response, remain two major challenges for reliable and accurate prolonged analysis.[127,128,134,135,137] To date, it seems that regular glucose monitoring remains the best option.[136,137] The major barrier to testing include the cost of disposables, pain of frequently lancing a body site, inconvenience to carry meters, lancet and test strips and the time that takes to test.[136,137] Diabetic patients will benefit from simple and less painful techniques of monitoring glucose.[136,137]

1.4.4 Glucose Sensors

1.4.4.1 Introduction

Glucose oxidase contains two flavin adenine dinucleotide (FAD) redox cofactors and two iron moieties[129] which catalyse the oxidation of glucose as represented in the following scheme:[129]

$$\beta\text{-D-glucose} + \text{GOx(FAD)} + 2\text{H}^+ \rightarrow \text{glucono-}\delta\text{-lactone} + \text{GOx(FADH}_2\text{)} \quad (1.23)$$

$$\text{GOx(FADH}_2\text{)} + \text{O}_2 \rightarrow \text{GOx(FAD)} + \text{H}_2\text{O}_2 \quad (1.24)$$

$$\text{glucono-}\delta\text{-lactone} + \text{H}_2\text{O} \rightarrow \text{D-gluconic acid} \quad (1.25)$$

$$\text{H}_2\text{O}_2 \rightarrow \text{O}_2 + 2\text{H}^+ + 2\text{e}^- \quad (1.26)$$

with Equation 1.26 eventually occurring at the electrode surface.

Though the concentration of glucose in solution can be determined by measuring the partial pressure of oxygen gas,[122] amperometric measurement of hydrogen peroxide like described in Equation 1.26 is at the moment the preferred alternative in order to avoid saturation of the enzyme and dependence from the partial O_2 pressure.[121,134] On the other hand, electroactive interferents in blood sample, *e.g.* ascorbic acid, uric acid and acetaminophen, impair the efficiency of the biosensors in the latter case.[12,134,138] Use of "artificial" electron acceptors in alternative to O_2, *e.g.*, ferrocene, osmium complexes and hydroquinone, lowers the potential at which H_2O_2 is detected and increases the rate

of the electron transfer.[12,121,124,129] Indeed, most of the commercial strips and pocket-sized sensors for self-testing of blood glucose employ this principle but the toxicity arising from leaching of the mediator hampers its application *in vivo*.[128,139,140] Introduction of redox polymers or hydrogels, Figure 1.18, as a mean for the localised immobilisation of enzymes on the electrode under concomitant electrochemical 'wiring' of the enzyme's active site has minimized the leaching issue.[12,121,128,129,141] However, these polymers have to be immobilized on the electrode surface by co-deposition, entrapment or cross-linking with other polymeric or gel matrix[12] which render the electrode-modification procedures less suitable for automation and miniaturization, *e.g.*, lack in the reproducibility and manual steps required, or can cause deterioration of the catalytic efficiency in the case of crosslinking with the enzyme.[12]

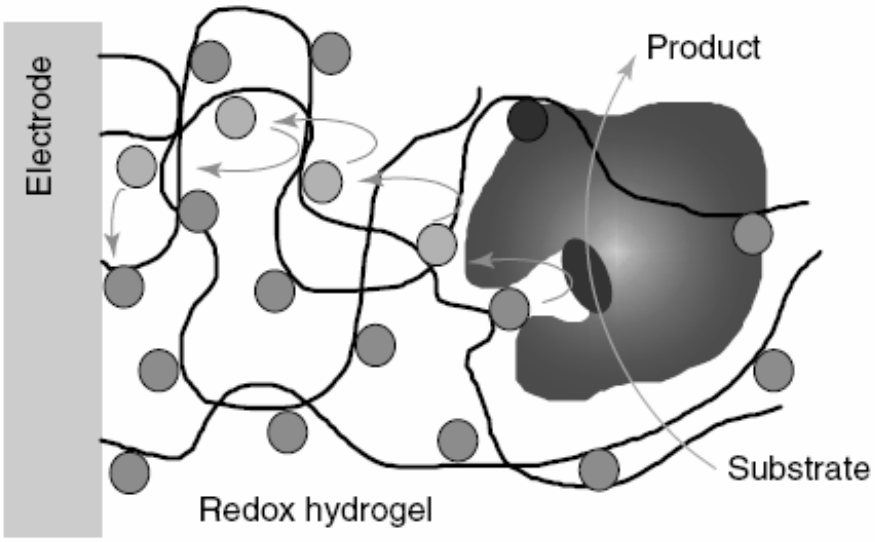

Figure 1.18 Representation of the immobilization of the enzyme within a redox hydrogel matrix. The metallic centres in the redox hydrogel mediate the electron transfer from the enzyme by electron hopping mechanism. Adapted from Schumann *et al.*.[12]

Several other immobilization techniques have been developed in the last thirty years.[12,121,129,134,142-146] The functionalization of electrodes with aryl diazonium salts[15, 147] or self-assembled monolayers of thiols[148] had a pivotal role as platform for glucose oxidase bindings. However, these procedures involve several steps and are limited to the formation of one enzyme monolayer covalently bound to the SAM which has shown to affect the GOx biocatalytic properties in some cases.[12,121,134]

One of the goals of this thesis is the development of glucose microsensors as described in Chapter 4. The small size of the latter should provide fast response time and it could be applied to "on the fly" glucose concentration measurement. Indeed, in these measurements, the probe is thought to have the function of lancet and sensor and the measurement of the analyte is done simultaneously to the penetration of the needle into the skin followed by a quick disengagement after the reading. Enzyme immobilization procedures have to be selected in order to achieve the highest degree of reproducibility. Besides, in terms of an output for industrial purposes, immobilization techniques should offer the chance to be easily automated and be compatible with mass production. From the literature reviewed, it appears that the entrapment of the biomolecules in electrochemically synthesized polymers, like depicted in Figure 1.19, is a better approach for the modification of ultramicroelectrodes. Indeed, these methods offer a better ability to control the distribution and amount of the immobilized enzyme irrespective of geometry, shape and dimension of the electrode and in addition these polymers are compatible for *in vivo* application.[130] The fact that the enzyme preserves its biologically active conformation within the matrix guarantees high sensitivities.[149] Besides to the entrapment within electropolymerized films, GOx direct deposition on platinum[16,150,151] and ruthenium/GOx co-electrodeposition[126,152,153] were considered interesting routes in the preparation of glucose biosensors. The four different strategies, which are employed in Chapter 4 to immobilize GOx at the electrode surface, are briefly reviewed in the following sections.

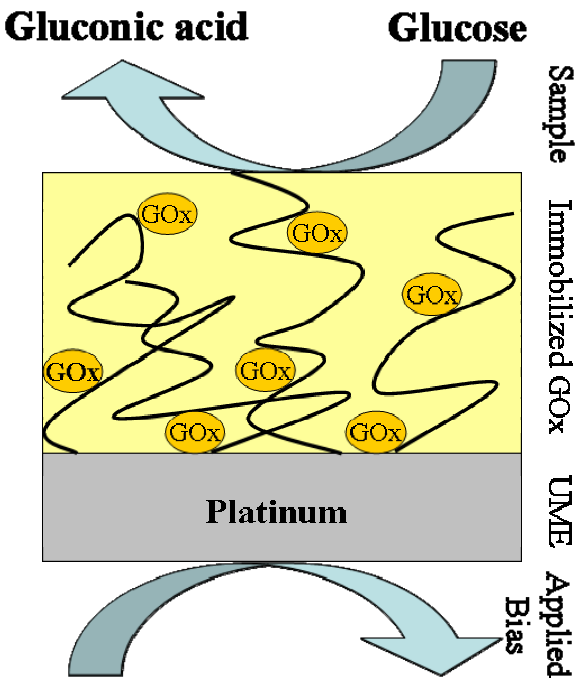

Figure 1.19 Sketch of the immobilization of GOx into an electropolymerized film grown at the electrode surface. The electrode is biased in order to oxidise the hydrogen peroxide produced from the reaction between the enzyme and glucose as described in Equations 1.23 – 1.26.

1.4.4.2 GOx Entrapment in Conducting Polymers (CPs)

Conducting polymers, CPs, show high electrical conductivity and low ionization potential thanks to the high degree of overlap of the π-molecular orbitals coupled with chemical or electrochemical doping[130,154] and their permselectivity helps in excluding interferents.[129] Main advantage of the conducting polymers over the non conducting matrices is that the thickness of the film can be controlled electrochemically and a larger amount of enzyme can be immobilized which might translate to a higher sensitivity.[129] Figure 1.20 shows that CPs have been employed in the attempt to "wire" the enzyme to the electrode but for enzymes with a deeply buried active site, like GOx, direct electron transfer has not been fully demonstrated.[12,129]

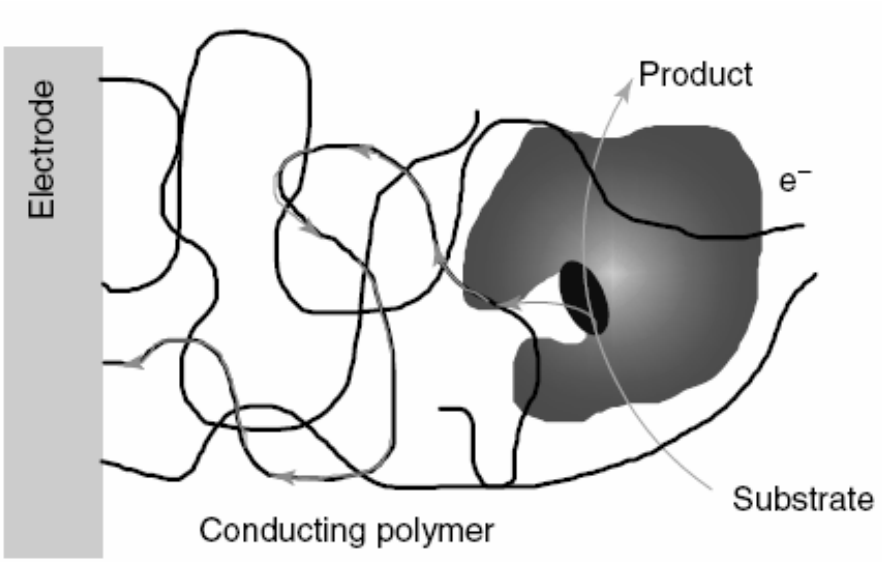

Figure 1.20 Representation of the immobilization of the enzyme in a conducting polymer matrix. The electron transfer from the enzyme could be mediated by the conducting polymer via "molecular wires" to the electrode surface. Adapted from Schuhmann *et al.*.[12]

Pyrrole is undoubtedly the most common conducting polymer employed in the fabrication of biosensors[155-158] and it is employed in Chapter 4. It is important to notice that also polyaniline[125,159] and polythiophene[123,160] have also been employed successfully. Synthesis of continuous polypyrrole (PPy) films by anodic oxidation was reported for the first time in 1979.[161] The process has been well studied and understood and its details can be found elsewhere.[154,161] During the electropolymerization of pyrrole from electrolyte aqueous solution with pH higher than the enzyme isoelectric point (pI), glucose oxidase is incorporated as a counter ion into the growing film.[162]

Chemically or electrochemically overoxidation of polypyrrole[159,163] is known to produce an electron-rich film, which exhibits cation permselectivity and works as inert immobilization matrix to GOx.[144,159,163-165] It is important to notice that use of amphiphilic pyrrole monomer to increase enzyme loading[166] and modification of polypyrrole with ferrocene[129] or osmium groups[149] to lower the detection potential have not always given the desired results. Here, it was decided to conduct the entrapment of GOx within a polypyrrole film in a preliminary evaluation of the feasibility of the preparation of the glucose microsensor.

1.4.4.3 Non-Conducting Polymers

Non conducting polymers, like polyphenylenediamine[121,129,131,134,153,159,165] and polyphenols[14,121,129,134,167] have been successfully employed as matrices for the immobilization of GOx. The main advantage of non conducting polymers is that they have uniform thickness and the electropolymerization is self-limiting as they form an insulating layer beyond which the reaction cannot take place.[153] Besides, they have permselectivity properties which have proved efficient in the removal of anionic interferents.[167] Phenol derivatives[167-169] have proven capable of improving sensors sensitivity up to ~ factor 2 but in a preliminary evaluation, polyphenol was chosen as the immobilization matrix for glucose oxidase in this work.

Electropolymerization of phenols has been well studied and it proceeds through ortho or para coupling of electrogenerated phenolate radicals allowing deposition of poly(phenylene oxide) films on the electrode.[167,169] The resulting films are hydrophobic, free from defects, with a thickness of usually 10 - 100 nm.[14,167] When the electropolymerization of phenols proceeds in presence of an enzyme, the latter is in entrapped in a thin layer, resulting in a fast response time for the biosensor.[170] Moreover, as oxidation of phenols results in the formation of quinoid structures (which react with primary amines of the enzyme *via* Michael addition), the polymer layer formed around the enzyme may also covalently bind to it.[14,151] The GOx loading has a significant influence on the properties of the GOx/phenol film.[14,170] A major drawback of this procedure is the limited amount of enzyme immobilized in the film which might compromise the biosensor sensitivity.

1.4.4.4 Direct Enzyme Deposition

The direct deposition of glucose oxidase on a platinum electrode was investigated by Matsumoto *et al.*[150] in function of the electrode potential. The authors found that the use of a non-ionic detergent, Triton X-100, above its critical micelle concentration, could be used to produce a multilayered deposit. According to the author, up to ~ 50 enzyme layers can be deposited but the mechanism is not completely clear and still

under discussion.[150] Very recently Tsai *et al.*[16] used this procedure to deposit GOx in poly(methyl methacrylate) nanochannels prepared by means of AFM. Their glucose sensor showed to be extraordinary sensitive to glucose *i.e.*, 6.5 $AM^{-1}cm^{-2}$ which is a factor 1000 larger than values typically observed. The direct enzyme electrodeposition was chosen as alternative to the entrapment in a non conductive polymer as a larger amount of glucose oxidase could potentially be immobilized on the electrode surface.

1.4.4.5 Metal and GOx Co-Electrodeposition

Metal electrodeposition, in presence of GOx, has been successfully reported for the preparation of glucose biosensors from carbon fiber-based ultramicroelectrodes.[138,152,171] Metal electrodeposition offers the benefit of dispersed catalytic sites which provide better electrocatalytic efficiency compared to the pure metal surface.[126] In particular, ruthenium has shown electrocatalytic activities towards the oxidation of hydrogen peroxide at ~ 600 mV superior to several metals and good stability of the coating material.[172,173] Differences in the morphology of the metal/enzyme deposits, in comparison to the metal deposits without the enzyme, were revealed by SEM investigations.[126] It was claimed that the enzyme might have an effect upon the nucleation and metal growth.[126] Surprisingly, it was also found that the electrodeposited Ru/GOx layers on carbon fibers were inactive for the oxidation of the interference substances like ascorbic acid and acetaminophen.[171]

Ruthenium dioxide has received a lot of attention since it has high, metal like conductivity ($2 - 4 \times 10^4$ $\Omega^{-1}cm^{-1}$) and good stability.[174,175] Moreover, ruthenium dioxide shows excellent electrocatalytic activity towards oxidation of glucose but only in strong alkaline media involving Ru(VII) as possible candidate for the ET mediation.[174,176,177] On the other hand, in neutral pH oxidation of ascorbic acid and hydrogen peroxide on RuO_2 electrodes has been demonstrated.[178] It is important to notice that ruthenium was not found able to significantly promote the electro oxidation of D-glucose.[179] In this work, electrodeposition of ruthenium in presence of GOx was carried out to verify the effect of a dispersed catalytic film with the enzyme in very close contact and compare the results with the immobilization within polypyrrole and polyphenol matrices and direct enzyme deposition induced by the applied potential.

Ruthenium was electrodeposited from solution of ruthenium nitrosyl nitrate as reported elsewhere.[138,171] This compound has a chemical formula corresponding to $Ru(NO)(NO_3)_x(OH)_y$ with $x + y = 3$ and it is illustrated in Figure 1.21. Quartz microbalance investigations seem to suggest that the electrodeposition from solutions of $Ru(NO)(NO_3)_x(OH)_y$ produced islands of ruthenium metal.[180-182]

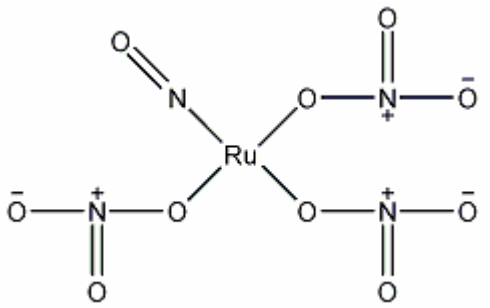

Figure 1.21 Chemical structure of ruthenium nitrosyl nitrate.

1.4.5 Michaelis-Menten Equation

Equation 1.27 describes the Michaelis-Menten model for the enzymatic reaction. Indeed, substrate, S, and the enzyme, E, form an initial complex ES which is then converted to product (P) with rate constant k_{cat} regenerating the enzyme.[12,183] Besides, k_1 and k_{-1} are the rate constant for the forward and backward reaction giving the ES complex.

$$E + S \underset{k_{-1}}{\overset{k_1}{\leftrightarrow}} ES \xrightarrow{k_{cat}} P + E \tag{1.27}$$

The rate of the enzymatic reaction, V, is expressed by Equation 1.28:[183]

$$V = \frac{k_{cat}[E_\Sigma][S]}{[S] + K_M} \tag{1.28}$$

where K_M is = $(k_{-1} + k_{cat})/k_1$ and $[E_\Sigma]$ and [S] are respectively the total concentration of the enzyme and the bulk concentration of the substrate. In an amperometric sensor, the current measured on the top of the background current, Δi_{ss}, after the addition of the substrate is given by:

$$\Delta i_{SS} = \frac{\Delta i_{max}[S]}{[S] + K_M^{app}} \quad (1.29)$$

where K_M^{app} is the apparent Michaelis-Menten constant and $\Delta i_{max} = nFAk_{cat}[E_\Sigma]$ with n as number of electrons involved, F as Faraday constant and A as area of the electrode. Equation 1.29 can be arranged in several ways to yield straight-plot which are the simplest method to extrapolate the K_M^{app} (Michaelis-Menten constant) and the Δi_{max} values.[167,183] In particular, Lineweaver-Burk and Eadie-Hofstee have been extensively employed. However, it should be noted that a non-linear least squares fitting is the most correct method to analyse the data according to the Michaelis-Menten model. Moreover, because of the availability of several software packages able to do this type of statistical analysis, the non linear regression has become a common tool.

1.4.6 Immunosensors

Immunosensor offer a significant tool for the detection of a broad range of analytes and their selectivity arises on the immunochemical reactions between antibodies and antigens which are strong and nearly irreversible.[12] Immunoassays relay mostly on the use of labels *e.g.*, radioactive compounds, fluorescent dyes, enzymes and ECL-based labels[6] to probe that the immunochemical reaction has occurred or not. However, the major drawback is that these methods are often expensive and require long preparation, *e.g.* labelling and washing steps in order to remove the unbound labelled molecules.[7] Introduction of microbeads has offered new strategies for the development of cheaper but efficient immunoassays.[184] For example, the surface of these particles can be sensitised with antibodies in order to bind specifically the corresponding antigen or vice versa. Agglutination and impedance were proposed as detection methods[184] but amperometric devices are very popular because of their ease, versatility and ability to work with extremely small samples and are generally preferred.[185]

Gorschluter *et al.*[7] proposed a simple principle for an amperometric detection of the immuno reaction. Specifically, when an object, *e.g.*, a microsphere, covers the microelectrode surface it causes the steady state current of a redox mediator to drop to a lower value because its diffusion towards the electrode is blocked by the sphere. The

authors proved that changes in the steady state oxidative current of $K_4[Fe(CN)_6]$ monitored at a microelectrode array could be controlled by magnetical removal of the beads from the electrode surface. In fact, the potential at the electrode array was held in order to drive the conversion of $K_4[Fe(CN)_6]$ at the steady state regime. Then, the settling of the microspheres on the microelectrode array surface caused the steady current to drop. Finally, with the help of a magnet these beads could be removed from the electrode surface *i.e.*, passage from a packed monolayer of spheres to chain-like structures and the current was restored almost to its previous value.[7]

The same principle has been used by Mak *et al.*[186] in the development of a device to measure binding forces between ligand-receptor molecular pairs, *i.e.*, NeutrAvidin and biotin or bovine serum albumin (BSA) and anti-BSA. Figure 1.22 shows this experiment. The magnetic beads were functionalized with one of the ligand-receptor molecular pairs and the microspheres with the other one.[186] The magnetic forces were ramped up till they specifically ruptured the ligand-receptor bond allowing its strength to be measured and non-specifically and specifically bound spheres to be distinguished.[186]

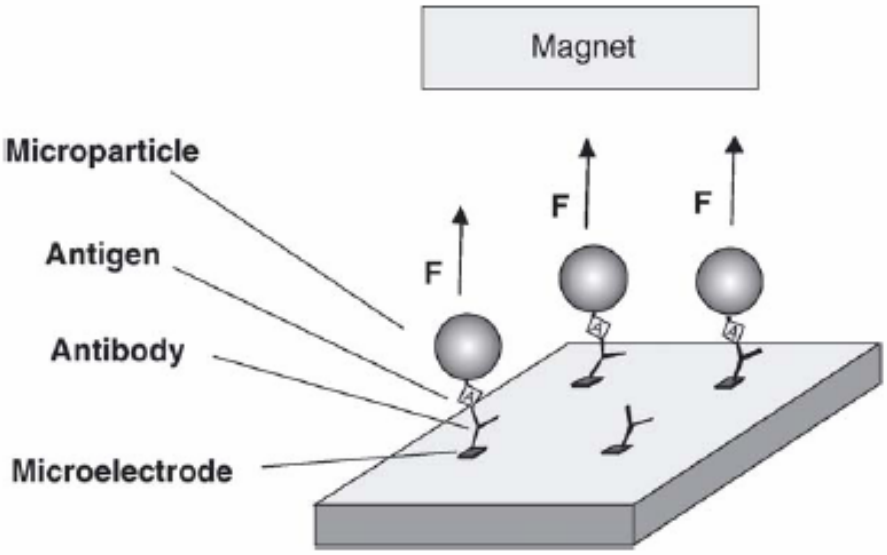

Figure 1.22 Scheme of the sensor for binding force measurements. In the sketch, the microelectrodes array are coated with antibody while the spheres are labelled with the specific antigen. The magnetic field is increased until the ligand-receptor bond is broken. Reprinted from Mak *et al.*.[186]

1.5 Conclusions

A brief description of the Scanning Electrochemical Microscopy, Cyclic Voltammetry and Chronoamperometry as main electrochemical techniques employed in this work was presented in this chapter. Special attention was given to SECM in order to explain its role as a significant research tool in the electrochemistry field particularly in combination with sub-micrometer probes which has allowed chemical and topographical imaging of interfaces with increased spatial and temporal resolution.[17,19,21,22,36,56,84,85,107,187,188]

The chapter outlined also the production and use of microelectrodes and nanoelectrodes as electrochemical tools, giving an overview of their original properties which are not exhibited by macroelectrodes at easily accessible timescales. Special attention was given to the construction of platinum inlaid disk microelectrodes using a laser puller which seems to offer a better approach than the etching/insulating procedure as a quicker and more reliable method for the preparation of these probes.[5] A brief discussion about the common techniques employed in the characterization of these probes was also given. Indeed, a wide range of techniques should give a better understanding of their geometrical factors and electrochemical properties in order to individuate defective behaviour.

The chapter concludes highlighting the importance of biosensors as new analytical tool and outlined their advantages over conventional analytical instruments. Indeed, miniaturized glucose oxidase based sensors can have important applications in the biomedical field. Some of the enzyme immobilization procedures were discussed. Particular attention was given to methods which would preserve the GOx biocatalytic activity, assuring high sensitivity, and would minimize the reproducibility of the microsensors. In fact, entrapment in polypyrrole or polyphenol matrix, direct deposition of glucose oxidase and co-electrodeposition of ruthenium and glucose oxidase were found as the most suitable options for the preparation of glucose microsensors. Finally, the amperometric immunosensor proposed by Gorschluter and co-workers,[7] which is based on the steady state current of a UME as transducing principle, was described.

1.6 References

(1) Heinze, H. *Angew. Chem.* **1984***, 23*, 831.

(2) Pons, S.; Fleischmann, M. *Anal. Chem.* **1987***, 59*, A1391.

(3) Forster, R. J. *Chem. Soc. Rev.* **1994**, 289.

(4) Zoski, C. G. *Electroanalysis* **2002***, 14*, 1041.

(5) Arrigan, D. W. M. *Analyst* **2004***, 129*, 1157.

(6) Hazelton, S. G.; Zheng, X.; Zhao, J. X.; Pierce, D. T. *Sensors* **2008***, 8*, 5942.

(7) Gorschlüter, A.; Sundermeier, C.; Roß, B.; Knoll, M. *Sensors and Actuators B: Chemical* **2002***, 85*, 158-165.

(8) Moulton, S. E.; Barisci, J. N.; Bath, A.; Stella, R.; Wallace, G. G. *J. Colloid Interface Sci.* **2003***, 261*, 312-319.

(9) Moulton, S. E.; Barisci, J. N.; Bath, A.; Stella, R.; Wallace, G. G. *Electrochimica Acta* **2004***, 49*, 4223-4230.

(10) Zhou, C.; Friedt, J.; Angelova, A.; Choi, K.; Laureyn, W.; Frederix, F.; Francis, L. A.; Campitelli, A.; Engenlborghs, Y.; Borghs, G. *Langmuir* **2004***, 20*, 5870.

(11) Giacomelli, C. E.; Bremer, M. G. E. G.; Norde, W. *J. Colloid Interface Sci.* **1999***, 220*, 13-23.

(12) Schuhmann, W.; Bonsen, E. M. In *Biosensors;* Unwin, P. R., Ed.; Encyclopedia of Electrochemistry. Volume 3. Instrumentation and Electroanalytical Techniques; Wiley Ltd.: Federal Republic of Germany, 2003; pp 350.

(13) Ciobanu, M.; Taylor, D. E.; Wilburn, J. P.; Cliffel, D. E. *Anal. Chem.* **2008***, 80*, 2717.

(14) Hrapovic, S. and Luong, J.H.T. *Anal. Chem.* **2003***, 75*, 3308.

(15) Polsky, R.; Harper, J. C.; Wheeler, D. R.; Brozik, S. M. *Electroanalysis* **2008***, 20*, 671.

(16) Tsai, Y.; Ho, C.; Liao, S. *Electrochem. Comm.* **2009***, 11*, 1316-1319.

(17) Schulte, A. and Schuhmann, W. *Angew. Chem. Int. Ed.* **2007***, 46*, 8760.

(18) Sun, P.; Laforge, O.; Abeyweera, T. P.; Rotenberg, S. A.; Carpino, J.; Mirkin, M. *PNAS* **2008***, 105*, 443.

(19) Mirkin, M. V. *Anal. Chem. News & Features* **1996**, 178A.

(20) Barker, A. L.; Gonsalves, M.; Macpherson, J. V.; Slevin, C. J.; Unwin, P. R. *Anal. Chim. Acta* **1999***, 385*, 223.

(21) Sun, P.; Laforge, F. O.; Mirkin M.V. *Phys. Chem. Chem. Phys.* **2007***, 9*, 802.

(22) Mirkin, M. V.; Horrocks, B. R. *Anal. Chim. Acta* **2000**, *406*, 119.

(23) Tsionsky, M.; Bard, A. J.; Dini, D.; Decker, F. *Chem. Mater.* **1998***, 10*, 2120.

(24) Liu, B.; Bard, A. J.; Mirkin, M. V.; Creager, S. E. *J. Am. Chem. Soc.* **2004***, 126*, 1485.

(25) Williams, M. E.; Stevenson, K. J.; Massari, A. M.; Hupp, J. T. *Anal. Chem.* **2000***, 72*, 3122-3128.

(26) Mullane, A. P.; Macpherson, J. V.; Unwin, P. R.; Cervera-Montesinos, J.; Manzanares, J. A.; Frehill, F.; Vos, J. G. *J. Phys. Chem. B* **2004***, 108*, 7219.

(27) Bertoncello, P.; Ciani, I.; Li, F.; Unwin, P. R. *Langmuir* **2006***, 22*, 10380-10388.

(28) Figgemeier, E.; Kylberg, W. H.; Bozic, B. In *In Scanning Photoelectrochemical Microscopy as Versatile Tool to Investigate Dye-Sensitized Nano-Crystalline Surfaces for Solar Cells;* Photonics for Solar Enegy Systems; SPIE: 2006; .

(29) Mahe', E. *Electrochimica Acta* **2007***, 52*, 5018.

(30) Bi, S.; Liu, B.; Fan, F. F.; Bard, A. *J. Am. Chem. Soc.* **2005***, 127*.

(31) Zoski, C. G.; Luman, C. R.; Fernandez, J. L.; Bard, A. J. *Anal. Chem.* **2007***, 79*, 4957-4966.

(32) Bard, A. J.; Fan, F. F. *Acc. Chem. Res.* **1996***, 29*, 572.

(33) Sun, P.; Mirkin, M. V. *J. Am. Chem. Soc.* **2008***, 130*, 8241-8250.

(34) Zoski, C. G., Ed.; In *Handbook of Electrochemistry.* Elsevier: Netherlands, 2007; , pp 935.

(35) Bard, A.J. and Mirkin, M.V., Ed.; In *Scanning Electrochemical Microscopy;* Marcel Dekker, Inc: United States of America, 2001; , pp 650.

(36) Takahashi, Y.; Hirano, Y.; Yasukawa, T.; Shiku, H.; Yamada, H.; Matsue, T. *Langmuir* **2006***, 22*, 10299.

(37) Wittstock, G.; Yu, K.; Haisall, B.; Ridgway, T. H.; Heineman, W. R. *Anal. Chem.* **1995***, 67*, 3578.

(38) Gyurcsanyi, R. E.; Jagerszki, G.; Kiss, G.; Toth, K. *Bioelectrochemistry* **2004***, 63*, 207.

(39) Shiku, H.; Matsue, T.; Uchida, I. *Anal. Chem.* **1996***, 68*, 1276.

(40) Zhang, X.; Peng, X.; Jin, W. *Anal. Chim. Acta* **2006***, 558*, 110-114.

(41) Turcu, F.; Schulte, A.; Hartwich, G.; Schuhmann, W. *Biosensors and Bioelectronics* **2004***, 20*, 925.

(42) Wain, A. J.; Zhou, F. *Langmuir* **2008***, 24*, 5155.

(43) Wang, J.; Zhou, F. *J. Electroanal. Chem.* **2002***, 537*, 95.

(44) Murray, R. W. *Chem. Rev.* **2008***, 108*, 2688-2720.

(45) Wei, C.; Bard, A. J. *J. Electrochem. Soc.* **1995***, 142*, 2523.

(46) Fernandez, J. L.; Walsh, D. A.; Bard, A. J. *J. Am. Chem. Soc.* **2005***, 127*, 357.

(47) Liu, B.; Bard, A. J. *J. Phys. Chem. B* **2002***, 106*, 12801.

(48) Unwin, P. R., Ed.; In *Instrumentation and Electroanalytical Chemistry;* Bard, A. J., Stratman, M., Eds.; Encyclopedia of Electrochemistry; Wiley-VCH: Weinheim, Germany, 2003; Vol. 3, pp 659.

(49) Wipf, D. O.; Michael, A. C.; Wightman, R. M. *J. Electroanal. Chem.* **1989***, 269*, 15.

(50) Wipf, D. W.; Bard, A. J. *J. Electrochem. Soc.* **1991***, 138*, 469.

(51) Kwak, J.; Bard, A. J. *Anal. Chem.* **1989***, 61*, 1221.

(52) Amphlett, J. L.; Denuault, G. *J. Phys. Chem. B* **1998***, 102*, 9946-9951.

(53) Lefrou, C. *J. Electroanal. Chem.* **2006***, 592*, 103.

(54) Cornut, R.; Lefrou, C. *J. Electroanal. Chem.* **2007***, 604*, 91.

(55) Cornut, R.; Lefrou, C. In *In 3D Steady-state Simulations of Scanning Electrochemical Microscopy Experiments with Microdisk Electrode;* Excerpt from the Proceedings of the COMSOL Users Conference 2007 Grenoble; .

(56) Katemann, B. B.; Schuhmann, W. *Electroanalysis* **2002***, 14*, 22.

(57) Ludwig, M.; Kranz, C.; Schuhmann, W.; Gaub, H. E. *Rev. Sci. Instrum.* **1995***, 66*, 2857.

(58) James, P. I.; Garfias-Mesias, L. F.; Moyer, P. J.; Smyrl, W. H. *J. Electrochem. Soc.* **1998***, 145*, L64.

(59) Hengstenberg, A.; Kranz, C.; Schuhmann, W. *Chem. Eur. J.* **2000***, 6*, 1547.

(60) Lee, Y.; Ding, Z.; Bard, A. J. *Anal. Chem.* **2002***, 74*, 3634-3643.

(61) Fan, F. F.; Bard, A. J. *J. Phys. Chem. B* **2003***, 107*, 1781.

(62) Garay, M. F.; Ufheil, J.; Borgwarth, K.; Heinze, J. *Phys. Chem. Chem. Phys.* **2004***, 6*.

(63) Katemann, B. B.; Schulte, A.; Schuhmann, W. *Electroanalysis* **2004***, 16*, 60.

(64) Etienne, M.; Anderson, E. C.; Evans, S. R.; Schuhmann, W.; Fritsch, I. *Anal. Chem.* **2006***, 78*, 7317.

(65) Bauermann, L. P.; Schuhmann, W.; Schulte, A. *Phys. Chem. Chem. Phys.* **2004***, 6*, 4003.

(66) Alpuche-Aviles, M. A.; Wipf, D. O. *Anal. Chem.* **2001***, 73*, 4873.

(67) Etienne, M.; Schulte, A.; Schuhmann, W. *Electrochem. Comm.* **2004***, 6*, 288.

(68) Eckhard, K.; Kranz, C.; Shin, H.; Mizaikoff, B.; Schuhmann, W. *Anal. Chem.* **2007***, 79*, 5435.

(69) Macpherson, J. V.; Unwin, P. R. *Anal. Chem.* **2001***, 73*, 550.

(70) Macpherson, J. V.; Unwin, P. R. *Anal. Chem.* **2000***, 72*, 276.

(71) Bard, A. J.; Faulkner, L. R. In *Electrochemical Methods. Fundamentals and Applications.* Wiley Inc.: United States of America, 2001; , pp 833.

(72) Forster, R. J. In *Microelectrodes-Retrospect and Prospect;* Unwin, P. R., Ed.; Encyclopedia of electrochemistry. Volume 3. Instrumentation and electroanalytical chemistry; Wiley Ltd: Federal Republic of Germany, 2003; pp 160.

(73) Forster, R. J. *Langmuir* **1995***, 11*, 2247.

(74) Chidsey, C. E. D. *Science* **1991***, 251*, 919.

(75) Forster, R. J.; Faulkner, L. R. *J. Am. Chem. Soc.* **1994***, 116*, 5444.

(76) Farrell, M. M. Electroanalysis in the Nanodomain: Quinone Monolayers and Nanometer Dimensioned Electrodes, Dublin City University, Dublin, 2003.

(77) Chen, J.; Aoki, K. *Electrochem. Comm.* **2002***, 4*, 24.

(78) Amatore, C. In *Electrochemistry at Ultramicroelectrodes;* Rubinstein, I., Ed.; Physical Electrochemistry. Principles, methods and applications; Marcell Dekker, Inc.: United States of America, 1995; pp 131.

(79) Amatore, C.; Maisonhaute, E.; Simonneau, G. *Electrochem. Comm.* **2000***, 2*, 81.

(80) Watkins, J. J.; Chen, J.; White, H. S.; Abruna, H. D.; Maisonhaute, E.; Amatore, C. *Anal. Chem.* **2003***, 75*, 3962.

(81) Bond, A. M.; Oldham, K. B.; Zoski, C. G. *Anal. Chim. Acta* **1989***, 215*, 177.

(82) Adams, R. N. *Anal. Chem.* **1976***, 48*, 1126A.

(83) Pendley, B. D.; Abruna, H. D. *Anal. Chem.* **1990***, 62*, 782.

(84) Shao, Y.; Mirkin, M. V. *Anal. Chem.* **1997***, 69*, 1627.

(85) Ufheil, J.; Heb, C.; Borgwarth, K.; Heinze, J. *Phys. Chem. Chem. Phys.* **2005***, 7*, 3185.

(86) Baltes, N.; Thouin, L.; Amatore, C.; Heinze, J. *Angew. Chem. Int. Ed.* **2004***, 43*, 1431.

(87) Bard, A. J.; Abruna, H. D.; Chidsey, C. E.; Faulkner, L. R.; Feldberg, S. W.; Itaya, K.; Majda, M.; Melroy, O.; Murray, R. W.; Porter, M. D.; Soriaga, M. P.; White, H. S. *J. Phys. Chem.* **1993***, 97*, 7147.

(88) Fang, Y.; Leddy, J. *Anal. Chem.* **1995***, 67*, 1259.

(89) Ferrigno, R.; Brevet, P. F.; Girault, H. H. *Electrochimica Acta* **1997***, 42*, 1895.

(90) Bartlett, P. N.; Taylor, S. L. *J. Electroanal. Chem.* **1998***, 453*, 49-60.

(91) Guo, J.; Lindner, E. *J. Electroanal. Chem.* **2009***, 629*, 180-184.

(92) Smith, C. P.; White, H. S. *Anal. Chem.* **1992***, 64*, 2398.

(93) Robertson, R. T.; Pendley, B. D. *J. Electroanal. Chem.* **1994***, 374*, 173.

(94) Slevin, C. J.; Gray, N. J.; Macpherson, J. V.; Webb, M. A.; Unwin, P. R. *Electrochem. Comm.* **1999***, 1*, 282.

(95) Fish, G.; Bouevitch, O.; Kokotov, S.; Lieberman, K.; Palanker, D.; Turovets, I.; Lewis, A. *Rev. Sci. Instrum.* **1995***, 66*, 3300.

(96) Penner, R. M.; Heben, M. J.; Longin, T. L.; Lewis, N. S. *Science* **1990***, 250*, 1118.

(97) Schulte, A.; Chow, R. H. *Anal. Chem.* **1996***, 68*, 3054.

(98) Ciani, I.; Daniele, S. *Anal. Chem.* **2004***, 76*, 6575.

(99) Nagahara, L. A.; Thundat, T.; Lindsay, S. M. *Rev. Sci. Instrum.* **1989***, 60*, 3128.

(100) Liu, B.; Rolland, J. P.; DeSimone J.M.; Bard, A. J. *Anal. Chem.* **2005***, 77*, 3013.

(101) Ufheil, J.; Borgwarth, K.; Heinze, J. *Anal. Chem.* **2002***, 74*, 1316.

(102) Williamson, R. L.; Miles, M. J. *J. Appl. Phys.* **1996***, 80*, 4804.

(103) Valaskovic, G. A.; Holton, M.; Morrison, G. H. *Applied Optics* **1995***, 34*, 1215.

(104) Levis, R. A.; Rae, J. L. *Biophysical Journal* **1993***, 65*, 1666.

(105) Canfield, J. G. *Journal of Neuroscience Methods* **2006***, 158*, 19.

(106) Sun, P.; Mirkin M.V. *Anal. Chem.* **2006***, 78*, 6526.

(107) Yasukawa, T.; Kaya, T.; Matsue, T. *Anal. Chem.* **1999***, 71*, 4637.

(108) Liljeroth, P.; Johans, C.; Slevin, C. J.; Quinn, B. M.; Konturri, K. *Electrochem. Comm.* **2002***, 4*, 67.

(109) Liljeroth, P.; Johans, C.; Slevin, C. J.; Quinn, B. M.; Konturri, K. *Anal. Chem.* **2002***, 74*, 1972.

(110) Caruana, D. J.; Bannister, J. V. *J. Electroanal. Chem.* **1997***, 424*, 197.

(111) Kim, Y.; Scarnulis, D. M.; Ewing, A. G. *Anal. Chem.* **1986***, 58*, 1782.

(112) Goldstein, J. I.; Newbury, D. E.; Joy, D. C.; Lyman, C. E.; Echlin, P.; Lifshin, E.; Sawyer, L. C.; Michael, J. R. In *Scanning Electron Microscopy and x-ray Microanalysis;* Kluwer Academic Publishers Group: United States of America, 2003; , pp 586.

(113) Menon, V. P.; Martin, C. R. *Anal. Chem.* **1995***, 67*, 1920.

(114) Fletcher, S. *Electrochimica Acta* **1990***, 35*, 1797.

(115) Baranski, A. S.; Szulborska, A. *Electrochimica Acta* **1996***, 41*, 985.

(116) Tschuncky, P.; Heinze, J. *Anal. Chem.* **1995***, 67*, 4020.

(117) Nomura, S.; Nozaki, K.; Okazaki, S. *Anal. Chem.* **1991***, 63*, 2665.

(118) D'Souza, S. F. *Biosensors and Bioelectronics* **2001***, 16*, 337-353.

(119) Wilner, I.; Katz, E. *Angew. Chem. Int. Ed.* **2000***, 39*, 1180.

(120) Gooding, J. J.; Hall, E. A. H.; Hibbert, D. B. *Electroanalysis* **1998***, 10*, 1130.

(121) Scheller, F. W.; Wollenberger, U. In *Enzyme Electrodes;* Wilson, G. S., Ed.; Encyclopedia of Electrochemistry. Volume 9. Bioelectrochemistry; Wiley-VCH: Federal Republic of Germany, 2002; pp 431.

(122) Clark, L. C.; Lyons, C. J. *Ann. NY Acad. Sci.* **1962***, 102*, 29.

(123) Nien, P. C.; Huang, M. C.; Chang, F. Y.; Ho, K. C. *Electroanalysis* **2008***, 20*, 635.

(124) Xie, H.; Tan, X. L.; Gao, Z. *Frontiers in Bioscience* **2005***, 10*, 1797.

(125) Wang, Z.; Liu, S.; Wu, P.; Cai, C. *Anal. Chem.* **2009***, 81*, 1638.

(126) Wang, J.; Lu, F.; Angnes, L.; Liu, J.; Sakslund, H.; Chen, Q.; Pedrero, M.; Chen, L.; Hammerich, O. *Anal. Chim. Acta* **1995***, 305*, 3-7.

(127) Wang, Y.; Xu, H.; Zhang, J.; Li, G. *Sensors* **2008***, 8*, 2043.

(128) Wang, J. *Chem. Rev.* **2008***, 108*, 814.

(129) Rusling, J. F.; Wang, B.; Yun, S. In *Electrochemistry of Redox Enzyme;* Bartlett, P. N., Ed.; Bioelectrochemistry. Fundamentals, Experimental Techniques and Applications; Wiley Ltd.: Great Britain, 2008; pp 39.

(130) Ahuja, T.; Mir, I. A.; Kumar, D.; Rajesh *Biomaterials* **2007***, 28*, 791-805.

(131) Yang, Q.; Atanasov, P.; Wilkins, E. *Biosensors and Bioelectronics* **1999***, 14*, 203-210.

(132) Kim, C. S.; Oh, S. M. *Electrochimica Acta* **1996***, 41*, 2433-2439.

(133) Cosnier, S. *Biosensors and Bioelectronics* **1999***, 14*, 443-456.

(134) Montornes, J. M.; Vreeke, M. S.; Katakis, I. In *Glucose Sensors;* Bartlett, P. N., Ed.; Bioelectrochemistry. Fundamentals, Experimental Techniques and Applications; Wiley: Great Britain, 2008; pp 199.

(135) Vadgama, P.; Schoenleber, M. In *In vivo Applications: Glucose Monitoring, Fuel Cells;* Bartlett, P. N., Ed.; Bioelectrochemistry. Fundamentals, Experimental Techniques and Applications; Wiley Ltd.: Great Britain, 2008; pp 443.

(136) Stuart, M. *Start-Up* **2007***, 12*, 14.

(137) Mugweru, A.; Clark, B. L.; Pishko, M. V. *Electroanalysis* **2007***, 4*, 453.

(138) Schuvailo, O. M.; Soldatkin, O. O.; Lefebvre, A.; Cespuglio, R.; Soldatkin, A. P. *Anal. Chim. Acta* **2006***, 573-574*, 110-116.

(139) Biegler, T. *J. Electrochem. Soc.* **1969***, 116*, 1131.

(140) Bindra, D. S.; Zhang, Y.; Wilson, G. S.; Sternberg, R.; Thevenot, D. R.; Moatti, D.; Reach, G. *Anal. Chem.* **1991***, 63*, 1692.

(141) Vilkanauskyte, A.; Erichsen, T.; Marcinkeviciene, L.; Laurinavicius, V.; Schuhmann, W. *Biosensors and Bioelectronics* **2002***, 17*, 1025-1031.

(142) Yoon, H.C. and Kim, H.-S. *Anal. Chem.* **2000***, 72*, 922.

(143) Yehezkeli, O.; Yan, Y.; Baravik, I.; Tel-Vered, R.; Wilner, I. *Chem. Eur. J.* **2009***, 15*, 2674.

(144) Palmisano, F.; Zambonin, P. G.; Centoze, D.; Quinto, M. *Anal. Chem.* **2002***, 74*, 5913.

(145) Xin, Q.; Wightman, R. M. *Anal. Chim. Acta* **1997***, 341*, 43-51.

(146) Masamichi, F.; Rubenstein, I.; Rusling, J. F., Eds.; In *Modified Electrodes;* Bard, A. J., Stratmann, M., Eds.; Encyclopedia of Electrochemistry; Wiley -VCH: Federal Republic of Germany, 2007; Vol. 10, pp 850.

(147) Liu, G.; Böcking, T.; Gooding, J. J. *J. Electroanal. Chem.* **2007***, 600*, 335-344.

(148) Masson, J.; Kranz, C.; Booksh, K. S.; Mizaikoff, B. *Biosensors and Bioelectronics* **2007***, 23*, 355-361.

(149) Tsujimoto, M.; Yabutani, T.; Sano, A.; Tani, Y.; Murotani, H.; Mishima, Y.; Maruyama, K.; Yasuzawa, M.; Motonaka, J. *Analytical Sciences* **2007***, 23*, 59.

(150) Matsumoto, N.; Chen, X.; Wilson, G. S. *Anal. Chem.* **2002***, 74*, 362.

(151) Chen, X.; Matsumoto, N.; Hu, Y.; Wilson, G. S. *Anal. Chem.* **2002***, 74*, 368.

(152) Wang, J. and Angnes, L. *Anal. Chem.* **1992***, 64*, 456.

(153) Daly, D. J.; O'Sullivan, C. K.; Guilbault, G. G. *Talanta* **1999***, 49*, 667-678.

(154) Wallace, G. G.; Spinks, G. M.; Kane-Maguire, L. A. P.; Teasdale, P. R. In *Conductive Electroactive Polymers. Intelligent Polymer System;* Taylor & Francis Ltd: United States of America, 2008; Vol. 1, pp 270.

(155) van Os, P. J. H. J.; Bult, A.; Koopal, C. G. J.; van Bennekom, W. P. *Anal. Chim. Acta* **1996***, 335*, 209-216.

(156) Chen, C.; Jiang, Y.; Kan, J. *Biosensors and Bioelectronics* **2006***, 22*, 639-643.

(157) Yabuki, S.; Shinohara, H.; Aizawa, M. *J. Chem. Soc. Chem. Commun.* **1989**, 945.

(158) Gros, P.; Bergel, A. *J. Electroanal. Chem.* **1995***, 386*, 65-73.

(159) Trojanowicz, M.; Krawczynski vel Krawczyk, T.; Geschke, O.; Cammann, K. *Sensors Actuators B: Chem.* **1995***, 28*, 191-199.

(160) Nien, P. C.; Tung, T. S.; Ho, K. C. *Electroanalysis* **2006***, 18*, 1408.

(161) Hwang, B. J.; Shieh, D. T.; Chieh, W. C.; Liaw, D.; Li, L. *Thin Solid Films* **1997***, 301*, 175-182.

(162) Shin, M.; Kim, H. *Biosensors and Bioelectronics* **1996***, 11*, 161-169.

(163) Belanger, D.; Nadreau, J.; Fortier, G. *J. Electroanal. Chem.* **1989***, 274*, 143.

(164) Arrigan, D. W. M.; Gray, D. S. *Anal. Chim. Acta* **1999***, 402*, 157-167.

(165) Carelli, D.; Centonze, D.; De Giglio, A.; Quinto, M.; Zambonin, P. G. *Anal. Chim. Acta* **2006***, 565*, 27-35.

(166) Cosnier, S.; Innocent, C.; Allien, L.; Poitry, S.; Tsacopoulos, M. *Anal. Chem.* **1997***, 69*, 968.

(167) Nakabayashi, Y.; Wakuda, M.; Imai, H. *Analytical Sciences* **1998***, 14*, 1069.

(168) Bartlett, P. N.; Tebbutt, P.; Tyrrell, C. H. *Anal. Chem.* **1992***, 64*, 138.

(169) Yuqing, M.; Jianrong, C.; Xiaohua, W. *Trends Biotechnol.* **2004***, 22*, 227-231.

(170) Arrigan, D. W. M.; Bartlett, P. N. *Biosensors and Bioelectronics* **1998***, 13*, 293-304.

(171) Kohma, T.; Oyamatsu, D.; Kuwabata, S. *Electrochem. Comm.* **2007***, 9*, 1012-1016.

(172) Newman, J. D.; White, S. F.; Tothill, I. E.; Turner, A. P. F. *Anal. Chem.* **1995***, 67*, 4594.

(173) O'Connell, P. J.; O'Sullivan, C. K.; Guilbault, G. G. *Anal. Chim. Acta* **1998***, 373*, 261-270.

(174) Dharuman, V.; Chandrasekara, P. *J. Solid State Electrochem.* **2006***, 10*, 967.

(175) Seddon, E. A.; Seddon, K. R. In *The chemistry of ruthenium;* Clark, R. J. H., Ed.; Topics in inorganic and general chemistry; Elsevier Science Publishers B.V.: Netherlands, 1984; Vol. 19, pp 1373.

(176) Kumar, A. S.; Chen, P.; Chien, S.; Zen, J. *Electroanalysis* **2005***, 17*, 211.

(177) Lyons, M. E. G.; Fitzgerald, C. A.; Smith, M. R. *Analyst* **1994***, 119*, 855.

(178) Wu, J.; Suls, J.; Sansen, W. *Electrochem. Comm.* **2000***, 2*, 90-93.

(179) Lee, E. C.; Bergens, H. S. *J. Electrochem. Soc.* **1998***, 145*, 4182.

(180) Vigier, F.; Gloaguen, F.; Léger, J. -.; Lamy, C. *Electrochimica Acta* **2001***, 46*, 4331-4337.

(181) Vukovic, M.; Cukman, D. *J. Electroanal. Chem.* **1999***, 474*, 167-173.

(182) Sakslund, H.; Wang, J.; Lu, F.; Hammerich, O. *J. Electroanal. Chem.* **1995***, 397*, 149-155.

(183) Bartlett, P. N.; Toh, C. S.; Calvo, E. J.; Flexer, V. In *Modelling Biosensor Responses;* Bartlett, P. N., Ed.; Bioelectrochemistry. Fundamentals, Experimental Techniques and Applications; Wiley Ltd: Great Britain, 2008; pp 267.

(184) Van Gerwen, P.; Laureyn, W.; Laureys, W.; Huyberechts, G.; Op De Beeck, M.; Baert, K.; Suls, J.; Sansen, W.; Jacobs, P.; Hermans, L.; Mertens, R. *Sensors and Actuators B: Chemical* **1998***, 49*, 73-80.

(185) Bakker, E. *Anal. Chem.* **2004***, 76*, 3285-3298.

(186) Mak, L. H.; Knoll, M.; Dankbar, N.; Sundermeier, C.; Gorschlüter, A. *Sensors and Actuators B: Chemical* **2006***, 114*, 132-140.

(187) Neugebauer, S.; Muller, U.; Lohmuller, T.; Spatz, J. P.; Stelzle, M.; Schuhmann, W. *Electroanalysis* **2006***, 18*, 1929.

(188) Lee, Y.; Ding, Z.; Bard, A. J. *Anal. Chem.* **2002***, 74*, 3634.

Chapter 2

Nano- and Micro-Electrodes: Fabrication and Characterisation

2.1 Introduction

Electrochemistry at electrodes with micro and nanoscopic dimensions is one of the most important frontiers in modern electrochemical science[1-4] but this area can be still considered in its infancy[5] as the construction of microelectrodes with radii smaller than 1 μm is still far from routine. The two steps procedure elaborated by Pendley *et al.*[6] seems to offer a more automated and reliable long-term approach to nanode fabrication because of the speed and reproducibility of production.[5] Indeed, this method has been efficiently employed in the fabrication of platinum nanoelectrodes.[7-10]

No extensive study of the yield of the platinum UMEs prepared with a laser puller has been described in the literature. Moreover, only one reference[6] mentioned this procedure for the preparation of gold probes but no characterisation data were presented. This chapter describes the manufacture of platinum nano- and micro probes with particular attention on the optimisation of the electrodes yield. Also, gold microelectrodes were prepared by the laser puller procedure and it is the first time that the details of the sealing and pulling programs are described and discussed for this metal.

When the size of the electrodes approaches these small scales, they have to be carefully characterized to avoid introducing artefacts especially in the measurement of kinetic parameters.[7] Geometrical factors, *e.g.*, radius, glass shield, electrochemical area, have to be determined and corroborated using different techniques. Moreover, the presence of defects or faults, *e.g.*, a recess or lagooned geometry and poor seals, have to be diagnosed and possibly removed. In this work, the electrodes are characterized employing Cyclic Voltammetry (CV), Scanning Electrochemical Microscopy (SECM), Scanning Electron Microscopy (SEM) and High Speed Chronoamperometry. The overview of the results obtained with such a wide spectrum of techniques gave a better insight of the properties of the probes and helped in understanding faults associated with the fabrication procedure.

Ring-disk microelectrodes have all the advantages of a dual probe, see Section 1.3.9 for some of the applications in the literature. In this perspective, the nano-sized platinum electrodes fabricated offer an excellent platform as the glass, which encapsulates the

platinum wire, can be metal coated and then insulated. Polishing of the tip of the electrode would expose the metal disk and ring which are separated by an insulator layer of a controlled thickness. Thus, dual probes have dimensions that are at least an order of magnitude smaller than what previously reported by Liljeroth *et al.* and Ufheil *et al.*.[9,11,12] However, some difficulties experienced during their preparation are reported.

2.2 Experimental

2.2.1 Materials and Chemicals

Ferrocenemethanol (97 %), potassium chloride (> 99 %), sulphuric acid (99,999%), nitric acid (70 %), sodium hydroxide (> 98 %) and sodium hydrogen sulphate (> 93 %) were all supplied from Sigma-Aldrich. Ruthenium hexamine chloride (98 %, Strem Chemicals), insulating varnish (mixture of: butan-2-one oxime syn-O,O'-di(butan-2-one oxime)diethoxysilane, Radionics), alumina powder (1.00 μm, 0.30 μm and 0.05 μm, Buehler). All chemicals were used as received. All the aqueous solutions were prepared from Milli-Q reagent water (Millipore Corp.), 18 MΩ cm.

The borosilicate capillaries (i.d.: 1.2 mm, o.d.: 2 mm, length: 20 cm) were donated from the Newcastle upon Tyne's university glass workshop. Borosilicate (0.50 mm-1.00 mm-10 cm and 0.3 mm-1.00 mm-7.5 cm), aluminosilicate (0.68 mm-1.0 mm-10 cm) and quartz (0.70 mm-1.00 mm-7.5 cm, 0.5 mm-1.00 mm-7.5 cm and 0.30 mm-1.00 mm-7.5 cm) capillaries were all supplied from Sutter Instruments. Soda (0.50 mm-1.1 mm-10 cm) glass capillaries were from Intracell. Ceramic tiles (Sutter Instruments) were employed for scoring capillaries. 50 μm annealed temper platinum wire, 25 μm hard and annealed temper platinum wires, 25 μm hard temper and 0.1 mm annealed gold wires, 5 μm and 1 μm Wollaston wires were all purchased from Goodfellow Cambridge Limited. Here, and in the following sections, the size of the metal wires is given as the diameter if not differently stated. Electrical contact was achieved using copper enamelled wires (0.6 mm, 0.4 mm, 0.2 mm, Rowan Cable Products LTD) and solder wire (32 swg, Combine Precision Components). The hook-up wire was glued to the glass walls with Araldite glue (Bostik). Alumina sheet (30, 15, 5, 3, 1 and 0.3 μm)

and a polishing table were from Thorlabs while the neoprene pad was from Struers. BV-10 grinding disks were from Sutters and according to manufacturer they are suitable for bevelling micropipettes ranging from 0.1 μm to 50 μm depending on the disk supplied.

2.2.2 Equipment and Methods

All the CV and SECM measurements were run inside a Faraday cage using the 900a CH-instruments potentiostat. The cage consisted of 1 mm thick aluminium foil fixed to the inner and outer walls of a 2 cm thick PVC box. The weight of the box reduced mechanical and acoustic vibrations which could affect the measurements. The most appropriate way to ground the cage was evaluated using resistors and consisted in grounding the outer and inner wall of the cage independently. A platinum wire was employed as the counter electrode and a custom-built Ag/AgCl (saturated KCl),[13] as reference electrode (~ -0.045 V *vs.* SCE). A 2 mm platinum disk electrode (CH instruments) polished on a wet pad with 0.05 μm alumina or alternatively an atomic flat gold wafer (Tyndall National Institute) was used as substrate in the SECM measurements. The approach curves on the metal disk and on the Teflon plastic surrounding the latter were fitted according to the expressions elaborated by Lefrou[14] and Cornut *et al.*[15], respectively, for the positive and negative feedback, Equations 1.5 and 1.9. R_G was evaluated from the fitting of the approach curve over the insulator as the negative feedback is more sensitive to this parameter.[16] To speed up the operations during the SECM approaches, a long-distance microscope helped in positioning the probe quite close to the substrate, *i.e.* ~ 50 - 100 μm far from the surface.

To carry out the chronoamperometric experiments, a custom built programmable function generator-potentiostat, which has a rise time of less than 10 ns, was used to apply potential steps of variable pulse width and amplitude directly to the two-electrode cell. The details of the instrument can be found elsewhere.[17] Transient decay of the capacitive current in aqueous 0.1 M KCl were obtained applying a 0.2 V bias against a custom built Ag/AgCl reference connected in parallel to a platinum wire to provide a high-frequency path.[17,18]

Microelectrodes were fabricated using the Sutter P-2000 laser puller with the help of a pump (N810.3FT.18, KNF Laboport) and some flexible silicone tubing (Cole Parmer) which generated a weak vacuum inside the capillary during the sealing step. If not otherwise stated, the size of the microelectrodes is given as radius. For optical microscopy, a Nikon ECLIPSE ME600D Microscope was employed and images were captured using a Panasonic DMC-FX01 Lumix digital camera. A Polaron Sputter Coater (Quorum Technologies) provided with a gold target was employed for gold coating. SEM images were captured with the S3000N (Hitachi) or the XL30 ESEM-FEG (Philips) Microscopes. A Nanoscope III Atomic Force Microscope (Veeco) was employed to capture images of the nanocavities array fabricated by nanosphere lithography. In fact, a monolayer of polystyrene spheres, (820 nm, Duke Scientific Corporation) was prepared on an atomic flat gold surface, then gold was electrochemically electrodeposited from a commercial aqueous gold plating solution through the gaps of the spheres. Finally, the spheres were dissolved with toluene. The nanocavities samples were kindly provided by Bincy Jose of the Tia Keyes research group following the procedure elsewhere described.[19]

2.2.3 Preparation of Pt Microelectrodes from 25 and 50 µm Wires

2.2.3.1 Large Glass Microelectrodes

The borosilicate glass tube (2.0 mm-1.5 mm-15 cm) was cut into pieces 4 - 5 cm long, then soaked in a 3 M HNO_3 solution for one hour. The solution was neutralized with NaOH and $NaHSO_4$ and rinsed several times with nanopure water. The capillaries were then oven dried overnight at 110 °C. Figure 2.1 shows the steps in the preparation of the microelectrode. Indeed, one end was exposed to the flame of a butane torch in order to reduce the hole to about 0.2 mm or less. A straight piece of 25 or 50 µm platinum wire was inserted from the partially closed end and pushed in until 1 mm or less protruded. Annealed or hard temper platinum wire were both employed with the latter eventually straightened by carefully heating over with a butane flame. Finally, while rotating the capillary continuously, the Pt wire was completely sealed in the glass.

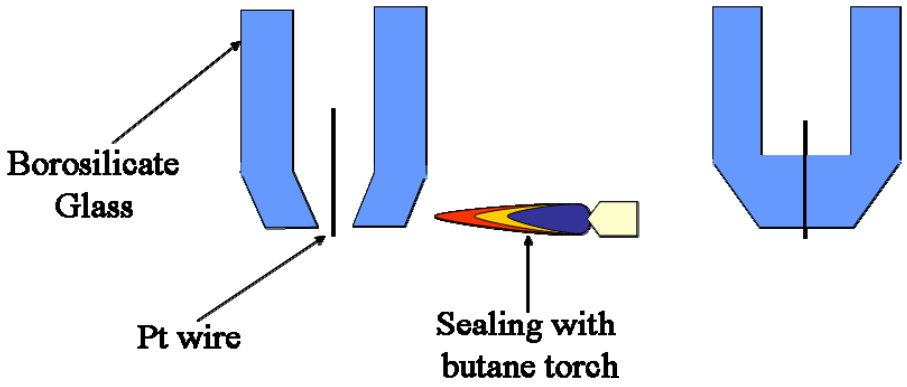

Figure 2.1 Sketch of the sealing of a platinum wire within a borosilicate tube. The platinum wire was inserted into the glass capillary through the partially closed end in the way 1 - 2 mm of the wire protruded out. Then, it was sealed tightly within the glass rotating the tube and heating it over a butane torch flame.

The copper wire was inserted from the open end of the tube along with a piece of low melting point solder, 2 - 3 mm long. Then, keeping the copper wire pushed forward, the solder was melted by heating the tube with a heat gun and an electrical contact was achieved. The copper and the soldered junction filled the glass barrel minimizing the movement of the Pt microwire which helped preventing its breakage but a further precaution was to fix the copper cable to the top of the capillary with Araldite glue. Microelectrodes were polished manually with decreasing size of alumina sheet set on the top of a polishing table or with alumina powder spread on the top of a wet porous neoprene pad. Microelectrodes were sharpened manually by tilting their body at ~ 45° and rolling the tip on the grinding surface. The capillary was sonicated in water for two minutes prior to moving to the next size of the alumina sheet or powder.

2.2.3.2 Small Glass Shield Microelectrodes

Another fabrication procedure was employed to achieve small R_G values so as to reduce the time which had to be dedicated to the sharpening step. Indeed, borosilicate capillaries (i.d. 0.58 mm) were pulled with the laser puller in order to obtain a reasonable sharp but short-taper tip. A satisfactory program was:

HEAT: 340; FIL.: 4; VEL.: 40; DELAY: 220; PULL: 50 (2.1)

The resulting taper was ~ 5 mm long and it was snapped by tapping it gently on the bench or better using a ceramic tile to obtain an open pipette with a diameter of 200 - 300 µm. An annealed Pt wire, already soldered to a copper cable, was pushed into the pulled capillary until few hundred micron protruded from the small hole. The wire was then sealed within the glass using a butane torch. As the latter step rounded the tip of the electrode, repeated but quick insertions (3 - 5 seconds long) into the flame only of the tip of the capillary spinning the glass barrel at the same time, minimized this effect. When a good seal was achieved (no gas bubbles trapped in the glass in proximity of the microwire) the electrode could be polished and sharpened as explained in the previous section. Optionally, the electrode could be inserted in a glass shield to increase robustness and prevent the risk of accidental breakage as shown in Figure 2.2.

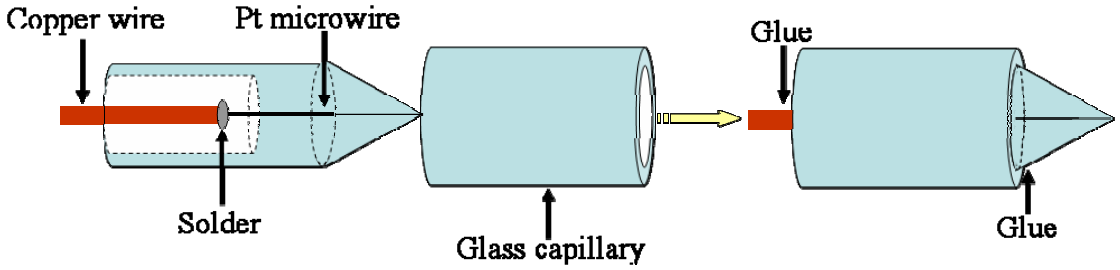

Figure 2.2 Insertion of the UME in a second larger glass capillary to improve its robustness. The copper cable and the tip of the UME were anchored to the larger capillary with glue.

2.2.4 Preparation of Pt Micrometer Electrodes by Wollaston Wire

Figure 2.3 shows the steps in the preparation of microelectrodes using the Wollaston wires. These wires were soldered to a copper wire and pushed into a capillary pulled using Program 2.1 until 1 cm of the wire protruded from the hole. Then 2 - 3 millimetres of the Wollaston wire were dipped in a solution of 8 M HNO_3 for at least 90 - 100 seconds, which was the time necessary usually to see the dissolution and the removal of the silver coating thus exposing the platinum underneath. During this step any contact between the glass and the nitric acid was avoided in case the following sealing was compromised. After dipping the exposed wire in nanopure water, the removal of the silver layer was checked using a microscope and the procedure repeated

if necessary. When the result was satisfactory, the Wollaston wire was pulled up by drawing the copper cable to which was connected, until few hundred micrometers of the exposed Pt wire protruded from the hole as seen using the optical microscope. Then the copper was anchored to the glass using Araldite glue and the Pt wire was sealed within the glass flaming the tip with a butane torch.

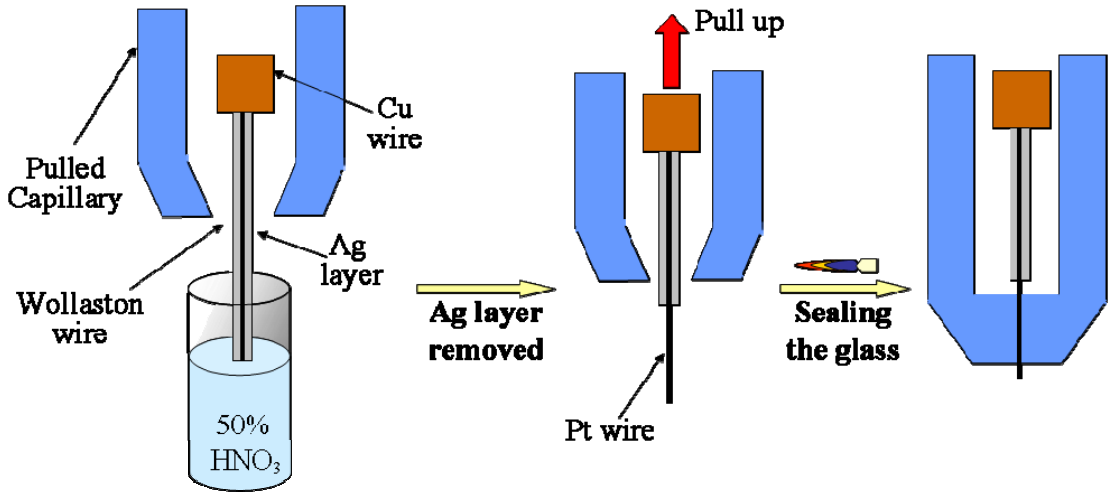

Figure 2.3 The steps involved in the preparation of microelectrodes with radius ≤ 5 μm using a Wollaston wire. The Wollaston wire, soldered to a copper cable, was inserted into the capillary in the way ~ 1 cm protruded from its pulled tip. Then, the silver coating was removed by dipping in 8 M HNO_3, which leaves exposed the platinum wire underneath. Drawing the copper wire, only 100 - 200 μm of the Pt wire were left protruding. Finally, the microwire was sealed tightly within the glass rotating the capillary and heating the tip over a butane torch flame.

2.2.5 Preparation of Nano- and Micro-Electrodes with Laser Puller

2.2.5.1 Preparation of Platinum Nanometer-sized Electrodes

A piece of 25 μm platinum wire, about 15 - 20 mm long, was cut from the reel and placed in the midpoint of the quartz capillary by tapping it gently. Figure 2.4 shows the sealing and pulling steps associated with the laser puller procedure. The glass-wire assembly was placed on the bars of the laser puller where silicon tubes were connected to both sides of the capillary open ends and custom-built stoppers blocked the bars, *i.e.*,

no pulling force could be exerted by the instrument. The pump was switched on and the capillary was evacuated. Proper HEAT and FILAMENT values (depending on the i.d./o.d. ratio and the glass type) had to be selected in order to seal the wire into the glass. The sealing programs set for 0.3 mm and 0.5 mm i.d. quartz capillaries were:

HEAT: 795 ± 5; FIL.: 5; VEL.: 255; DELAY: 255; PULL: 0 (2.2)

and

HEAT: 730 ± 5; FIL.: 5; VEL.: 255; DELAY: 255; PULL: 0 (2.3)

respectively. Each program was run for 40 seconds and after a pause of 20 seconds repeated. A total of 4 and 3 heating/cooling cycles were performed in the case of Programs 2.2 and 2.3, respectively.

As soon as the sealing program finished running, the vacuum tubes and the stoppers were removed. Then, after one minute from the end of the last sealing step, the program for the hard pulling was selected which was common to both the glass sizes:

HEAT: 710 ± 20; FIL.: 1 ± 1; VEL.: 43 ± 2; DEL.: 124 ± 3; PULL: 120 ± 60 (2.4)

On average, the glass-wire assembly was pulled in 4 - 5 and 3.5 - 4 seconds, respectively for 0.3 and 0.5 mm inner diameter capillaries, depending on the parameters chosen. Further electrical contact at the back of the capillary was accomplished to create a nano-sized electrode as explained in Section 2.2.3.1.

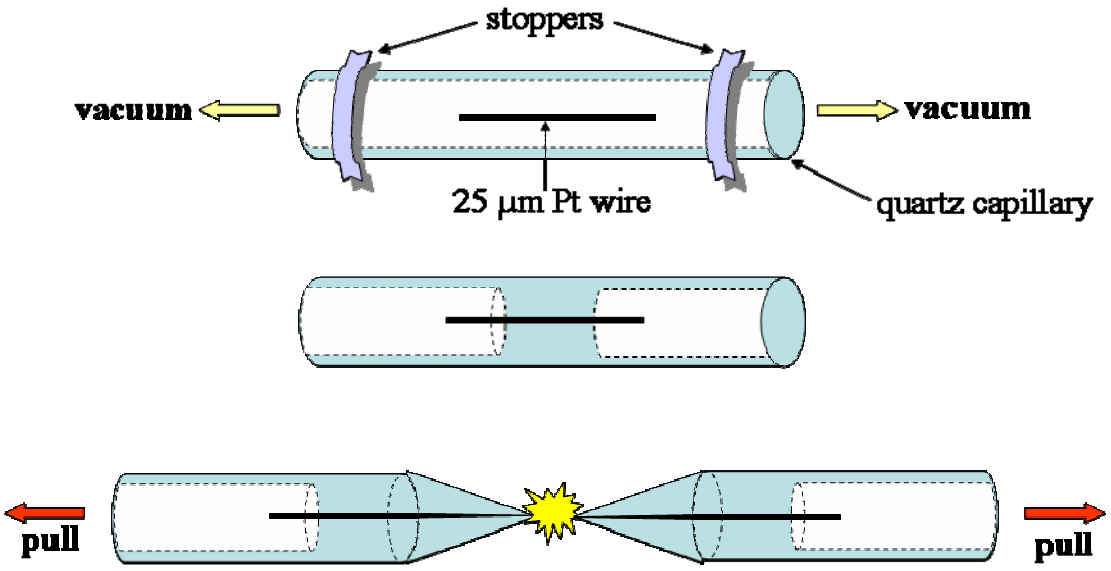

Figure 2.4 Sketch of the preparation of microelectrodes with a laser puller. The 25 µm platinum wire was inserted into the glass capillary and placed in its midpoint by tapping the capillary gently on the bench. Vacuum was applied at both sides of the open ends of the capillary. A specific program in the laser puller was selected. The use of stoppers at this stage prevents the hard pulling to happen and allowed only the melting of the quartz glass around the microwire. After removing the stoppers, a second program was selected and the quartz/platinum assembly pulled to a fine tip.

2.2.5.2 Preparation of Gold Ultramicroelectrodes

Similarly to what explained in the previous section, a piece of 25 µm gold wire was sealed within a glass capillary and then the assembly pulled using the laser puller. Different programs were set depending on the glass types and sizes employed in order to find the best suitable for the manufacture of the gold microelectrodes.

At first borosilicate capillaries with i.d. of 0.5 mm and o.d. of 1.0 mm were used. The sealing program was:

HEAT: 287 ± 5; FIL.: 5; VEL.: 255; DELAY: 255; PULL: 0 (2.5)

Program 2.5 was run for 40 seconds, followed by a 20 seconds pause. A total of 5 heating/cooling cycles were performed. As soon as the sealing program finished

running, the vacuum tubes and the stoppers were removed. Then, after one minute after the end of the last sealing step, the program below was selected for the hard pulling:

HEAT: 310 ± 10; FIL.: 2; VEL.: 31 ± 1; DEL.: 117 ± 1; PULL: 100 ± 20 (2.6)

Program 2.6 pulled the capillaries apart in ~ 4.0 – 4.5 seconds.

Second, borosilicate capillaries with same outer diameter but with 0.3 mm as inner diameter were employed. The programs set for the sealing and pulling steps were:

HEAT: 315 ± 5; FIL.: 5; VEL.: 255; DELAY: 255; PULL: 0 (2.7)

and

HEAT: 330 ± 10; FIL.: 1 ± 2; VEL.: 32; DEL.: 126 ± 2; PULL: 160 ± 40 (2.8)

respectively. Program 2.7 was run for 40 seconds, followed by a 20 seconds pause. A total of 4 heating/cooling cycles were performed. After a pause of one minute from the end of the last sealing step, during which stoppers and vacuum were removed, Program 2.8 pulled the capillaries apart in ~ 4.0 – 4.5 seconds.

Third, soda glass capillaries were used and programs set up for the sealing and the pulling steps were:

HEAT: 290 ± 5; FIL.: 5; VEL.: 255; DELAY: 255; PULL: 0 (2.9)

and

HEAT: 305 ± 10; FIL.: 2; VEL.: 30 ± 1; DEL.: 117 ± 1; PULL: 100 ± 20 (2.10)

respectively. Program 2.9 was run for 40 seconds, followed by a 20 seconds pause. A total of 5 heating/cooling cycles were performed. After a pause of one minute from the end of the last sealing step, during which stoppers and vacuum were removed, Program 2.10 pulled the capillaries apart in ~ 4.0 – 4.5 seconds.

Finally, aluminosilicate capillaries were employed. The programs set up for the sealing and the pulling steps were:

HEAT: 310 ± 5; FIL.: 5; VEL.: 255; DELAY: 255; PULL: 0 (2.11)

and

HEAT: 320 ± 10; FIL.: 2; VEL.: 33; DEL.: 118 ± 2; PULL: 120 ± 40 (2.12)

respectively. Program 2.11 was run for 40 seconds, followed by a 20 seconds pause. A total of 5 heating/cooling cycles were performed. Program 2.12 was run after a pause of one minute, in which stoppers and vacuum were removed, and the capillaries were pulled apart in ~ 3 - 3.5 seconds.

Further electrical contact, at the back of the capillaries, was accomplished as explained in Section 2.2.3.1.

2.2.5.3 Polishing and Sharpening Procedures

The probes with a taper longer than 3 mm, *i.e.*, on average metal disk < 2 μm, were polished by setting them in the holder of the beveller (electrode at 90° degree on the polishing surface). The grinding disks provided with the beveller or alumina sheet mounted on the top of a non alumina coated disk provided by Sutter were employed. The rotation of the grinding disk could not be changed and it was 60 rpm. When sharpening of these long taper probes was required, they were set in the chuck of a minidrill, held with a stand at an angle of ~ 45° on the plane of the grinding disk. The chuck rotated in the opposite direction to the grinding plate and the rotation speed was controlled by a variable power supply and set between 200 and 300 rpm. This additional movement provided an improved cutting force exerted on the electrode tip. The electrode was lowered towards the grinding disk using a fine screw mechanism.

The microelectrodes whose taper was cut, *i.e.*, on average radius > 2 μm, were polished manually with decreasing size of alumina sheet set on the top of a polishing table. These UMEs were sharpened manually tilting their body at ~ 45° and rolling the tip on the grinding surface. The electrodes were sonicated in water for two minutes prior to moving to the next size of alumina.

2.2.6 Preparation of Platinum Disk/Gold Ring Microelectrodes

The platinum disk microelectrodes were prepared as explained in Section 2.2.5.1. Their tapers were cut at different lengths using a ceramic tile and polished as explained in the previous section. Then, a 200 - 300 nm thick gold layer was sputtered on the top of the electrode glass by adjusting the two control parameters:

Voltage: 2 kV; Current: ~15 mA.

At these conditions, a gold layer was deposited with a rate of ~ 0.17 nm s^{-1}. However, as the coating is asymmetric, *i.e.*, the top part of the sample was coated preferentially, the electrode was flipped and gold sputtered in two times each of them ~ 19 minutes long.

The gold layer had to be insulated and several methods were attempted: brushing nail varnish on the top of it, dipping the electrode body in an insulating varnish solution or depositing a 0.5 μm thick SiO_2 layer on the top of the gold layer using plasma technique deposition. In the latter case, the coating of the samples was kindly done by Dr. Ram Prasad of the Dr. Stephen Daniels research group. Finally, the insulator layer was removed from the tip of the electrode by polishing, as explained in the previous section, which exposed the gold ring and the platinum disk.

2.3 Results and Discussion

2.3.1 12.5 and 25 μm Platinum Electrodes

These electrodes were prepared by sealing platinum wires, 25 and 50 μm, in a glass capillary as described in Section 2.2.3. The radius of the electrodes was determined by cyclic voltammetry at 2 mVs^{-1} and SECM approach curves using ferrocenemethanol or ruthenium hexamine chloride as redox mediator. The values obtained from the two techniques were reasonably close, *i.e.*, < 5 %, and confirmed the achievement of a good seal. The difference between the radius calculated and that expected by employing a specific wire size was on average < 20 % and possibly arose from a tilted wire profile during the sealing which might produce a more elliptical shape and the wire

manufacture tolerance (± 10 %). SEM helped in the evaluation of the roughness arising after the polishing step and Figure 2.5 shows a typical picture for one of these microelectrodes.

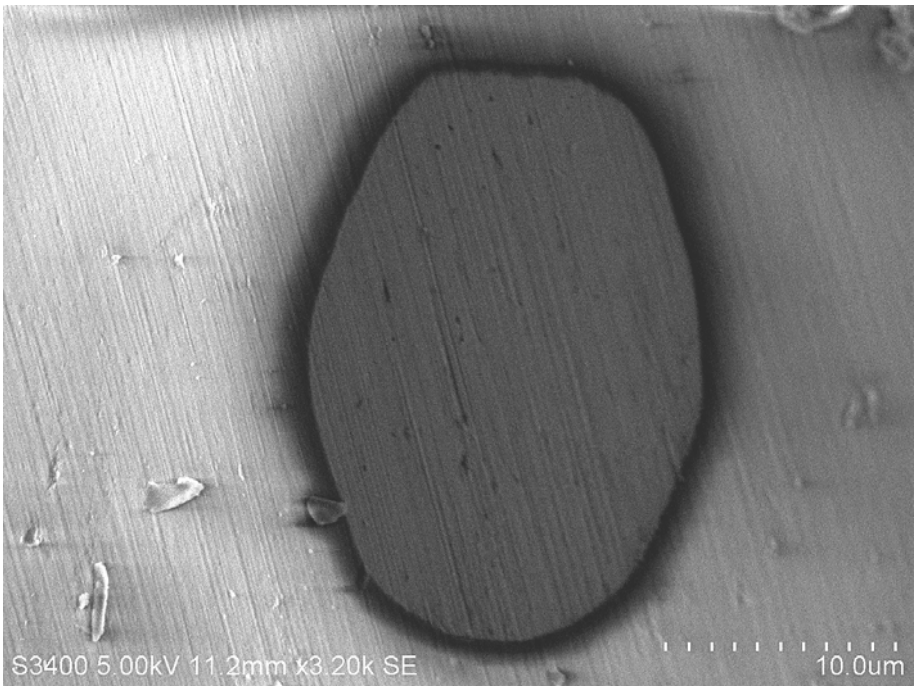

Figure 2.5 SEM image of a ~ 12.5 μm platinum microelectrode. The probe was prepared sealing a 25 μm wire in a glass capillary and then the electrode was sharpened and polished manually as explained in Sections 2.2.3.2 and 2.2.5.3, respectively. The sample was tilted in the SEM chamber with an angle of 45° in order to have a better visualization. The scale, magnification and accelerating voltage are shown on the image.

Figure 2.6 shows that, in a SECM approach curve using an inlaid disk UME, the glass shield of the latter normally touches the substrate instead than the wire. This contact causes the current to stop increasing in the positive or decreasing in negative feedback SECM approach curve as shown in Figure 2.7. Indeed, at this "contact" point the experimental curve deviates from the fitted one. Figure 2.6 suggests also that it is very hard to achieve a perpendicular approach of the tip during the SECM experiment, and this is the reason that a decrease of the R_G factor allows the probe to approach closer the substrate. The fabrication procedure described in Section 2.2.3.2 facilitated the sharpening step of these microelectrodes. Insertion of electrode in a glass shield compromised the alignment of the platinum disk with the axis of the second capillary

and then this step was practised only if the microelectrode was not to be used in a SECM measurement.

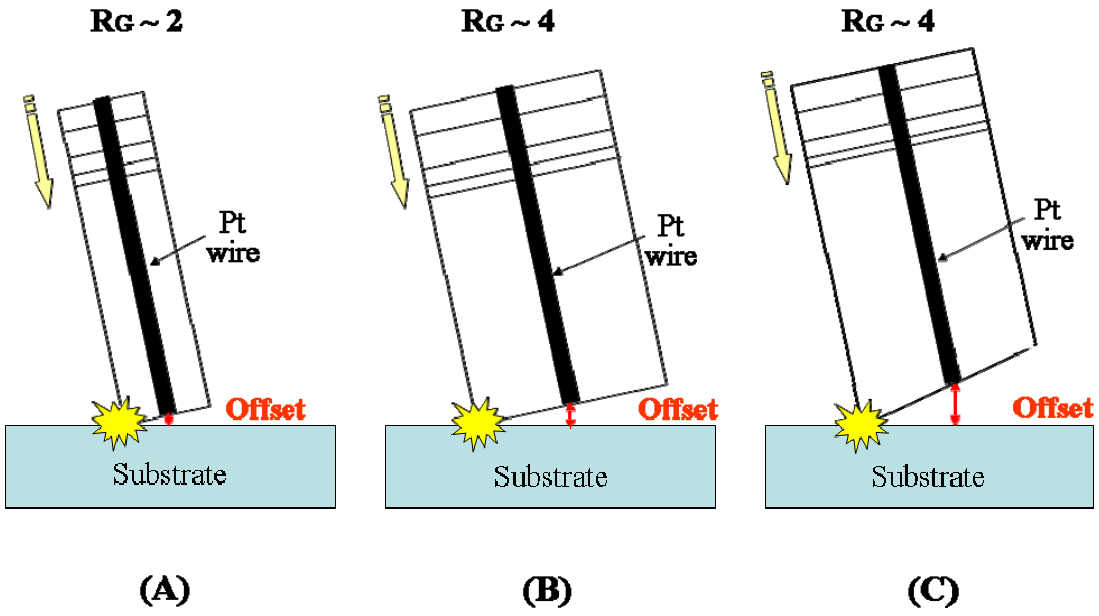

Figure 2.6 Probes approaching a substrate in a SECM experiment. The electrodes have the same metal disk radius but different glass shield size in (A) and (B) or shape of the latter in (C). The offset increases in function of the R_G factor in the case of a bad alignment (~ 15° in the cartoon) as appear comparing (A) with (B). Besides, in (C) an irregular profile of the probe might dictate a larger offset despite the probe has the same R_G factor of the electrode in (B). Images not fully to scale.

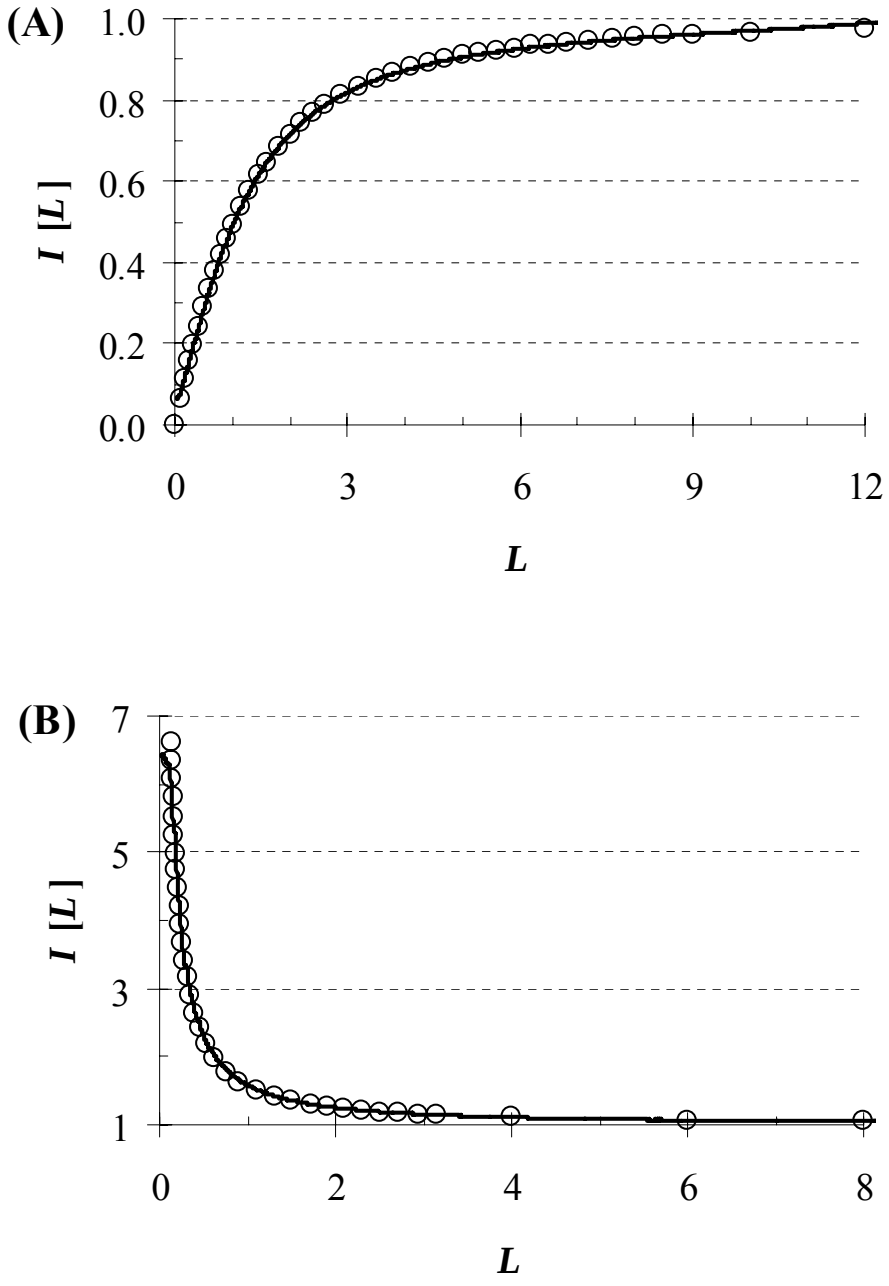

Figure 2.7 (A) Negative and (B) positive feedback SECM approach curves during the oxidation of 1.033 mM FcMeOH in aqueous 0.1 M KCl as the tip approaches over a Teflon substrate and a 2 mm platinum disk substrate, respectively. In both cases, the tip was a 11.2 μm Pt UME and its approach rate was 0.1 μm s^{-1}. The tip was held at +0.4 V *vs.* Ag/AgCl to drive the oxidation of FcMeOH at the diffusion controlled rate. Experimental curves are shown by the solid lines (—) while the theoretical curves generated for 11.4 and 11.0 μm electrodes, both with R_G of 1.1, are indicated by the open circles (○) respectively in (A) and (B).

2.3.2 Platinum Microelectrodes from Wollaston Wire

The intrinsic difficulty in handling platinum wires having diameter less than 25 μm and the need of smaller microelectrodes in the work carried in the next two chapters drove the use of Wollaston wires. However, no working electrode was successfully prepared according to the procedure explained in Section 2.2.4. In fact, the silver-coated section of the Wollaston wire had to be far from the area of the flaming else it could spoil the sealing and/or break because of the heat produced by the flame. This problem was solved by exposing a longer piece of Pt wire. However, even if a perfect seal was obtained and the electrical contact detected, when the electrode was sonicated the junction between the bare and the silver-coated section of the Wollaston wire broke. A heat coil in order to seal that junction and so strengthen the whole structure might solve the latter problem.[13]

2.3.3 Nano- and Micro-Electrodes Prepared with Laser Puller

2.3.3.1 Platinum Nanoelectrode Fabrication

The use of the laser puller in the fabrication of platinum nanoelectrodes has been proved successful as shown in few examples in the literature.[7-10] The preparation of platinum probes advanced the approach developed by Mauzeroll and LeSuer.[13] Indeed, adopting the method followed in Schuhmann's group[8] resulted in significant difficulties in obtaining symmetrical shafts and the results were irreproducible. These problems might arise from the fact that the pulling step was run immediately after the sealing step and the temperature of the capillary-wire assembly did not have time to equilibrate. However, even where reported previously, the instrument parameters have to be optimised. Firstly, each laser puller has its own optical alignment, *i.e.*, tilting number.[20] Secondly, the vacuum is of pivotal importance and strongly depends on the connection of the capillary ends with the pump; then adjustments of the pulling parameters, especially of the HEAT value, are necessary to produce functioning nanodes.

The target of the sealing phase was to collapse the glass around the wire in a reasonable number of cycles. Heating the glass too much during this step should be avoided or the cylindrical symmetry in the melted portion of the capillary could be lost (which

compromised the pulling step) or even melting of the platinum could be observed. Only HEAT and FILAMENT were meaningful parameters to change because the custom-built stoppers avoided the hard pulling. The first choice one has to set in the sealing program is the FILAMENT. Indeed, FILAMENT 5, which is the largest possible pre-set filament, was chosen in all the sealing programs of this work and it guaranteed an area approximately 8 mm long was swept by the laser beam. The second parameter to choose is the HEAT value, which can be set, as suggested by Ufheil and co-workers,[10] using the RAMP test of the instrument. This test allows the user to systematically establish the minimum HEAT value required to melt the glass with any given combination of FILAMENT and glass. Experimentally, it was found that ~ 20 - 30 units had to be added to the RAMP test value when the platinum wire was inside of the capillary as the wire possibly removed part of the heat transferred to the glass. Thus, a sealing program was set and run for 40 seconds, at the end of which, the wire-capillary assembly was removed from the bars and the result checked with a microscope. The amount of glass collapsed during the sealing step clearly depended on the HEAT value. However, rather than increasing the HEAT parameter above the ~ 30 units added to the RAMP test value, it was decided to repeat the cycle until a good sealing was observed. In principle, increasing the HEAT value to have the glass collapse on the platinum wire in one run of the program, should have the same effect as repeating a program with a smaller HEAT value several times, though this option was not explored. Following these guidelines, Programs 2.2 and 2.3 were set up and it is important to note that a good seal, like the one in Figure 2.8A, was always achieved in the cycle before the last one. The value of HEAT selected had an uncertainty of ± 5 units. Values greater than 15 units of those reported in the Programs 2.2 and 2.3 produced at the end of the sealing cycles a double neck profile while values smaller than 15 units had an incomplete sealing, like the one in Figure 2.8B.

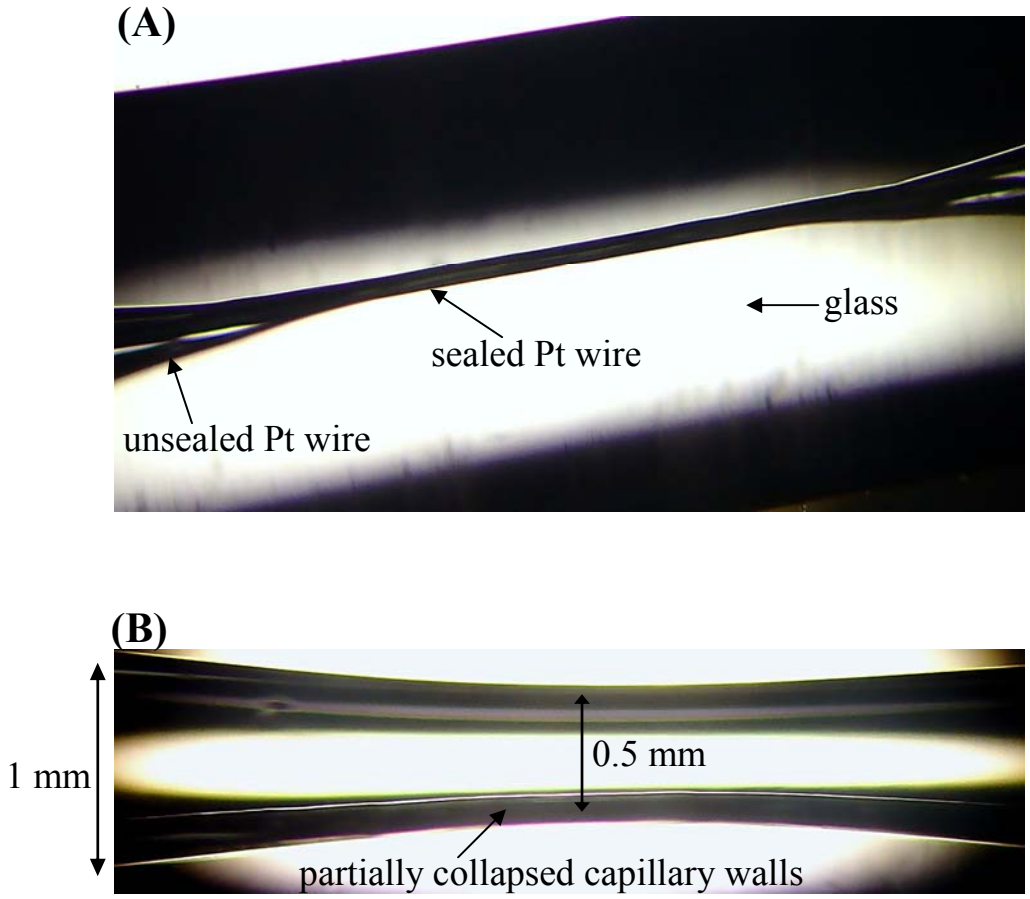

Figure 2.8 (A) The portion of the glass capillary swept by the laser beam was melted and collapsed around the Pt wire. From the optical microscope image the formation of a good seal between metal and glass appeared. (B) The capillary walls in the region swept by the laser beam were partially collapsed, however the number of cycles was not enough and/or the HEAT value was too low to accomplish the sealing of the wire. The platinum wire is covered under the shade in this case.

Regarding the pulling step, the parameters were set in order that the hard pull occurred between 4 and 6 seconds which, according to the puller manufacturer, assures the best results. Indeed, it was noticed that longer times produced electrodes with uneven taper lengths while for shorter times the platinum wire was not drawn with the glass when the hard pull was executed.[21] FILAMENT 0, 1 or 2 was chosen in this step because a shorter portion of the sealed glass had to be subjected to the hard pull. In principle, working with other FILAMENT values should not compromise the success of the pulling, but here, all the following considerations were adjusted for these values. The effect of HEAT, VELOCITY and PULL on the geometrical properties of the resulting UMEs has already been reported.[13] However, FILAMENT values in this work

appeared to have also a great influence *i.e.*, smaller FILAMENT values produced microelectrodes with shorter taper and/or smaller tip. Nevertheless, it was possible to control the size of the Pt wire at some extent during the polishing step which it was found a more practical solution. The length of the taper was on average between 0.6 and 1.1 cm depending on the parameters in the pulling program. In seeking an efficient pulling program, it was found that it was better to obtain two symmetrical shafts and to avoid the presence of a gap in any portion of the wire.

Program 2.4 contains a range of HEAT, VELOCITY, DELAY, FILAMENT and PULL values. Indeed, the reproducibility of the pulling upon repetition of the same program results was limited and after some runs, cracks in the platinum wire occurred near the end of the taper. While they could be random, they could also depend on a subtle change in the performance of the instrument. In the latter case, *i.e.*, when experienced consecutively for more than three times, the HEAT, VELOCITY and especially the DELAY parameters had to be re-optimised. Mauzeroll and LeSuer[13] gave some suggestions on the adjustment of these parameters depending on the position of the crack in the filament. The values of these three parameters were always re-adjusted within the uncertainty reported in Program 2.4. Following this principle, the percentage of successful tips was ~ 50 - 60 % as determined by optical microscopy which did not decrease substantially after electrical contact at the back of the microwire. However, in the case of an unsuccessful pull with a crack somewhere in the fine taper region, it was possible to cut the glass just below the interruption and then polish it. With the latter approach the percentage of "successful" electrodes was raised to 80 - 90 %. Mauzeroll and LeSuer[13] mentioned that yield higher than 60 % were not generally achieved. FILAMENT and PULL values do not appear to significantly affect the efficiency of the pulling step and they were mainly used to tune the size of the tip and the length of the taper.

A stereo microscope gave a first insight into the resulting pulled capillaries *i.e.*, presence of cracks in the platinum wire and shape of the second taper offering a very rapid screening technique. Figure 2.9A shows a pulled capillary where the HEAT value was too low and the platinum wire was not drawn with the glass. On the other hand, Figure 2.9B, shows a pulled capillary with improved conditions which allowed the wire to be drawn with the glass up to half of the taper length where a crack in the wire

occurred. Finally, Figure 2.10A shows a well fabricated nanometer sized electrode where no cracks could be observed under the optical microscopy. However, nanogaps could be still present in the second taper, where the features of the metal were too small to be observed, Figure 2.10B. The presence of those nanogaps could be addressed only after the platinum wire was exposed by bevelling and electrical contact at its back achieved, testing the probes in a solution containing a redox species. Indeed, lack of electrical contact, *i.e.*, nanocracks present somewhere in the wire but not visible with the microscope, resulted in zero current voltammograms. If so, the bevelling was repeated or the taper was progressively cut with a ceramic tile until the contact in the wire was found.

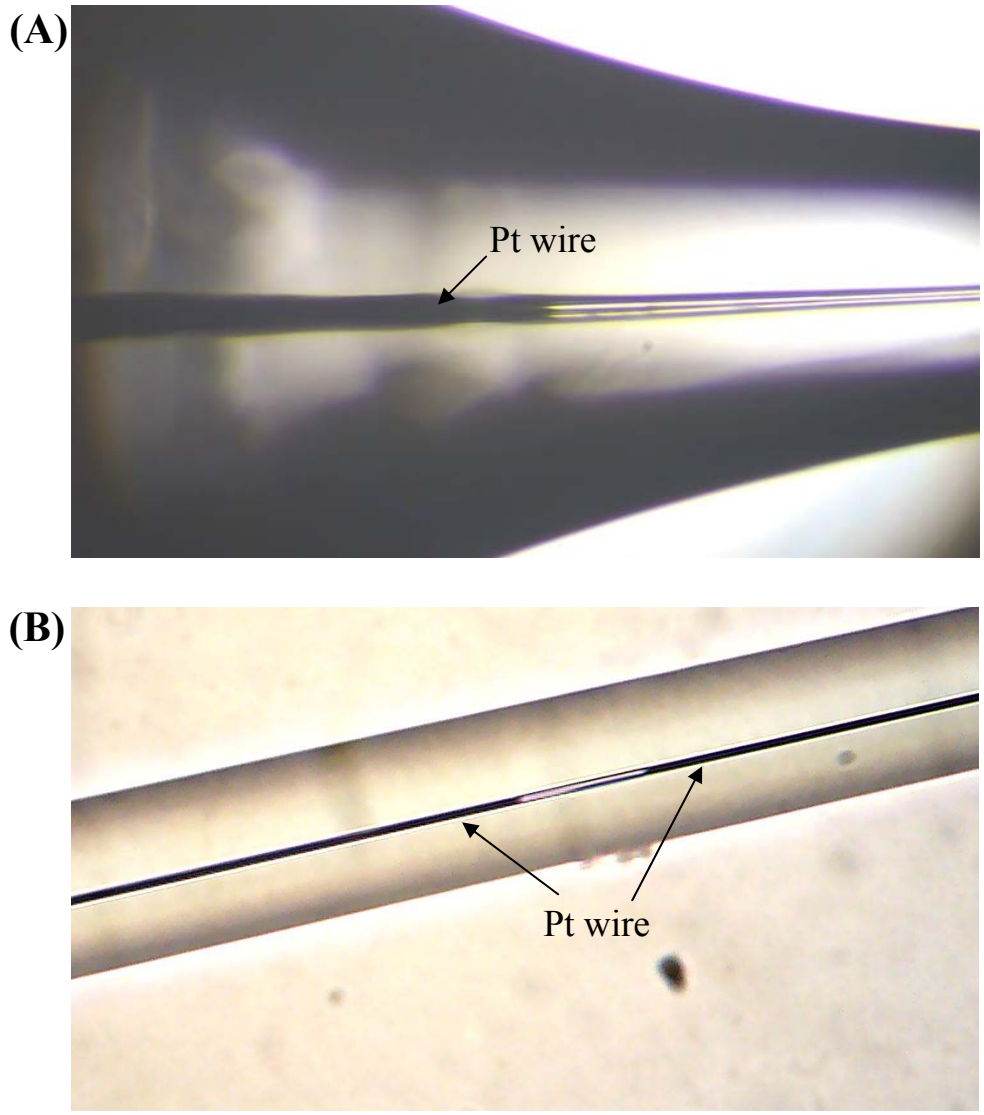

Figure 2.9 Optical microscope images of unsuccessful pulled capillaries. In (A) the wire was not drawn with the glass at the very begin of the pulled area because the HEAT value was too small *i.e.*, the temperature during the pulling was too low. In (B) the HEAT value was higher and the platinum was drawn with the glass till a crack in the wire appeared in the taper region. The latter was due to the fact that the cooling of the wire in the taper was too fast and the DELAY value had to be lowered to sort the problem.[13]

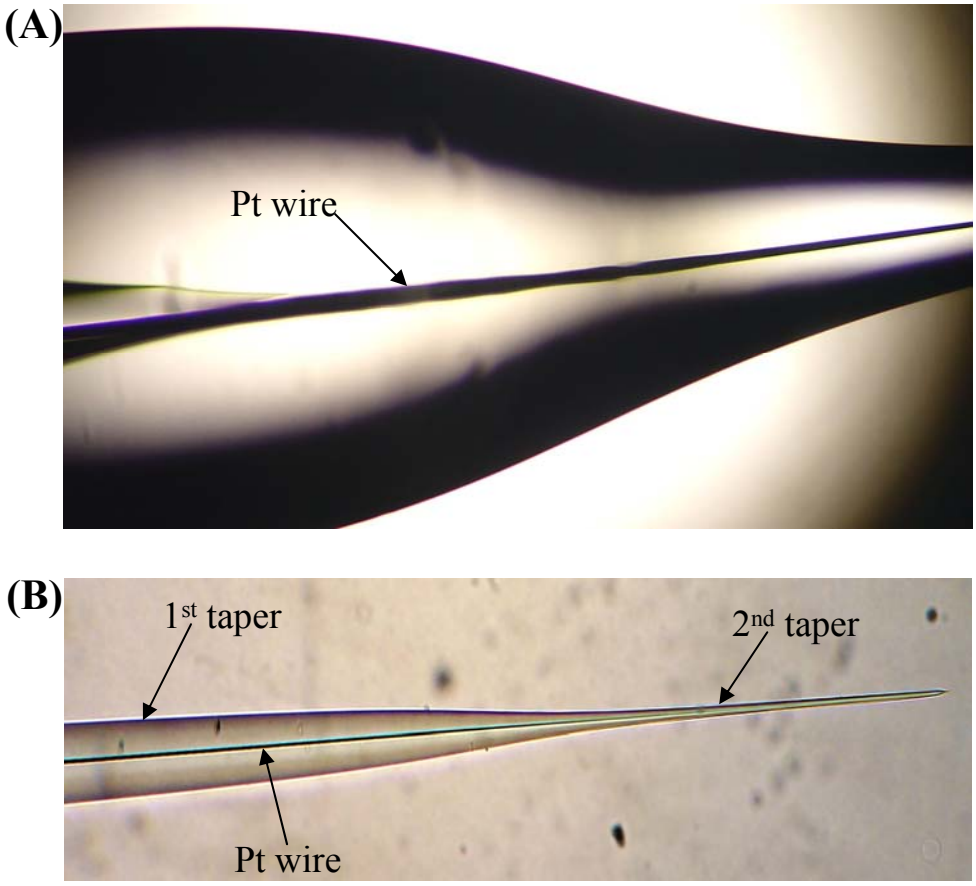

Figure 2.10 Optical microscope images of the different areas of a capillary/wire assembly successfully pulled. (A) The wire at very begin of the pulled area has been drawn with the glass. (B) No crack in the wire was apparent at least at the microscope resolution. The parameters, HEAT, VELOCITY and DELAY were appropriately set and allowed the preparation of this nanometer sized electrode with apparent no crack in the wire.

Both hard temper and annealed Pt wire were used but, the attempt with the former was not pursued extensively as the percentage of the successful tips was lower despite the fact that it has been suggested that adjustments of the laser puller parameters should solve this issue.[13] 0.3 mm, 0.5 mm and 0.7 mm i.d. quartz capillaries were used but the latter size was discarded immediately because of the abrupt loss of symmetry during the sealing phase, which compromised the result of the pulling. No significant difference for the resulting pulled electrodes in terms of tip shape, taper length and continuity of the platinum wire was apparent when Program 2.4 was run both using 0.3 and 0.5 mm inner diameter capillaries. Nevertheless, the 0.3 mm i.d. capillaries, as predicted, offered a better offset of the wire *i.e.*, shorter distance of the wire from the capillary

axis. Because of that, the pulling of the 0.5 mm i.d. capillaries was not extensively pursued, although they might find some application in the preparation of feedback independent probes for shear force-based constant-distance SECM as in this type of tips the metal disk has to be slightly off-centre.[22]

2.3.3.2 Gold Ultramicroelectrode Fabrication

The same considerations for the sealing and pulling steps discussed in the previous section for the platinum UMEs fabrication with the help of a laser puller also held for gold. Gold wire is available in two tempers: annealed and hard. The smallest annealed temper is 0.1 mm and it was immediately realized that the manufacture of nano-sized electrodes with this wire was impossible. 25 μm hard temper gold wire was the only size employed throughout this section. Several glass types were employed in the search of efficient sealing and pulling programs. Initial results obtained with borosilicate capillary (inner diameter: 0.5 mm) and soda glass were not entirely satisfactory. Indeed, Figure 2.11 shows that the uniformity of the drawn wire was generally compromised. It is possible that, as the position of the sealed wire was offset compared to the capillary axis, unbalanced forces during the pulling step might be responsible for this behaviour. Thus, the chances of a breakage of the wire at the very beginning of the first taper were enhanced compared to what observed with platinum in the previous section and imperfect seal often occurred. Moreover, the mechanical properties, *i.e.* flexibility, of the borosilicate glass and soda are poorer than quartz. Indeed, the glass taper formed during the pull step had a length of 7 - 9 mm but Figure 2.12 shows that it was often bent and in addition it could be easily snapped during the polishing step because of its lack of flexibility. The difficulty in handling the taper structure during the polishing step and its bending, suggested that the best solution was to cut the taper up to its beginning using a ceramic tile. At this point, in order to sharpen the tip, a lot of glass should be removed, but the beveller was not suitable for this purpose as too much pressure on the grinding disk blocked its rotation. The polishing and sharpening steps were often carried manually. A more robust bevelling system is required if instrumental bevelling of these probes is to be successful.

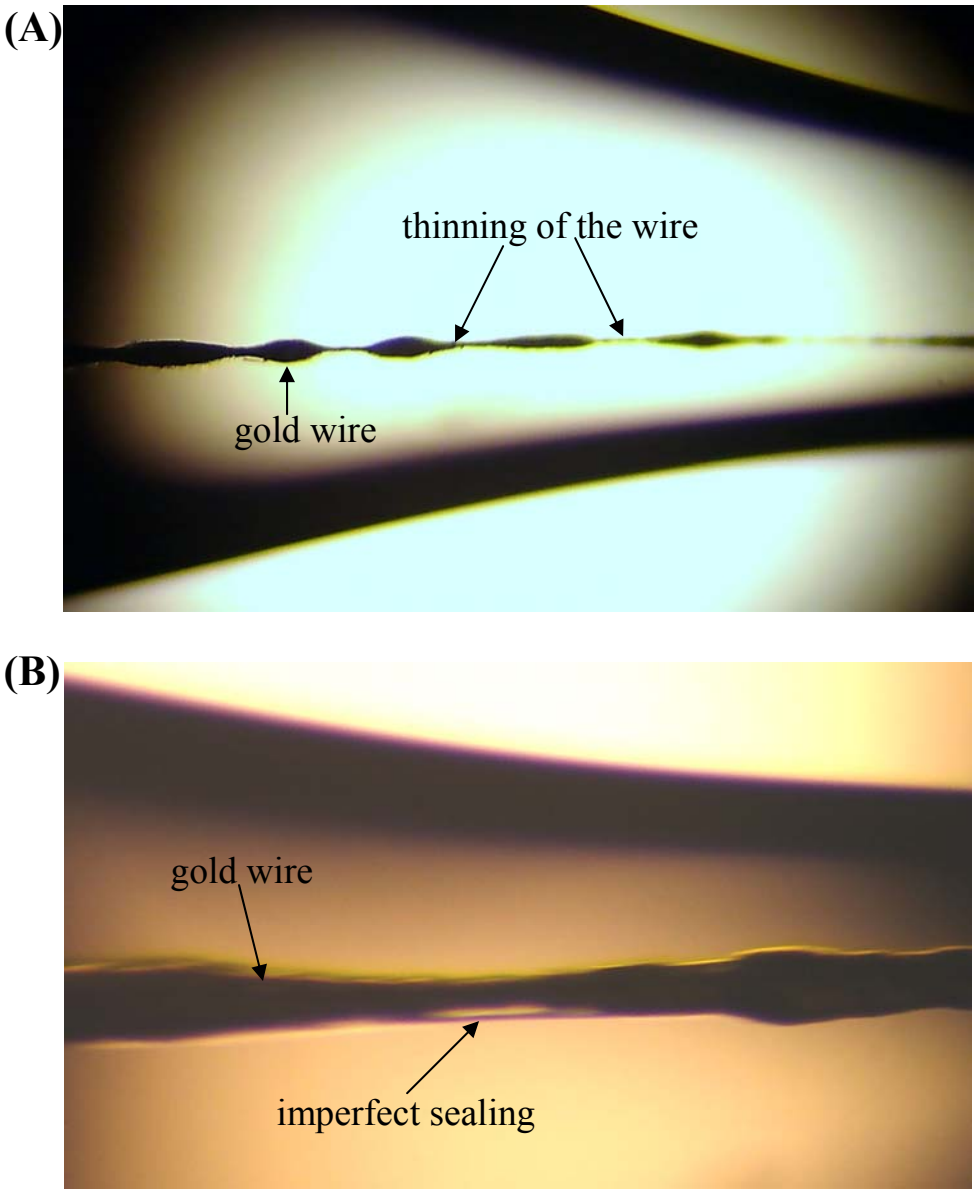

Figure 2.11 Optical microscope images showing the initial area of the pulled electrodes prepared using 25 μm gold wire and 0.5 mm borosilicate capillaries as described in Section 2.2.5.2. Two major faults in the fabrication procedure affected the resulting pulled electrodes. (A) Unbalanced forces on the wire or temperature factors during the pulling step possibly caused the gold wire to thin eventually leading to its breakage. (B) The seal of the wire after the pulling step appeared imperfect.

Figure 2.12 A gold microelectrode fabricated with a laser puller using a 0.5 mm i.d. borosilicate capillary and 25 µm gold wire as described in Section 2.2.5.2. As apparent from the SEM picture, the taper was bent. The scale, magnification and accelerating voltage are shown on the image.

These results were in part improved using borosilicate capillaries with smaller inner diameter (0.3 mm) and selecting a lower FILAMENT value during the pulling step. Figure 2.13 shows that better stretching and an improved seal of the wire within the glass were on average observed. However, the taper of the electrode, because of its fragility, had still to be cut to avoid its breakage during the polishing step.

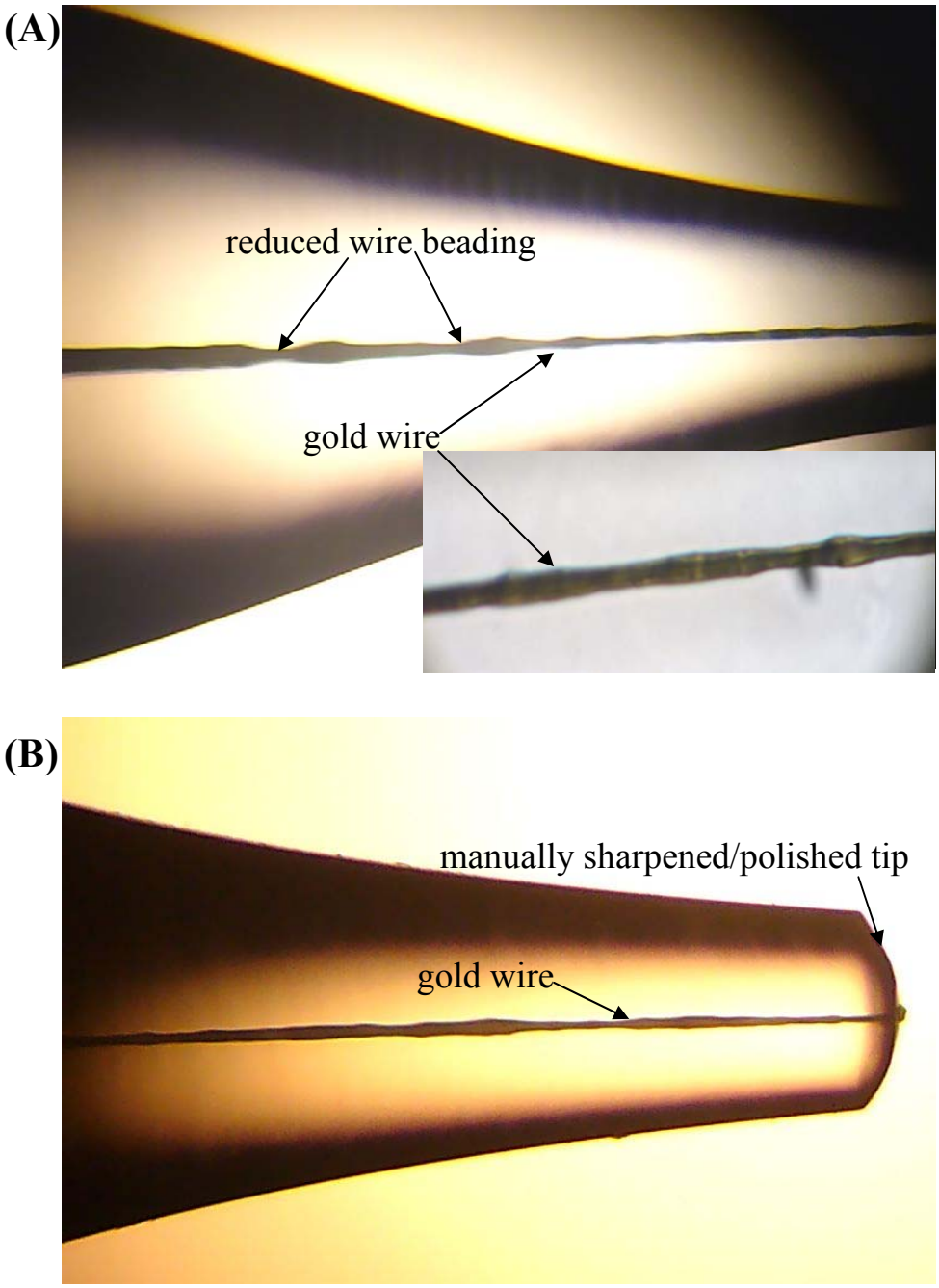

Figure 2.13 Optical microscope pictures showing the pulled electrodes fabricated using 25 µm gold wire and 0.3 mm borosilicate capillaries as explained in Section 2.2.5.2. The smaller offset of the sealed wire improved the drawing of the wire during the pulling step. (A) The wire resulted well sealed within the glass and its beading was significantly reduced which decreased the chance of breakage during the pulling step. The inset in (A) shows an enlargement of the metal seal within the glass. (B) Image of a successfully pulled electrode after cutting the long taper and manually sharpening and polishing steps.

Aluminosilicate glass has better flexibility than borosilicate or soda glass and allowed preparation of gold electrodes with long tapers which could be polished. Figure 2.14 shows how the aluminosilicate looked after the pulling step (2^{nd} taper was not present because of the pulling parameters selected) and after its polishing. Indeed, keeping the taper structure intact is of pivotal importance in order to achieve smaller size *i.e.*, submicrometer electrodes. From the optical microscopy, the gold wire seemed to have a lower number of interruptions and more uniform drawing when electrodes were successfully pulled using aluminosilicate instead than borosilicate. It is possible that, the higher temperature to melt the aluminosilicate (higher HEAT value has to be set) might be responsible for this behaviour. However, the results were not as good as the ones reported with the platinum in the previous section in terms of size and yield achieved. These limitations might depend on the different physical properties of gold and/or glass type but the large inner diameter of the aluminosilicate capillaries employed might be responsible as well. Indeed, Figure 2.15 shows that the cylindrical symmetry at the very beginning of the 1^{st} taper was lost after the sealing due to the thin capillary walls. Unbalanced forces arising from this asymmetry might act on the wire during the pulling step and might be responsible for the low yield.

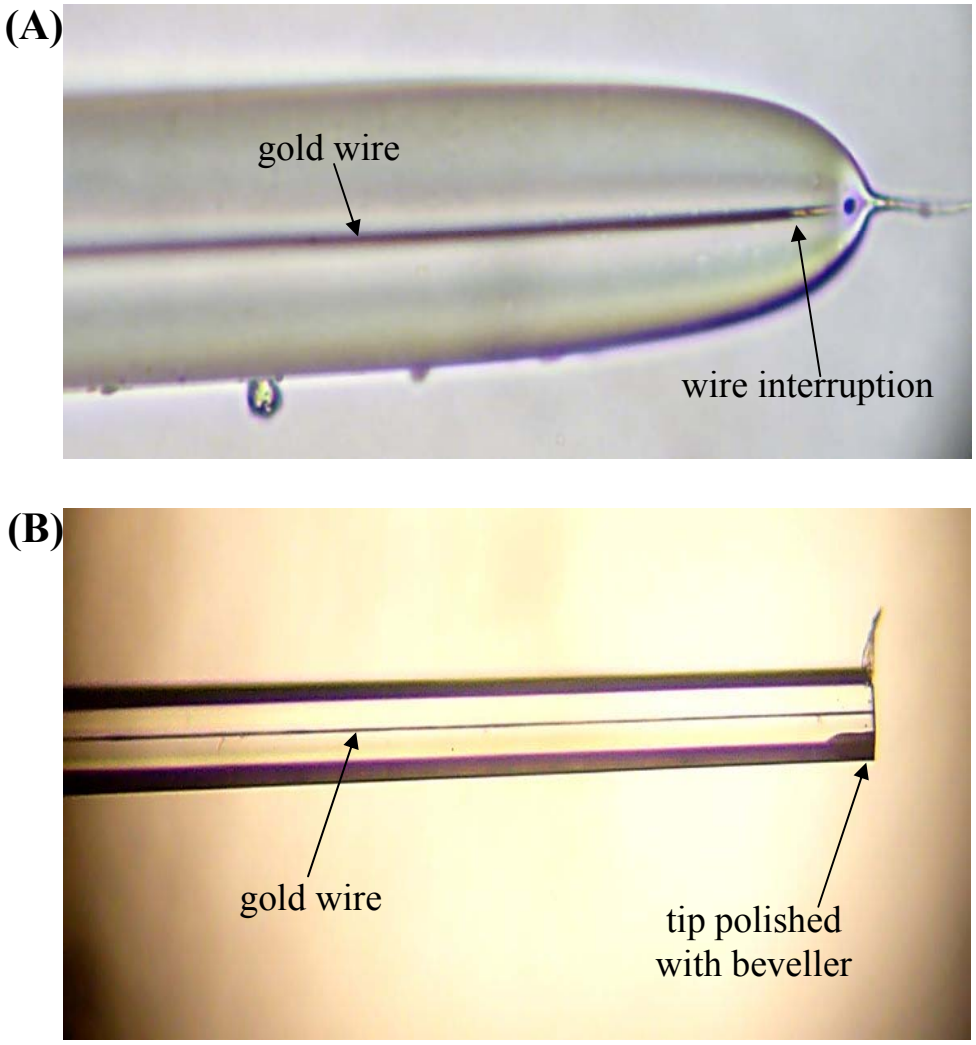

Figure 2.14 Optical microscope pictures showing probes fabricated from aluminosilicate glass capillary and 25 μm gold wire, as described in Section 2.2.5.2. The mechanical properties of the aluminosilicate glass allowed the taper structure to be maintained and the electrode could be polished using the beveller. (A) The taper tip after the pulling step. The 2nd taper was not formed because of the parameters chosen *i.e.*, DELAY value too large. (B) The taper tip after the instrumental polishing step.

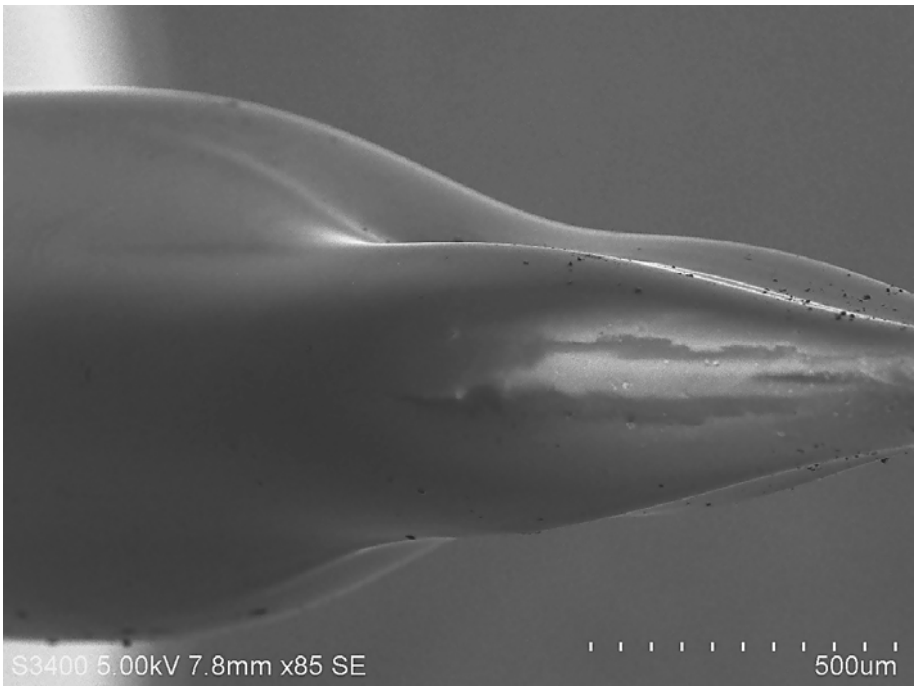

Figure 2.15 SEM image showing a probe prepared using 0.7 mm i.d. aluminosilicate glass capillary and 25 μm gold wire as described in Section 2.2.5.2. The picture shows that the cylindrical symmetry was lost during the sealing step because of the thin capillary walls compromising often the result of the pulling. The scale, magnification and accelerating voltage are shown on the image.

2.3.3.3 Polishing and Sharpening of Long Tapered Electrodes

The following discussion is valid only for the long tapered microelectrodes prepared using platinum and quartz capillaries or gold and aluminosilicate capillaries as explained in Sections 2.2.5.1 and 2.2.5.2, respectively. Figures 2.16A and 2.16B show respectively SEM pictures of the transition between the 1st and 2nd taper and of the main 1st taper body. It was noticed by optical microscopy that sharp changes in the size of the metal wire occurred in parallel with the changes in the glass *i.e.*, at the joint between the main body capillary and beginning of the 1st taper, and between the 1st and 2nd tapers. In particular, when platinum electrodes with radius < 100 nm were to be prepared, polishing of the second taper had to be done very carefully. The help of a long distance microscope and an intense light source was found advisable to address this task. Despite these precautions, the presence of nanogaps in the drawn platinum

wire in the second taper was found beyond the control of the pulling program parameters. In addition to that, a certain fragility of the 2nd taper structure determined that probes with radius < 100 nm were the 20 – 30 % of the overall pulled capillaries when conditions in the sealing and pulling programs were optimized. It is important to note that the wire dimension did change smoothly along the body of the first taper. In fact, with the conditions employed in this work, the size of the platinum wire from the beginning of the 1st taper till roughly a third of its length ranged between ~ 100 nm and ~ 1000 nm. The latter aspect simplified the preparation of submicrometer electrodes because, at some extent, it was not important in which region of the taper the platinum wire was exposed. In the case of gold, several interruptions in the drawn wire in the 1st taper did allow the preparation of probes with radius < 500 nm.

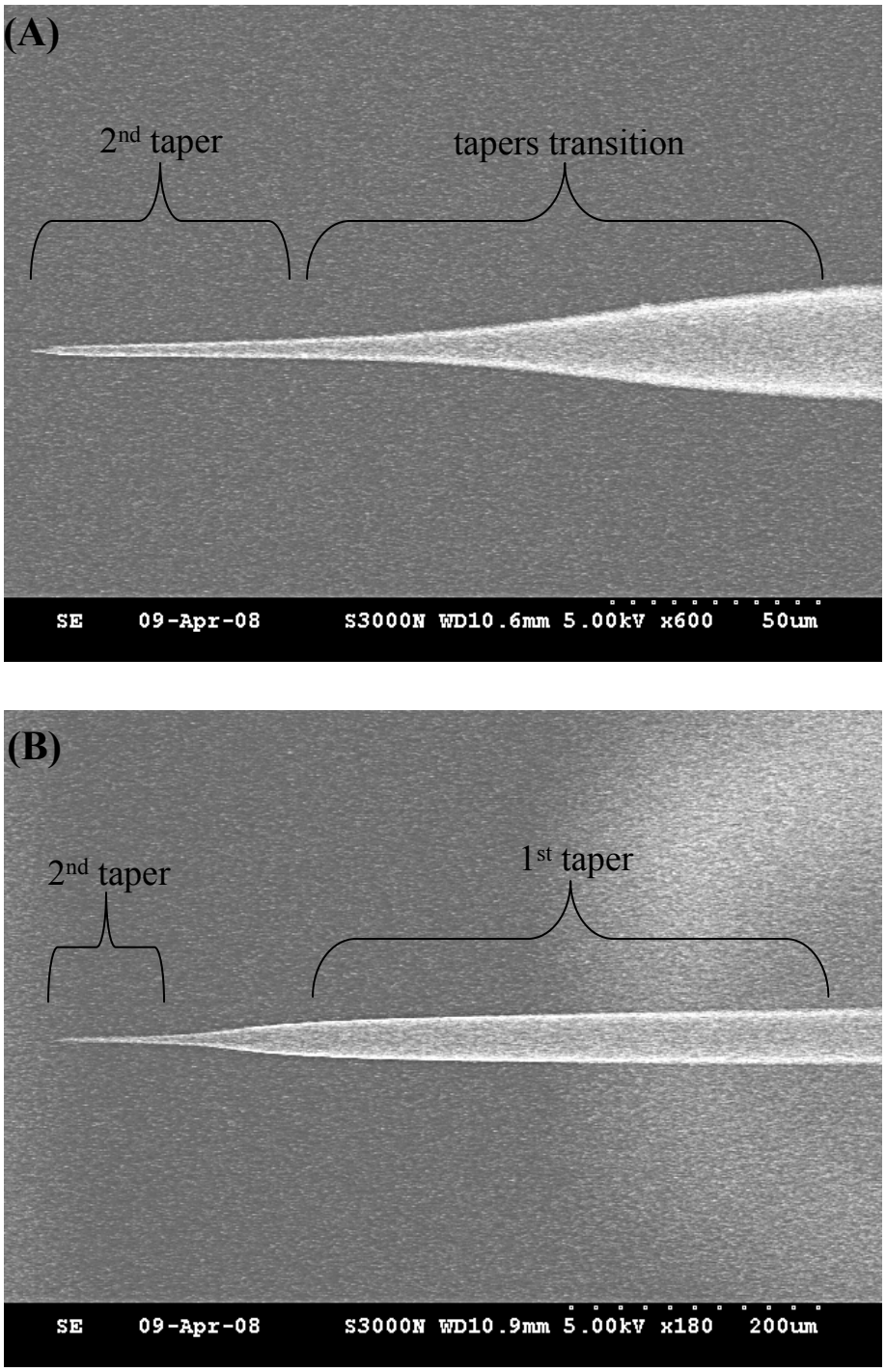

Figure 2.16 SEM picture of the taper of a platinum nanometer-sized probe fabricated as explained in Section 2.2.5.1. A) Details of the second taper and the transition between the latter and the first. B) Overall view of the two tapers. The scale, magnification and accelerating voltage are shown on the individual image.

When a capillary was successfully pulled *i.e.*, no apparent crack in the drawn wire, the quickest way to expose the metal was to insert the shaft into the chuck of the minidrill and to lower it until the tip touched the surface of the grinding disk. Then the electrode was pushed in order to have a ~ 15° bend of the taper at its end *i.e.*, to have an angle ~ 30° or smaller between the taper tip and the grinding disk as depicted in Figure 2.17. Then, the rotations of the drill and of the grinding disk were started and 2 – 3 minutes were on average needed to obtain a result similar to the shown in Figure 2.18. This figure shows that the tip had an almost conical shape except few bumps apparent on the top of the glass shield which might arise from the precession of the taper because of the misalignment with the rotating chuck axis. The rapid rotation of the drill provided an additional cutting force which shortened the time to expose the wire.

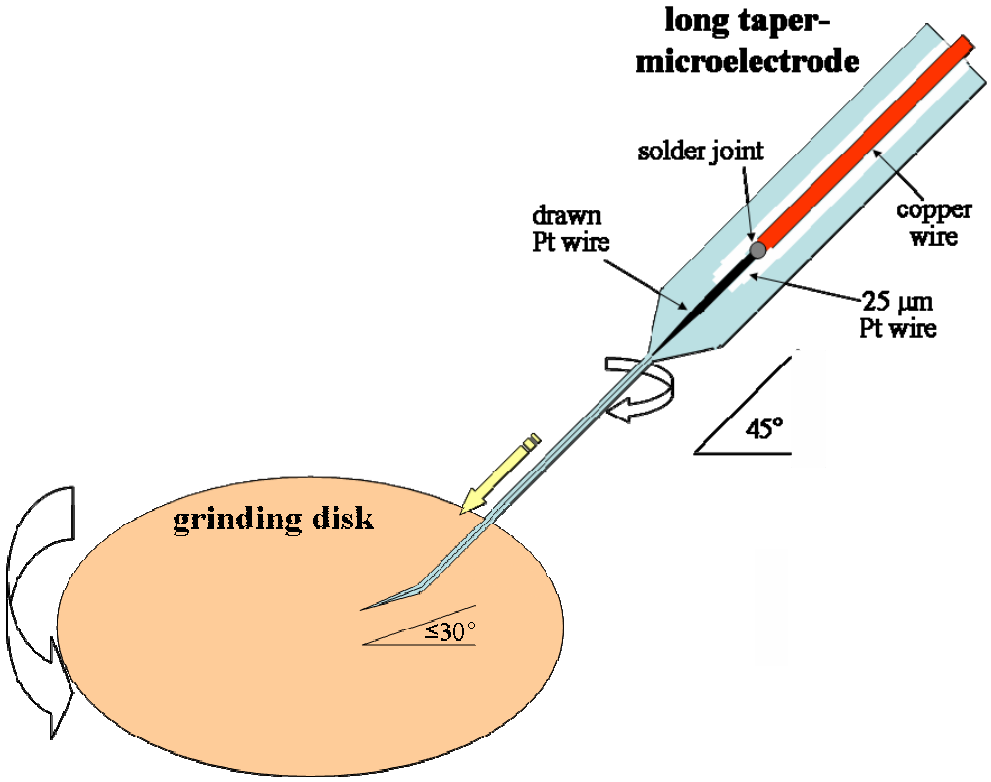

Figure 2.17 Sketch of the bevelling of a long taper microelectrode. The electrode was inserted in the chuck of the drill which was held at ~ 45° from the plane of the grinding disk. The taper was lowered towards the grinding disk by a fine screw mechanism and then pushed against it till an angle of ~ 30° between the bent tip and the surface was achieved. Then the rotations of beveller and minidrill were started.

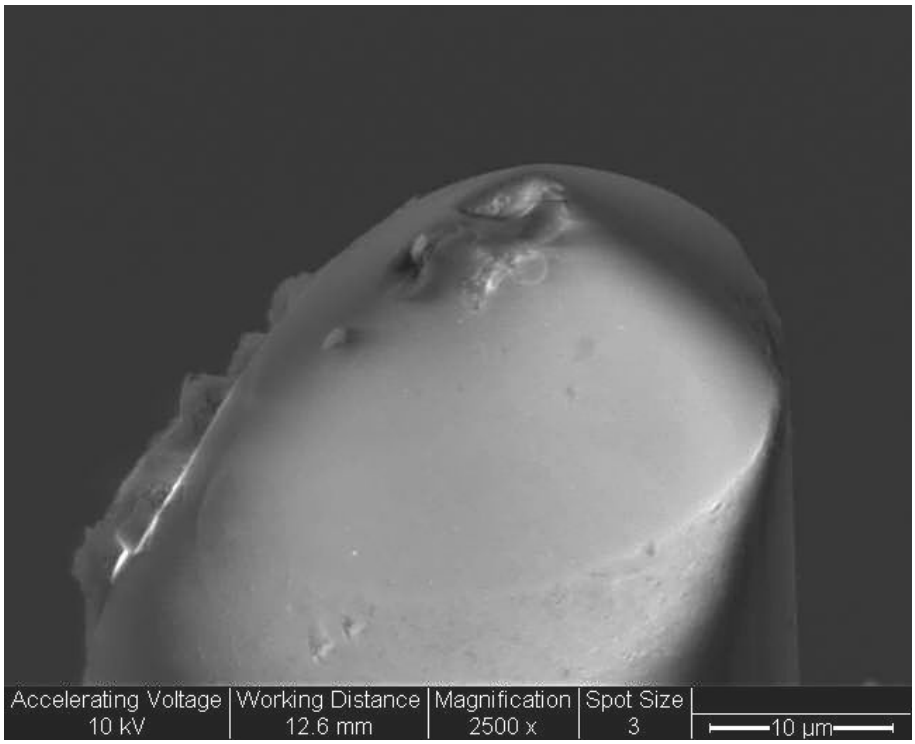

Figure 2.18 SEM image of a sharpened long-tapered platinum microelectrode fabricated as described in Section 2.2.5.1. The electrode was inserted in the chuck of a minidrill which was held at an angle of ~ 45° from the plane of the grinding disk and sharpened. The SEM picture shows that an almost conical shape was obtained but a few imperfections are apparent on the top part of the glass shield and underneath one of them the platinum wire was possibly buried. The scale, magnification and accelerating voltage are shown on the image.

After this first step, the electrode was removed from the chuck of the drill and inserted in the beveller holder so that the taper was perpendicular to the grinding disk. The electrode was lowered down towards the grinding disk, which was rotating, till the tip gently touched the surface as appeared from a slight movement of the taper using the long distance microscope. One or two minutes were on average sufficient to expose the wire. A frustum cone geometry or flat disk geometry were achieved depending on the time of the polishing step, see next section for examples. These two steps (bevelling and polishing) were repeated till an electrical contact was found. However, this procedure could be time consuming especially when a crack in the wire was far from the very end of the tip. Thus, cutting the taper below the gap could be a quicker option in order to expose the wire and yet have a submicrometer electrode because the size of the platinum wire did not change significantly in the body of the 1st taper as previously

observed. Scissors or snapping the taper on the bench were found inappropriate because the total lack of control and because they left deep cracks and stress lines in the glass, as shown in Figure 2.19, which often compromised the final result. A ceramic tile was found to be a better tool when the taper had to be partially cut. After the metal was exposed and the electrical contact found, the electrode was polished as described above.

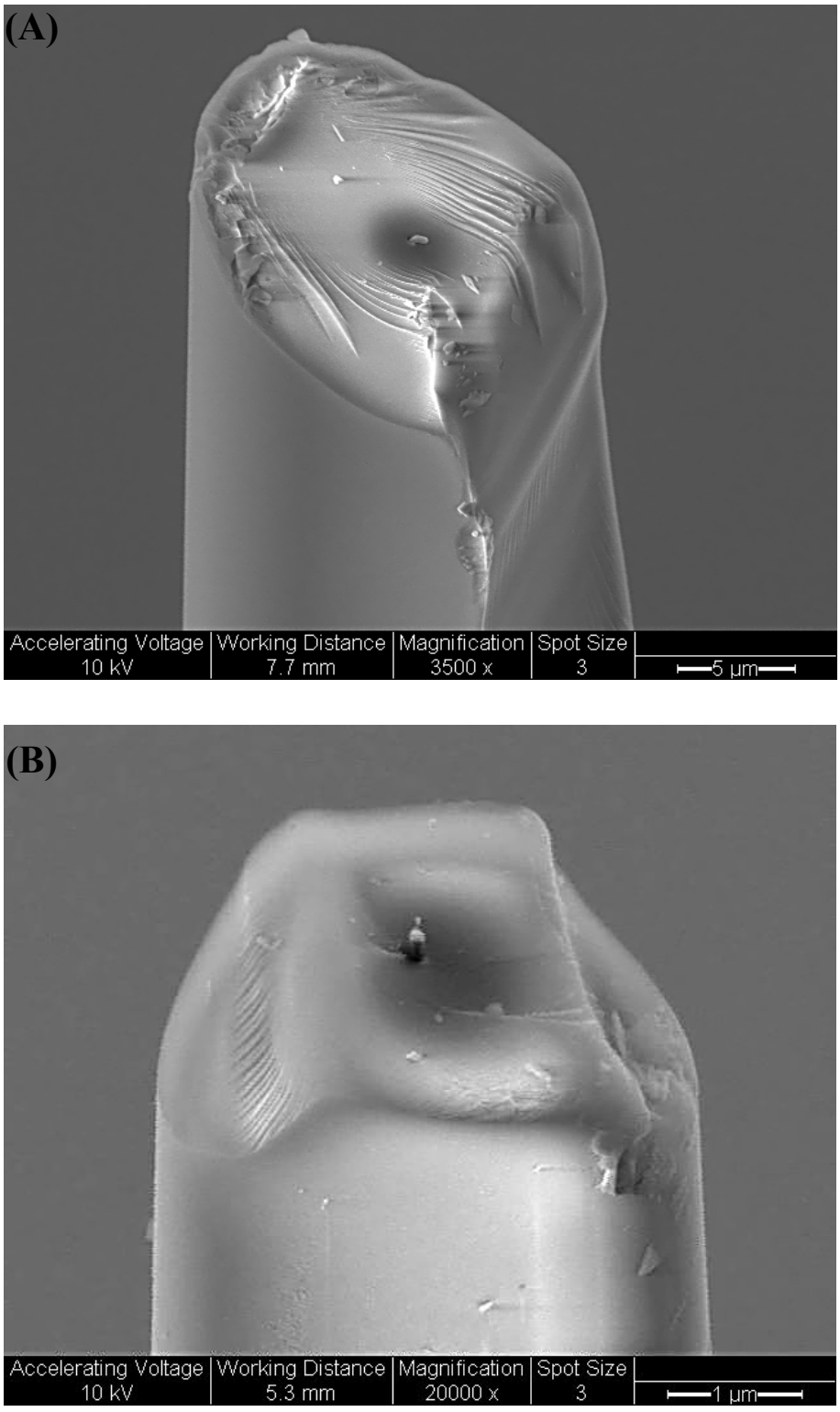

Figure 2.19 SEM images of long tapered Pt microelectrodes fabricated as described in Section 2.2.5.1. The taper was (A) cut with scissors and (B) snapped against the bench. The scale, magnification and accelerating voltage are shown on the individual image.

2.3.3.4 Characterization by Scanning Electron Microscopy

SEM measurements were complicated by the charging of the non conductive surfaces which did not allow details of electrodes with radius < 2 μm to be captured. These difficulties were in part overcome using a Field Emission Source SEM or by coating the sample with a ~ 4 - 10 nm thin layer of gold which reduced the charging effects of the glass. Figures 2.20 and 2.21 show the typical frustum of cone geometry of the platinum long tapered nanoelectrodes achieved after the sharpening and polishing procedures described in the previous section. The frustum of cone could be completely bevelled off when longer times were used during the polishing step (data not shown). In both figures, an offset of the metal disk in respect of the glass shield was apparent. The quality of the seal of the wire within the glass appeared to be good from these images but it had to be corroborated by other instrumental data. In Figure 2.20B a small recess is apparent but it could not be instrumentally quantified. Nevertheless, the images show that the quartz glass and platinum wire were pulled to very small dimensions by the micropipette puller and agreed with an inlaid disk geometry.

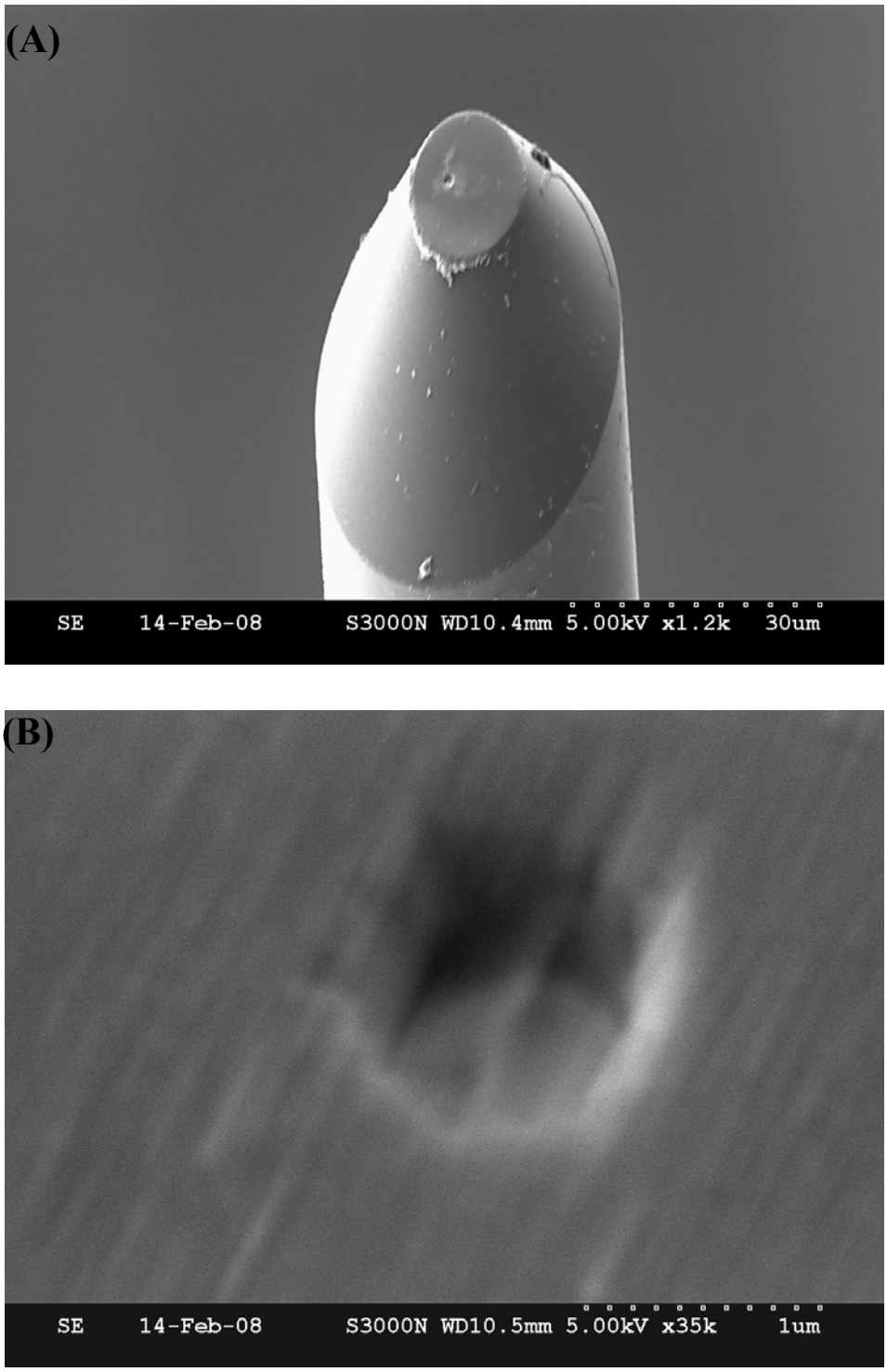

Figure 2.20 SEM images of nanometer-sized platinum electrodes fabricated, sharpened and polished as explained in Sections 2.2.5.1 and 2.3.3.3, respectively. The images show (A) the distinctive frustum of cone shape of the probe achieved and (B) a detail of the platinum disk which was slightly recessed within the glass. The SEM suggested the radius of the metal disk was ~ 490 nm. The scale, magnification and accelerating voltage are shown on the individual image.

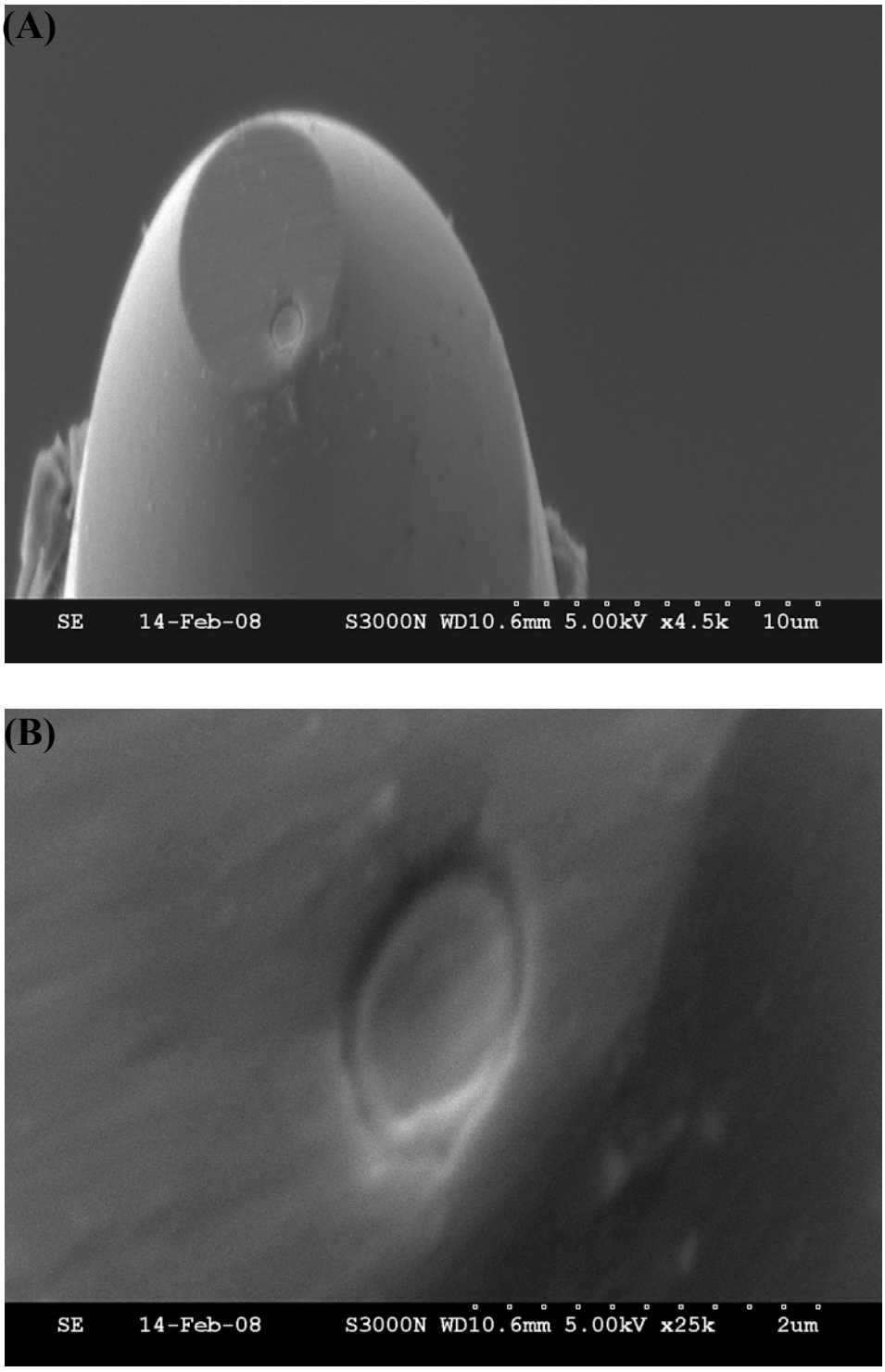

Figure 2.21 SEM images of nanometer-sized platinum electrodes fabricated, sharpened and polished as explained in Sections 2.2.5.1 and 2.3.3.3 respectively. The images show (A) the distinctive frustum of cone shape of the probe achieved and (B) a detail of the platinum wire which appeared to be well sealed within the glass. The image agrees with an approximately inlaid disk geometry with a radius of ~ 440 nm. The scale, magnification and accelerating voltage are shown on the individual image.

Figure 2.22A shows a typical SEM picture of a gold probe fabricated using 25 μm gold wire and 0.3 mm borosilicate capillaries as explained in Section 2.2.5.2. In this case, the image was acquired with a SEM instrument provided with a tungsten filament because the sample size was enough large and the resulting picture was in focus. However, the effect of the charging in the glass appeared as a darker ring surrounding the gold disk. The evaluation of the electrode size using a tungsten filament SEM with the secondary electrons detector was found very poor as the image could be severely stretched and these data should be taken only qualitatively. Low vacuum mode and backscattered electron detection helped dissipate the charge on the insulator and increased the contrast between the wire and the glass, slightly improving the evaluation of electrode size. When the gold microelectrode in Figure 2.22A is compared to Figure 2.22B, which shows a platinum electrode with similar size, it is apparent that the roughness between the two metals was different. Indeed, gold microelectrodes fabricated from borosilicate were often characterized by a rougher metal surface, which might not depend solely on the polishing procedure but it could be also associated with the intrinsic melting/cooling processes outgoing during the pulling step. In fact, when gold microelectrodes were fabricated from aluminosilicate, the surface roughness, which appeared from the SEM images, resulted reduced though not as much as in the platinum case (results not shown).

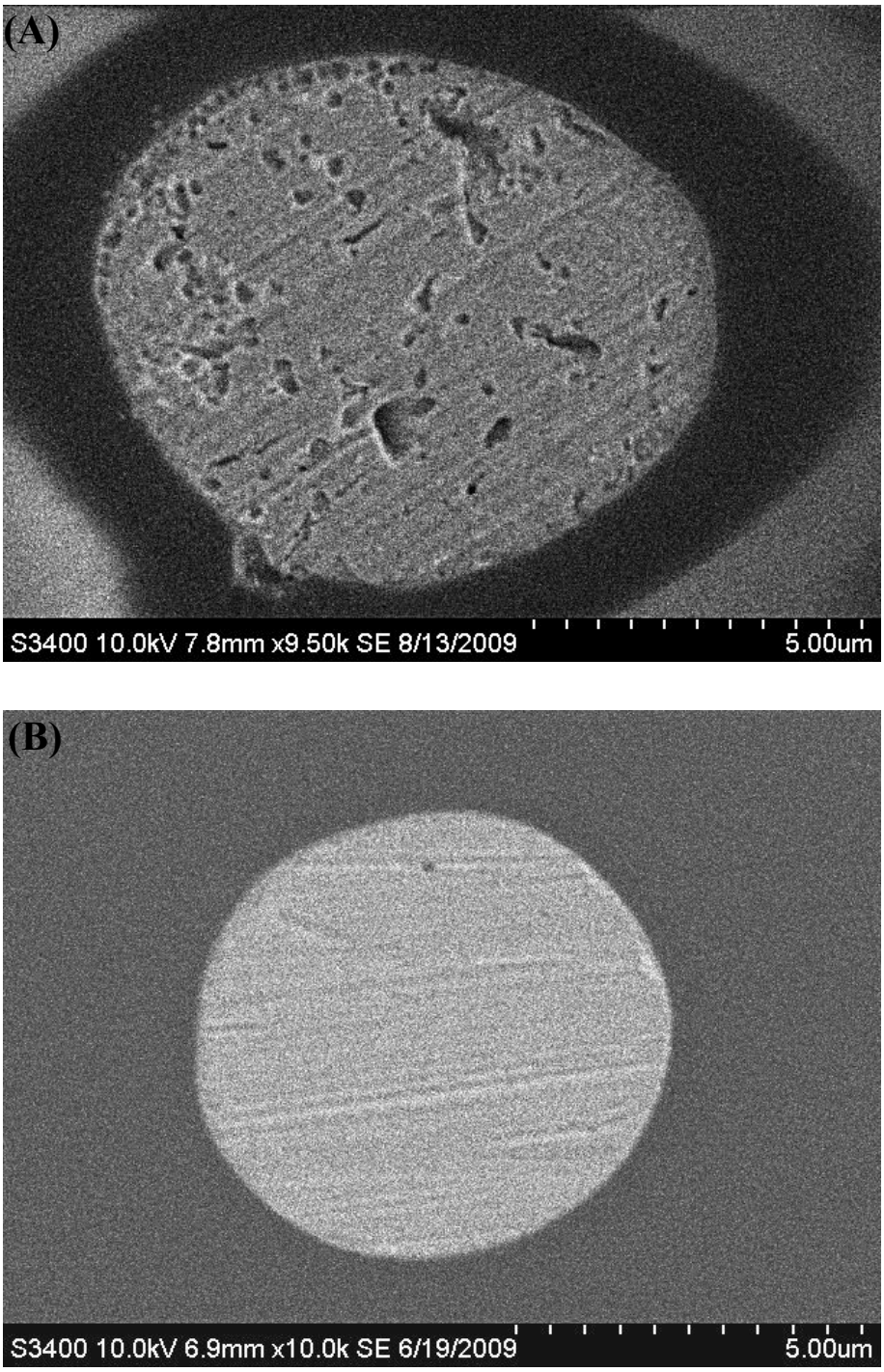

Figure 2.22 SEM pictures of a (A) gold and (B) platinum microelectrode. The electrodes were fabricated as described in the Section 2.2.5.2 and 2.2.5.1 respectively using 25 μm gold wire with 0.3 mm borosilicate capillaries and 25 μm platinum wire with quartz capillaries. The taper of the electrodes was in both cases cut off with a ceramic tile and they were hand polished with 0.3 μm alumina polishing sheet and sonicated for 2 minutes prior to their use. The scale, magnification and accelerating voltage are shown on the individual image.

2.3.3.5 Characterization by Cyclic Voltammetry

The measurement of the steady state current in a voltammogram at slow scan rate allows the radius of the electrode to be evaluated from Equation 1.14. The diffusion coefficient for FcMeOH and $[Ru(NH_3)_6]^{3+}$ are reported elsewhere as 6.7×10^{-6} cm^2s^{-1} and 5.48×10^{-6} cm^2s^{-1} and they were used in the CV and SECM analysis.[8,23] In this work, the steady state was measured at scan rate $\leq$ 5 mVs^{-1}, which assured that the linear diffusion component could be neglected according to the criteria elaborated by Fang and Leddy and explained in Section 1.3.3.[24] The steady-state current, *i.e.*, flat branches, and the retracing of the reverse scan on the forward scan are signs of a good seal of the exposed portion of the wire.[7,13,25] However, it is important to not limit the CV analysis to the slow scan rates, but to extend it at higher scan rates in order to test for resistive and capacitive effects. In this work, the capacitive contribution was calculated from the CV by monitoring the separation of the oxidative and reductive branches in a non faradic region (Δi) in function of the scan rate (v). From Equation 1.18, this gap should be equal to $2vC_d$[26] and the capacitance was then calculated from the slope of the plot.

Figure 2.23 compares two voltammograms at different platinum nanometer sized electrodes. Indeed, the taper of the electrode in Figure 2.23A was cut with scissors to expose the wire, and the electrode was then sharpened and polished as explained in Section 2.3.3.3. On the other hand, the taper of the electrode in Figure 2.23 was left intact and the wire was exposed by careful bevelling as explained in the same section. From the steady state current, a radius of 79 nm could be determined in Figure 2.23A while one of 52 nm in Figure 2.23B. In Figure 2.23A a resistance appeared as a slope superimposed to the steady state current. This behaviour could not arise from a contribution of the linear diffusion, at least for probes having radius smaller than ~ 0.5 - 0.6 μm and at these scan rates, as verified using the criteria elaborated by Fang and Leddy.[24] Indeed, considering the largest scan rate in Figure 2.23A, *i.e.*, 0.5 Vs^{-1}, the scan rate parameter, δ (= RTD/nFv) , is ~ 5.9 μm. It follows that δ/a is ~ 10, which confirms that the linear diffusion contribution was practically negligible at this scan rate. From the plot of Δi in function of the scan rate, as explained above, the capacitance values in the two cases were determined: ~ 82 pF and 10.8 pF (or 418 $mFcm^{-2}$ and 129 $mFcm^{-2}$ normalizing for the geometrical area) for the electrodes

respectively in Figures 2.23A and 2.23B. So the 79 nm platinum electrode in Figure 2.23A was affected by higher capacitance values and resistance effects than the 52 nm shown in Figure 2.23B. This behaviour might be a sign of a non ideal geometry[13] and it was often noticed when the taper of the electrode was cut with the scissors or snapped on the bench to expose the platinum wire.

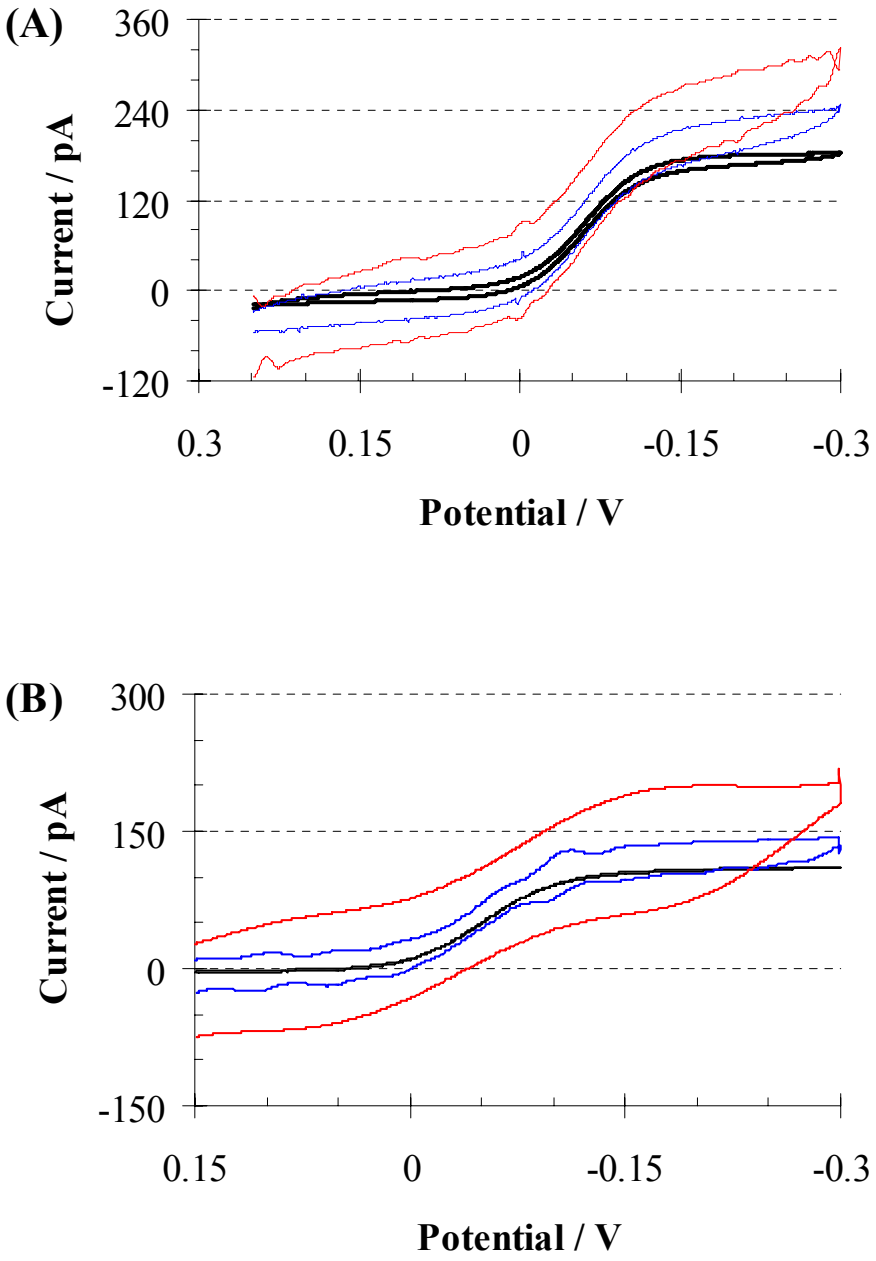

Figure 2.23 Cyclic voltammetry at platinum nanometer-sized electrodes fabricated as described in Section 2.2.5.1. (A) The taper of the electrode was cut with scissors and then sharpened and polished as described in Section 2.3.3.3. The scan rates were (—) 5, (—) 100 and (—) 500 mVs^{-1}. (B) The taper of the electrode was left intact and bevelled as described in the same section. The scan rates were (—) 5, (—) 1000 and (—) 5000 mVs^{-1}. Both the electrodes were immersed in 10 mM $[Ru(NH_3)_6]^{3+}$ in aqueous 0.1 M KCl. The radius of the electrodes were (A) 79 nm and (B) 52 nm as calculated from the steady state current in the CV run at 5 mVs^{-1}.

However, voltammograms of electrodes with radius < 1 μm recorded at scan rate > 1 Vs^{-1} were often affected by significant noise which swamped the faradaic component of the current. For example, Figure 2.24A compares the voltammograms at 5 and 1000 mVs^{-1} for an 83 nm platinum nanode. Figure 2.24B reports the Fourier spectrum against frequency of the 1 Vs^{-1} voltammogram. Indeed, this figure suggests that the noise arose from the capacitive coupling with the mains, caused by the leads and electrical connections, as the signal was centred at 50 Hz.

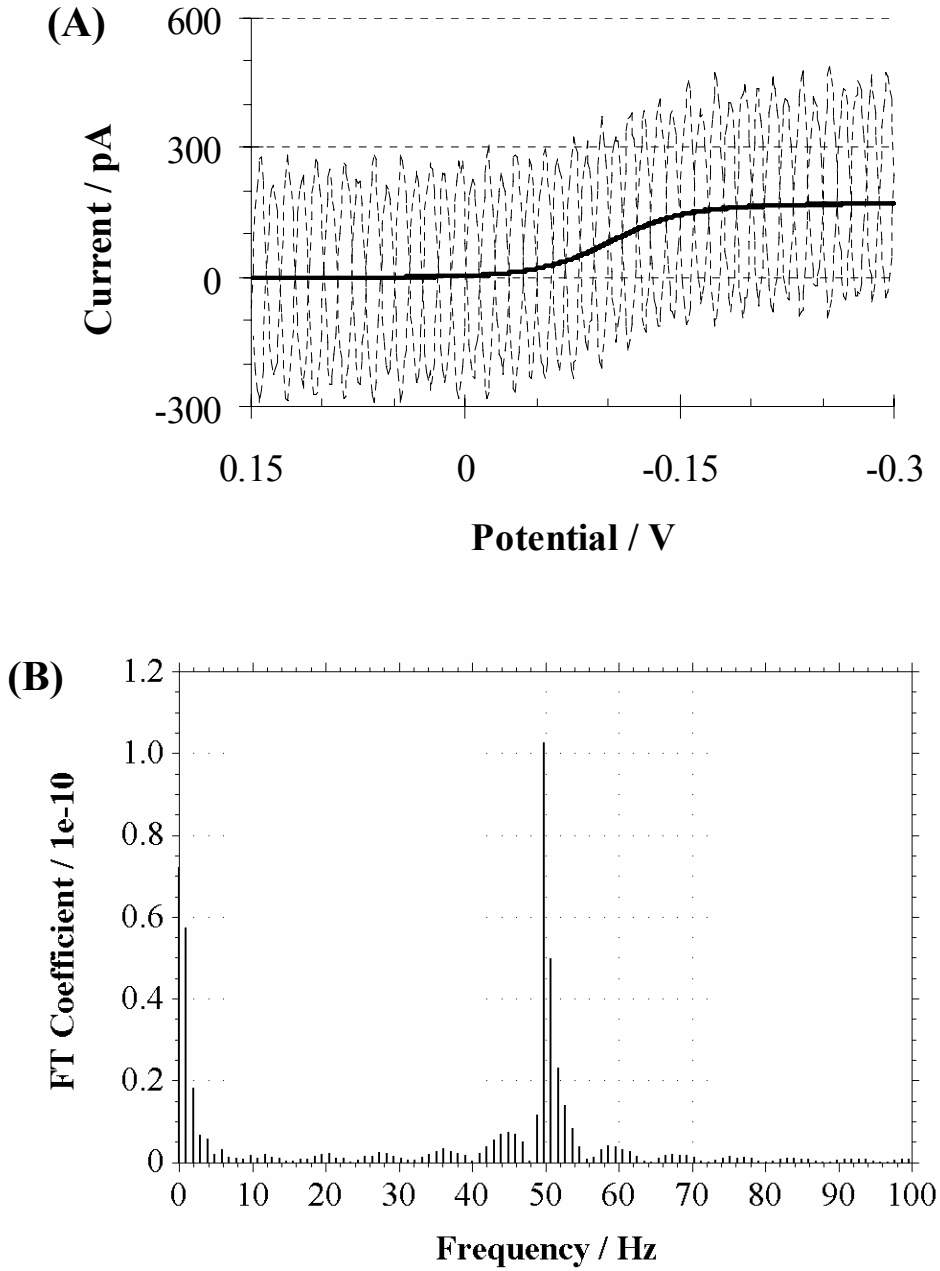

Figure 2.24 (A) Cyclic voltammetry at a platinum nanometer-sized electrode fabricated as described in Section 2.2.5.1. The taper was left intact and bevelled as described in Section 2.2.3.3. The probe was immersed in 10 mM $[Ru(NH_3)_6]^{3+}$ in aqueous 0.1 M KCl. The solid line (—) and the dashed (□ □) show the voltammogram at 5 and 1000 mVs^{-1}, respectively. The radius of the nanode was 83 nm as calculated from the steady state current in the CV run at 5 mVs^{-1}. (B) The Fourier spectrum obtained from the voltammogram at 1000 mVs^{-1} using the 900a CH software.

It is important to note that Faulkner and co-workers[27] as well as Wightman[28] attributed large stray capacitive currents to the electrode design. The authors reported that when silver epoxy or mercury was used to make an electrical connection between the microwire and the hook up wire, large cell time constants resulted.[21] This behaviour arose from the formation of the (electronically conducting/mercury/glass insulator/ionically conducting solution) junctions causing a large stray capacitance. Watkins and co-workers[29] prepared microelectrodes by coating platinum wires with electrophoretic paint and they estimated that, varying the depth of immersion of the probe tip in the solution, the electrode/polymer layer/solution capacitance was ~ 0.2 μFcm^{-2} (in a 0.2 M KCl solution). Now, the radius of the platinum wire drawn into the taper of the nanoelectrodes here fabricated was generally less than 1 μm and surrounded by glass shield ~ 25 μm thick as shown in Figure 2.16. As quartz dielectric layer was thicker than the one obtained from the coating with electrophoretic paint (4 - 6 μm)[25] and, even assuming a similar dielectric constant, a value smaller than 0.2 μFcm^{-2} should be expected. However, no significant change of the capacitive current was observed upon to changes of the depth of the immersion of the probes (results not shown). Studies of the dependence of the cell time constant (*RC*) on the tip immersion depth could not be carried out due to instrumental limitations, see Section 2.3.3.8.

For gold and platinum electrodes with radius > 1 μm, noise phenomena were not observed and voltammograms could be recorded up to several Vs^{-1}. For example, Figure 2.25A shows the voltammograms recorded at a gold microelectrode fabricated from 0.3 mm borosilicate capillaries with 25 μm wire as explained in Section 2.2.5.2. At sufficient scan rates crossover between the oxidative and reductive branches occurs which possibly arise from adsorption of the redox mediator on the electrode surface.[30] Figure 2.25B shows the voltammograms at a platinum UME fabricated as described in Section 2.2.5.1. In the CV at 50 Vs^{-1} the appearance of an anodic peak agreed with the transition towards linear diffusion regime which is what expected using Faddy and Leddy criteria as δ is 0.59 μm and then $\delta/a < 1$.[24] The radius of the electrodes in Figures 2.25A and 2.25B were 1.36 um and 4.4 μm respectively while the capacitance values were 49.7 and 278 pF (or 853 μFcm^{-2} and 457 μFcm^{-2} normalizing the values for the geometrical area) respectively. Table 2.1 and 2.2 in the next section summarises the results obtained with the CV analysis respectively for platinum and gold electrodes and compare them to what obtained by SECM and in some cases by SEM.

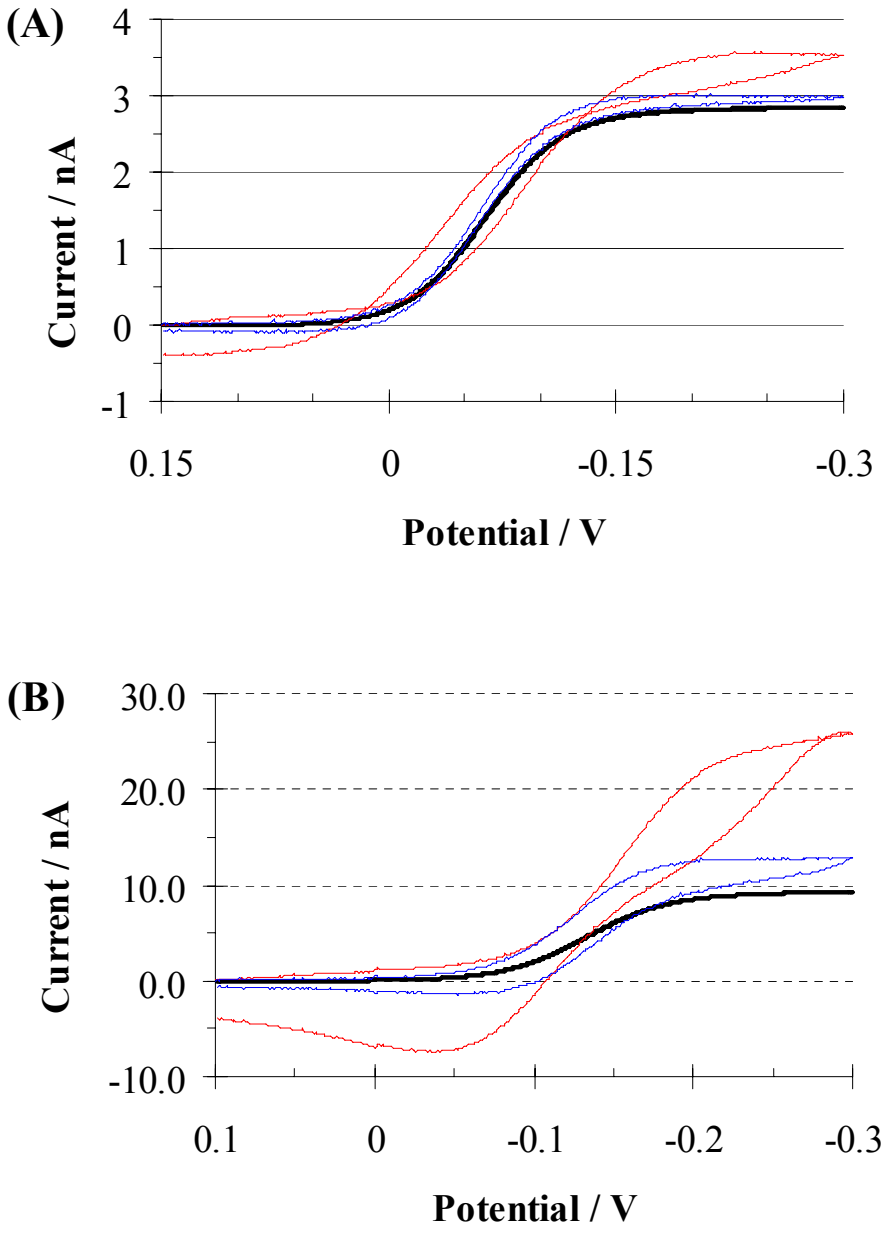

Figure 2.25 Cyclic voltammetry at different scan rates. (A) Gold UME was employed to record CVs at (—) 5 mVs^{-1}, (—) 1 Vs^{-1} and (—) 10 Vs^{-1}. (B) Platinum microelectrode was employed to record CVs at (—) 5 mVs^{-1}, (—) 5 Vs^{-1} and (—) 50 Vs^{-1}. The UMEs were fabricated from 25 µm gold wire with 0.3 mm borosilicate capillaries as described in Section 2.2.5.2 and from 25 µm platinum wire with quartz capillaries as described in Section 2.2.5.1. In both cases the taper was cut with a ceramic tile and then they were polished manually. The probe was immersed in 10 mM $[Ru(NH_3)_6]^{3+}$ in aqueous 0.1 M KCl for both figures. The radius of the electrodes was (A) 1.36 and (B) 4.4 µm as determined from the 5 mVs^{-1} voltammograms.

2.3.3.6 Scanning Electrochemical Microscopy Characterization

SECM is a powerful characterisation technique because it allows the simultaneous determination of the electrode radius and of the R_G factor during the fitting of the approach curves. Thus, it gives an insight of the geometrical properties of the probe which is very important especially at the scales where SEM imaging suffers from charging effects. Because the values in Tables 2.1 and 2.2 are based on a single measurement (data do not contain standard deviation), a *t*-test cannot be performed and it is not possible to establish whether the radius values of the electrodes calculated using different methods were significantly different or not. The ultimate decision whether the electrodes have to be discarded and re-polished should be based on the results of the latter test. However, in this work the data of the radius calculated using two different methods were plotted against each other (results not shown). The data determined using CV and SECM (average radius of the values of positive and negative feedback) showed excellent correlation, *i.e.*, R-squared values > 0.995, slope ~ 0.96 and small intercept. Only the electrode indicated with the symbol $^{\#}$ in Table 2.1 seems to deviate from this trend. Excellent correlation was also shown by the radius derived from the SECM positive and negative feedback. On the other hand, SEM seems to overestimate the radius of the probes when the "electrochemical" radius was smaller than approximately 300 nm.

As the electrodes radius decreases, approaching the substrate becomes challenging because of the tip/substrate alignment issue[31] as previously explained. For example, a radius of the glass shield size of ~ 7.5 μm and a tilt uncertainty of the probe during the approach curve ≤ 5° are taken as values. Then, trigonometry rules would dictate that the metal disk (assumed for simplicity in the middle of the glass shield) is ~ 0.65 μm away from the substrate when the glass shield touches the latter. Then it was expected that inlaid disk probes with radius < 500 nm might hardly approach the substrate at L < 1, where L is the substrate-tip normalized distance. Indeed, SECM approach curves with tips < 500 nm where the latter was able to achieve normalized distance < 0.2 have not been reported in the literature for this reason. Figure 2.26 gives the geometrical construction of the main criteria employed in this work to establish if the probe had a normalized recess depth, H, < 1. Indeed, the fact that electrodes were able to approach the substrate for L < 1 during the SECM positive feedback approach curve, L_{min}^{pos} < 1,

was a sign of a inlaid disk or slight recessed ($H < 1$) geometry when (L_{min}^{pos} -0.7) ≤ L_{min}^{neg} < L_{min}^{pos} where L_{min}^{neg} is the value of L achieved in the negative feedback approach curve. If the criteria above was not fulfilled and the probe was ~ 500 nm, a non ideal geometry of the electrode was probably responsible of this behaviour. Indeed, absence or limitation of the positive feedback (compared to negative) can be sign of a recessed or lagooned geometry, as the metal tip is further inside a cavity into the glass[7] while limitation of the negative feedback can be sign of a protruding geometry.[16,32]

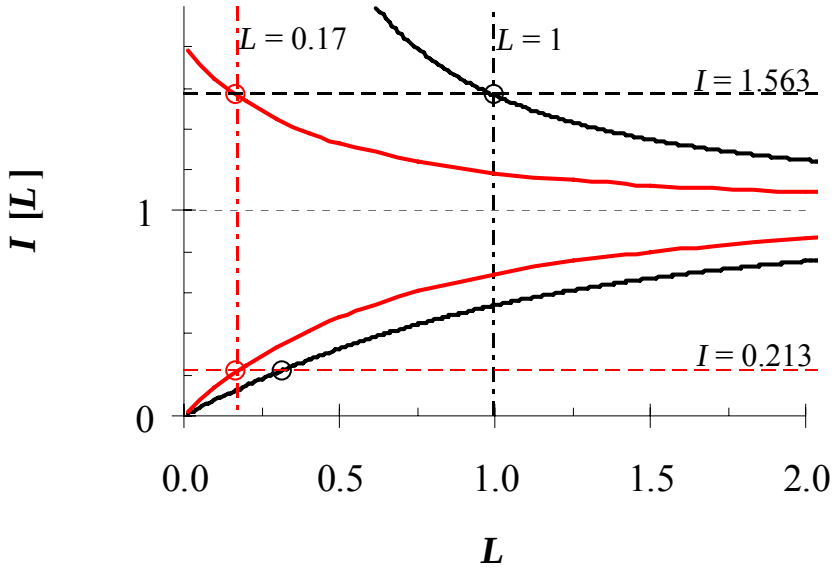

Figure 2.26 Geometrical construction in order establish if the probe was inlaid disk or recessed but with $H < 1$. The solid black lines (—) represent the positive (above 1) and negative (below 1) feedback approach curve for a inlaid disk probe.[14,15] The dashed dotted black line (□ · □) where $L = 1$ crosses the positive feedback line (—) at I = 1.563. The solid red lines (—) represent the positive (above 1) and negative (below 1) feedback approach curve for a disk probe with $H = 1$.[33,34] The dashed black line (□ □) where $I = 1.563$ crosses the ($H = 1$) positive feedback line (—) at $L = 0.17$. The dashed dotted red line (□ · □) where $L = 0.17$ crosses the ($H = 1$) negative feedback line at I = 0.213. Finally, the dashed red line (□ □) where $I = 0.213$ crosses the negative feedback curve (—) at $L = 0.32$. Therefore, when a probe is assumed to be inlaid disk, and the positive feedback approach curve can be fitted till $L = 1$, it follows that, if the negative feedback can be fitted at L values < 0.32, a recess with $H > 1$ should be present.

Figure 2.27 shows the two approach curves for the platinum nanoelectrode whose SEM image was shown in Figure 2.20. The radius determined from the SECM approach curves (average between the two fitted values) was 532 nm which is reasonably close to the 565 nm calculated from the steady state current in the CV. Because (L_{min}^{pos} - L_{min}^{neg}) is equal to 0.3, according to the criteria explained above the recess apparent in Figure 2.20 had to be smaller than 1 radii. Some minor deviations from the theoretical feedback curves are apparent in both the figures and they might arise from contacts between the glass shield and the substrate as suggested by Sun and Mirkin.[31] However, no significant difference in the fitted values was observed when the approach curves were repeated over time which means no damage or fouling of the electrode occurred.

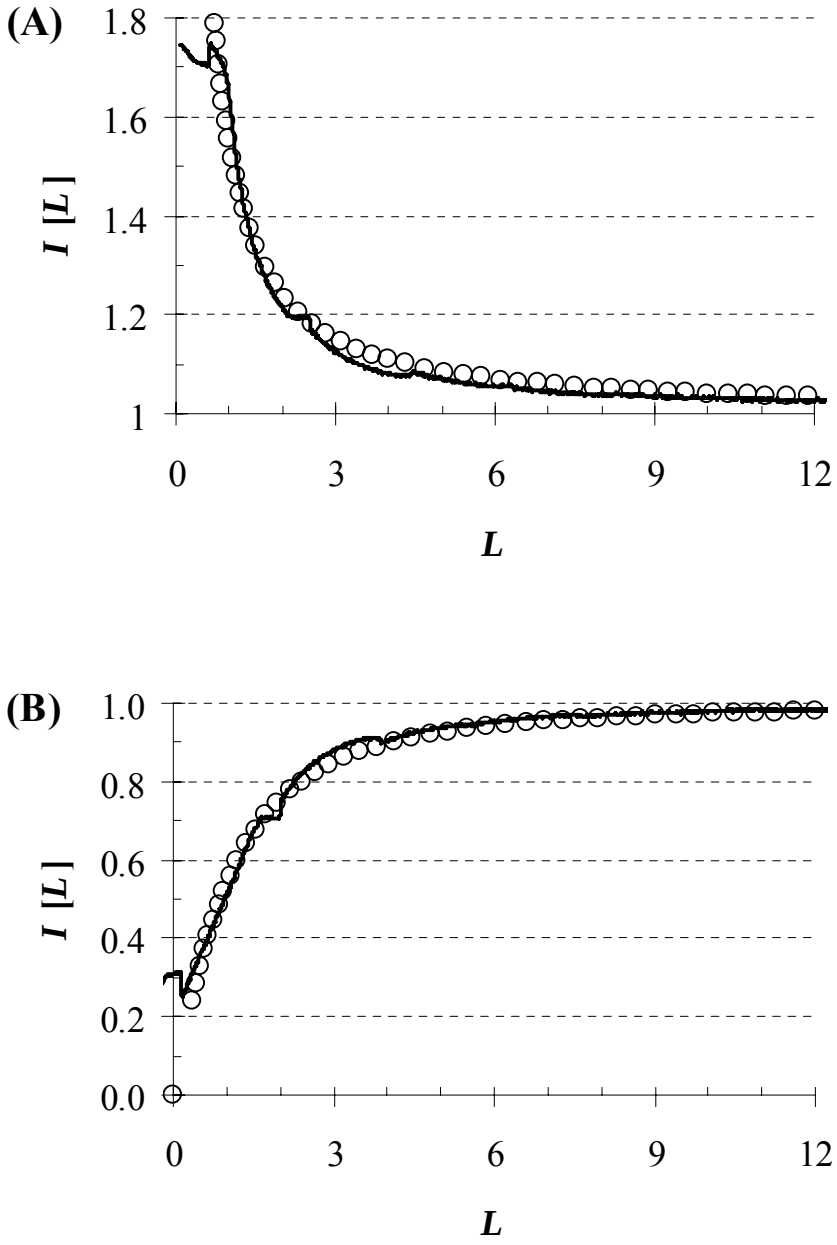

Figure 2.27 (A) Positive and (B) negative feedback approach curves obtained during the reduction of $[Ru(NH_3)_6]^{3+}$ as the SECM tip approached a 2 mm Pt electrode and a Teflon substrate respectively. The SECM tip was a ~ 532 nm platinum electrode and it was immersed in a solution of 10 mM $[Ru(NH_3)_6]Cl_3$ in aqueous 0.1 M KCl. The probe potential was held at -0.3 V *vs.* Ag/AgCl to drive its reduction at the diffusion controlled rate. The solid line (—) was the experimental curve while the open circles (○) represent the theoretical curves for inlaid disk electrodes with radius of (A) 526 and (B) 538 nm and R_G value of 7 as listed in Table 2.1. The tip approach speed was 40 and 50 nm s^{-1} respectively in (A) and in (B).

Tables 2.1 and 2.2 report the results obtained from the SECM analysis for the platinum and gold electrodes respectively and compare them to the data resulting from CV and SEM analysis as described in the two previous sections. It is significant to note that, two out of the three electrodes in Table 2.1, which show (L_{min}^{pos} - L_{min}^{neg}) > 0.7 (indicated by the symbol ^ in the table), were characterized by higher capacitance values and by resistive effects similarly to what shown in Figure 2.23A. The non ideal behaviour of these electrodes in both the techniques might be a sign of a problem with the electrode geometry or seal quality even if this is not apparent in SEM.

Table 2.1 Platinum nano- and micro-electrodes fabricated as described in Section 2.2.5.1. The table reports the geometrical properties of the electrodes obtained by different characterization methods. The radius, a, and the specific capacitance, C_d^0, of the probes were calculated from the voltammogram of a redox mediator as explained in Section 2.3.3.5. Employing the electrodes as SECM probes allowed the determination of their radius and R_G factor. L_{min} represents the minimum normalized distance which was achieved during an approach curve. SEM was used in some cases to image the tip but offered more qualitative insights than the other two methods.

SECM					**CV**		**SEM**	
Negative Feedback			**Pos. Feedback**					
a / nm	L_{min}^{neg}	R_G	a / nm	L_{min}^{pos}	a / nm	C_d^0 / mFcm^{-2}	a / nm	R_G
131	2.7	11	152	1.8	117	57.0	d.r.	/
#221	1.0	11	216	1.6	154	32.3	270	14
194	0.9	14	191	0.8	186	14.4	260	15
453	0.3	7	472	0.8	494	/	/	/
74	5.1	28	74	2.1	79	418	/	/
538	0.6	7	526	0.9	565	1.26	490	*15
^230	0.7	11	231	3.0	216	128	/	/
^660	3.6	10	628	0.9	651	1.48	/	/
^443	0.3	20	427	2.2	432	25.3	/	/
40	6.2	15	54	5.5	52	129	/	/
73	1.9	8	74	3.6	72	139	/	/
7	$	$	6	$	8	/	/	/
66	3.1	8	65	4.2	83	87.0	/	/
4000	1.0	16	4000	0.2	4100	178	/	/
7660	0.7	20	7770	0.2	7800	/	/	/

#Radius values from CV and SECM seems to suggest non ideal behaviour. d.r. stands for deep recess *i.e.*, metal disk not visible in the SEM image. *Not symmetrical glass shield. ^L_{min} values in SECM and resistive effects in CV might suggest geometrical faults. $Due to the lack of points for the fitting the data were not calculated.

Table 2.2 Gold microelectrodes fabricated as described in Section 2.2.5.2. The table reports the geometrical properties of the electrodes obtained by different characterization methods. The radius, a, and the specific capacitance, C_d^0, of the probes were calculated from the voltammogram of a redox mediator as explained in Section 2.3.3.5. Employing the electrodes as SECM probes allowed the determination of their radius and R_G factor. L_{min} represents the minimum normalized distance which was achieved during an approach curve. SEM imaging gave in some cases an insight of the tip and offered a more qualitative comparison than the other two methods.

SECM					**CV**		**SEM**	
Negative Feedback			**Pos. Feedback**					
a / nm	L_{min}^{neg}	R_G	a / nm	L_{min}^{pos}	a / nm	C_d^0 / μFcm^{-2}	a / nm	R_G
3.4	1.2	49	3.4	0.5	3.2	1263	/	/
5.6	0.6	23	5.6	0.2	5.4	886	5.5	*10-28
3.6	1.1	20	3.8	1.6	3.6	1158	3.3	*12-18
2.3	0.4	30	2.4	1.1	2.4	578	/	/
5.7	0.6	17	6.0	0.3	5.8	353	/	/
1.36	2.0	28	1.36	0.7	1.36	853	/	/
2.3	0.4	54	2.3	1.6	2.4	/	/	/

*Not symmetrical glass shield

From Table 2.1 it is apparent that the platinum tip < 100 nm showed a lack of both positive and negative feedback and then the fitted R_G values contain large errors and they have to be taken only qualitative. It is probable that this behaviour arose from poor tip/substrate alignment.[7,34] At present status the SECM analysis could not guarantee that electrodes with radius < 100 nm were not recessed. It is significant to note that the substrate roughness might have an important role in the substrate/tip alignment issue.[7,31,33,34] The use of an atomically flat gold wafer as substrate seemed to have improved slightly this aspect but a larger statistical sample of data would be necessary to draw definitive conclusions (results not reported). Both platinum and gold microelectrodes with radius > 2 μm were generally prepared cutting the taper off. However, as explained above, instrumental sharpening and polishing was difficult and

in some cases these steps were carried out manually. So, in this case, the lack of positive and negative feedback experienced arose from the large R_G factors (on average > 20) or non straight profile of the glass shield. Nevertheless, because these electrodes were not employed in SECM investigations in this work, the instrumental bevelling issue was not addressed.

2.3.3.7 Determination of the Electrochemical Area

Voltammetry in 1.0 M H_2SO_4 was used to calculate the electrochemical area of the platinum and gold electrodes and from that the apparent roughness factors as explained in Section 1.3.6. Tables 2.3 and 2.4 report the data of the electrodes radius (determined from CV or SEM) in decreasing order and the measured roughness factor. The radius of the electrodes was in the most of the cases determined from the steady state current for a redox mediator in solution using Equation 1.14. In light of the fact that the resistive effects in a CV of a redox probe as shown in Figure 2.23A were found most likely arising from non ideal geometric properties, electrodes showing this behaviour were discarded and not used in the calculation of the roughness factors. In addition, probes which did not achieve a steady state current at slow scan rates, *i.e.*, flat branches, were discarded from this analysis because the latter behaviour is consistent with leaking through the glass shield.

Table 2.3 Surface roughness factors for platinum probes fabricated as described in Section 2.2.5.1. The electrochemical area was determined from the reduction peak of the platinum oxide cycling between the oxygen and hydrogen evolution regime at 0.2 Vs^{-1} in 1.0 M H_2SO_4 solution. The surface roughness was calculated as the ratio between the electrochemical and the geometrical areas as explained in Section 1.3.6. The radius of the platinum electrodes was determined from the steady state current of a redox mediator voltammogram at scan rates ≤ 5 mVs^{-1} or from SEM imaging.

CV	**SEM**	**H_2SO_4**
***a* / µm**	***a* / µm**	**ρ**
/	25.4	2.3
/	24.0	4.5
/	13.0	3.9
12.8	/	2.2
7.1	5.5	5.9
7.1	4.9	7.5
0.967		351
0.727	/	287
0.693	/	613
0.665	/	375
0.225	/	174

Table 2.4 Surface roughness factors for gold probes fabricated as described in Section 2.2.5.2. The electrochemical area was determined from the reduction peak of the gold oxide cycling between the oxygen and hydrogen evolution regime at 0.2 Vs^{-1} in 1.0 M H_2SO_4 solution. The surface roughness was calculated as the ratio between the electrochemical and the geometrical areas as explained in Section 1.3.6. The radius of the gold electrodes was determined from the steady state current of a redox mediator voltammogram at scan rates ≤ 5 mVs^{-1}.

CV	H_2SO_4
a **/ μm**	**ρ**
0.44	555
0.52	169
3.7	200
3.5	29

It was found that, especially for platinum probes with radius < 1 μm and for all gold microelectrodes, the apparent roughness factors were strikingly large with values of up to several hundreds when these factors were calculated from the charge under the metal oxide reduction peak in the voltammogram run at scan rate < 500 mVs^{-1}. It is also significant that electrodes prepared by sealing of a 12.5 and 25 μm (radius) platinum wires in a glass capillary and hand-polished with the same final polishing sheet (0.3 μm), as explained in Section 2.2.3, showed roughness factor between 2 and 4. In all cases the number of voltammetric cycles was minimized so as to avoid roughening of the electrode surface.

Figure 2.28A shows the voltammogram obtained at 5 Vs^{-1} for a platinum microelectrode immersed in 1.0 M H_2SO_4. This voltammogram is well defined with a clear metal oxide reduction peak being observed at approximately 0.45 V and from the charge passed under the oxide reduction peak a roughness factor of 1.9 was determined. In this figure well defined hydrogen adsorption and desorption peaks are also apparent suggesting a clean surface. Voltammetry of gold microelectrodes in 1 M H_2SO_4 at 5 Vs^{-1} showed also well defined metal oxide reductions at approximately 0.85 V (results not shown). Indeed, roughness factors calculated from the charge passed under the gold oxide

reduction at scan rate of 5 Vs^{-1} gave values between 2 and 3.1. However, as shown in Figure 2.28B, the voltammetric response changes significantly as the scan rate is decreased. In particular, the oxide reduction peak broadens and the hydrogen adsorption/desorption peaks become much less defined. Indeed, Figure 2.29 reports the values of the apparent roughness factor calculated for a couple of gold and platinum microelectrodes in function of the scan rate of the voltammogram run cycling the electrode potential between the oxygen and hydrogen evolution regime in 1.0 M H_2SO_4. It is apparent that the roughness factors depend significantly on the scan rate and that ρ levels off to "more usual" values with scan rates above 5 Vs^{-1}. While parasitic Faradaic process from low concentrations of adventitious impurities in solution may contribute to the observed response, they are unlikely to be dominant. Also, an imperfect seal between the metal wire and the glass body could increase the area available for the oxide formation. However, the observation of a well defined steady state current, low capacitance, small R_uC_d, and consistency of the electrode areas as determined using SEM and voltammetry, suggest that a poor seal is not the origin of the large apparent roughness measured at slow scan rates. Gold and platinum dissolution during the reductive sweep has also been reported in the literature[35] but, in the experimental conditions of this work, it should not be responsible for the high roughness factor.[36,37] Microelectrodes with very high roughness factors have been fabricated by Elliot *et al.*[38] electrodepositing platinum film from a hexagonal lyotropic liquid crystalline plating solution. The resulting mesoporous lattice was responsible for the increase in the surface area. However, the formation of a similar structure during the melting/cooling of the wire in the pulling step is very unlikely as proved by the very low capacitance values, see next section.

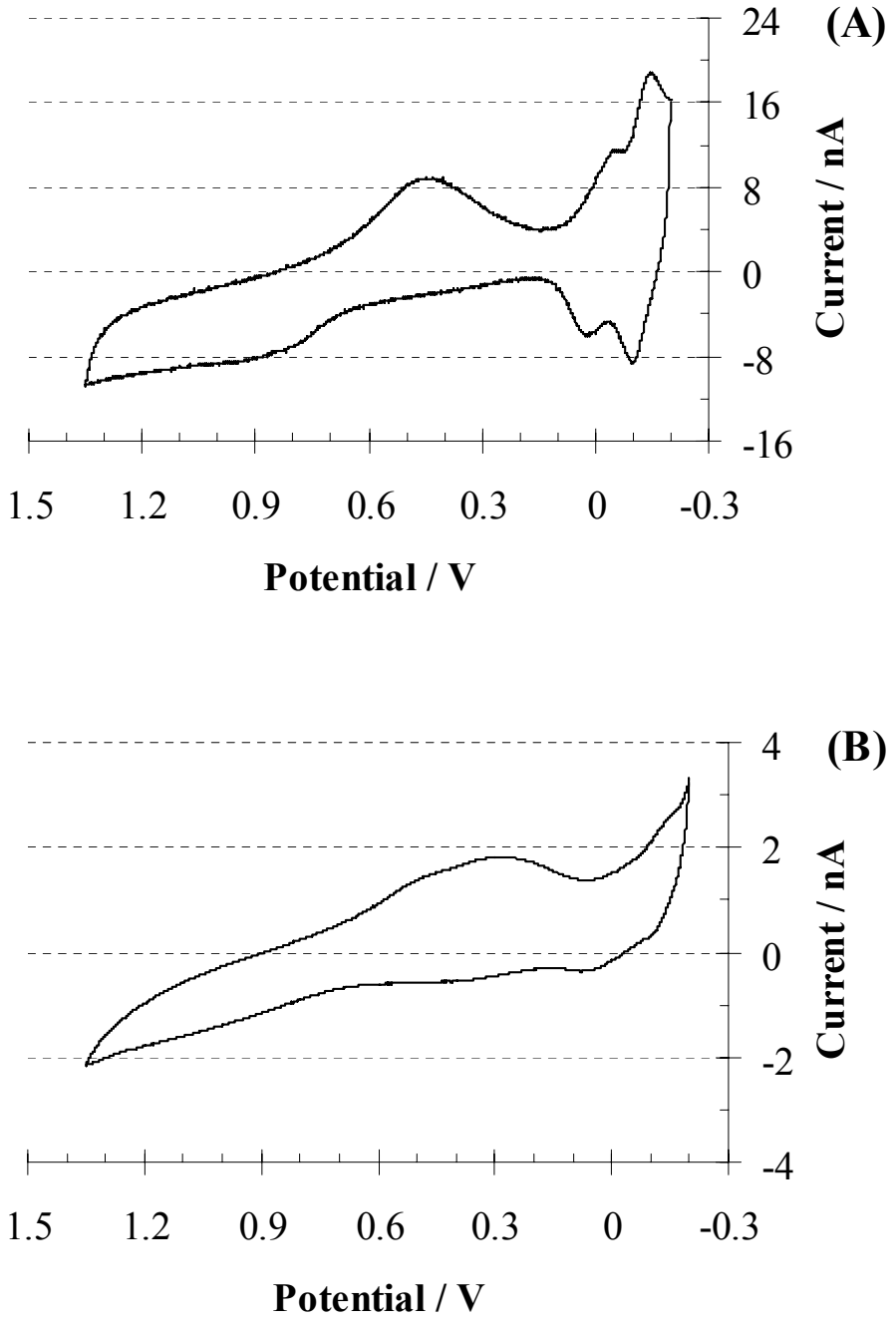

Figure 2.28 Cyclic voltammetry of a 3.7 μm platinum inlaid disk electrode immersed in 1.0 M H_2SO_4 aqueous solution. Voltammogram was recorded at the scan rate of (A) 5 Vs^{-1} and (B) 100 mVs^{-1}. The probe was fabricated as described in Section 2.2.5.1, then the taper was cut with a ceramic tile and polished manually on a polishing table using a final alumina sheet of 0.3 μm. The radius of the microelectrode was determined from the steady state current of a 5 mVs^{-1} voltammogram run in a solution of 10 mM $[Ru(NH_3)_6]Cl_3$ in aqueous 0.1 M KCl.

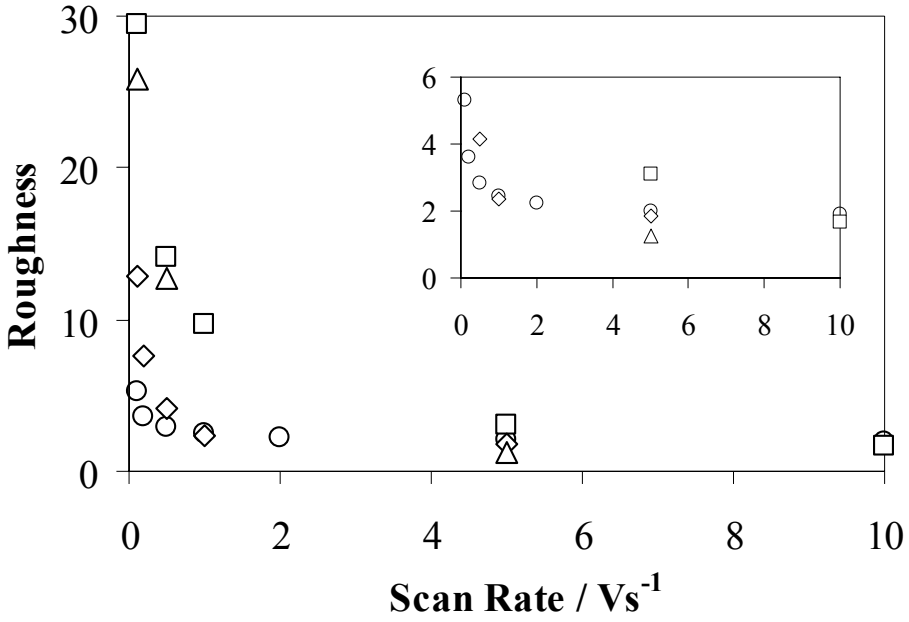

Figure 2.29 Roughness factor calculated for gold and platinum microelectrodes in function of the scan rate of the voltammogram run with the probes immersed in 0.1 M H_2SO_4. The roughness factor was calculated from the charge passed under the metal reduction peak as explained in Section 1.3.6. The potential was swept between -0.25 V and 1.5 V in case of gold UMEs or between -0.2 V and 1.35 V in case of platinum UMEs. (○) 5.2 μm gold, (□) 4.8 μm gold, (Δ) 2.6 μm platinum and (◊) 3.7 μm platinum electrodes were employed in this study. The inset shows an enlargement of the plot. The units of measure in the inset are the same as in the main figure.

Previous studies exploit the fast response time of microelectrodes to probe the kinetics of oxide layer growth over a wide time domain. Indeed, chronoamperometry conducted on the microsecond timescale was employed to probe the platinum oxidation processes at a 2 μm microelectrode stepping the potential from 0 to +1.2 V in 0.1 M H_2SO_4. The study highlighted the fact that the oxide grows with two different rates. In fact, charge passed within the initial 10 μs agreed with the formation of a dense oxide monolayer with a first order constant rate of $7.5 \pm 0.6 \times 10^4$ s^{-1}. Moreover, it was also demonstrated that this process was reversible when the potential was stepped to +0.3 V. However, at times between 10 μs and 1.5 ms it was noticed that the platinum oxide grew with a smaller first order constant rate which is equal to $4.2 \pm 0.3 \times 10^2$ s^{-1} and that the charge passed was equivalent to that associated with more than 30 oxide monolayers. Significantly, this oxide could not be removed by stepping the potential to

+0.3 V but only at lower potential. Therefore, this investigation is consistent with the dependence of the roughness factor of gold and platinum UMEs from the scan rate observed in this work. In conclusions, it appears that thick oxide layers can be formed on these microelectrodes, most likely by a high field growth mechanism,[37,39] when the probes are cycled in sulphuric acid solutions at slow scan rates.

2.3.3.8 High Speed Chronoamperometry

The charging current, i_c, passing though a resistor, R_u, is described by Equation 1.11 and using the logarithm notation:

$$\ln(i_c) = \ln\left(\frac{\Delta E}{R_u}\right) - \frac{t}{R_u C_d} \qquad \text{(Eq. 2.1)}$$

where C_d is the double layer capacitance. The plot described by Equation 2.1 is linear with the time and R_u and C_d can be determined from the intercept and the slope. Indeed, this approach was employed in the evaluation of the R_uC_d cell time constant for platinum UMEs using a custom built function generator-potentiostat.[17] The accuracy of the latter was verified monitoring the *RC* cell time constant of dummy cells consisting of a capacitor and a resistor connected in parallel. The capacitor was connected as working electrode while the resistor as reference/counter. The potential was then stepped to 0.2 V against this reference and the capacitive decay was recorded. The capacitor and resistor were chosen to mimic the R_uC_d cell time constant of 12.1, 8.2, 5.6, 3.8, 2.6 and 1.2 μm Pt UMEs taking 40 μFcm^{-2} and 0.0128 $\Omega^{-1}cm^{-1}$ as values for C_d^0 and κ (in a 0.1 M KCl solution) and assuming a roughness factor of 1.2.[13] Table 2.5 compares the expected data with the ones experimentally determined. Considering an error of ± 10 % on the capacitance and ± 1 % for the resistance, as specified by the supplier, an error ± 10 % associated to the experimental *RC* could be expected which on average agrees with the results reported in the table.

Table 2.5 Accuracy of the custom-built function generator-potentiostat evaluated monitoring the cell time constant, *RC*, of dummy cells fabricated connecting in parallel a capacitor and a resistor. Capacitance and resistance values of the dummy cells are reported. The cell time constant experimentally (last column) determined can be compared to the expected one (third column) given by multiplication of resistance and capacitance values.

C_d / pF	R_u / kΩ	*RC* / μs	*RC* / μs
2.2	160	0.35	0.46 ± 0.01
10	75	0.75	0.83 ± 0.01
22	51	1.12	1.21 ± 0.01
47	39	1.83	1.90 ± 0.02
100	24	2.4	2.58 ± 0.02
220	16	3.6	3.64 ± 0.03

The cell time constants were determined from the chronoamperometric decays of the capacitive current for a size range of platinum microelectrodes. The radius of those was determined from the steady state voltammogram at 5 mVs^{-1} during the reduction of ruthenium hexamine chloride. Besides, capacitance values were calculated plotting the Δi between forward and reverse scan branches, taken from a non faradic region of the redox mediator voltammograms, in function of the scan rate as described in Section 2.3.3.5. In some cases minor resistive effects, *i.e.*, slight sloping of the steady state could be seen upon increasing the scan rate. However, independently from that behaviour, for probes smaller than 3 μm, the decays were too small and too short to be resolved. In the latter case, from the end of the potential perturbation on the current, it could be only estimated that the R_uC_d values were smaller than 0.2 μs, which is in good agreement with the small size of those electrodes. Figures 2.30A and 2.30B show the chronoamperometric decay of a 3.2 and 0.143 μm platinum electrodes, respectively. Despite a noticeable environmental noise at approximately 50 MHz, it is important to note that the two decays were significantly similar. The latter behaviour agrees with the fact that the capacitance of probes smaller than 3 μm was dominated by stray capacitance rather than the capacitance of the double layer charging at the metal disk/solution interface.

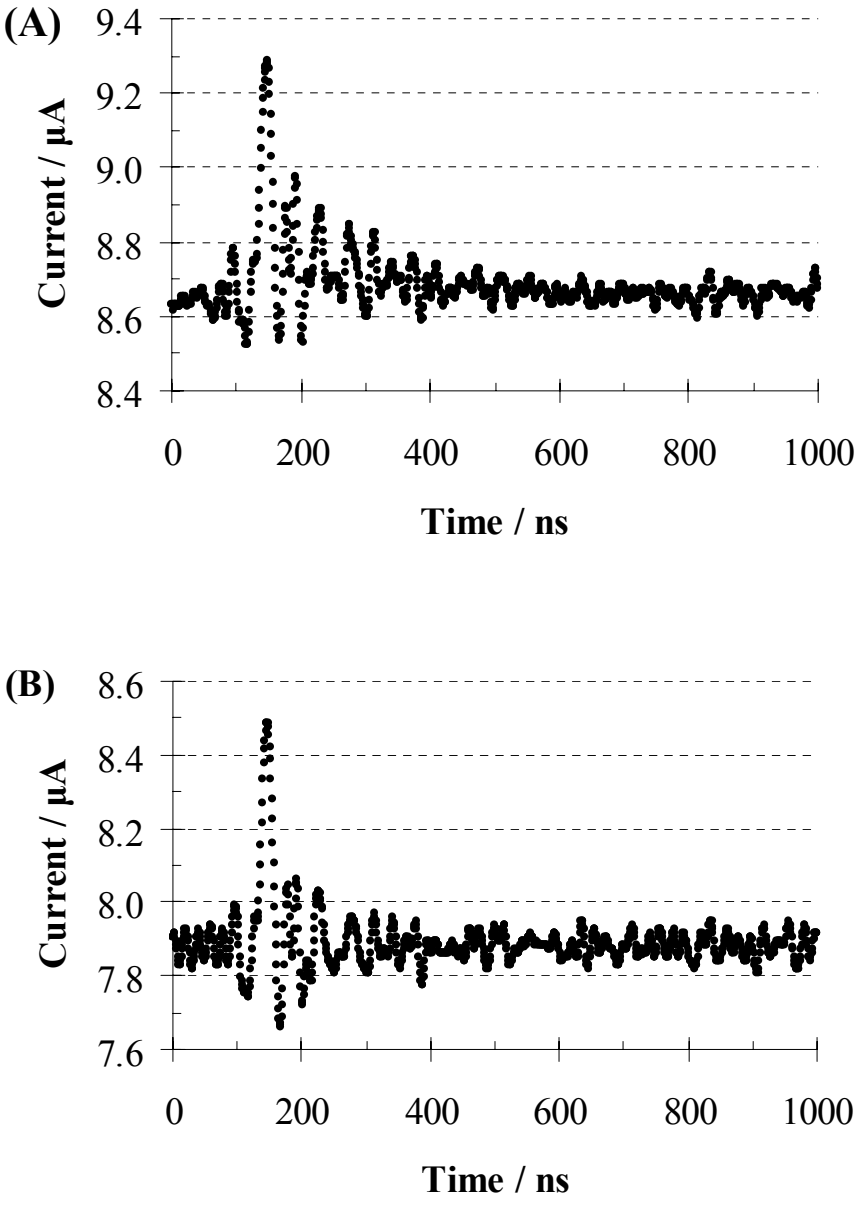

Figure 2.30 Chronoamperometric decay of the capacitive current in aqueous 0.1 M KCl at (A) a 3.2 µm and (B) 143 nm platinum probes. The potential was stepped from 0 to 0.2 V against an Ag/AgCl reference connected in parallel to a Pt wire. The electrodes were prepared and polished as described in Section 2.2.5.1 and 2.2.5.3.

Figure 2.31A shows a representative chronoamperometric decay for electrodes with radius > 3 μm. Figure 2.31B reports the semi-logarithmic plot of this decay from which R_u and C_d were estimated. Table 2.6 summarises the R_uC_d values of some platinum UMEs obtained from the chronoamperometry analysis. In addition, the values of capacitance measured from the voltammogram of a redox probe in a non faradic region are also reported in this table. It is significant that these values are at least ~ two orders of magnitude higher than the ones determined from the chronoamperometric decay of the capacitive current. Cables and leads are likely to be responsible for this difference. The capacitance values obtained from the chronoamperometry experiment, when normalized by the geometrical area, are lower (between factor 2 and 10) than 40 μFcm^{-2}, value often reported.[13] However, this behaviour might arise in part from instrumental limitation as the capacitance of the dummy cells was also affected by an error between 30 and 50 %.

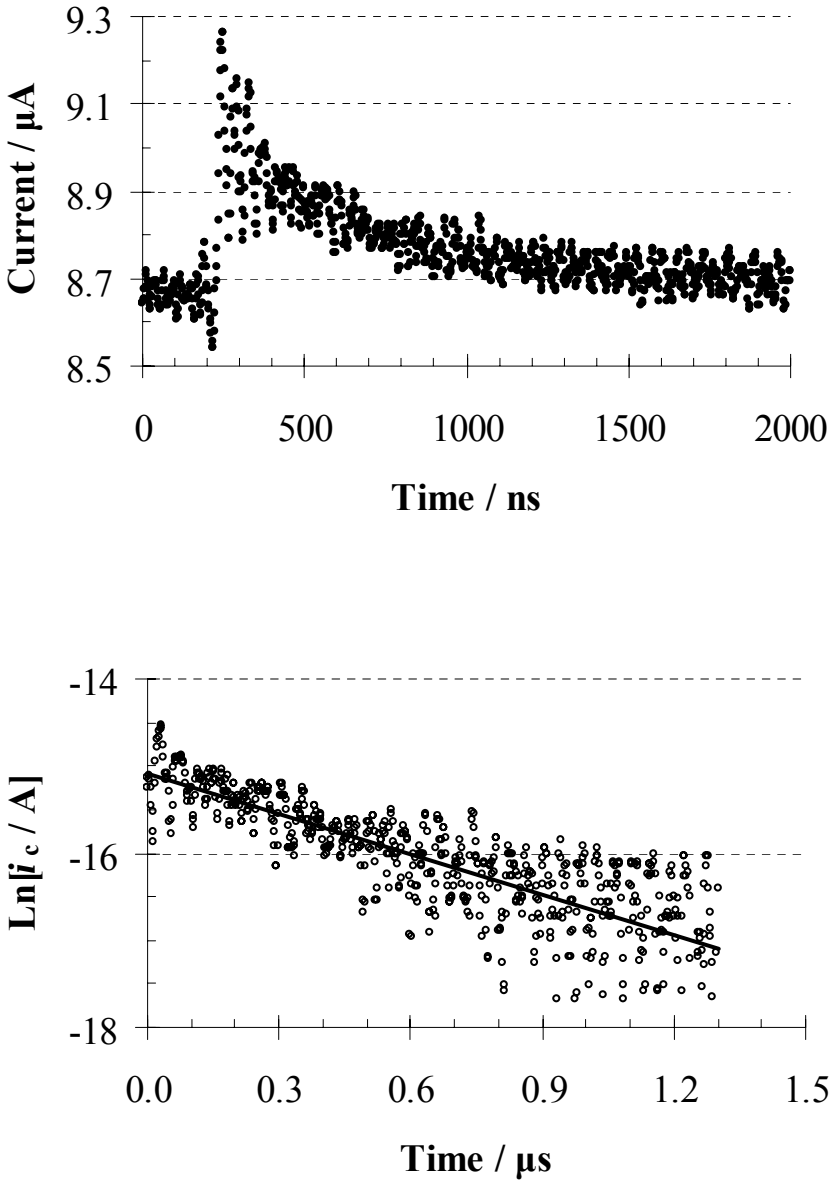

Figure 2.31 (A) Chronoamperometric decay of the capacitive current in aqueous 0.1 M KCl at a 6.7 µm platinum electrode. (B) Semi-logarithm plot of the current from (A). The thick solid line (—) in (B) is the linear fitting of the experimental data represented by the empty circles (○). The potential was stepped from 0 to 0.2 V *vs.* an Ag/AgCl reference connected in parallel to a Pt wire. The electrode was prepared and polished as described in Sections 2.2.5.1 and 2.2.5.3.

Table 2.6 Values of the cell time constant for platinum UMEs fabricated and polished as described in Sections 2.2.5.1 and 2.2.5.3. The radius of the platinum electrodes was determined from the steady state current of the 5 mVs^{-1} voltammogram of a solution of 10 mM $[Ru(NH_3)_6]Cl_3$ in aqueous 0.1 M KCl. The capacitance values were calculated from the voltammograms at different scan rate plotting the Δi between oxidative and reductive branches in a non faradic region in function of the scan rate as explained in Section 2.3.3.5. The cell time constant was calculated from the chronoamperometric decay of the capacitive current in aqueous 0.1 M KCl as explained in the text above.

CV		**Chronoamperometry**	
***a* / µm**	**C_d / pF**	**R_uC_d / µs**	**C_d / pF**
12.3	/	2.60 ± 0.06	80.8 ± 1.5
7.3	595	0.77 ± 0.09	3.1 ± 0.3
6.7	620	0.65 ± 0.04	0.88 ± 0.04
6.0	421	0.79 ± 0.07	4.3 ± 0.3
3.2	126	0.17 ± 0.05	0.11 ± 0.03
1.96	25.9	< 0.2	/
0.853	5.7	< 0.2	/
0.143	2.0	< 0.2	/

The cell time constant reported in Table 2.6 are plotted in Figure 2.32 as a function of the probe radius together with those found for the dummy cells. (The dummy cells mimic the behaviour of certain sizes of platinum UMEs and then their *RC* are reported in function of an "equivalent radius"). As explained above, there is an uncertainty on the R_uC_d of UMEs with radius smaller than 3 µm, but from Figure 2.30 it is reasonable to assume that the R_uC_d did not change significantly as the stray capacitance contribution seemed to become predominant. From Figure 2.32 it is apparent that the dummy cells *RC* lie almost on the trend line which describes the expected behaviour of platinum electrodes assuming 40 μFcm^{-2}, 0.0128 $\Omega^{-1}cm^{-1}$ and 1.2 as values for C_d^0 and κ (in a 0.1 M KCl solution) and roughness factor respectively.[13] On the other hand, the experimental R_uC_d of the platinum UMEs lie below this line and the linear regression fitting these data (not shown in the figure) has a similar slope but a negative intercept. The latter fact is not fully understood.

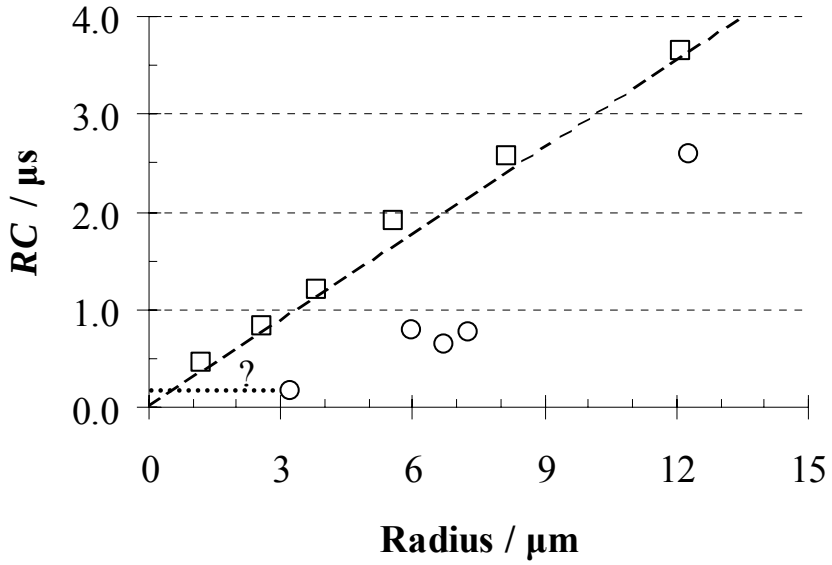

Figure 2.32 Time cell constant (*RC*) found for (○) the platinum UMEs and for (□) the dummy cells in function of their radius or the equivalent one, respectively, as calculated from the chronoamperometric decay of the capacitive current as explained above in the text. The microelectrodes were prepared and polished as described in Section 2.2.5.1 and 2.2.5.3 respectively. The solid dashed line (□ □) represents the R_uC_d values expected for platinum probes in function of their size when 40 μFcm^{-2}, 0.0128 Ω^{-1}cm^{-1} and 1.2 are assumed as values for C_0, κ and roughness factor. R_uC_d values for platinum UMEs with radius < 3 μm could not be determined and their uncertainty is represented with a dotted line (···) in the figure. The error bars are not indicated because they are smaller than the symbols size employed in the graph.

2.3.4 Platinum Nanoelectrodes in SECM Imaging

SECM cannot compete with other techniques (like SEM and AFM) for imaging purposes but introduction of smaller probes has the immediate advantage of increased resolution.[10,40] In this work an array of nanocavities was chosen as substrate. Figure 2.33 shows the details of the array imaged by AFM. From this figure it was established that the cavities had an aperture of ~ 600 – 700 nm and a depth of ~ 500 nm.

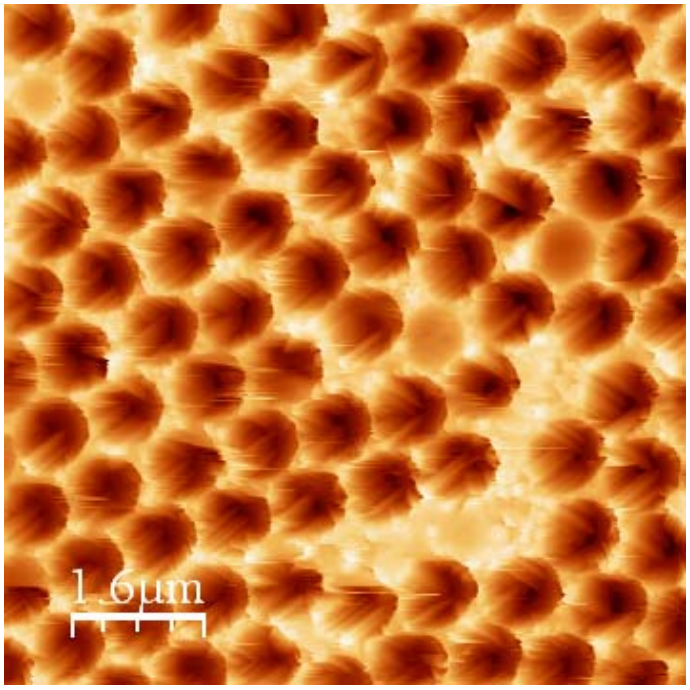

Figure 2.33 AFM image of a gold nanocavities array prepared using nanosphere lithography techniques as elsewhere described.[19]

Considering conical diffusion from the tip towards the substrate, the radius of the portion of the substrate surface participating in the SECM feedback loop, a_s, can be evaluated as:[41]

$$a_s = a + 1.5d \qquad \text{(Eq. 2.2)}$$

where a is the radius of the probe and d the distance between the tip and the substrate. In addition, considering a value of the normalized distance, L, ~ 1.5 - 2 (in order to avoid any collision during the imaging), it follows that only a probe with radius ≤ 200 nm would be capable of resolving the features of such an array. Indeed, the probe used to accomplish this task had a radius of 202 nm as calculated from the steady state current of the 5 mVs^{-1} voltammogram of a solution of 10 mM $[Ru(NH_3)_6]Cl_3$ in aqueous 0.1 M KCl. This value is reasonably close to 177 nm which was the value found by fitting the SECM positive feedback approach curve.

The approach of the tip towards the gold nanoarray substrate was stopped manually at L = 2.5 *i.e.*, ~ 410 nm far away from the substrate. This procedure caused an uncertainty in the offset of the fitting *i.e.*, substrate-tip distance when the glass shield of the tip touches the substrate as shown in Figure 2.6. However, two arguments could minimize

this issue. First, the substrate roughness, which was ~ 50 nm between individual cavities, appeared to be significant when compared to the radius of the tip. Second, the substrate features sized in the same order of magnitude of the probe and then use of the Equation 1.5 for the positive feedback probably underestimated the substrate-tip distance. With the probe ~ 410 nm above the substrate, the tip was scanned in the *x*-*y* plane and Figure 2.34 shows the resulting image. Cavities, which have diameter ~ 600 nm, are apparent in the figure, showing an excellent lateral resolution thanks to the small tip size *i.e.*, negligible diffusion broadening effects. Moreover, the difference in the current allows the determination of the cavity edge-bottom height which, using Equation 1.5 can be estimated to be around 210 nm. The latter data is lower than the value established by AFM. However, feedback current from the bottom and from the edges of the cavity should be partially convoluted because the curvature of the cavity itself. Thus, a lower value for the cavity bottom-edge height can be expected.

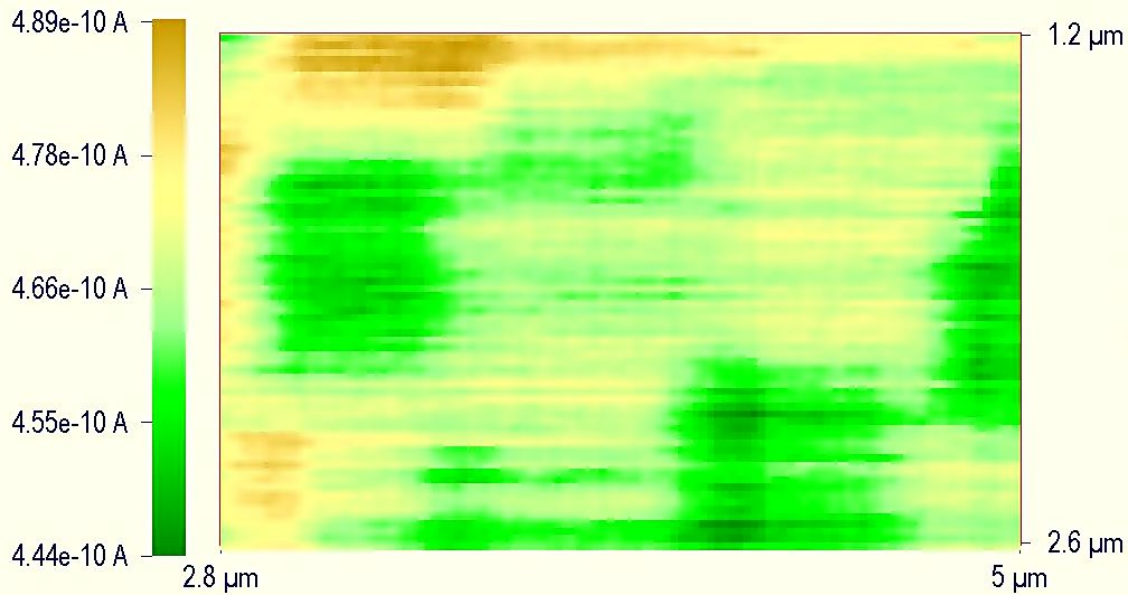

Figure 2.34 SECM image produced by recording i_T while scanning the tip (at the constant distance of ~ 410 nm) across the surface of the substrate in the *x*−*y* plane at 330 nm s^{-1}. The substrate was an array of gold nanocavities prepared by nanosphere lithography technique. The probe had a radius of ~ 177 nm and R_G of 3 and its potential was held at -0.3 V *vs.* Ag/AgCl in order to drive the reduction of a solution of 10 mM $[Ru(NH_3)_6]Cl_3$ in aqueous 0.1 M KCl at the diffusion controlled rate. The substrate was unbiased.

2.3.5 Platinum Disk – Gold Ring Dual Microelectrodes

The preparation of the platinum disk-gold ring microelectrodes, as described in Section 2.2.6, is at this stage unsuccessful. The main problem arises from the mechanical-electrochemical stability of the insulator coating layer. Indeed, a perfect covering of the gold layer with insulating varnish was not achieved despite the several coating applications as the air-solution SECM approach curve indicated (results not shown). Besides, 0.5 μm thick SiO_2 film deposited on the top of the gold layer using plasma technique showed a very homogenous coverage but they were not mechanically stable (results not shown) during the polishing step.

2.4 Conclusions

This chapter described the details of the fabrication of platinum nanoelectrodes and gold microelectrodes using a micropipette puller. The main advantage of the method was the easy nature of the process once optimised parameters had been identified. The sealing and pulling steps were studied independently with particular attention to the materials used (glass kind, inner diameter of the capillaries, wire temper and size) and the laser puller parameters in relation to the final result. It was found that, despite the fact that the size of the electrodes could be controlled at some extent by the laser puller parameters (FILAMENT and PULL in particular), this control could be achieved more practically during the bevelling step. In fact, the wire dimension followed the changes in the glass structure and the sharpest changes occurred in correspondence of the tapers joint.

The results obtained with platinum were very significant and probes small as a few tens of nanometres could routinely prepared. Besides, this work enlightened that adjustments of the pulling parameters during the fabrication allowed achieving better yield of the successful pulled tips while in previous reports the latter was found not higher than 60 %.[13] However, the electrodes having radius smaller than 100 nm (~ 30 % of the total capillaries pulled) showed a lack of feedback in the SECM approach curves which did not allow to establish if these probes were recessed or not. The percentage of successful pulled probes for the overall fabrication ranging between 100

and 1000 nm was around 60 %. These tips were characterized by wide spectrum of techniques. Only with a synergic characterization by CVs of redox probes (possibly up to several Vs^{-1}), SECM approach curves and SEM imaging, it is possible to test the properties of electrodes with radius < 500 nm and unambiguously establish whether their behaviour is ideal or not. The platinum probes have smooth and long tapers with a lot of mechanical strength which makes them very attractive for SECM applications *e.g.*, higher resolution and limited damage occurring during crashes.[42] Indeed, in this work, a nanocavities array, prepared by nanosphere lithography, was employed as substrate and imaged in the SECM feedback mode by a ~ 200 nm platinum tip to prove the potential of these probes in this scanning probe technique.

The results obtained with gold UMEs were encouraging though electrodes with radius smaller than 500 nm could not be prepared. Indeed, it was possible to fabricate gold probes ranging between 0.5 and 5 μm with an overall yield of 60 - 70 % but only 10 % had submicrometer size. The procedure here presented could be an interesting option when experiment requiring gold microelectrodes are envisaged. It is possible that use of aluminosilicate capillaries with inner diameter of 0.3 mm could be helpful in the fabrication of probes with smaller dimensions.

It is important to note that surface roughness factors two orders of magnitude higher than values generally reported for polished metal electrodes, *i.e.*, 1.2 – 3, were observed for platinum electrodes with radius < 1 μm and for gold microelectrodes. However, the shape of the characteristic "fingerprint" peaks of platinum and gold improved with the scan rate and the apparent roughness factor decreased with the scan rate. It is highly improbable that this behaviour arose from an imperfect seal of the metal within the glass shield. Indeed, well established steady state of redox CVs, *i.e.*, flat branches, similar radius values determined from CVs, SECM and SEM analysis and finally the low capacitance values observed during chronoamperometric decay of the capacitive current disagreed with this hypothesis.

2.5 References

(1) Heinze, H. *Angew. Chem.* **1984**, *23*, 831.

(2) Pons, S.; Fleischmann, M. *Anal. Chem.* **1987**, *59*, A1391.

(3) Forster, R. J. *Chem. Soc. Rev.* **1994**, 289.

(4) Zoski, C. G. *Electroanalysis* **2002**, *14*, 1041.

(5) Arrigan, D. W. M. *Analyst* **2004**, *129*, 1157.

(6) Pendley, B. D.; Abruna, H. D. *Anal. Chem.* **1990**, *62*, 782.

(7) Shao, Y.; Mirkin, M. V. *Anal. Chem.* **1997**, *69*, 1627.

(8) Katemann, B. B.; Schuhmann, W. *Electroanalysis* **2002**, *14*, 22.

(9) Ufheil, J.; Borgwarth, K.; Heinze, J. *Anal. Chem.* **2002**, *74*, 1316.

(10) Ufheil, J.; Heb, C.; Borgwarth, K.; Heinze, J. *Phys. Chem. Chem. Phys.* **2005**, *7*, 3185.

(11) Liljeroth, P.; Johans, C.; Slevin, C. J.; Quinn, B. M.; Konturri, K. *Anal. Chem.* **2002**, *74*, 1972.

(12) Liljeroth, P.; Johans, C.; Slevin, C. J.; Quinn, B. M.; Konturri, K. *Electrochem. Comm.* **2002**, *4*, 67.

(13) Zoski, C. G., Ed.; In *Handbook of Electrochemistry*. Elsevier: Netherlands, 2007; , pp 935.

(14) Lefrou, C. *J. Electroanal. Chem.* **2006**, *592*, 103.

(15) Cornut, R.; Lefrou, C. *J. Electroanal. Chem.* **2007**, *604*, 91.

(16) Bard, A.J. and Mirkin, M.V., Ed.; In *Scanning Electrochemical Microscopy;* Marcel Dekker, Inc: United States of America, 2001; , pp 650.

(17) Forster, R. J.; Faulkner, L. R. *J. Am. Chem. Soc.* **1994**, *116*, 5444.

(18) Fletcher, S. *Electrochimica Acta* **1990**, *35*, 1797.

(19) Mallon, C. Interfacial Electroactive Assemblies: From Molecular Electronics to Biological Applications, Dublin City University, Dublin, 2008.

(20) Hu, H.; Xie, S.; Meng, X.; Jing, P.; Zhang, M.; Shen, L.; Zhu, Z.; Li, M.; Zhuang, Q.; Shao, Y. *Anal. Chem.* **2006**, *78*, 7034.

(21) Farrell, M. M. Electroanalysis in the Nanodomain: Quinone Monolayers and Nanometer Dimensioned Electrodes, Dublin City University, Dublin, 2003.

(22) Etienne, M.; Anderson, E. C.; Evans, S. R.; Schuhmann, W.; Fritsch, I. *Anal. Chem.* **2006**, *78*, 7317.

(23) Anicet, N.; Bourdillon, C.; Moiroux, J.; Saveant, J. *J. Phys. Chem. B* **1998**, *102*, 9844-9849.

(24) Fang, Y.; Leddy, J. *Anal. Chem.* **1995**, *67*, 1259.

(25) Ciani, I.; Daniele, S. *Anal. Chem.* **2004**, *76*, 6575.

(26) Bard, A. J.; Faulkner, L. R. In *Electrochemical Methods. Fundamentals and Applications.* Wiley Inc.: United States of America, 2001; , pp 833.

(27) Faulkner, L. R.; Walsh, M. R.; Xu, C. In *In New Instrumental Approaches to Fast Electrochemistry at Ultramicroelectrodes;* Contemporary Electroanalytical Chemistry; Plenum Press Div. Plenum Publishing Corp.: New York, 1990; , pp 5-14.

(28) Wipf, D. O.; Michael, A. C.; Wightman, R. M. *J. Electroanal. Chem.* **1989**, *269*, 15.

(29) Watkins, J. J.; Chen, J.; White, H. S.; Abruna, H. D.; Maisonhaute, E.; Amatore, C. *Anal. Chem.* **2003**, *75*, 3962.

(30) Aoki, K.; Chen, J.; Hua, Z. *J. Electroanal. Chem.* **2007**, *610*, 211-217.

(31) Sun, P.; Mirkin M.V. *Anal. Chem.* **2006**, *78*, 6526.

(32) Zoski, C. G.; Liu, B.; Bard, A. J. *Anal. Chem.* **2004**, *76*, 3646.

(33) Sun, P.; Mirkin, M. V. *J. Am. Chem. Soc.* **2008**, *130*, 8241-8250.

(34) Sun, P.; Mirkin, M. V. *Anal. Chem.* **2007**, *79*, 5809.

(35) Cadle, S. H.; Bruckenstein, S. *Anal. Chem.* **1974**, *46*, 16.

(36) Conway, B. E.; Tremiliosi-Filho, G.; Jerkiewicz, G. *J. Electroanal. Chem.* **1991**, *297*, 435.

(37) Alsabet, M.; Grden, M.; Jerkiewicz, G. *J. Electroanal. Chem.* **2006**, *589*, 120-127.

(38) Elliot, J. M.; Birkin, P. R.; Bartlett, P. N.; Attard, G. S. *Langmuir* **1999**, *15*, 7411.

(39) Jerkiewicz, G.; Vatankhah, G.; Lessard, J.; Soriaga, M. P.; Park, Y. *Electrochimica Acta* **2004**, *49*, 1451-1459.

(40) Katemann, B. B.; Schulte, A.; Schuhmann, W. *Electroanalysis* **2004**, *16*, 60.

(41) Sun, P.; Laforge, F. O.; Mirkin M.V. *Phys. Chem. Chem. Phys.* **2007**, *9*, 802.

(42) Mirkin, M. V.; Horrocks, B. R. *Anal. Chim. Acta* **2000**, 119.

Chapter 3

UME as Immunosensors

3.1 Introduction

Immunoassays offer a significant tool in the detection of a broad range of analytes and, thanks to the specificity of the immuno reactions between antibodies and antigens, these devices are highly sensitive and selective. Electrochemical immunoassays offer some advantages over the ones based on optical detection as the electrochemical process occurs at the electrode interface *i.e.*, ability to work with small, turbid and coloured samples.[1] This chapter investigates a transducing principle for an electrochemical immunosensor which is based on the change of the redox steady state current at a microelectrode as shown in Figure 3.1. Indeed, in this figure the microsphere and the microelectrode are labelled with primary and secondary antibodies pair. The UME is immersed in a solution containing a redox mediator and the potential is held in order to drive the oxidation or reduction of the latter at the diffusion controlled rate *i.e.*, steady state current. The primary antibodies immobilized at the electrode surface capture antigen present in the solution. Then, the secondary antibodies labelled microspheres are added to the solution and these bind to the antigen. The particle shields the electrode reducing the mass transport of the redox mediator towards its surface which causes a drop in the steady state current.[1] Thus, the presence of the analyte in the sample is amplified through the binding of the sphere on the electrode surface and transduced in a current signal. The principle of this immunosensor was proposed by Gorschluter and co-workers[1] but the authors did not show any experimental result of an immunosensor based on this principle. In fact, these authors studied only the change of the steady state current at a microelectrode array induced by physical settling of microspheres on the array surface. They also suggested that only one sphere was responsible for the current drop at a single microelectrode under their experimental conditions. Mak and co-workers[2] used the same principle in order to measure binding forces between bovine serum albumin (BSA) and Anti-BSA. It was noticed in this reference that the injection of Anti-BSA labelled spheres could produce a drop in the steady state current which differed up to a factor two between microelectrodes.[2] The variations in the diameter of the electrodes or the spheres were unlikely to be responsible for these differences. However, the authors did not give any reason for the discrepancy.

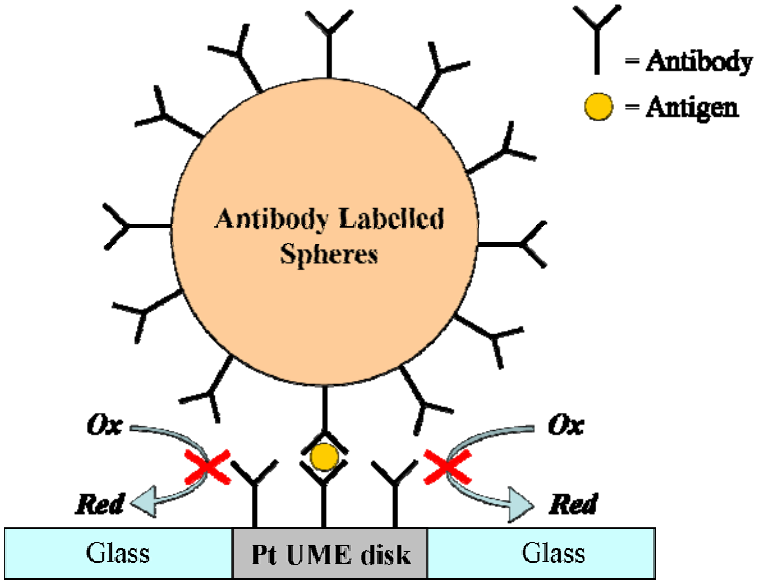

Figure 3.1 Sketch of an immunoassay in order to detect a specific antigen in a sample. The immunoassay uses the steady state current produced by the reduction of a redox mediator at the microelectrode as transducing principle. Indeed, the microelectrode and the microsphere are labelled with primary and secondary antibodies pair. In the presence of the opportune antigen, the sphere binds to the electrode surface and its shielding effect affects the diffusion profile of the redox species. The drop in the steady state current corresponds then to a detection of antigen in the solution.

There are several points which have not been fully investigated. Firstly, the assumption that only one single microsphere affects the diffusion profile of the redox species undergoing a chemical reaction at the microelectrode and consequently the UME steady state value. Secondly, though Gorschluter and co-workers[1,2] argued that electrophoretic transport of the beads might play a significant role, no direct proof was given. Finally, these authors have noticed that the ratio between the spheres and the electrode size should control the amount of the current drop but the hypothesis was not investigated. These three key points are addressed in Section 3.3.1 and their understanding is of fundamental importance in the development of the final immunosensor. In Section 3.3.2, human immunoglobulin G (hIgG) coated microelectrodes and anti-hIgG labelled latex microspheres were employed as model of the immunosensor in Figure 3.1 to evaluate its feasibility. Indeed, hIgG is the most abundant immunoglobulin in humans and it has been considered as model protein in several studies for the development of immunosensors.[3-6]

3.2 Experimental

3.2.1 Chemicals, Materials and Equipment

Silica (1, 4, 12 μm in diameter), NH_2-coated silica (1, 4, 12 μm in diameter), goat anti-hIgG-coated polystyrene (7.4 μm in diameter) microspheres were purchased from Kisker-Biotech. Human immunoglobulin G from human serum (> 95 %), phosphate buffered saline tablets (pH = 7.2), ferrocenemethanol (97 %), sulphuric acid (99,999%), Tween® 80, albumin from bovine serum (> 98 %) were purchased from Sigma-Aldrich while ruthenium hexamine chloride (98%) was from Strem Chemicals. All the chemicals were used as received. All the aqueous solutions were prepared from Milli-Q reagent water (Millipore Corp.), 18 MΩ cm.

A submarine UME cell configuration was chosen to facilitate the settling of the microspheres on the electrode surface. Figure 3.2 shows the two cells which were employed in this work in order to check the effects of cell geometry on the experiments. Cell 1 is 0.7 mm deep and has a diameter of 1.6 cm, while Cell 2 is 3 cm deep and has a diameter of 0.5 cm. The electrode was positioned at the bottom of the Teflon cylinder through a suitable O-ring seal. A platinum wire was employed as the counter electrode and custom-made Ag/AgCl (saturated KCl) as reference electrode (~ -0.045 V *vs.* SCE). All the electrochemical measurements were run using the 900a CH-instruments potentiostat.

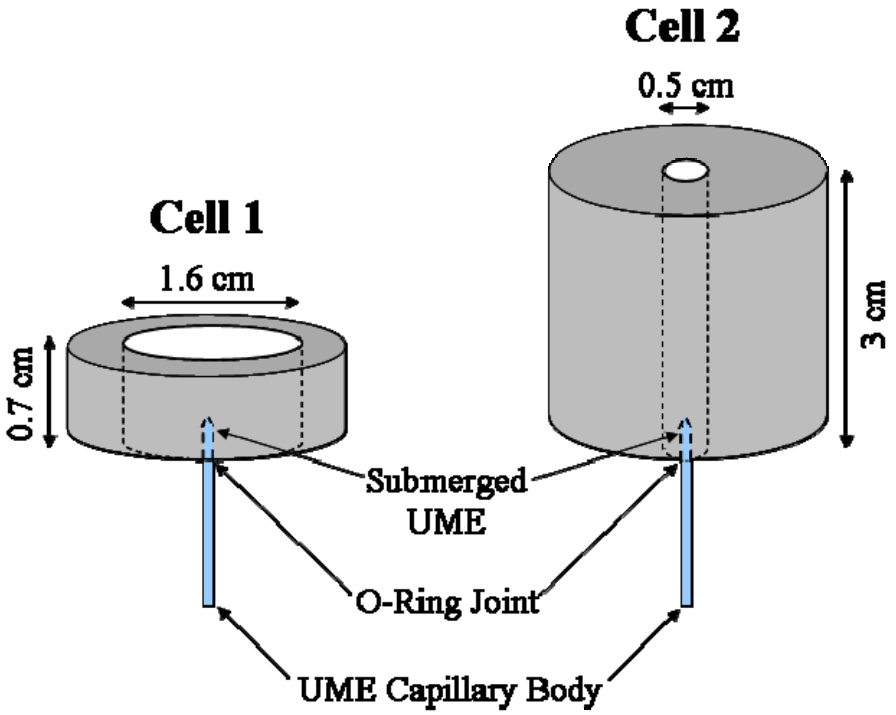

Figure 3.2 Sketch of the two inverted cells employed in this chapter. The inverted design helps the settling of the microspheres on the top of the microelectrode which was fixed at the bottom of the cell by an O-ring.

3.2.2 Experimental Procedures

The UMEs were hand polished prior to each experiment as described in Section 2.3.3.3. The electrode size was determined using Equation 1.14 from the steady-state current of a voltammogram run at 2 mVs^{-1} using a suitable redox mediator. In some cases, Scanning Electron Microscopy was also employed in order to confirm the data and to image the effectiveness of the polishing step *i.e.*, seal and roughness of the UME. All the microspheres stock solution were vortexed for a minute, then sonicated for 5 minutes prior to every experiment. If not otherwise stated, the size of the microspheres and electrodes is given as the diameter.

In the experiments described in Section 3.3.1.1, the probe was immersed in a solution of the mediator and the potential stepped in order to drive the reaction at the diffusion controlled rate. Then, a precise volume of stock solution of the microspheres was injected into the cell, just above the microelectrode, and their effect on the steady state

current was recorded. In this approach, the amount of stock solution to be added was controlled as to achieve a hexagonal closed packed monolayer of spheres taking the cell cross sectional area into account *i.e.*, disk with a diameter of 1.6 cm and 0.5 cm respectively for Cell 1 and 2.

In the experiments described in Sections 3.3.1.2 and 3.3.2, a precise volume of stock solution was added to a much larger volume of the mediator solution (concentration essentially unchanged). The solution was vortexed for a minute, sonicated for 5 minutes and finally poured into the electrochemical cell. Then, only at this moment, the potential was stepped in order to drive the redox reaction at the diffusion controlled rate. As the tip of the electrode is protruding for ~ 2 mm from the bottom of the cell, in this case only the volume of solution above the microelectrode tip was taken in account for the calculation of the equivalent monolayers. The spheres should settle as shown in Figure 3.3, covering the bottom of the cell and the electrode tip depending on the characteristic settling velocity. The density of the spheres present in a hexagonal closed packed monolayer is equal to 0.907.[7]

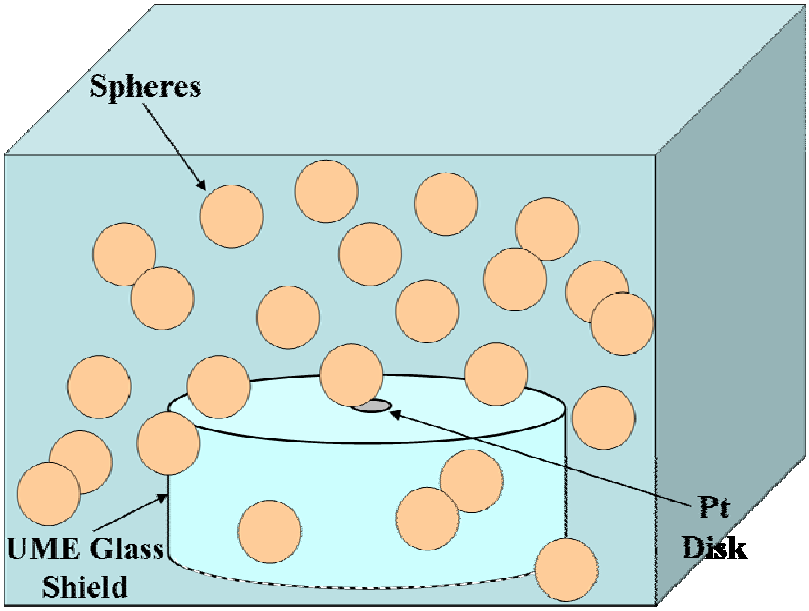

Figure 3.3 Sketch of the dynamic settling of the spheres on the UME surface. In this image, the platinum disk is partially covered by a sphere which then shields the diffusion of the redox mediator towards the metal surface. The image is not fully to scale.

3.2.3 Physioadsorption of Human Immunoglobulin G

The electrode was dipped overnight in a 10 μg mL^{-1} hIgG solution in PBS buffer at 4 °C. After that it was rinsed with deionised water. Quartz Crystal Microbalance studies showed that the protein adsorption is a rather fast and irreversible process and that concentration of hIgG approximately of 10 μg mL^{-1} assures a fully covered monolayer though an uncertainty regarding the protein "end on" or "flat on" orientation.[5] Besides, studies of the physioadsorption of hIgG on hydrophilic silica by infrared spectrometry showed that the secondary structure of the adsorbed protein is relatively similar to its conformation in solution.[6] Alternatively, another protocol was followed. In fact, after the hIgG physioadsorption step, the microelectrode was rinsed with phosphate buffer solution and left in a 1% BSA/PBS solution for 1 hour. Then, it was copiously washed with a 5% Tween® /PBS solution and ready to be used. BSA and Tween® 80 have been employed as blocking layers to backfill surfaces modified with a primary antibody and decrease the extent of the non specific binding in sandwich immunoassays.[8,9]

3.3 Results and Discussion

3.3.1 Physical Settling of Microspheres

3.3.1.1 Spheres Injection during the Amperometric Measurement

In this arrangement, an amount of spheres necessary to form a hexagonal close packed monolayer all over the section area of the electrochemical cell was injected. To achieve monolayer formation, the drop should spread, settle and completely cover the area of the cell. However, the hydrodynamics of a drop falling and mixing into a steady solution cannot be easily described. Indeed, the drop falls very rapidly reaching the bottom of the cell in few seconds.

Figures 3.4 and 3.5 shows the results obtained injecting a monolayer of the spheres or multiple of this in Cell 1 while ferrocenemethanol is oxidised at the electrode and the current monitored. Silica microspheres of three different sizes were used, precisely 1 and 4 μm in Figure 3.4 and 12 μm in Figure 3.5. Some conclusions can be drawn. In the first moments that followed the injection, an induced stirring of the solution

disturbed the current signal. A decrease in the steady-state current in all cases supports the idea that some of the spheres settled and covered the electrode surface. However, it was not possible to detect the exact moment of the arrival of the sphere/s on the top of the metal disk and understand how much a single particle contributed to the decrease of the current. In Figure 3.4A the decrease of the current after the injection of 1 μm spheres was progressive till it reaches a steady value (~ 300 seconds) while in Figure 3.5A, after the injection of 12 μm spheres, the decrease was step-like and almost instantaneous. This result indicates that the shielding of the mass transport of the ferrocenemethanol towards the electrode depends on the sphere size. Further addition of stock solution, independently from the sphere size, contributed to an additional decrease of the current. Indeed, the maximum current drop was observed with the 12 μm silica sphere *i.e.*, ~ 60 % of the initial steady state current upon injection of 7 equivalent monolayers of spheres. Finally, it is significant that the particle charge appeared to influence the microspheres settling on the metal surface. Indeed, in Figure 3.5B NH_2-coated beads were injected and the current does not diminish beyond the value achieved after the first monolayer addition which differs from what observed in Figure 3.5A for the 12 μm uncoated silica spheres. This behaviour might arise from the repulsion between the spheres because of the higher charge density. Though the zeta potential of the beads could not be determined, the NH_2-groups density in these beads is 3.3×10^{-16} mol/particle and the pK_a of the primary amine coating is between 9.5 and 10 as stated by the manufacturer. Thus, the total charge must be then $< 3.2 \times 10^{-11}$ C.

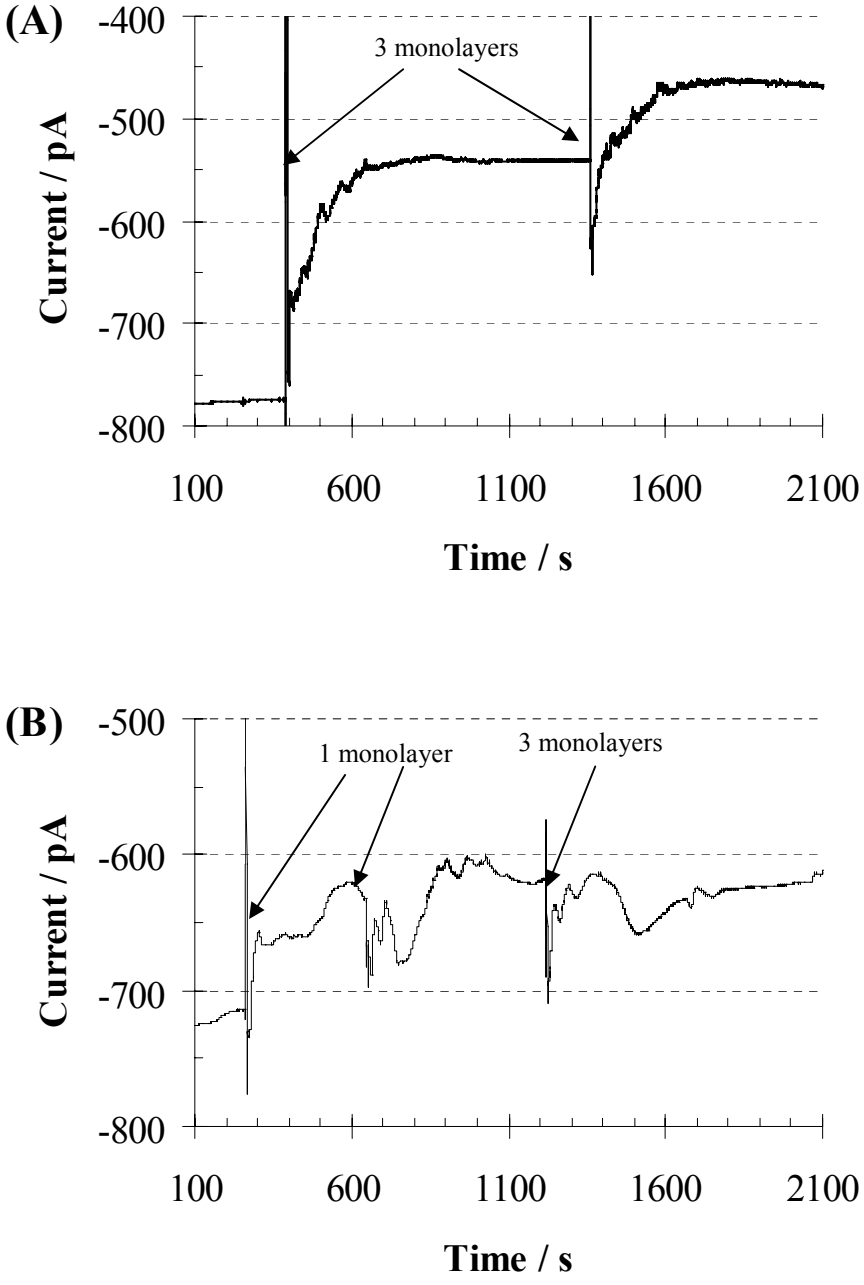

Figure 3.4 Amperometric profiles at (A) a 4.6 μm microelectrode upon 1 μm Si spheres injection and (B) a 4.2 μm microelectrode upon 4 μm Si spheres injection. The electrochemical cell contained 1 mM FcMeOH in aqueous 0.1 M KCl. The amount of microspheres is labelled in each figure and the moment of their injection is indicated by arrows. The potential was held at +0.4 V *vs.* Ag/AgCl in both figures. Cell 1 was employed.

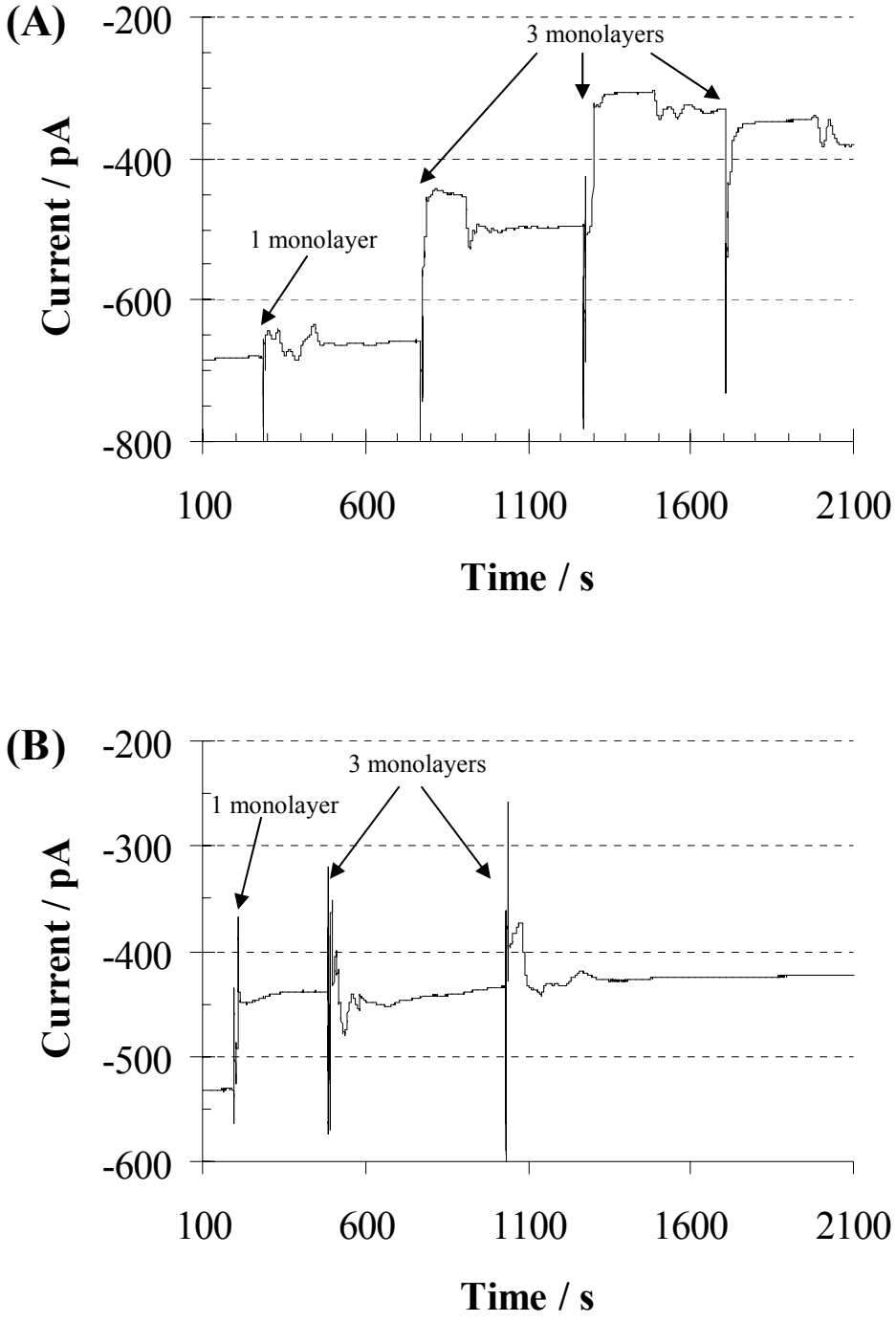

Figure 3.5 Amperometric profiles at (A) a 4.2 μm microelectrode upon 12 μm Si spheres injection and (B) a 3.8 μm microelectrode upon 12 μm NH_2-coated Si spheres injection. The electrochemical cell contained 1 mM FcMeOH in aqueous 0.1 M KCl. The amount of microspheres is labelled in each figure and the moment of their injection is indicated by arrows. The potential was held at +0.4 V *vs.* Ag/AgCl in both figures. Cell 1 was employed.

It is very hard to explain and to compare the results of this section because of the degree of irreproducibility of the experiments *e.g.*, hydrodynamics of the drop mixing into the solution, irreproducibility of the injection itself, different volumes of the stock solutions injected depending on the sphere size. Cell 2 was designed in order to slow down the dispersion due to the initial injection and promote a dense monolayer formation. However, it did not solve these problems and similar results to Cell 1 were obtained. The conclusions in this experimental section are limited to a qualitative level but do demonstrate the feasibility of using electrode blocking by the beads to determine analyte concentrations.

3.3.1.2 Effect of Spheres Concentration on the Current Response

In this section the microspheres stock solution was mixed to the solution of the redox probe, and then, after the vortixing and sonicating the mixture, the latter was poured into the electrochemical cell and the experiment started. Despite settling is a random process, this approach helps to minimize the degrees of freedom of the system, and facilitates the comparison of the results. In fact, apart from the cell design, the only variable in the experiments is the settling velocity which depends on the size and density of the microspheres. The settling velocity, v_s, can be calculated according to Equation 3.1:[10]

$$v_s = 5.448 \times 10^{-5} (\rho_s - 1) d_s^2 \qquad (3.1)$$

where ρ_s and d_s are the density and the diameter of the solid beads. Table 3.1 reports the values of the settling velocity for the microspheres employed in this work. The complete settling of the spheres during the experimental time window depends on the height of solution above the electrode and this is the reason why the cell geometry might affect the results.

In reference [1], as only one step-like drop in the current at the microelectrode was mainly observed, despite several injections of spheres, it was concluded that the decrease in the current had to be associated with only one sphere settling on the electrode surface. However, in the experimental conditions of this work it is important to understand whether the spheres have completely settled or not to avoid

misinterpretation of the results. Indeed, the effect of a second sphere on the redox species mass transport may not be seen simply because a significant fraction of the spheres are still suspended in the solution.

Table 3.1 Values of the settling velocity calculated for each sphere size and type according to Equation 3.1. The last two rows represent the (vertical) distance that the spheres travel in 0.5 hours, which was the typical experimental time window.

Sphere Type	**Silica**			**Polystyrene**
Sphere Diameter / μm	1	4	12	7.4
v_s / μms^{-1}	0.5	8.7	78	1.2
Time* / min	153	10	1	70
Time$^{\#}$ / min	857	54	6	391

*Time necessary for a sphere to travel a distance equal to 5 mm. #Time necessary for a sphere to travel a distance of 2.8 cm.

As the settling process governs the arrival of the sphere/s on the metal disk, the concentration of the microspheres can be lowered to the point where statistically only one sphere settles in a given time on the electrode surface. Indeed, the aim of this section is to control the extent of the current decrease due to a particle by modulating the ratio between the sphere and the microelectrode size. Finally, the role that the electrophoretic effects may play on the current drop was also investigated.

Figures 3.6 and 3.7 show the typical amperometric profile for 1 mM FcMeOH/0.1 M KCl solution in the presence of 1 μm silica spheres employing Cell 1. In Figure 3.6A and 3.6B the concentration of the spheres above the metal disk was possibly too high (10 and 1 equivalent monolayer, respectively) and the settling of individual particles might not be time resolved. This hypothesis might explain why no clear step-like decrease can be seen. In Figure 3.7, with the lowest content of 1 μm Si-spheres, step-like jumps in the current of ~ 1 - 2 pA are apparent. The step-like drop is evaluated using the following expression:

$$\frac{\Delta i}{i_i}(\%) = 100 \times \frac{\left|i_f - i_i\right|}{\left|i_i\right|} \qquad (3.2)$$

where i_f and i_i are respectively the current at the end and begin of the jump and Δi is the difference between them. As Δi and i_i are both proportional to the mediator concentration their ratio is independent. In Figure 3.7, the $\Delta i/i_i$ of a single step-like drop is ~ 0.18 - 0.36 %. Considering an electrode with diameter of ~ 4 μm, then ~ 15 of 1 μm beads are necessary to have a hexagonal closed packed monolayer on such area. Every time the particle settles on the metal surface, the current is expected to drop instantaneously to a lower steady state value because part of the electrode surface is now blocked. Then 15 step-like jumps should be seen in Figure 3.7. However, from Table 3.1 it follows that not all the spheres above the electrode had settled in the experimental time window and that might explain the difference.

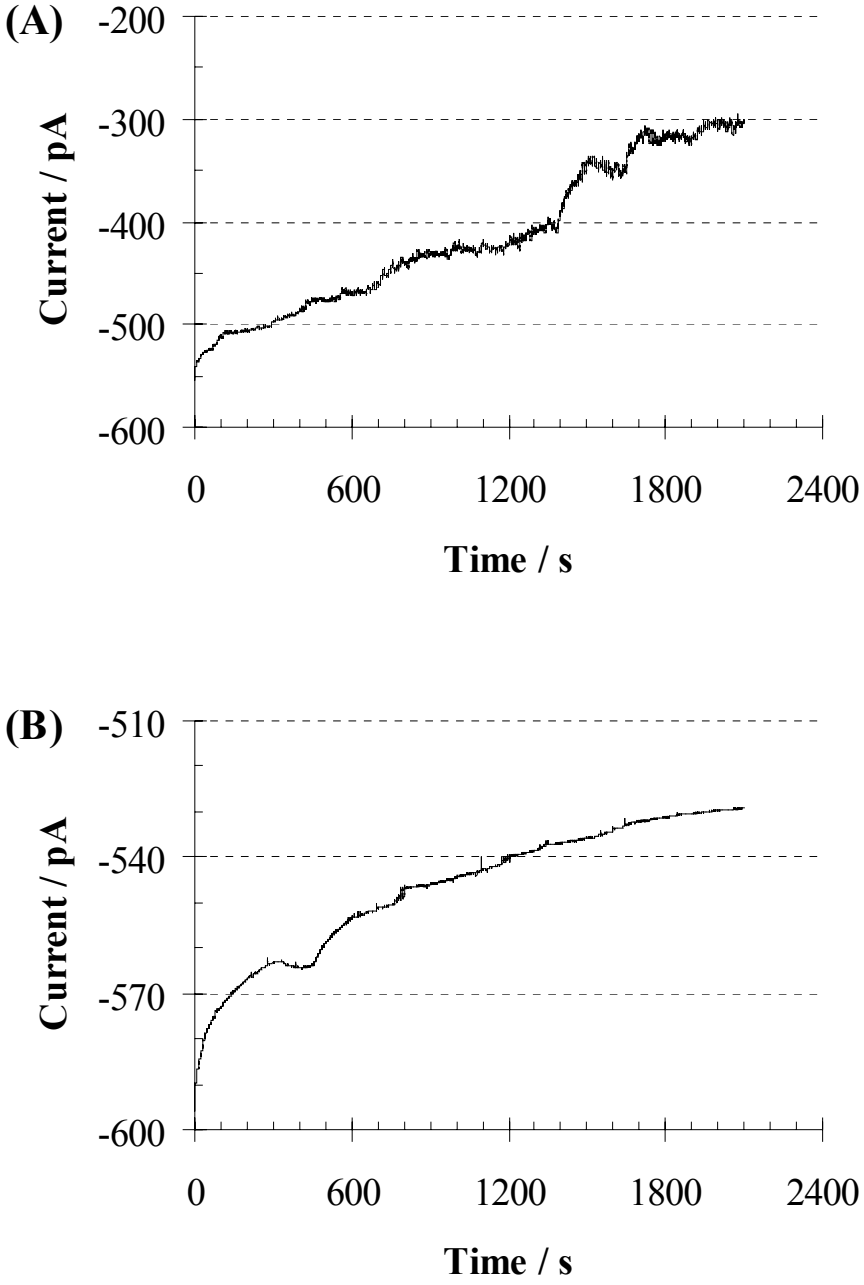

Figure 3.6 Effect of the settling of 1 μm silica beads on a microelectrode. Amperometric profile at (A) a 4.4 μm microelectrode; $C_{spheres}$ = 2.4 × 10^9 mL^{-1} (equivalent to 10 monolayer) and at (B) a 4.6 μm microelectrode; $C_{spheres}$ = 2.4 × 10^8 mL^{-1} (equivalent to 1 monolayer). Potential was held at +0.4 V *vs.* Ag/AgCl in order to oxidise 1 mM FcMeOH in aqueous 0.1 M KCl at the diffusion controlled rate. Cell 1 was employed.

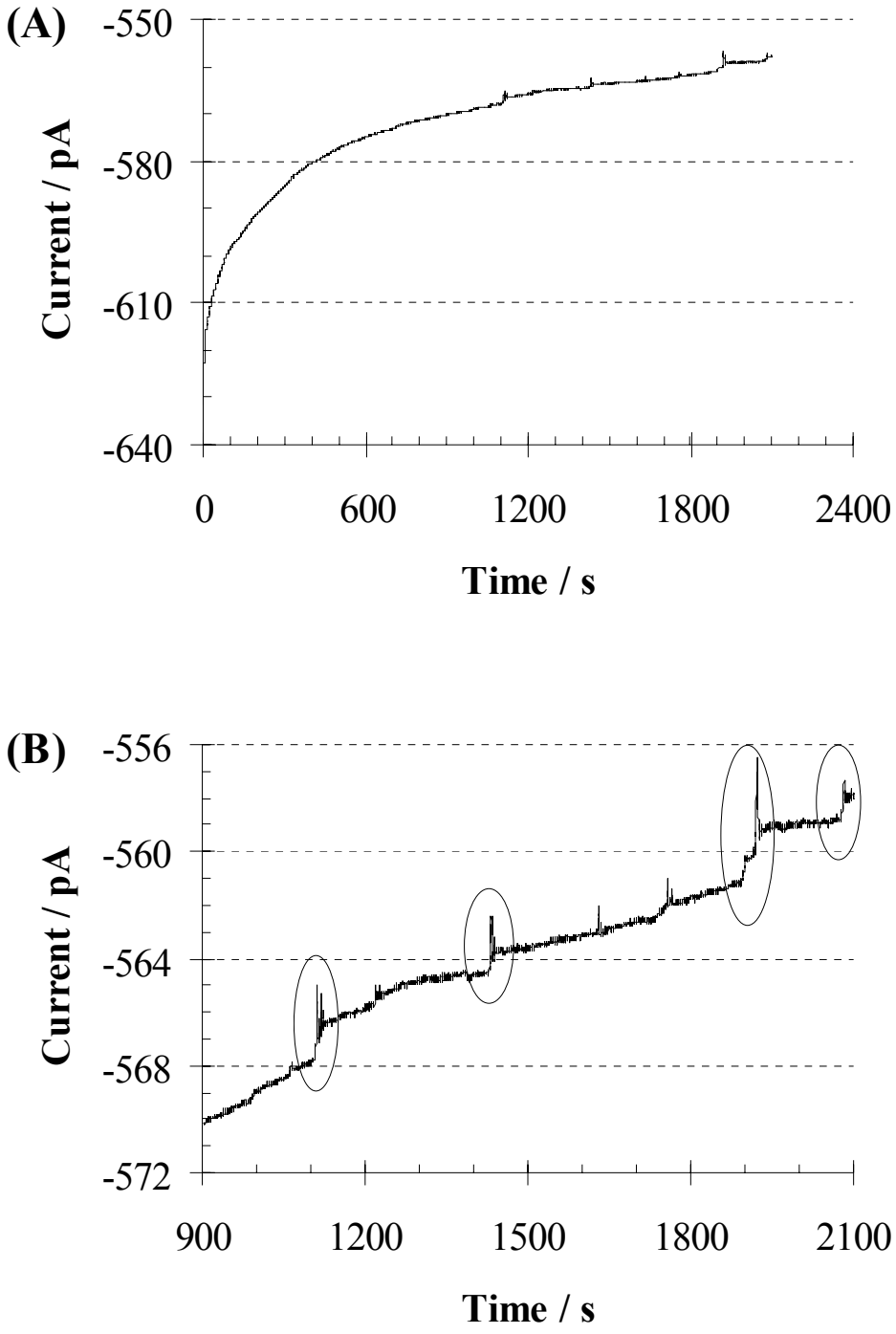

Figure 3.7 Effect of the settling of 1 μm silica beads on a microelectrode. Amperometric profile at (A) a 4.6 μm microelectrode; $C_{spheres}$ = 1.2 × 10^8 mL^{-1} (equivalent to 0.5 monolayer) and (B) expansion of the current in (A). The main step-like drops in the current are indentified in the figure with circles. The potential was held at +0.4 V *vs.* Ag/AgCl to oxidise 1 mM FcMeOH in aqueous 0.1 M KCl at the diffusion controlled rate. Cell 1 was employed.

The results for the settling of 4 μm silica beads are reported in Figures 3.8 and 3.9. Step-like drops in the current can be noticed and are indentified with circles in Figure 3.8. The Δi values are ~ 2 - 5 pA, which is slightly bigger (factor 2 – 3) than when 1 μm silica spheres were employed. The latter behaviour agrees with the idea that a larger object on the microelectrode surface shields mass transport of a species diffusing towards the electrode to a greater extent and then causes a larger drop of the current. Figure 3.10 illustrates this simple physical principle.

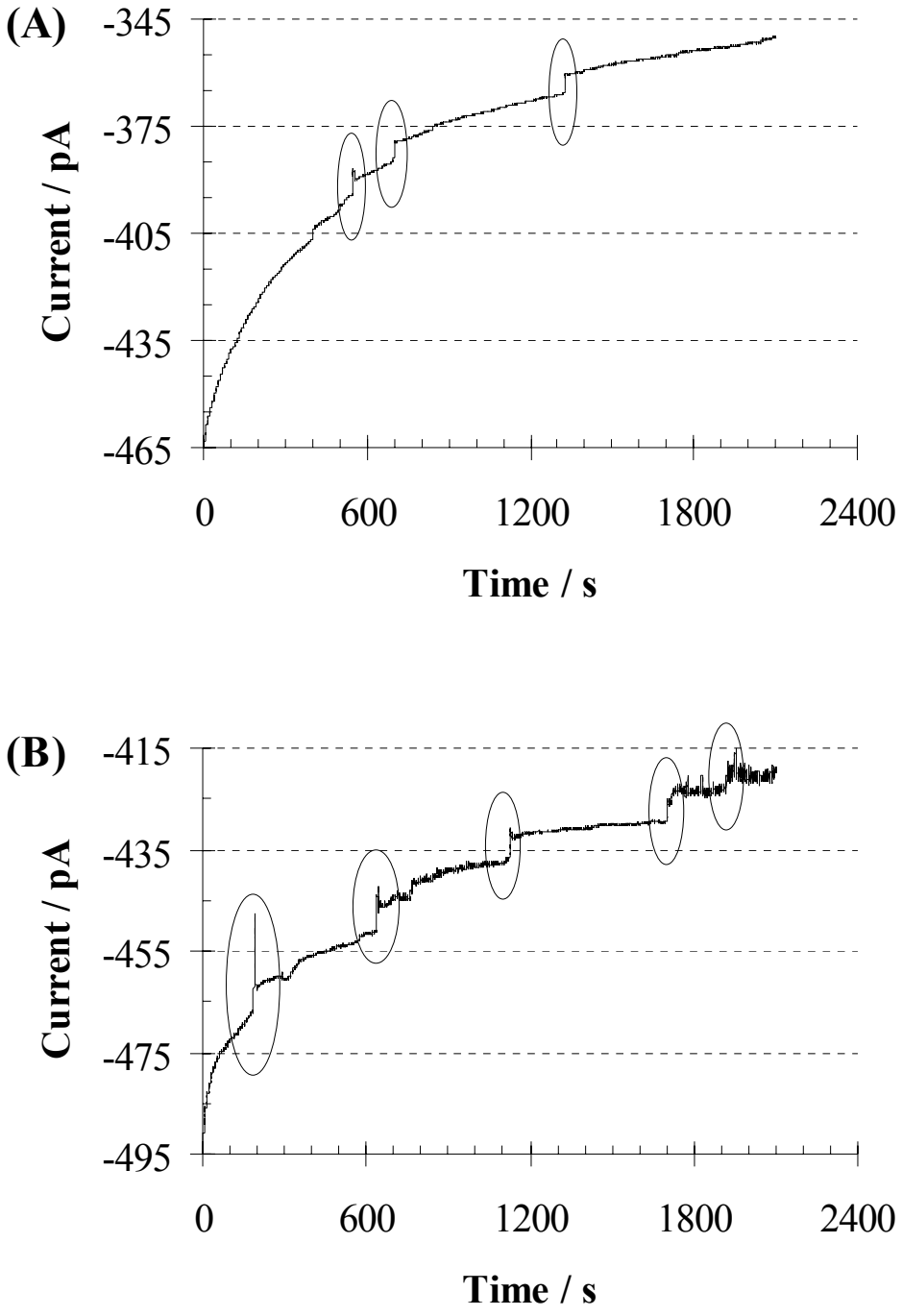

Figure 3.8 Effect of the settling of 4 μm silica beads on a microelectrode. Amperometric profile at (A) a 3.6 μm microelectrode; $C_{spheres}$ = 1.4 × 10^7 mL^{-1} (equivalent to 1 monolayer) and (B) a 3.8 μm microelectrode; $C_{spheres}$ = 7.1 × 10^6 mL^{-1} (equivalent to 0.5 monolayer). In the figures the main step-like drops in the current are identified with circles. The potential was held at +0.4 V *vs.* Ag/AgCl to oxidise 1 mM FcMeOH in aqueous 0.1 M KCl at the diffusion controlled rate. Cell 1 was employed.

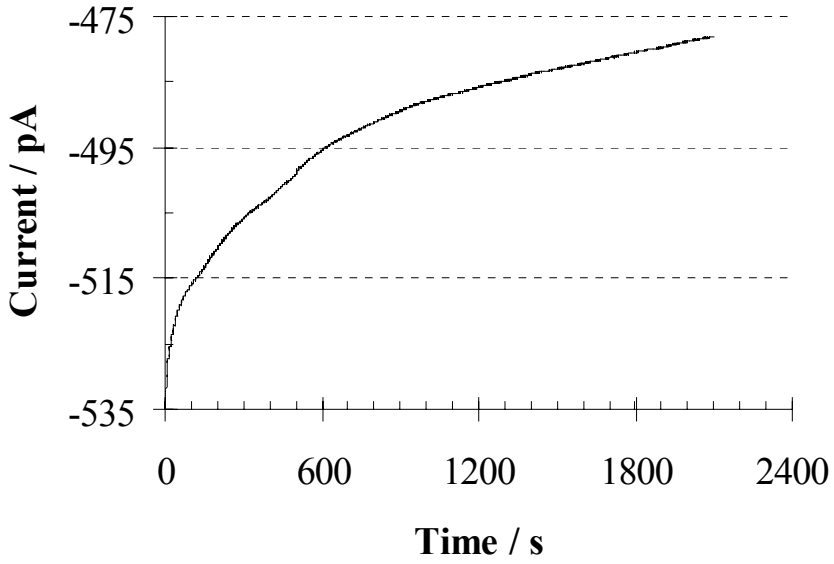

Figure 3.9 Effect of the settling of 4 μm silica beads on a microelectrode. Amperometric profile at (A) a 3.8 μm microelectrode; $C_{spheres}$ = 1.4 × 10^6 mL^{-1} (equivalent to 0.1 monolayer). Potential was held at +0.4 V *vs.* Ag/AgCl to oxidise 1 mM FcMeOH in aqueous 0.1 M KCl at the diffusion controlled rate. Cell 1 was employed.

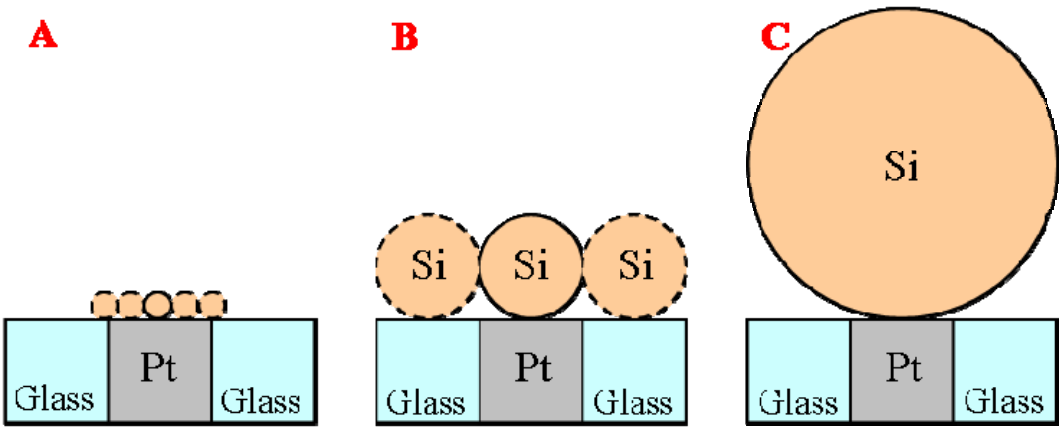

Figure 3.10 Sketch of the microsphere/s ideally settled on the top of the electrode surface. Sphere/electrode ratio: (A) 1 : 4, (B) 1 : 1, (C) 3 : 1. The Si label indicates the silica beads, while Pt correspond to the platinum microelectrode sealed in a glass shield. The images are not fully to scale.

From Figure 3.10B, it is apparent that a single sphere sitting in the middle of the metal disk does not physically leave any room for a second when the ratio between the size of the particle and the electrode is 1. Then only a single major step-like drop in the steady state current is expected but Figure 3.8 shows multiple step-like jumps. This behaviour agrees with the fact that the spheres packing on the side of the perfect centred one interfere with the diffusion profile of the electrode. Indeed, in SECM it is well known that the substrate starts interacting with the diffusion profile at the probe when the distance between the two is ~ 10 tip radii. In addition, it is unlikely that a microsphere settles exactly in the middle of the metal disk. Figure 3.11 depicts two alternative scenarios with the sphere/electrode size ratio (R_{SE}) equal to 1 where more than one sphere is responsible for the partial covering of the electrode surface. For instance, in Figures 3.11A, because each of the three spheres covers a projected area ~ 33 % of the metal disk, three major step-like drops in the steady state current can be expected.

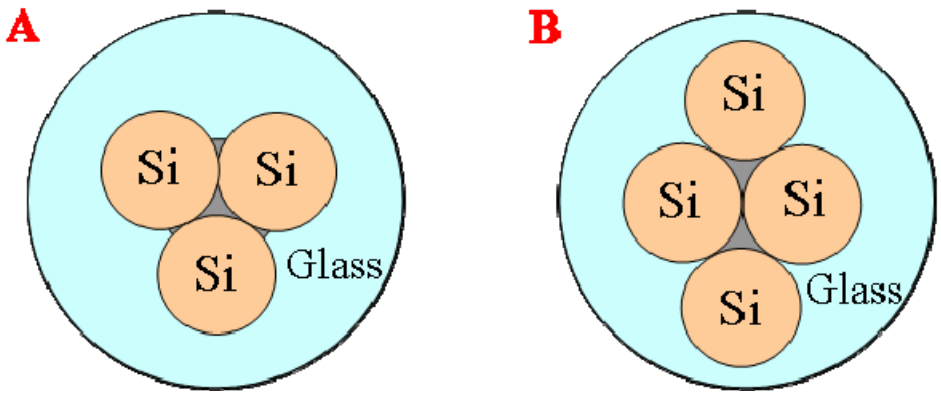

Figure 3.11 Two possible configuration for the packing of microspheres on the top of the electrode when the ratio of sphere/electrode size is 1. The Si label indicates the silica spheres while the platinum microelectrode is partially covered by the beads. The images are not fully to scale.

Table 3.2 reports the $\Delta i/i_i$ values associated with the step-like jumps of the current in Figure 3.8 due to the settling of 1 and 0.5 monolayers of 4 μm silica spheres. All the 4 μm spheres should settle in 10 minutes according to Table 3.1. However, some of the step-like jumps in Figure 3.8 occured later than this time. This might be explained by an underestimation of the settling time from Equation 3.1 or could be due to the lateral displacement/re-adjustment of spheres "captured" on the electrode surface. In Figure 3.9 the concentration of beads was probably too low because no step-like drop in the

amperometric profile is visible. The results obtained for the settling of 4 μm silica spheres are significantly different from the conclusions reported by Gorschluter and co-workers[1] who employed electrodes and spheres with similar diameter *i.e.*, 3.2 μm and 2.8 μm, respectively. In fact, in this reference, despite the ratio between microelectrode and particle size being ~ 1, only a single step-like jump in the recorded current is observed. Besides, the average $\Delta i/i_i$ associated to the latter was ~ 40 % of the initial steady state current. The assumption in this reference that the step-like drop is due only to a single sphere has already been criticized above in the text. However, it should be noticed that the authors employed recessed (~ 250 nm) microelectrodes which might explain the larger $\Delta i/i_i$ as the recess could be somehow tailored to host the sphere. The particles used in this reference also have a magnetic core and their density might be larger than the silica ones employed in this work.

Table 3.2 Values of Δi and $\Delta i/i_i$ calculated from the step-like drops in Figures 3.8A and 3.8B, corresponding respectively to the effect of 1 and 0.5 monolayer of 4 μm microspheres on the amperometric current monitored at 3.6 μm and 3.8 μm platinum electrodes. The electrode potential was held at +0.4 V *vs.* Ag/AgCl to drive the oxidation of 1 mM FcMeOH in aqueous 0.1 M KCl at its diffusion controlled rate. Cell 1 was employed.

4 μm silica spheres settling				
1 monolayer		**0.5 monolayer**		
Δi (pA)	**$\Delta i/i_i$ (%)**	**Δi (pA)**	**$\Delta i/i_i$ (%)**	
3	0.74	5	1.07	
4	1.02	4	0.89	
5	1.30	3	0.67	
5	1.37	5	1.14	
/	/	5	1.17	
/	/	1	0.24	
17	4.43	23	5.18	**Tot.**

It is apparent from the previous figures that the achievement of a steady state in the current is significantly slow *i.e.*, the current tends to decrease with the time. Now, for a 3 μm (radius) electrode, like the ones employed in this chapter, the achievement of the 99 % of the steady state is expected in ~ 6 seconds.[11,12] Taking Figure 3.9 as example for this calculation, it follows that the current for times longer than 6 seconds should not decrease more than 1 % of the value reached at that time. However, considering that the ratio $(i_{t=2100} - i_{t=6})/i_{t=2100}$ is > 10 % it must be concluded that under the experimental circumstances there was a delay in achieving the steady state because the cottrelian decay was slower than the theoretical value. The criteria employed in the temporal determination of the steady state condition at an electrode apply only when diffusion is the only mean of transport for the molecules. However, as the particles settle, they may interfere with the diffusion profile of the redox mediator at the electrode. In reality, the amperometric profile recorded during the oxidation or reduction of the redox mediator at the diffusion controlled rate without particle settling was in some cases affected by a similar drift in the current. The origin of this drift is not fully understood but, it might arise from a passivation of the electrode because the absolute value of the current always decreased.

Figure 3.12 shows the results obtained employing concentration of the 12 μm silica beads that yielded submonolayer coverage. (The result employing 1 monolayer of 12 μm Si spheres is not reported as the fast settling of the spheres did not allow resolving the step-like jumps occurring at the very beginning of the amperometric measurement). From this figure it is apparent that the moment of the sphere arrival was shorter than with 1 and 4 μm beads. The faster arrival on the electrode surface agrees with the larger settling velocities of the 12 μm spheres. The small step-like jumps indicated by circles in Figure 3.12A possibly arose from position adjustment of the settled spheres on the metal surface or from the effect of new arriving particles on the diffusion profile. However, the submonolayer concentration of the spheres in this experiment supports the former hypothesis. In Figure 3.12A two main step-like drops in the current are apparent and possibly correspond to a configuration similar to what depicted in Figure 3.13A. Moreover, a lower number of beads should be responsible for the major blocking of the diffusion of the redox mediator towards the electrode surface when the ratio of the sphere/electrode size is larger as evident comparing Figure 3.11 and 3.13.

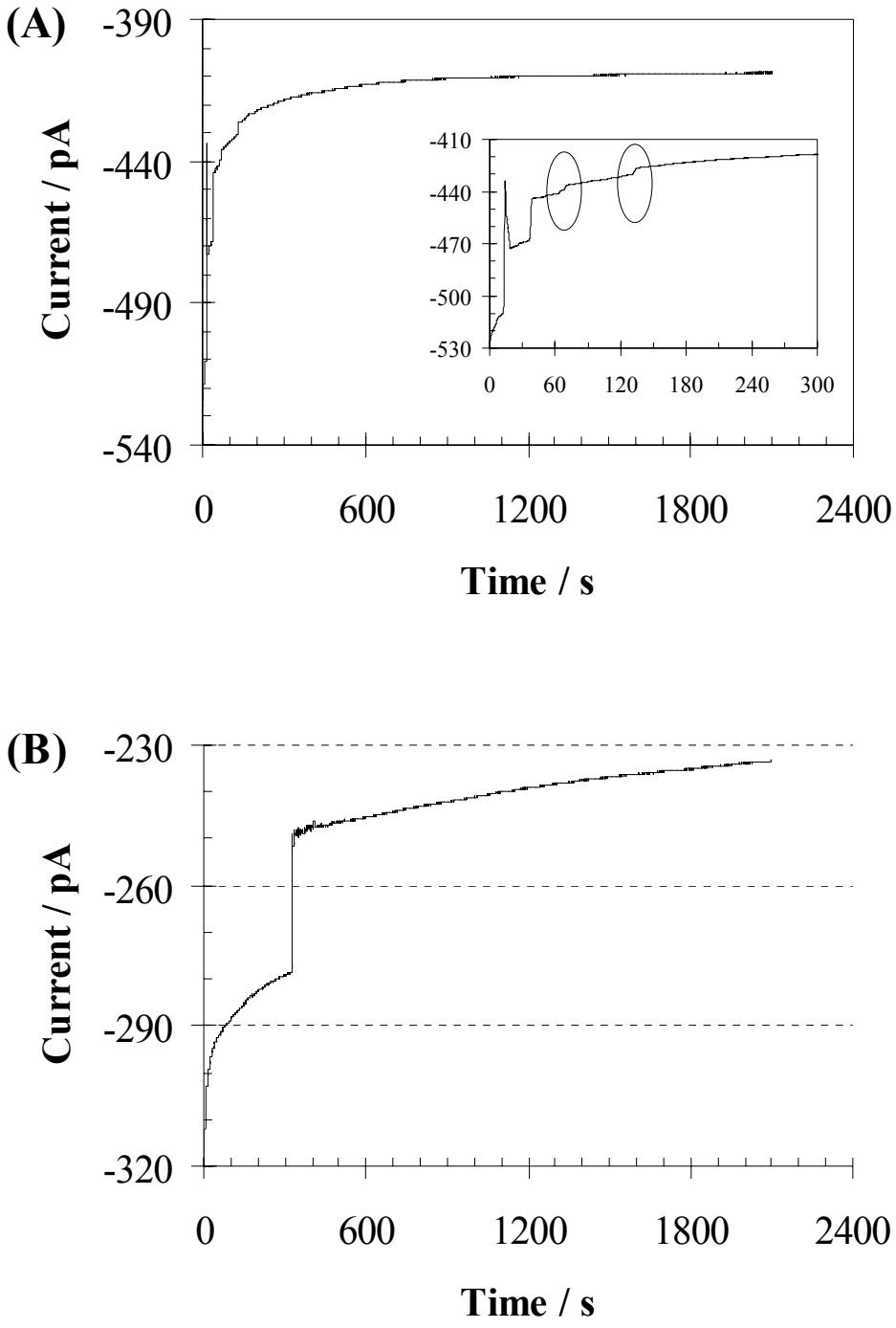

Figure 3.12 Effect of the settling of 12 μm silica beads on a microelectrode surface. Amperometric profile at (A) a 4.0 μm microelectrode; $C_{spheres} = 8 \times 10^5$ mL^{-1} (equivalent to 0.5 monolayer) and (B) a 2.2 μm UME; $C_{spheres} = 1.6 \times 10^5$ mL^{-1} (equivalent to 0.1 monolayer). Potential was held at +0.4 V *vs.* Ag/AgCl to oxidise 1 mM FcMeOH in aqueous 0.1 M KCl at the diffusion controlled rate. Cell 1 was employed.

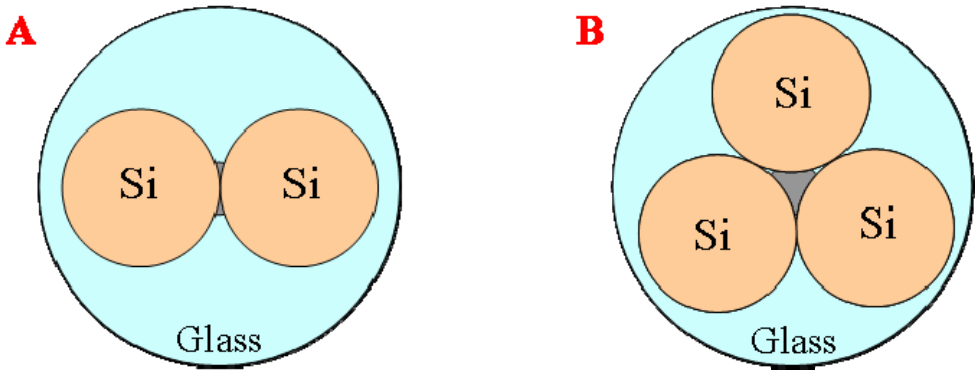

Figure 3.13 Two possible configuration for the packing of microspheres on the top of the electrode when $R_{SE} = 3$. The Si label indicates the silica spheres while the platinum microelectrode is partially covered by the spheres. The images are not fully to scale.

Table 3.3 reports the values of $\Delta i/i_i$ associated with the step-like jumps of the current shown in Figure 3.12 upon settling of 0.5 and 0.1 monolayers of 12 μm silica spheres. The $\Delta i/i_i$ values are larger than what observed with 1 and 4 μm spheres which agrees with the conclusions presented above, *i.e.*, a larger object sitting on the electrode surface blocks the diffusion of the species undergoing an electrochemical reaction to a greater extent. Two major step-like jumps are apparent in Figure 3.12A while only one in Figure 3.12B. The two drops in the current in Figure 3.12A might be caused by the same sphere which rolled towards the middle of the metal surface, more efficiently blocking the diffusion and causing another drop in the current. However, it is probable that a second microsphere caused the second step-like drop in Figure 3.12A, which agrees with the larger spheres concentration used and with the fact no "rolling" of the particle occurs in Figure 3.12B. In conclusion, the concentration of the beads had to be lowered in order to avoid that two spheres contributed at the same time to the decrease of the current. The latter is the key point in the development of the immunosensor in Figure 3.1 because ideally only the particle bound to the electrode surface should be responsible of the generation of the analyte signal.

Table 3.3 Values of Δi and $\Delta i/i_i$ calculated from the step-like drops in Figures 3.12A and 3.12B, corresponding respectively to the effect of 0.5 and 0.1 monolayer of 12 μm microspheres on the amperometric current monitored at 4.0 μm and 2.2 μm platinum electrodes. The electrode potential was held at +0.4 V *vs.* Ag/AgCl to drive the oxidation of 1 mM FcMeOH in aqueous 0.1M KCl at the diffusion controlled rate. Cell 1 was employed.

12 μm silica spheres settling				
0.5 monolayer		**0.1 monolayer**		
Δi (pA)	**$\Delta i/i_i$ (%)**	**Δi (pA)**	**$\Delta i/i_i$ (%)**	
37	7.3	29	10.4	
23	4.9	/	/	
5	1.1	/	/	
4	0.9	/	/	
69	14.2	29	10.4	**Tot.**

The role played by the particles charge on their settling was studied in this work by employing NH_2-coated silica spheres and two different redox mediator, ferrocenemethanol and ruthenium hexamine chloride, which have a positive and a negative standard potential respectively. Indeed, the potential during the settling of these particles was held at +0.4 and -0.35 V in order to drive the oxidation of ferrocenemethanol and the reduction of ruthenium hexamine chloride at the diffusion controlled rate. It should be noticed that, as the potential of zero charge (PZC) for platinum is ~ +0.18 V,[13] the electrode surface is positively and negatively charged respectively during FcMeOH oxidation and $[Ru(NH_3)_6]Cl_3$ reduction. This investigation is important to evaluate the feasibility of removing the spheres from the metal disk by change of the applied potential and electrostatic repulsion. The latter method may assure an easy separation of the unbounded beads from the electrode surface and elimination of the false signal generated by the non specific binding.

Only the largest size of beads was investigated because they produced the largest decrease but the least number of step-like drops in the current. The NH_2 groups of the

microspheres coating are positively charged at neutral pH, like in the condition of these experiments. Figure 3.14 shows the typical amperometric profile during the oxidation of FcMeOH employing 12 μm NH_2-coated silica. Because of the electrophoretic force *i.e.*, movement of dispersed particles induced by an electrical field,[14] it should be expected that the spheres are repulsed away from the electrode. According to this argument, the settling of the spheres might be hampered. However, Figure 3.14A shows a step-like decrease of the current occurring at ~ 100 seconds similarly to the experiment run with uncoated 12 μm beads and reported in Figure 3.12A, in which it occurred at ~ 20 seconds. The small difference in the arrival time might be ascribed to the random settling of the spheres rather than an electrophoretic effect. Besides, the $\Delta i/i_i$ value of the step-like drop in Figure 3.14A is 8.6 % which is not distinguishable from the ones reported in Table 3.3 for the same size but uncoated beads. The fact that no other step-like jumps are visible in Figure 3.14A and they are completely absent in Figure 3.14B could be explained by electrostatical repulsion between the electrode and the particles. However, repulsion between the spheres (due to their charge) may also be important. Thus, it is not possible to draw a definitive conclusion about the electrostatic effects between the electrode and the microspheres at this stage.

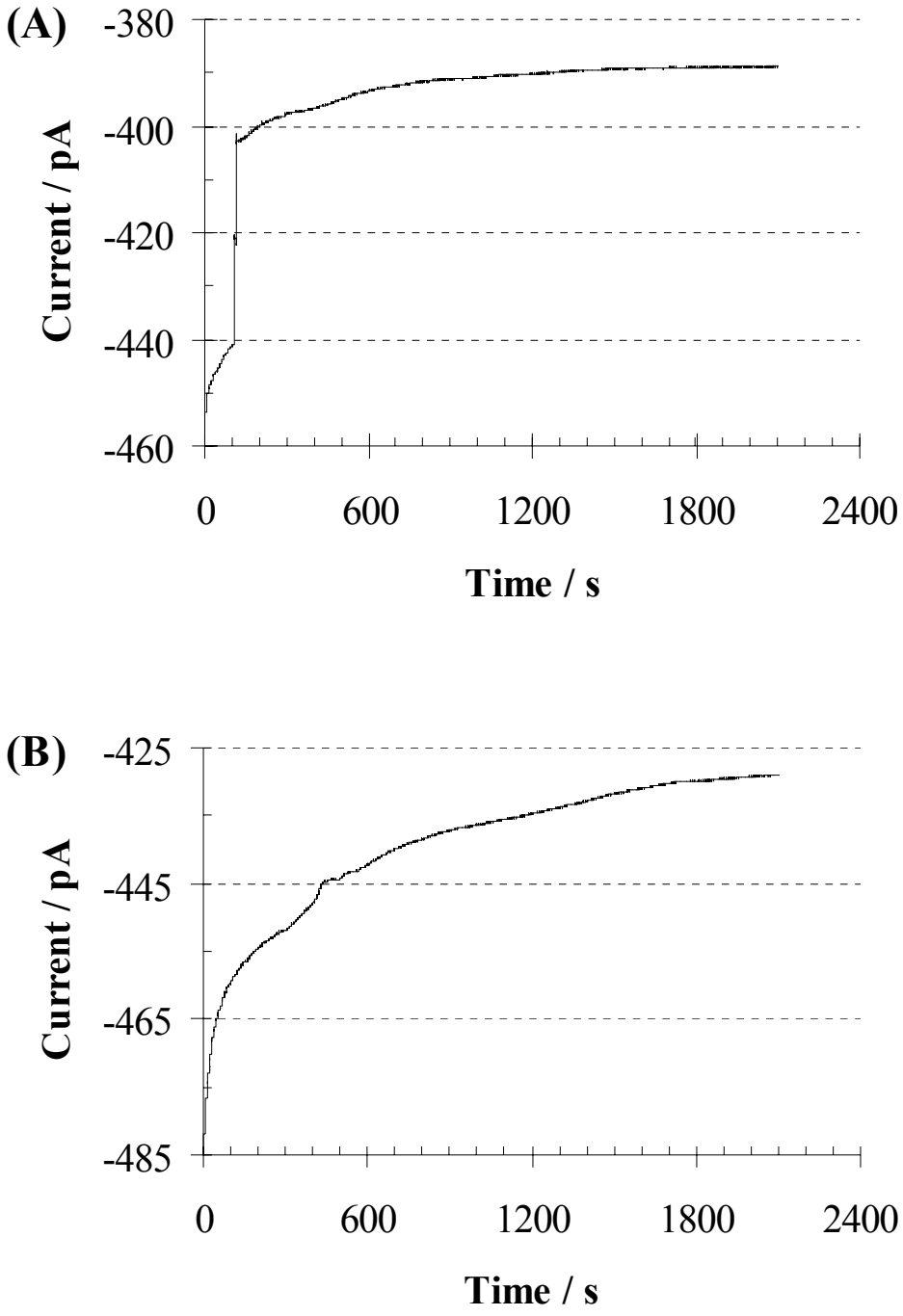

Figure 3.14 Effect of the settling of 12 μm NH_2-coated silica beads on a microelectrode surface. Amperometric profile at (A) a 3.8 μm microelectrode; $C_{spheres}$ = 8×10^5 mL^{-1} (equivalent to 0.5 monolayer) and (B) a 3.6 μm microelectrode; $C_{spheres}$ = 1.6×10^5 mL^{-1} (equivalent to 0.1 monolayer). Potential was held at +0.4 V *vs.* Ag/AgCl to oxidise of 1 mM FcMeOH in aqueous 0.1 M KCl at the controlled diffusion rate. Cell 1 was employed.

The role of electrostatic effects was further investigated by settling 12 μm NH_2-coated silica spheres during reduction of ruthenium hexamine at a potential of -0.35 V *vs.* Ag/AgCl. However, prior to conducting this study, the settling of 12 μm coated and uncoated silica particles during monitoring of the current due to the FcMeOH oxidation were repeated using Cell 2. In Cell 2, the spheres concentration was smaller and a slower arrival of the sphere on the electrode surface was expected as the cell was taller. The change in the electrochemical cell allowed the initial moments of the amperometric profile to be monitored *i.e.*, a very quick arrival of a sphere on the electrode surface was not missed. Tables 3.4 and 3.5 show the results obtained using Cell 2. The $\Delta i/i_i$ values in those tables are significantly smaller than those obtained previously using Cell 1, as seen in Figures 3.13 and 3.14 and reported in Table 3.3. However, it is important to note that in Tables 3.4 and 3.5 the ratio of the sphere/electrode sizes was smaller. In order to deal with the variability in the electrode size due to the fabrication procedure, at the end of the section the $\Delta i/i_i$ obtained are plotted against the sphere/electrode ratio.

Table 3.4 Values of Δi and $\Delta i/i_i$ calculated from the step-like drops in the current upon to the settling of 1 and 0.5 monolayer of 12 μm silica microspheres on 4.9 and 5.6 μm platinum electrodes. The electrode potential was held at +0.4 V *vs.* Ag/AgCl to oxidise 2 mM FcMeOH in aqueous 0.1 M KCl at the diffusion controlled rate. Cell 2 was employed.

12 μm Si spheres settling				
1 monolayer		**0.5 monolayer**		
Δi (pA)	**$\Delta i/i_i$ (%)**	**Δi (pA)**	**$\Delta i/i_i$ (%)**	
47	4.4	33	3.1	
30	3.0	40	3.8	
14	1.5	12	1.2	
18	1.9	10	1.0	
109	10.8	95	9.1	**Tot.**

Table 3.5 Values of Δi and $\Delta i/i_i$ calculated from the step-like drops in the current upon to the settling of 1 and 0.5 monolayer of 12 μm NH_2 coated silica microspheres at 6.6 and 5.4 μm platinum electrodes. The electrode potential was held at +0.4 V *vs.* Ag/AgCl to oxidise 2 mM FcMeOH in aqueous 0.1 M KCl at the diffusion controlled rate. Cell 2 was employed.

12 μm NH_2-coated Si spheres				
1 monolayer		**0.5 monolayer**		
Δi (pA)	**$\Delta i/i_i$ (%)**	**Δi (pA)**	**$\Delta i/i_i$ (%)**	
7	0.6	14	1.2	
15	1.2	6	0.5	
22	1.8	20	1.7	**Tot.**

Figure 3.15 shows the effect of the settling of 12 μm NH_2-coated silica spheres on the amperometric profile during the reduction of $[Ru(NH_3)_6]Cl_3$. The results are summarized in Table 3.6. It is apparent that the step-like drops are significantly larger (factor 2 - 10) than the ones reported in Table 3.5 obtained with the same spheres but during the oxidation of ferrocenemethanol. The larger slope of the current drift in the initial moment of the amperometric experiments in Figure 3.15 is not responsible for an overestimation of the $\Delta i/i_i$ (%) values larger than 0.1 units. Moreover, the differences in $\Delta i/i_i$ did not arise from the electrode size as the R_{SE} factors in Table 3.6 are smaller than in Table 3.5. Thus, the reason of these large $\Delta i/i_i$ values should have a different explanation. In Figure 3.15 the time of the arrival of the first sphere occurs at times < 50 seconds. On the other hand, employing the same cell while oxidising FcMeOH, the arrival of the spheres, independently from the coating or not, occurs at times > 400 seconds. The larger $\Delta i/i_i$ might arise from the electrostatic attraction of the particles towards the electrode. However, considering that the potential applied at the electrode should mainly drop in the diffuse layer, which should be smaller than ten nanometer[11] in the experimental condition of this work ($C_{electrolyte}$ = 0.1 M), it seems unlikely that the latter was responsible for the faster arrival time of the beads on the surface.

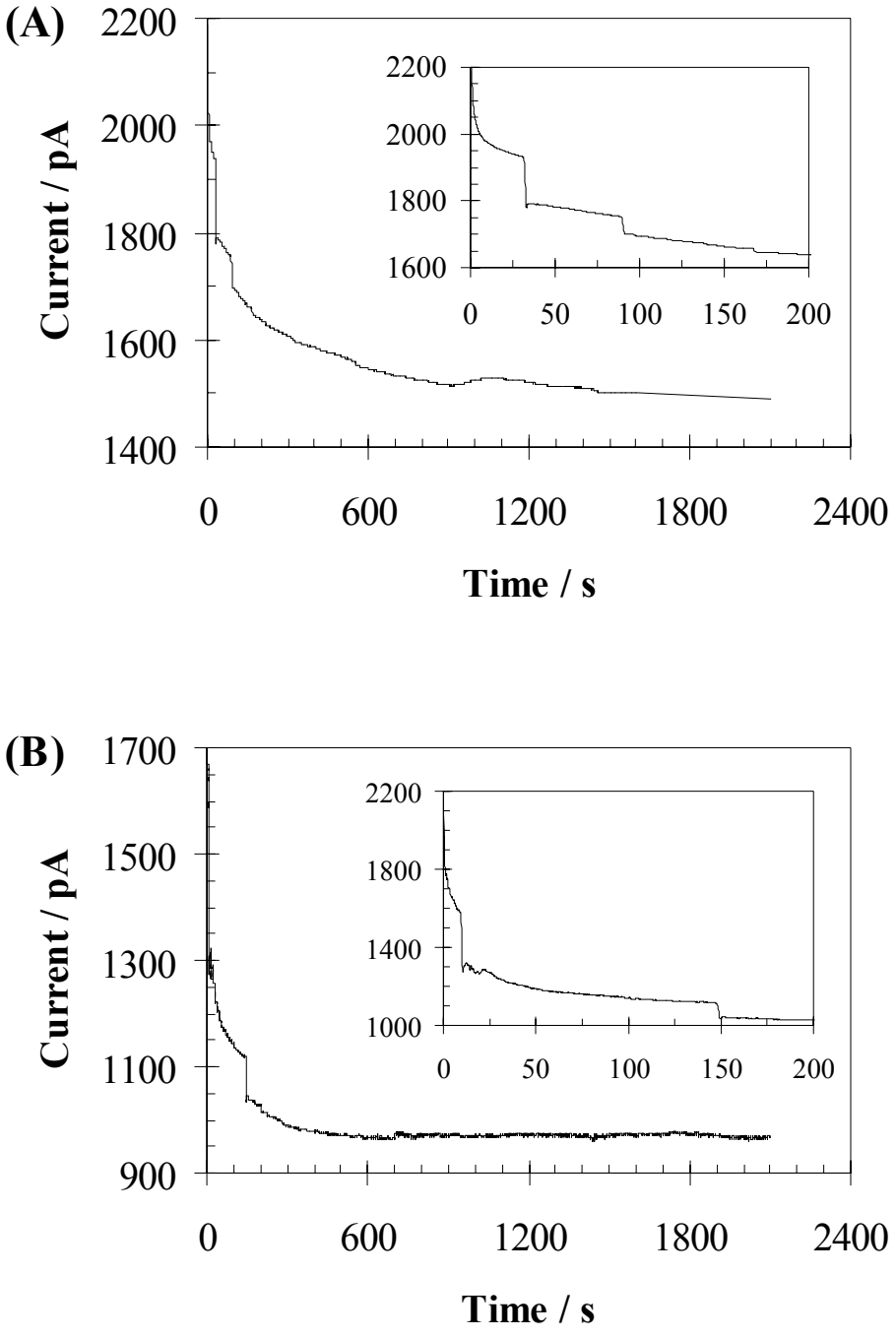

Figure 3.15 Effect of the settling of 12 μm NH_2-coated silica beads on a microelectrode surface during the monitoring of the current of 2 mM $[Ru(NH3)_6]Cl_3$ in aqueous 0.1 M KCl. Amperometric profile at (A) a 7.0 μm microelectrode; $C_{spheres}$ = 2.7×10^5 mL^{-1} (equivalent to 1 monolayer) and (B) a 6.6 μm microelectrode; $C_{spheres}$ = 1.4×10^5 mL^{-1} (equivalent to 0.5 monolayer). Potential was held at -0.35 V *vs.* Ag/AgCl. Cell 2 was employed. Each figure contains an inset showing an enlargement of amperometric profile within the first 200 seconds.

Table 3.6 Values of Δi and $\Delta i/i_i$ calculated from the step-like drops upon to the settling of 1 and 0.5 monolayer of 12 μm NH_2-coated silica microspheres on respectively 7.0 μm and 6.6 μm platinum electrodes. The electrode potential was held at -0.35 V *vs.* Ag/AgCl to oxidise 2 mM $[Ru(NH_3)_6]Cl_3$ in aqueous 0.1 M KCl at the diffusion controlled rate. Cell 2 was employed.

12 μm NH_2 coated Si spheres settling				
1 monolayer		**0.5 monolayer**		
Δi (pA)	**$\Delta i/i_i$ (%)**	**Δi (pA)**	**$\Delta i/i_i$ (%)**	
140	7.3	280	17.7	
50	2.9	78	7.0	
190	10.2	358	24.7	**Tot.**

Assumed that the electrostatic effect might play a role in the particles settling, the feasibility of ejecting the sphere from the platinum disk by electrostatic repulsion has been evaluated. Indeed, during an amperometric experiment the potential was switched from the value where the reaction of the redox mediator occurs at the diffusion controlled rate to a potential negative of the PZC such as that shown in Figure 3.16A where FcMeOH was employed. Figure 3.16B shows the amperometric curve due to the oxidation of FcMeOH in the presence of 12 μm silica spheres. The step-like decrease indentified with a circle is due to the settling of one sphere on the metal disk as already explained above. After 900 seconds the potential was switched to -0.3 V for 900 seconds and finally after 1800 seconds from the start of the experiment it was stepped back to +0.4 V and held for the remaining 900 seconds. It can be noticed that the current at times > 1800 seconds is very close to the current monitored just after the step-like drop. This behaviour indicated that the electrostatic repulsion of the sphere from the electrode surface, once it settled, was not possible in these experimental conditions. Similar results (not shown) were obtained employing $[Ru(NH_3)_6]Cl_3$ and 12 μm NH_2coated silica upon change of the applied potential from -0.35 V to +0.4 V and back in the same fashion as shown in Figure 3.16A. The higher particle charge did not help the repulsion of the sphere/s from the metal disk.

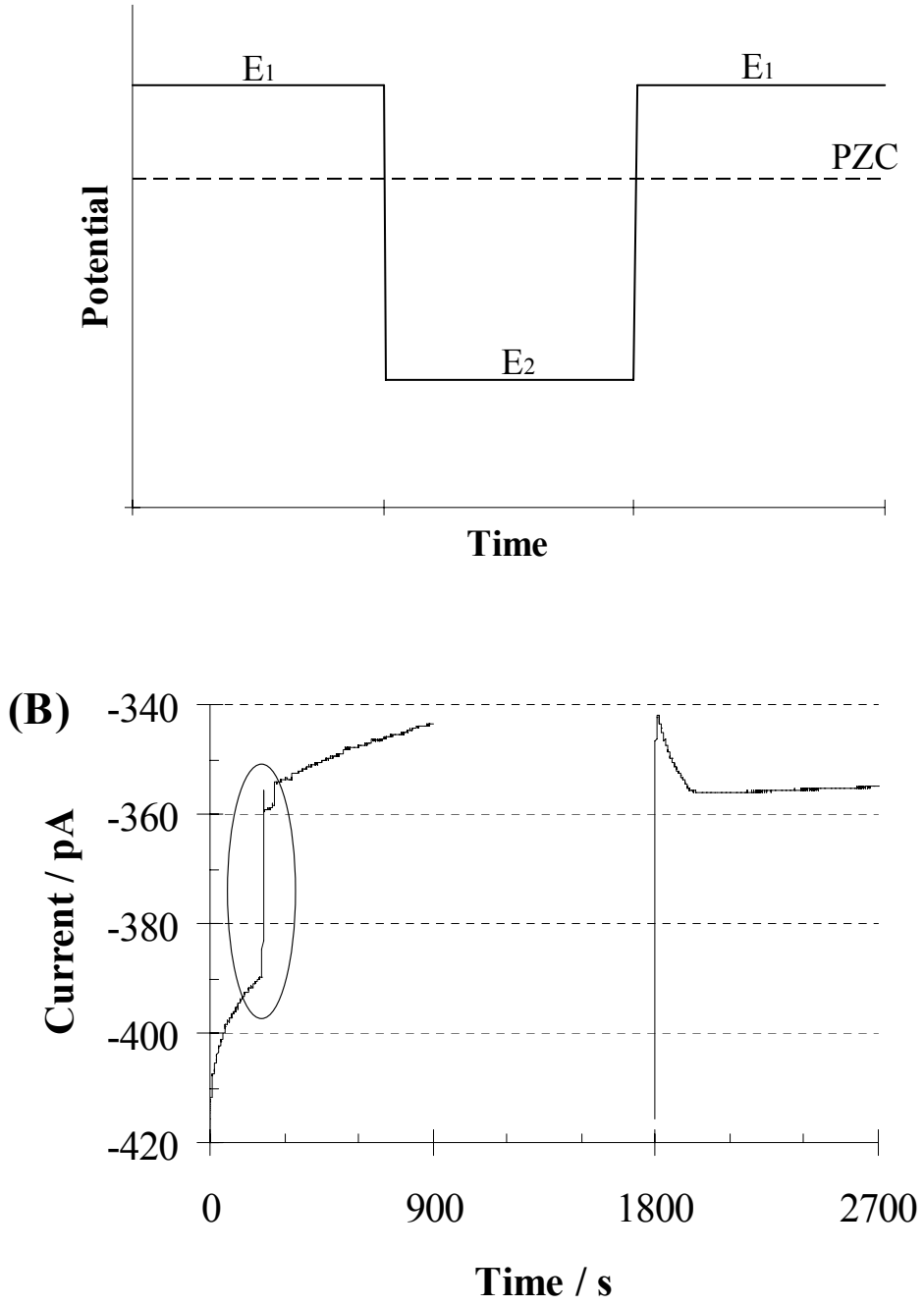

Figure 3.16 (A) Sketch of the potential program set in the amperometric experiment in (B) to evaluate if the particle can be electrostatically repulsed from the electrode surface. (B) Effect of the settling of 12 μm silica beads on a 3 μm microelectrode surface during the monitoring of the current of 1 mM FcMeOH in aqueous 0.1 M KCl. $C_{spheres}$ = 2.7 × 10^5 mL^{-1} (equivalent to 1 monolayer). E = E_1 = +0.4 V when 0 < t < 900 s and 1800 < t < 2700 s; E = E_2 = -0.3 V when 900 s < t < 1800 s. Cell 2 was employed.

Figure 3.17 shows the relationship between the $\Delta i/i_i$ and the ratio of the sphere/electrode size found in this work. The assumption is that each of the step-like drops observed, it was produced by one microsphere settling on the electrode surface (or near) and is reported as single point in this figure. It is very hard to see a trend of $\Delta i/i_i$ with R_{SE} and quadratic or cubic relationship ($\Delta i/i_i \propto R_{SE}^2$ or R_{SE}^3) were not seen as well. There are two possible reasons for this behaviour. Firstly, the shielding of the diffusion profile due to a particle might have a more complicated dependence. Secondly, the $\Delta i/i_i$ associated with the settling of one sphere appeared to depend significantly on the location of the latter in respect to the metal disk. In conclusion, the $\Delta i/i_i$ values seemed to increase as R_{SE} become larger but not in a linear way. Besides, on one hand, the settling of NH_2-coated Si spheres during the reduction of $[Ru(NH_3)_6]Cl_3$ produced a significant larger $\Delta i/i_i$ than the data of uncoated 12 μm spheres with similar R_{SE} ratio. On the other hand, the settling of NH_2-coated Si spheres during the oxidation of FcMeOH produced a significantly smaller $\Delta i/i_i$ than the data of uncoated 12 μm spheres with similar R_{SE} ratio. The latter behaviour might be due somehow to the electrostatic effect.

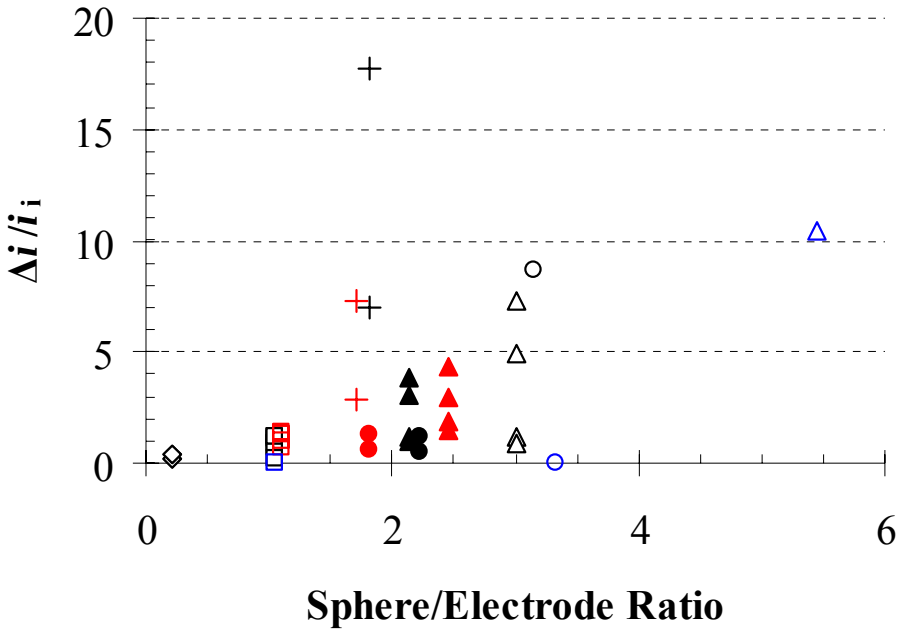

Figure 3.17 Effect of the ratio between sphere and electrode size on the $\Delta i/i_i$ of a step-like drop in the current for the all experiments conducted in this section. Every step-like decrease is reported as a single point assuming it has been produced by one sphere. The symbols represent the different experimental conditions: (◊) 1 μm silica spheres, (□) 4 μm silica spheres, (Δ) 12 μm silica spheres, (○) 12 μm NH_2 coated silica spheres during the oxidation of FcMeOH and employing Cell 1. The colour of the symbols indicates the amount of monolayers in the cell. So for example: (Δ) 1 monolayer, (Δ) 0.5 monolayer and (Δ) 0.1 monolayer of 12 μm silica spheres. When the symbol is filled, Cell 2 was employed. So for example: (▲) 12 μm silica spheres, Cell 2, oxidation of FcMeOH. Finally, (+) 1 monolayer and (+) 0.5 monolayer of 12 μm NH_2-coated silica spheres during the reduction of $[Ru(NH_3)_6]Cl_3$ in Cell 2.

Figure 3.18 shows the relationship between the overall $\Delta i/i_i$ (sum of all the single contributions) and the R_{SE} ratio. Similar conclusions can be made here as for Figure 3.17. Besides, from Figure 3.18 it seems that the fraction of monolayer present in solution did not affect the overall $\Delta i/i_i$ except when the concentration of the spheres was so low that slightly smaller overall $\Delta i/i_i$ or lack of step-like drops was observed. This behaviour agrees with the fact that settling is a random process *i.e.*, at submonolayer sphere concentration the particle might or might not cover the electrode disk.

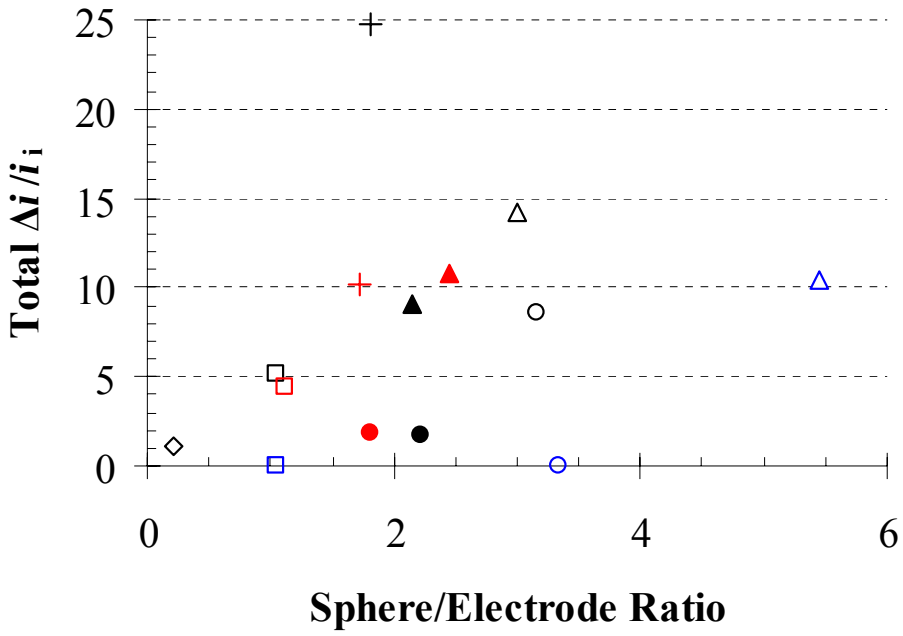

Figure 3.18 Effect of the ratio between sphere and electrode size on the overall $\Delta i/i_i$ in the current for the all experiments conducted in this section. The overall $\Delta i/i_i$ is the sum of the all single step-like drops. The symbols represent the different experimental conditions: (◊) 1 µm silica spheres, (□) 4 µm silica spheres, (Δ) 12 µm silica spheres, (○) 12 µm NH_2 coated silica spheres during the oxidation of FcMeOH and employing Cell 1. The colour of the symbols indicates the amount of monolayers in the cell. So for example: (Δ) 1 monolayer, (Δ) 0.5 monolayer and (Δ) 0.1 monolayer. When the symbol is filled, Cell 2 was employed. So for example: (▲) 12 µm silica spheres, Cell 2, oxidation of FcMeOH. Finally, (+) 1 monolayer and (+) 0.5 monolayer of 12 µm NH_2-coated silica spheres during the reduction of $[Ru(NH_3)_6]Cl_3$ in Cell 2.

In conclusion, every step-like drop during the amperometric curves shown in this section could be related to a single microsphere settling on the metal disk (or near) and to the adjustment of the spheres monolayer which then displaced a sphere on the electrode surface. Even when the beads oversize the electrode, more than just one sphere affected the diffusion profile of the redox mediator and then the measured current. These decreases were essentially instantaneous and from the current readings the packing of the sphere over time appeared to be stable. The $\Delta i/i_i$ values were sensitive to the spheres/electrode ratio and particle charge. In fact, electrostatic attraction might be responsible for causing larger individual and total $\Delta i/i_i$ values as

shown in Figures 3.17 and 3.18 for the settling of NH_2-coated beads during amperometric reduction of $[Ru(NH_3)_6]Cl_3$. Despite the latter hypothesis, the ejection of 12 μm silica sphere from the metal disk by electrostatic repulsion was apparently not possible independently from the particle charge *i.e.*, NH_2 groups coating. However, use of lighter density spheres with smaller sizes might produce positive results.

It is significant to note that the $\Delta i/i_i$ values observed were always < 20 %. Figure 3.10 shows the reason for this behaviour. Indeed, a bead sitting on the middle of the electrode surface leaves a thick ring of the metal uncovered. The steady-state current at ring microelectrodes (when c/b < 1.25) is given by:[15]

$$i_{ss} = nFDC^* l_0 \tag{3.3}$$

where $l_0 = [\pi^2(b+c)]/\ln[16(b+c)/(c-b)]$ (3.4)

and n is the number of electron exchanged, F is the Faraday constant, D and C^* are respectively the diffusion coefficient and the bulk concentration of the redox mediator, b and c are the inner and outer ring UME radius. The ratio of the steady state current between a ring and a disk electrode with $a = c$ is equal to l_0/a. Assuming $c/b = 1.25$, l_0/a is equal to 0.89 and then the current at the ring UME is only ~ 11 % lower than at the disk UME even if the ring UME area is 64 % smaller than the disk UME one (with $a = c$). In Table 3.3 a $\Delta i/i_i$ value of 10.4 % was reported during the amperometric oxidation of FcMeOH at a 2.2 μm UME employing 12 μm silica spheres. Therefore, the settling of a microsphere ~ 5 times bigger than the electrode disk, correspond to a reduction of its available electrochemical area of ~ 64 % employing the ring electrode analogy. The high current density at the ring electrodes dictates a minimal drop in the steady state current because of an inefficient blocking of the electrochemical surface by a microsphere even for high R_{SE} ratio. It is clear that the use of beads with different shape, *e.g.*, disc particles or recessed electrodes as done by Gorschluter and co-workers,[1] is essential if a larger decrease of the current has to be achieved.

3.3.2 Anti hIgG Spheres and hIgG UMEs for Immunosensing

The feasibility of the immunosensor depicted in Figure 3.1 relies on the expectation that the sphere which binds the electrode surface cause a drop in the current. In this section, anti hIgG labelled spheres and hIgG coated UMEs were employed to test this idea. However, from the experiments carried in the previous section, it is apparent that spheres settling on the microelectrode, even if not specifically bound to it, caused a decrease of the steady state current. The key question to be addressed in this section is whether physically adsorbed and chemisorbed spheres produce a different signal and then they could be distinguished or not *i.e.*, need of washing steps after that the coated microelectrode has been exposed to the labelled spheres. Based on the data presented in the previous section, it was decided to use the largest commercially available anti-hIgG coated spheres in order to have the biggest R_{SE} ratio and then the biggest drop in the steady state current upon binding of the particle. Besides, the settling of the silica spheres does not correspond to a dynamic situation where the beads arrive and leave the surface as supported from the fact that the step like drops in the amperometric curve observed in the previous section were stable. From this point of view, the latex spheres were preferred to silica because use of lighter particles might minimize the background contribution *i.e.*, the beads are less prone to reside on the electrode surface because of gravity.

The settling of the anti hIgG 7.4 μm polystyrene spheres on uncoated microelectrodes was preliminary carried in order to evaluate the signal produced by non specifically bound spheres, *i.e.*, the background, using the same criteria described in the previous section. Figures 3.19 and 3.20 shows the typical amperometric profiles for the oxidation of FcMeOH and reduction of $[Ru(NH_3)_6]Cl_3$ while the labelled particles settled on uncoated UMEs. These results are significantly different compared to the ones obtained with the silica spheres described in the previous section. In fact, the step-like drops in the current did not occur instantaneously and, on average, 20-50 seconds were necessary to reach the new current value. Only one or two of these drops were observed despite increasing experimental time window to 1 hour. This behaviour most likely arises from the slow settling velocity which is reported in Table 3.1. In Figure 3.19 the settling of the sphere on the electrode surface seems to be unstable because the current slowly returns to the value it had before the particle arrived. The spike

identified with arrows in Figure 3.20 might be produced by a collision of the particle with the electrode surface. These behaviours might arise from the lower density of the latex particles. The $\Delta i/i_i$ values were considered 0 when the current returned to the original value and eventual spikes like the one in Figure 3.20 were not counted (Δi taken at times as indicated by the arrows).

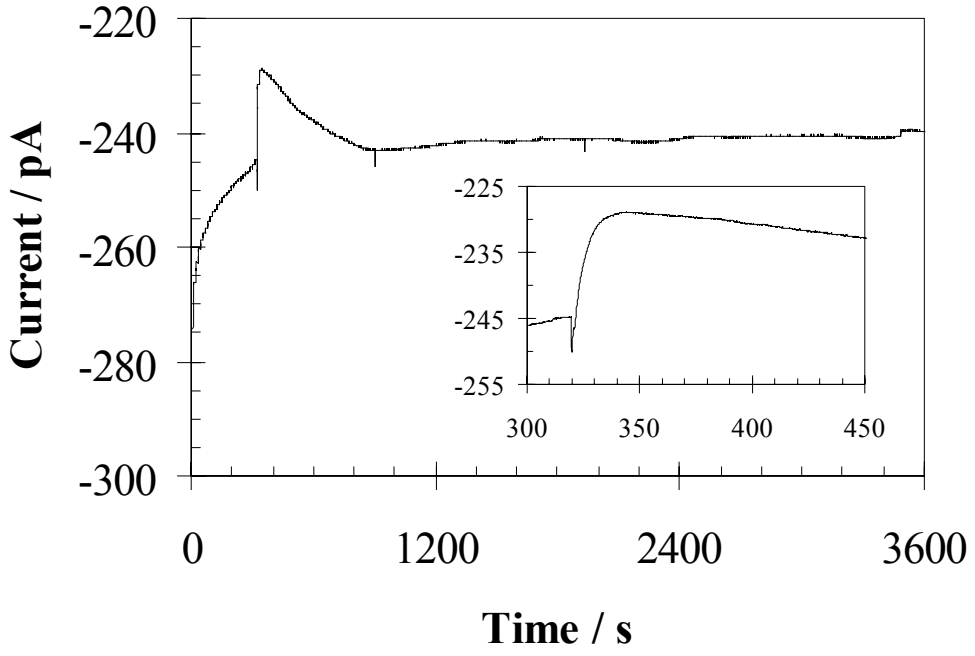

Figure 3.19 Amperometric profile at a 3.4 μm uncoated microelectrode upon to the settling of 7.4 μm anti hIgG-coated polystyrene beads. The concentration of the spheres was: $C_{spheres} = 7.1 \times 10^5$ mL^{-1} (equivalent to 1 monolayer). Potential was held at +0.40 V to oxidise 1 mM FcMeOH in 10 mM PBS at the diffusion controlled rate. Cell 2 was employed. The inset shows an enlargement of the plot. The units of measure in the inset are the same as in correspondent figure.

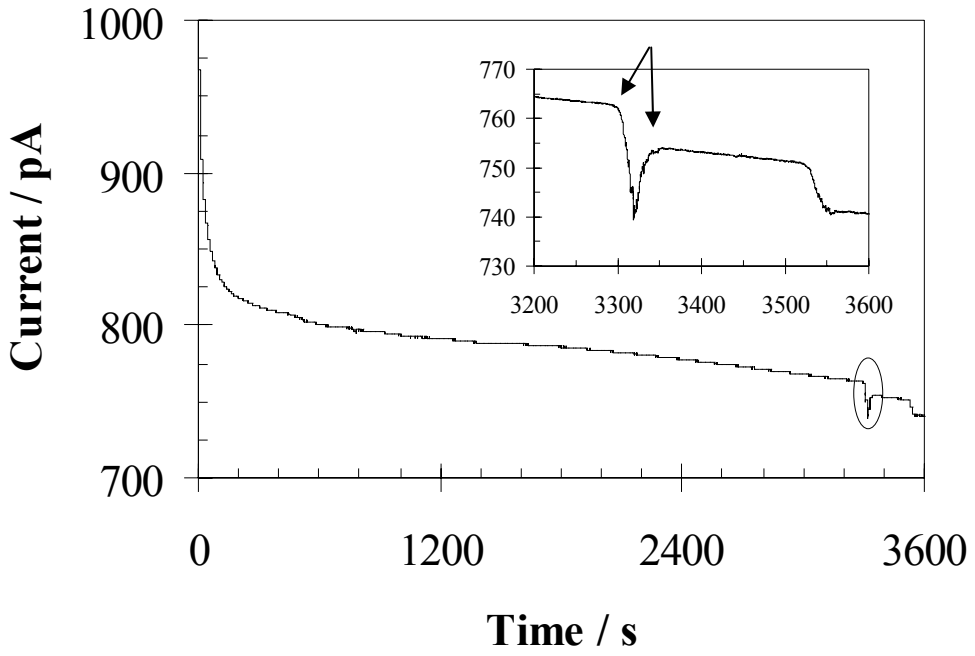

Figure 3.20 Amperometric profile at a 2.6 μm uncoated microelectrode upon to the settling of 7.4 μm anti hIgG-coated polystyrene beads while monitoring the reduction of $[Ru(NH_3)_6]Cl_3$. The concentration of the spheres was: $C_{spheres}$ = 7.1 × 10^5 mL^{-1} (equivalent to 1 monolayer). Potential was held at -0.35 V to reduce of 3 mM $[Ru(NH_3)_6]Cl_3$ in 10 mM PBS at the diffusion controlled rate. Cell 2 was employed. The inset shows an enlargement of the plot. The units of measure in the inset are the same as in the figure.

Figures 3.21A and 3.22A show the voltammograms obtained for ferrocenemethanol and ruthenium hexamine chloride respectively at the microelectrodes before and after that the latter were coated with hIgG. On average, the decrease of the steady state current after the coating step was quite irreproducible ranging from 1 % to 25 %. This variability might arise from the irreproducibility associated with the immunoglobulin G adsorption or the antibody configuration. It is important to note that, according to AFM studies in the literature,[5] the hIgG physioadsorption should produce a protein film with thickness between 4 and 10 nm. Besides, the efficiency of hIgG layers in blocking the electron transfer at the electrode has been studied by Moulton and co-workers[3,4] using potassium ferricyanide. These authors observed a decrease in the peak currents of ~ 90 % and a significant shift of the peak potentials (~ 150 mV) after exposing a gold

electrode to a 1 mg mL^{-1} hIgG solution for 30 minutes at the open circuit potential. However, it has been shown that the permeability of molecular probes through film pores or pinholes depend on the chemical and physical factors, *e.g.* electron transfer heterogeneous standard constant, size and ionic charge of the molecular probes,[16-18] which might explain the different behaviour. Besides, Moulton and co-workers[3,4] used concentration of hIgG two order to magnitude higher than in this work.

Figures 3.21B and 3.22B show the typical effect of the settling of the labelled spheres when the microelectrode was coated with hIgG and the immuno reaction occurred using the redox current of FcMeOH and $[Ru(NH_3)_6]Cl_3$ as transducing principle, respectively. These figures are not significantly different from the ones obtained with a bare electrode and previously reported in Figures 3.19 and 3.20. It is important to note that the washing step with Tween® and BSA of the hIgG coated UMEs prior to start the amperometric experiment did not significantly change these results. Besides, use of 0.1 M KCl instead than 10 mM PBS as electrolyte did not affect the experimental results.

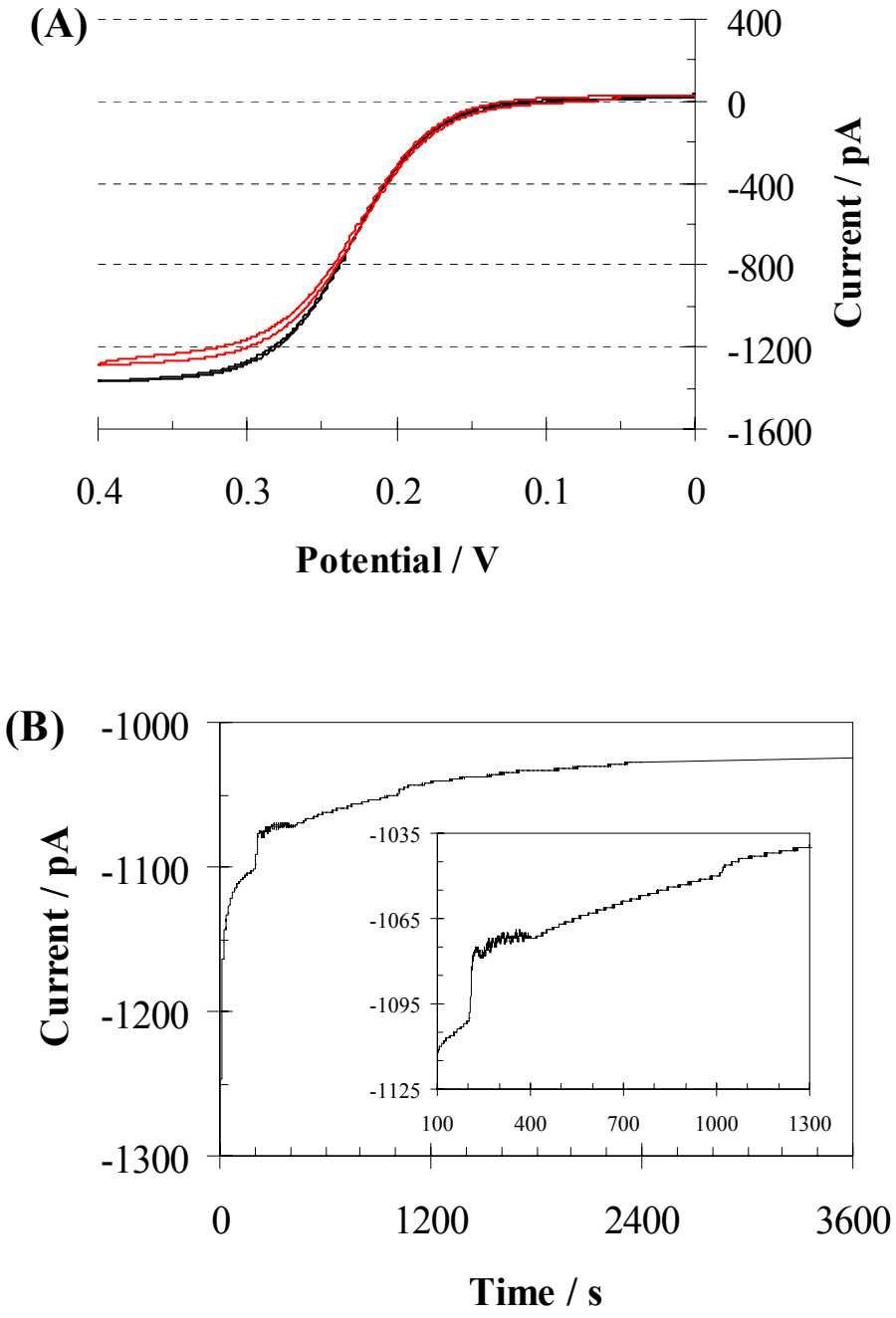

Figure 3.21 (A) Voltammograms at 5.2 µm UME (—) before and (—) after the hIgG adsorption step. (B) Amperometric profile at the same 5.2 µm hIgG coated microelectrode upon exposure to 7.4 µm anti hIgG coated latex spheres. $C_{spheres}$ = 7.1 × 10^5 mL^{-1} (equivalent to 1 monolayer). The potential was held at +0.4 V. The inset in (B) shows an enlargement of the plot. The units of measure in the inset are the same as in correspondent figure. In both the figures a solution of 2 mM FcMeOH in 10 mM PBS was employed. Cell 2 was employed

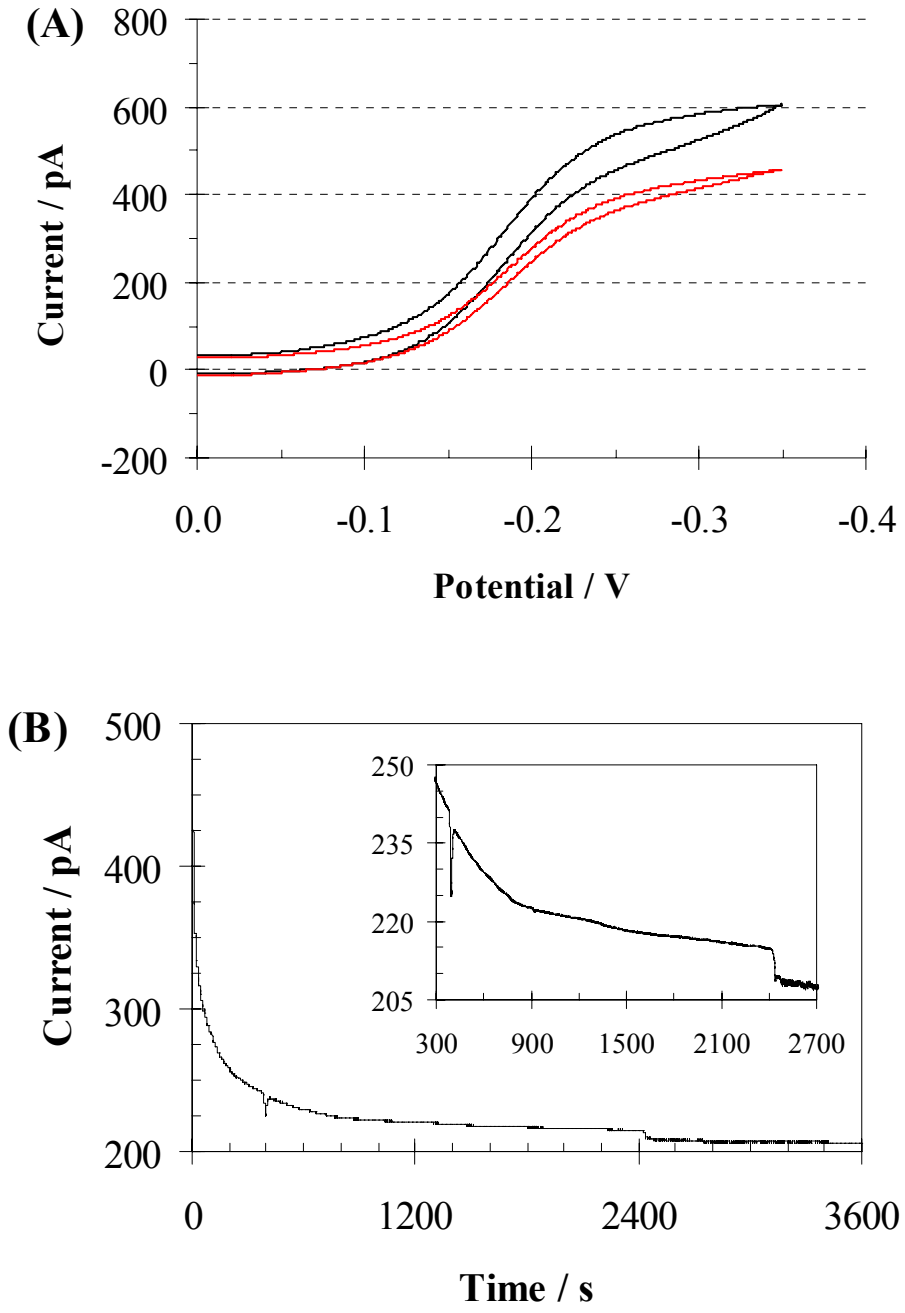

Figure 3.22 (A) Voltammograms at a 3.8 µm UME (—) before and (—) after that the latter was coated with hIgG and washed with BSA and Tween®. (B) Amperometric profile at the same 3.8 µm hIgG coated microelectrode upon exposure to 7.4 µm anti hIgG coated latex spheres. $C_{spheres}$ = 7.1 × 10^5 mL^{-1} (equivalent to 1 monolayer). The potential was held at -0.35 V. The inset in (B) shows an enlargement of the plot. The units of measure in the inset are the same as in correspondent figure. In both the figures a solution of 1 mM $[Ru(NH_3)_6]Cl_3$ in 10 mM PBS was used. Cell 2 was employed.

In conclusion, the step-like drops in the current did not seem to be affected by the hIgG coating on the microelectrodes. Indeed, when a stable bond between hIgG on the UME and anti hIgG on the particle was formed or when the labelled sphere physically settled on the bare microelectrode surface, a step-like decrease with similar $\Delta i/i_i$ was observed. This behaviour agrees with the conclusion that the shielding of the sphere on the diffusion of the redox mediator towards the electrode is the same whether the immuno reaction occurred or not. However, the hIgG coating of the electrode affected the probability, *i.e.* frequency, to have a stable step-like drop in the steady state current. Indeed, Figure 3.23 summarizes the results obtained with hIgG coated and uncoated microelectrode letting the anti hIgG spheres settle down and it reports the overall $\Delta i/i_i$ values in function of the R_{SE} ratio. From this figure, it is apparent that total $\Delta i/i_i$ due to the "binding" events at coated UMEs was different than the one due to the "settling" events at uncoated microelectrodes because in the latter case two total $\Delta i/i_i$ equal to 0 were found upon three repetitions of the experiment. However, when $[Ru(NH_3)_6]Cl_3$ was employed, the total $\Delta i/i_i$ obtained from the settling of labelled spheres on coated and uncoated microelectrodes were in the same range. The reason of the discrepancy between the behaviour with the two redox mediators is not fully understood but it might arise from an electrostatic effect. The zeta potential of the anti hIgG coated particles was not supplied by the manufacturer neither could be instrumentally determined. However, it has been reported that hIgG molecules have a pI value between 4.35 and 9.95 but the majority have a pI between 7 and 9.[19] Thus, it is possible that the anti hIgG layer of the microspheres was positively charged at the pH (= 7.2) used in the experimental conditions of this work. The negative potential applied during the reduction of $[Ru(NH_3)_6]Cl_3$ might be responsible for holding electrostatically the particles on the electrode surface even in absence of any immunochemical binding. In the case of the oxidation of FcMeOH, the electrode potential was positive and the electrostatic repulsion of the anti hIgG labelled spheres (assuming they are positively charged) might be responsible for the unstable step-like decreases of the current at uncoated microelectrodes. However, when the UMEs were coated with hIgG the biochemical reaction with the anti hIgG layers of the labelled microspheres would assured a stable bond between the two despite any electrostatic effect. Finally, it is important to note that the individual and total $\Delta i/i_i$ values in Figure 3.23 were smaller (factor 2 – 5) than the ones with similar R_{SE} factor and employing 12 μm silica spheres previously reported in Figure 3.18. This difference is not fully understood but it might

arise from the higher density of the silica beads but without the data of the zeta potential for the two types of spheres this hypothesis is not certain.

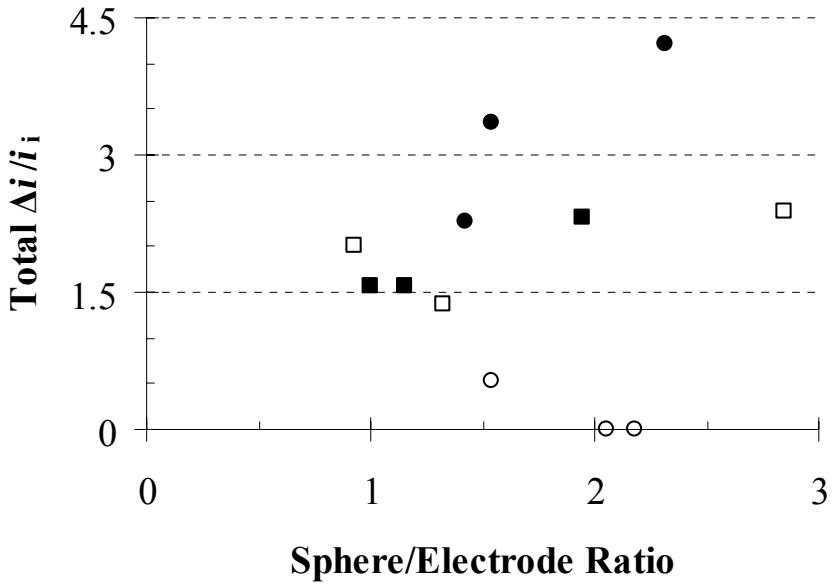

Figure 3.23 Effect of the ratio between sphere and electrode size on the overall $\Delta i/i_i$ for each experiments conducted in this section employing 7.4 μm anti hIgG coated latex spheres. The overall $\Delta i/i_i$ is the sum of the all single step-like drops counted in the experiment. The symbols represent the different experimental conditions: reduction of $[Ru(NH_3)_6]Cl_3$ at (□) bare and (■) hIgG coated microelectrode; and oxidation of FcMeOH at (○) bare and (●) hIgG coated microelectrodes.

Figure 3.24 is an optical picture showing the "capture" of the spheres on an hIgG modified microelectrode surface. This behaviour was observed only when the electrodes were coated with hIgG which supports the conclusions above. In this figure the spheres are bound both on the metal disk and on the surrounding glass, which arose from the fact that hIgG physioadsorption occurred on the glass also. Washing off the particles was not possible, which supports the fact that the strong bonds between anti hIgG and the hIgG were able to hold the spheres on surface.

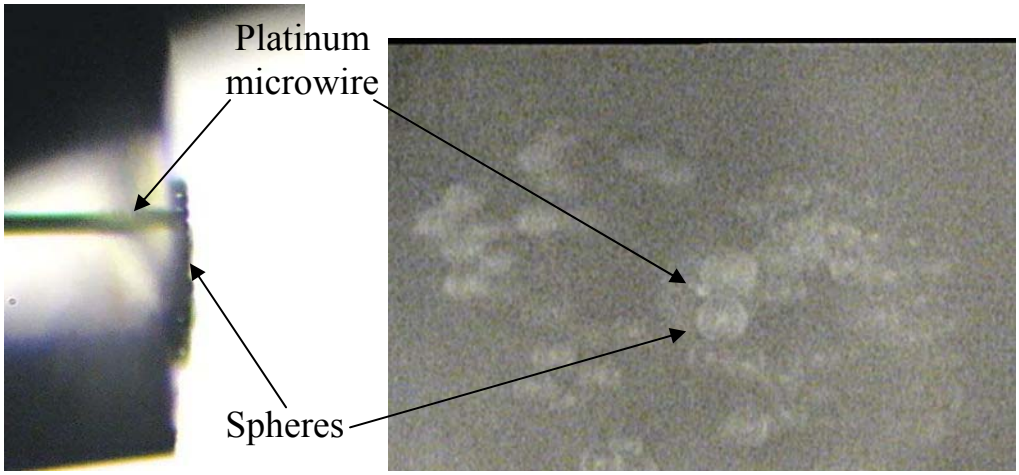

Figure 3.24 Optical picture showing 7.4 μm anti hIgG coated silica spheres attached to the surface of a 5.2 μm UME which was coated with hIgG as described in Section 3.2.3.

3.4 Conclusions

This chapter deals with the feasibility of an immunosensor which uses the changes in the steady state current upon microparticle arrival on the electroactive UME surface as the transducing principle. A preliminary study of the physical settling of silica spheres onto the electrode surface led to several key conclusions. The settling of the particles caused step-like drops in the current but it has been noticed that not only one sphere was responsible for the decrease even when the R_{SE} ratio was greater than 1. The $\Delta i/i_i$ values were sensitive to the ratio between sphere and electrode size but no direct relationship was observed. Gravity appears to dominate the behaviour at least for the particle sizes employed in this work. Indeed, the settling of the spheres was not impeded by electrostatic repulsion neither it seems possible to electrostatically repulse the beads from the electrode surface once they settle on by changing the applied potential. However, the electrostatic attraction between the particles and the electrode might be responsible for the larger $\Delta i/i_i$ values observed in some cases. Finally, this investigation highlighted two important issues concerning the feasibility of the immunosensor whose transducing principle was here studied. Firstly, more than one particle influenced the steady state current monitored at the microelectrode. Secondly, the $\Delta i/i_i$ values were small *i.e.*, always < 20 %, while it would be good to bring them above 90 % for single particle counting. There are two possible solutions for both the

problems here described. First, the use of a recessed electrode, as reported by Gorschluter and co-workers[1]. However, the recess should be somehow tailored for the sphere size as the latter should "touch" the electrode surface in order to allow the eventual biosensing reaction to occur (in this work the binding between hIgG and anti hIgG). So, this need dictates the recess cannot be too deep and it limits the capacity of the sphere to shield the diffusion of the redox mediator towards the electrode. Indeed, in reference [1] the $\Delta i/i_i$ values were always < 50 %. Second, the use of disc shaped microparticles which would not require a very strict control in the size of the electrode/s and particles and, as far as the disc shaped particles oversize the electrode, larger $\Delta i/i_i$ values can be expected.

An evaluation of the immunosensors was also carried in this work and similar conclusions to those above apply also in this case *e.g.*, multiple step-like drops in the current and $\Delta i/i_i$ values sensitive to the R_{SE} ratio. Two major problems should be addressed in the development of this immunosensor. First, the contribution from the non specifically bound hIgG coated particles which produced a false signal. Indeed, these spheres were weakly bound to the bare electrode surface, because of their weight or van der Waals forces, but they produced step-like drop in the current similar to when the electrodes were coated with hIgG and a proper chemical bond was formed. However, the step-like drops in the current appeared to be unstable when uncoated microelectrodes were employed. Second, the electrostatic attraction appeared to be able to strengthen the interaction between the non specifically bound particles and the electrode because the step-like drops were stable in this case. In conclusion, this study supports the idea that in the experimental conditions the interactions between spheres and electrode scale in the following order: gravity ≥ chemical bond ≥ electrostatic effect > van der Waals. A possible solution is to insert the immunosensors in a microfluidic device where a constant flow of solution has to be calibrated opportunely to flush the non specifically bound spheres and then eliminate the problem of the false signal.

3.5 References

(1) Gorschlüter, A.; Sundermeier, C.; Roß, B.; Knoll, M. *Sensors and Actuators B: Chemical* **2002***, 85*, 158-165.

(2) Mak, L. H.; Knoll, M.; Dankbar, N.; Sundermeier, C.; Gorschlüter, A. *Sensors and Actuators B: Chemical* **2006***, 114*, 132-140.

(3) Moulton, S. E.; Barisci, J. N.; Bath, A.; Stella, R.; Wallace, G. G. *J. Colloid Interface Sci.* **2003***, 261*, 312-319.

(4) Moulton, S. E.; Barisci, J. N.; Bath, A.; Stella, R.; Wallace, G. G. *Electrochimica Acta* **2004***, 49*, 4223-4230.

(5) Zhou, C.; Friedt, J.; Angelova, A.; Choi, K.; Laureyn, W.; Frederix, F.; Francis, L. A.; Campitelli, A.; Engenlborghs, Y.; Borghs, G. *Langmuir* **2004***, 20*, 5870.

(6) Giacomelli, C. E.; Bremer, M. G. E. G.; Norde, W. *J. Colloid Interface Sci.* **1999***, 220*, 13-23.

(7) Hung, C.; Holoman, T. R. P.; Kofinas, P.; Bentley, W. E. *Biochemical Engineering Journal* **2008***, 38*, 164-170.

(8) Chen, H.; Jiang, J.; Li, Y.; Deng, T.; Shen, G.; Yu, R. *Biosensors and Bioelectronics* **2007***, 22*, 993-999.

(9) Cid, C. C.; Riu, J.; Maroto, A.; Rius, X. F. *Analyst* **2008***, 133*, 1005.

(10) Cantarero, L. A.; Butler, J. E.; Osborne, J. W. *Analytical Biochemistry* **1980***, 105*, 375.

(11) Bard, A. J.; Faulkner, L. R. In *Electrochemical Methods. Fundamentals and Applications.* Wiley Inc.: United States of America, 2001; , pp 833.

(12) Bartlett, P. N.; Taylor, S. L. *J. Electroanal. Chem.* **1998***, 453*, 49-60.

(13) Osawa, M.; Tsushima, M.; Mogami, H.; Samjeské, G.; Yamakata, A. *J. Phys. Chem. C.* **2008***, 112*, 4249.

(14) Marina, M. L.; Ríos Castro, A.; Valcárcel Cases, M., Eds.; In *Analysis and Detection by Capillary Electrophoresis;* Wilson & Wilson's comprehensive analytical chemistry; Elsevier Science: Amsterdam, 2005; Vol. 45, pp 767.

(15) Lee, Y.; Amemiya, S.; Bard, A. J. *Anal. Chem.* **2001***, 73*, 2261.

(16) Williams, M. E.; Stevenson, K. J.; Massari, A. M.; Hupp, J. T. *Anal. Chem.* **2000***, 72*, 3122-3128.

(17) Cannes, C.; Kanoufi, F.; Bard, A. J. *J. Electroanal. Chem.* **2003***, 547*, 83-91.

(18) Chailapakul, O.; Crooks, R. M. *Langmuir* **1995***, 11*, 1329.

(19) Ahrer, K.; Buchacher, A.; Iberer, G.; Jungbauer, A. *Journal of Chromatography A* **2004***, 1043*, 41-46.

Chapter 4

Glucose Microsensors

4.1 Introduction

The miniaturization of the amperometric biosensors offer some intrinsic advantages including a steady state response achieved in a short time, implantation feasibility and smaller quantity of biomaterials and reagents.[1] However, the development of miniaturized transducers is still challenging as the signal decreases with the electrode dimensions and the long term stability of the biosensing coating hampers often their commercialization.[1] Indeed, reproducibility, stability and sensitivity of miniaturized sensors depend significantly on the biosensing interface and on the techniques employed for the enzyme immobilization.[2,3] Though enzyme electrodes have been subject of extensive research in the last thirty years, only few papers deal with the preparation of micro-biosensors and the majority have size larger than 100 μm[4-8] and anyway above 10 μm.[3,9-13] *Ex-vivo* and *in-vivo* clinical applications, including the measurements of metabolites in biological microenvironments with high spatial and temporal resolution,[14,15] subcutaneous substrate monitoring (needle-type probes)[4,6,12,16-19] and point-of-care would tremendously benefit from top-down process leading to smaller sensors.[2,20-22]

In principle, an important requirement for a sensor, apart from appropriate sensitivity and accuracy, is that it should quickly respond to changes in the substrate concentration. From this point of view, immobilizing the enzyme in a thin layer rather than a thick one could represent an advantage.[23] Moreover, if the response time is short as a few seconds and the background current is smaller than the analyte signal *i.e.*, S/N > 3, one might think to operate such sensor for amperometric "on the fly" glucose measurement with the probe having the double function of being both the lancet and the sensor. A subcutaneous glucose sensor could have similar sensing core inside a small needle. Though they have been studied for a long time,[4,6] at the moment, they require an *in vitro* or *in vivo* calibration[6,24] and their use in "on the fly" measurements has not been reported. The decrease of the electrode size can reduce the *RC* cell time constant ($RC \propto a$) and allows a steady state to be achieved upon faster times ($\propto 1/a^2$), see Section 1.3. At the moment, despite the extended literature on glucose sensors, it is found that only one paper presented results obtained with immobilized glucose oxidase microelectrodes having radius smaller than 10 μm.[20] The author electropolymerized phenol/allylphenol GOx mixture on 6.8 - 10 μm (diameter) platinum

ultramicroelectrodes prepared by etching/insulation procedure as described in Section 1.4.4.3

Electropolymerization and electrodeposition are particularly attractive for creating ultrasmall sensors since they offer a one step controllable localization of the enzyme on the transducer surface.[25] Immobilization of the glucose oxidase at the electrode surface allows the generation of hydrogen peroxide upon to reaction between the enzyme and the glucose, see Section 1.4.4. Poising the electrode at the potential which drives the oxidation of the hydrogen peroxide, then allows monitoring the glucose concentration in the sample. Moreover, platinum has a high catalytic activity for hydrogen peroxide electro-oxidation.[22,26,27]

In this work, four different routes in the immobilization of the glucose oxidase are carried and evaluated: electropolymerization of polypyrrole in the presence of GOx, electropolymerization of phenol/allylphenol in the presence of GOx, direct electrodeposition of GOx, and finally electrodeposition of ruthenium from nitrosyl nitrate solution in the presence of GOx. Section 1.4.4 deals with the literature review regarding these methods. The chosen immobilization procedures can be automated and then they are compatible with mass-production.[1] The enzyme immobilization was usually carried on two different UMEs geometries: inlaid disk and recessed.

Examples of enzyme recessed microelectrodes can be found in the literature.[5,7,9,13] As the recess of a bare microelectrode becomes larger, the steady state current decreases.[28] Moreover, the 99% of the steady state response is achieved sooner as the recess is deeper.[29] However, the effect of a non conductive membrane coated on the top of an electrode surface is to slow the diffusion of the substrate then delaying the achievement of the steady state.[30-32] There are other benefits of a recessed design. Firstly, it assures protection of the coated layers from accidental collisions and from exposition to the bulk of the solution helping their adhesion to the surface.[9] Secondly, an increase of the electrode surface after the etching step[33-35] should allow a higher loading of GOx in the case of a thin enzyme film, *e.g.* entrapment within polyphenol matrix, which might produce a larger amperometric response to the analyte. Moreover, capillary action might be an additional benefit for sample delivery if these probes are for point-of-care measurement (glucose sensor in the very core of the lancet itself). Finally, it was also

claimed that a recess might contribute in reducing the glucose transport to the electroactive surface, spanning the linear response range.[7]

4.2 Experimental

4.2.1 Chemicals, Materials and Equipment

Pyrrole (> 97 %), ruthenium (III) nitrosyl nitrate in diluted nitric acid, N-(2-Hydroxyethyl)piperazine-N′-(2-ethanesulfonic acid) (> 99.5 %), calcium chloride (> 93 %), phosphate buffered saline (pH = 7.2), hydrogen peroxide 3% solution, D-(+)-glucose (> 99 %), L-ascorbic acid (> 99 %), acetaminophen (> 99 %), urea (> 98 %), Triton X-100 reduced, potassium chloride (99 %), potassium hexacyanoferrate(II) trihydrate (> 98.5 %), glucose oxidase Type X-S from *Aspergillus niger* (147000 Ug^{-1}) ascorbic acid (> 99 %) were purchased from Sigma Aldrich while phenol (> 99 %), 2-allyphenol (> 99 %), 2-buthoxyethanol (> 99 %) were from Acros Organics. Ruthenium hexamine chloride (98%) was from Strem Chemicals.

All the chemicals were used as received except pyrrole which was distilled under vacuum at 80 °C and then stored in 2 mL plastic vials at -18 °C. An AC transformer (Mascot, Type 9580 Output 9V AC) was employed for etching the platinum wire. D-Glucose solutions were allowed to mutarotate for 24 h before use and then stored at -4 ºC not longer than one week. All the electrochemical measurements were run using the 900a CH-instruments potentiostat. A platinum wire was employed as the counter electrode and custom-made Ag/AgCl (saturated KCl) as reference electrode (~ -0.045 V *vs.* SCE). All the aqueous solutions were prepared from Milli-Q reagent water (Millipore Corp.), 18 MΩ cm.

4.2.2 Microelectrode Preparation

UMEs were prepared and hand polished as described in Chapter 2. The diameter of the electrodes was determined by cyclic voltammetry, using ruthenium hexamine chloride (6.7×10^{-6} cm^2s^{-1})[36] or potassium hexacyanoferrate trihydrate (6.50×10^{-6} cm^2s^{-1})[20]

and/or SEM which allowed the roughness of the surface to be measured and the presence of any defect to be identified. All the electrodes employed have radius between 2 and 5 μm, except in the case of the ruthenium/GOx coated sensors, see Section 4.3.4, where the high sensitivity achieved allowed the use of UMEs with radius < 1 μm. If not otherwise stated, the size of the microelectrodes is given as radius.

For etching, the electrodes were placed in a two-electrode cell containing (37% HCl)/(5M aqueous $CaCl_2$)/(H_2O) in the ratio 10:30:60 as reported by Sun *et al.*.[37] A platinum wire was used as counter electrode. With the help of an AC transformer, instead of a function generator[37] or a more expensive device[38], the platinum wire was etched.[34,35,39] Placement of the entire cell in an ultrasonic bath was essential in order to etch the platinum wire sealed within the glass. Depending on the electrodes radius, an etching time between 4 and 30 seconds was sufficient to produce a recess having an absolute depth ($H = h/a$) between 1 and 7. The etching time appeared to be roughly proportional to the amount (volume) of the platinum being etched. Thus, smaller electrodes had to be etched for a shorter time than UMEs with larger radius if a similar depth (H) had to be achieved. After the etching step, the microelectrodes were sonicated in water for two minutes.

The recess depth was evaluated with cyclic voltammetry according to Equation 1.15. The validity of using this equation and not more complicated ones, as explained in Section 1.3.3, is justified because, after the etching step, the real shape of the platinum wire within the glass was probably conical.[34,35,39] This uncertainty is likely to dominate the accuracy of the determination of the recess depth rather than the expression employed. Nevertheless, the data obtained using Equation 1.15 suggested that H was generally bigger than 1 in agreement with the assumptions of this expression.

Before the enzyme immobilization, the electrodes were cleaned by cycling in 1.0 M H_2SO_4 between the hydrogen and oxygen evolution regimes. The electrochemical surface area was calculated as explained in Section 1.3.6 and this value used in order to normalize the sensitivity of the biosensors except in the case of polypyrrole. The electrochemical instead than the geometrical area was preferred because this normalization allows the comparison with the data of the recessed electrodes and takes in account the difference in the roughness factor. The enzyme was immobilized on the electrode surface according to the procedures described in the following section. The

term U is introduced as the quantity of the enzyme able to oxidize 1.0 μmole of β-D-glucose to D-gluconolactone and H_2O_2 per minute at pH 5.1 and at 35 °C, equivalent to an O_2 uptake of 22.4 μl per minute.[40] After the coating step, the electrodes were rinsed with PBS and stored overnight in PBS before an amperometric test was run. This allows any loose unbound enzyme to be released out of the membrane.[41]

The UMEs were placed in a three-electrode cell where Ag/AgCl electrode and a platinum wire were employed as reference and counter electrode. All the potentials reported, if not differently stated, are against this reference. The cell contained 3.5 mL of PBS buffer and the solution was stirred by a magnetic stirrer at 400 rpm for few seconds after the glucose injection. The potential was held at 0.65 V *vs.* Ag/AgCl. After the current reached a stable steady value, small aliquots of a very concentrated glucose solution (~ 1 M) were added to the solution in order to produce millimolar concentration. All the measurements were run in a Faraday cage. The calibration curves (Δi_{ss} *vs.* C_{glu}) were constructed plotting the current output of the enzyme sensors against the bulk concentration of glucose. These data were fitted by non linear regression using the GraphPad Prism software package (GraphPad Software Inc.) allowing the determination of Δi_{max} and K_M^{app} values.

4.2.3 Glucose Oxidase Immobilization Procedures

4.2.3.1 Polypyrrole/GOx Coated UMEs

Three main different conditions were studied in order to polymerise pyrrole in presence of GOx. In the first, UMEs were immersed in 0.3 M pyrrole/100 UmL^{-1} GOx solutions in 10 mM HEPES and polymerization of pyrrole driven potentio-statically (ΔE = 0.8 V for ~ 600 seconds) or by dynamically scanning the potential between -0.2 V and 1.4 V thirty times at 100 mVs^{-1}. Then, 0.05 M pyrrole/1000 Uml^{-1} GOx solutions in aqueous 0.05 - 0.1 M KCl were employed and polymerization was driven by scanning the potential between 0 V and 1.3 V thirty times at 100 mVs^{-1} or holding the potential at 0.75 V for ~ 100 seconds. Finally, polypyrrole was grown from 0.3 - 3 M pyrrole/1000 UmL^{-1} GOx solutions in 20 mM HEPES buffer both potentio-statically (ΔE = 0.8 V for

~ 100 seconds) and by dynamically sweeping the potential between -0.2 V and 0.9 - 1.4 V twenty times at 100 mVs^{-1}.

4.2.3.2 Polyphenol/GOx Coated UMEs

The films were deposited from solutions containing 60 mM phenol, 150 mM allylphenol, 2% buthoxyethanol and 1000 Uml^{-1} GOx in PBS buffer similarly to what reported by Hrapovic *et al.*.[20] The polyphenol chains were expected to be cross-linked via the allyl groups to form an insulating polymer network.[20] The authors performed the electrodeposition at 4.0 V for 14 min, while in this work a potentio-dynamic polymerization, was preferred as the enzyme had more time to diffuse to the polymer surface.[42] The potential was scanned between 0.1 V and 0.9 V *vs.* Ag/AgCl at 10 mVs^{-1} ten times. The electrodes were left in the solution for at least 10 minutes up to 1.5 hours prior to start the electropolymerization step. This preliminary step should drive the enzyme adsorption which might affect the phenol/GOx films properties and then the amperometric response because of the different enzyme loading.

4.2.3.3 GOx Coated UMEs

3000 UmL^{-1} GOx and 0.8 mM Triton X-100 reduced solution in PBS buffer was employed for the enzyme electrodeposition. A constant potential of 1.3 V *vs.* Ag/AgCl was applied for times between 10 minutes and 1 hour as reported by Matsumoto *et al.*.[43] As soon as the UME was dipped in the solution, the potential was stepped to 1.3 V. According to Matsumoto and co-workers[43], at this electrodeposition potential the thickest GOx layer should result *i.e.*, ~ 500 nm.

4.2.3.4 Ruthenium/GOx Coated UMEs

3000 U of GOx were dissolved in 1 mL of PBS buffer then 0.5 mL of the ruthenium nitrosyl nitrate solution was added. After stirring, the pH of the mixture was measured ≈ 4.5, which, according to Schuvailo and co-workers,[10] seems to be the optimal pH for

the electrodeposition of ruthenium (highest pH value at which the solution still remains stable, no ruthenium hydrate precipitation). The electrode was dipped into the mixture and a first CV acquired at this time (t = 0). After a certain time (between 20 minutes and 1.5 hours), a second CV was acquired and then ruthenium deposited at a constant potential (-0.5 V *vs.* Ag/AgCl) for five or ten minutes. Electrodeposition potential and enzyme concentration were chosen according to the best results reported by Schuvailo *et al.*[10] and Kohma *et al.*[12], respectively. Leaving the UMEs in the solution for a different time, prior to the electrodeposition step, can affect the loading of the enzyme as the latter might adsorb on the electrode surface and consequentially the ruthenium/GOx films properties and the amperometric response. In the case of the recessed microelectrodes, as the size of the latter was smaller, see Section 4.3.4, the electrodeposition time was decreased to 2 minutes and they were left dipping in the solution prior to the coating step for 20 minutes.

4.3 Results and Discussion

Linearization models *e.g.*, Lineweaver-Burk or Eadie-Hofstee expressions, are a simple and widely employed way to analyze enzyme kinetic data.[44] However they suffers from amplification of the errors associated with the data at low substrate concentration.[44] In this work it was then preferred to calculate the values of Δi_{max} and K_M^{app} from non linear regression fitting based on the Michaelis-Menten equation.

The following abbreviations are here given: Pt = platinum, Et = etched, PPy = polypyrrole, PPh = polyphenol, Ru = ruthenium, GOx = glucose oxidase. So for example, Pt-Et-PPy/GOx are recessed microelectrodes where pyrrole has been electropolymerized in presence of the enzyme.

Preliminary experiments with inlaid disk and recessed uncoated platinum microelectrode *i.e.*, no immobilized enzyme, showed that glucose oxidation was not visible at the potentials applied for the detection (results not shown).

4.3.1 Polypyrrole/GOx Microsensors

The polymerization on the platinum recessed microelectrodes (2.3 μm < a < 5.5 μm, 1 < H < 3.5) was successfully achieved employing solutions of 100 UmL^{-1} GOx and 0.3 M pyrrole in 10 mM HEPES buffer under both potentiodynamic and potentiostatic control. The current in Figure 4.1A is negative (oxidative) in line with the mechanism of pyrrole polymerization.[45-47] After 40 - 50 seconds a sharp increase in the current might suggest deposition of polypyrrole beyond the electrode recess. Indeed, Figure 4.1B shows the presence of a polymer deposit covering the microcavity. Significantly, these electrodes did not show any response to glucose. In order to understand if the lack of a response arose from the thick polymer membrane covering the platinum surface, hydrogen peroxide was injected, in order to have in the cell a 0.01 mM H_2O_2 concentration, while the electrode potential was paused at 0.65 V and the current was monitored. Under these circumstances, an oxidation current superimposed to the background was observed which agrees with the oxidation of hydrogen peroxide (result not shown). The latter result suggested that low GOx loading might be responsible for a production of H_2O_2 which was too small to be detected. The same behaviour was obtained when the protruding layer of polypyrrole was removed by careful polishing.

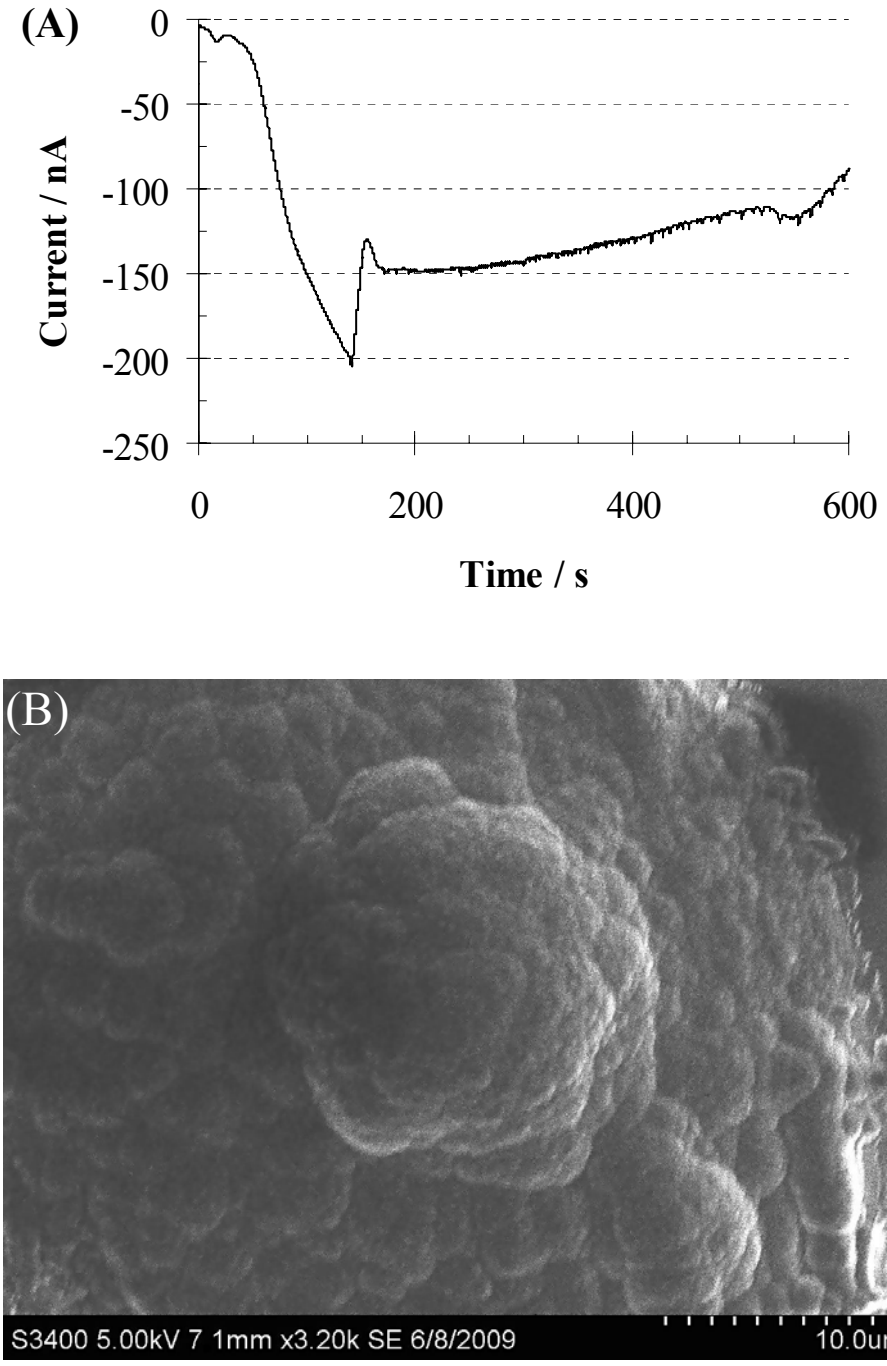

Figure 4.1 (A) Amperometric profile during polymerization from a 0.3 M pyrrole/100 UmL^{-1} GOx solution in a 10 HEPES buffer at a recessed electrode (a = 5.4 μm, H = 3.3). (B) SEM picture of the same microelectrode after pyrrole polymerization which shows the deposit protruding from the microcavity.

In order to increase the enzyme loading, electropolymerization under potentiostatic or potentiodynamic control was carried on platinum recessed microelectrodes (2.9 μm < a < 5.6 μm, 1.5 < H < 3) from solutions having a higher GOx content (1000 UmL^{-1}) and a

lower pyrrole concentration (0.05 M) in aqueous 0.05 - 0.1 M KCl. Voltammograms and amperometric curves were typically like the ones represented in Figures 4.2 and 4.3, respectively. In fact, an oxidative peak with an $E_{1/2} \sim 0.8$ V is present in the first scan in Figure 4.2. However, the peak is quite small and it disappears in the following scans. Then, it is very hard to understand if the voltammogram agrees with the traditional pyrrole polymerization mechanism *i.e.*, peak which progressively shifts toward less oxidative potential and whose current intensity slowly decreases in the following scans.[47] Moreover, Figure 4.3 shows that the current at three different microelectrodes was dominated by a reductive component. It must be concluded that such current was not consistent with the oxidative propagation mechanism of the polypyrrole as apparent comparing Figure 4.3 with 4.1A. It is probable that the polymerization of pyrrole did not happen in the conditions of Figure 4.3.

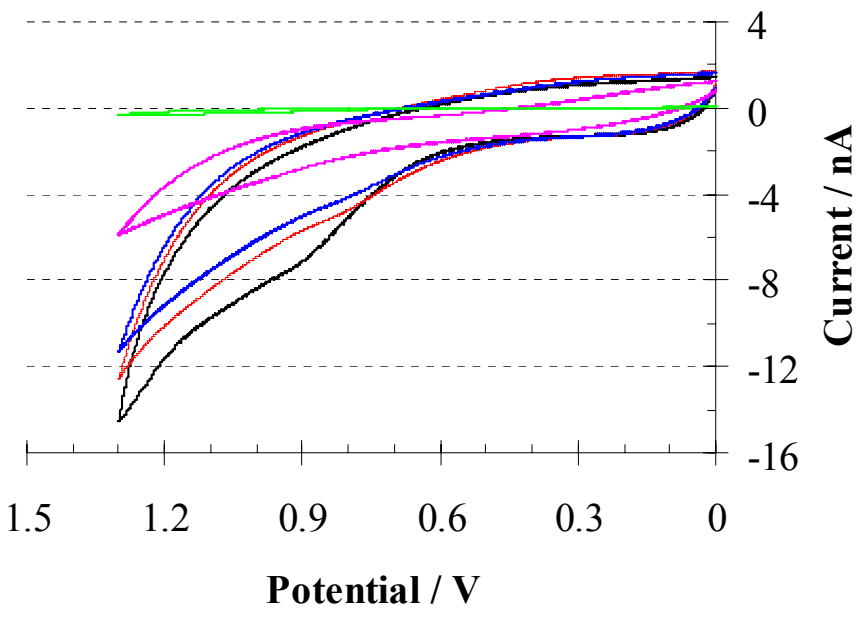

Figure 4.2 Electropolymerization of pyrrole at Pt-Et-PPy#3 from a 0.1 M pyrrole/1000 UmL^{-1} GOx solution in 0.1 M KCl by sweeping the potential from 0 V to 1.3 V at 100 mVs^{-1} for thirty times. The graph shows the (—) 1st, (—) 6th, (—) 12th, (—) 18th and (—) 24th sweep recorded during the polymerization. The microelectrode had radius and a recess depth of 2.9 μm and 1.8, respectively.

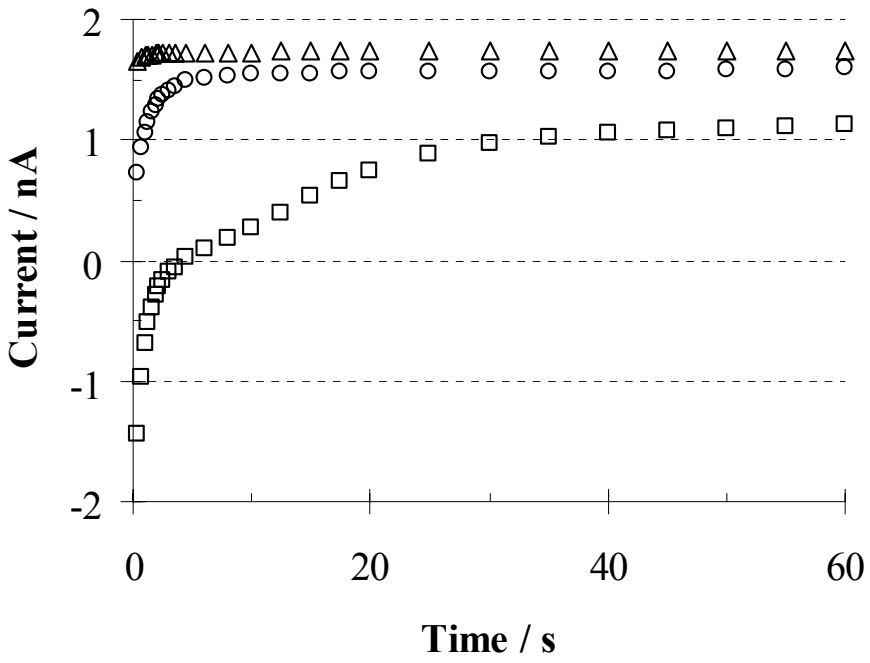

Figure 4.3 Potentiostatic electropolymerization of pyrrole from a 0.05 M pyrrole/1000 UmL^{-1} GOx solution in aqueous 0.05 mM KCl for three microelectrodes: (Δ) Pt-Et-PPy#4 (a = 3.4 μm, H = 2.6), (○) Pt-Et-PPy#5 (a = 4.7 μm, H = 2.7) and (□) Pt-Et-PPy#7 (a = 4.4 μm, H = 2.8). Potential was held at 0.75 V *vs.* Ag/AgCl.

The enzyme electrodes so fabricated were poorly sensitive to glucose. Besides, background currents in the order of 1.6 - 1.8 nA were experienced while glucose addition generated at best a signal of few $pAmM^{-1}$. Belanger *et al.*[48] argued that enzymatically produced H_2O_2 might be oxidizing the PPy film instead than being detected at the electrode. Attempts to decrease the background current by chemical overoxidation of the polypyrrole, by dipping of the microelectrodes in a low concentration hydrogen peroxide solution, did not give good results. However, an increase in the sensitivity was apparent (two or three order of magnitude) which agrees with the conclusions by Belanger and co-workers.[48] Figure 4.4 reports the changes in the current against glucose concetration plot for one of the polypyrrole/GOx sensor upon treatment with hydrogen peroxide.

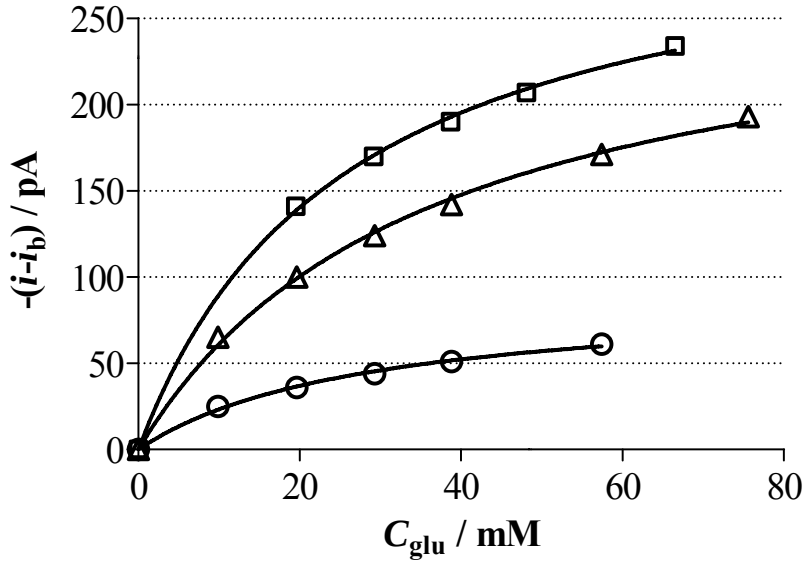

Figure 4.4 Changes in the current *vs.* glucose concentration plot for Pt-Et-PPy#3 (a = 2.9 μm, H = 1.8) when the electrode was treated with H_2O_2. The sensor was prepared by potentiodynamic polymerization of pyrrole from a 0.05 M pyrrole/1000 UmL^{-1} solution in aqueous 0.1 M KCl as described in Section 4.2.3.1. The graph shows the response of the electrode to glucose when (○) the latter was stored overnight in PBS buffer after the pyrrole polymerization, (Δ) following immersion in 0.6 mM H_2O_2 for 5 minutes and at last after (□) it was immersed in 10 mM H_2O_2 for 1.5 hours. The solid lines (—) show the best fitting in the three cases above explained assuming that Michaelis-Menten kinetics is followed. i_b and C_{glu} are the background current and the glucose concentration.

Table 4.1 reports the data obtained with the PPy/GOx sensors. The best result was obtained when the electrode was prepared under potentiodynamically polymerization control with a electrolyte concentration (KCl) of 0.05 M. This might arise from a more effective enzyme entrapment in the polypyrrole matrix in the potentiodynamic procedure. However, this was the only working electrode of three fabricated employing the same procedure that exhibits this improved performance and the hypothesis was not investigated substantially. Besides, the stability of the signal was not satisfactory as a positive (reductive) drift of the current was apparent (results not shown). Because of the drift in the signal, the data in Table 4.1 might not be very accurate. Electrochemical stability of polypyrrole has already been questioned by several investigators.[42,45]

Table 4.1 Glucose sensor microelectrodes fabricated as entrapping GOx in an electrochemical grown polypyrrole film. In particular, sensors were prepared from a 0.05 M pyrrole/1000 Uml^{-1} GOx solution in aqueous 0.05 - 0.1 M KCl as described in Section 4.2.3.1. Δi_{max} and K_M^{app} values were calculated fitting the Δi_{ss} *vs.* C_{glu} plots by non linear regression and assuming Michaelis-Menten kinetics. i_b and Sens are respectively the background current and the sensitivity of the sensors.

Electrode	i_b / nA	Δi_{max} / pA	K_M^{app} / mM	Sens / nAM^{-1}
^Pt-Et-PPy#3	1.69	89 ± 5	28.4 ± 3.5	2.5
Pt-Et-PPy#4	1.74	10 ± 1	14.7 ± 1.9	0.4
Pt-Et-PPy#5	1.75	10 ± 1	16.6 ± 4.4	0.4
Pt-Et-PPy#7	1.76	13 ± 1	19.7 ± 3.5	0.4

^This electrode was prepared by potentiodynamic polymerization of pyrrole as described in Section 4.2.3.1.

Some reports argued about the difficulty of growing polypyrrole in the presence of GOx which eventually resulted in a less conductive film or irreproducible results.[45,46] Indeed, GOx adsorption on the electrode surface seems to affect the nucleation of the polypyrrole.[46] Moreover, the physically entrapped enzyme sterically hinders the growth of polypyrrole leading to shorter chain length or a higher amount of defects.[46] To address this possibility the polymerization of pyrrole from 1000 UmL^{-1} GOx solutions was carried on inlaid disk UMEs (2.7 μm < a < 3.7 μm). The advantage is that the eventual coating layer can be easily imaged with SEM. Indeed, Figure 4.5 shows that the polypyrrole/GOx coverage on the microelectrode surface was poor even when concentrations of pyrrole up to 4 M were employed for the electropolymerization. It is concluded that the enzyme adsorption at concentration ≥ 1000 Uml^{-1} hampered the polypyrrole formation. Differences in the polymer growth *i.e.*, thinner rods in Figure 4.5A than in Figure 4.5B, most likely arose from the different polymerization methods *e.g.*, pyrrole concentration and type of electrolyte.

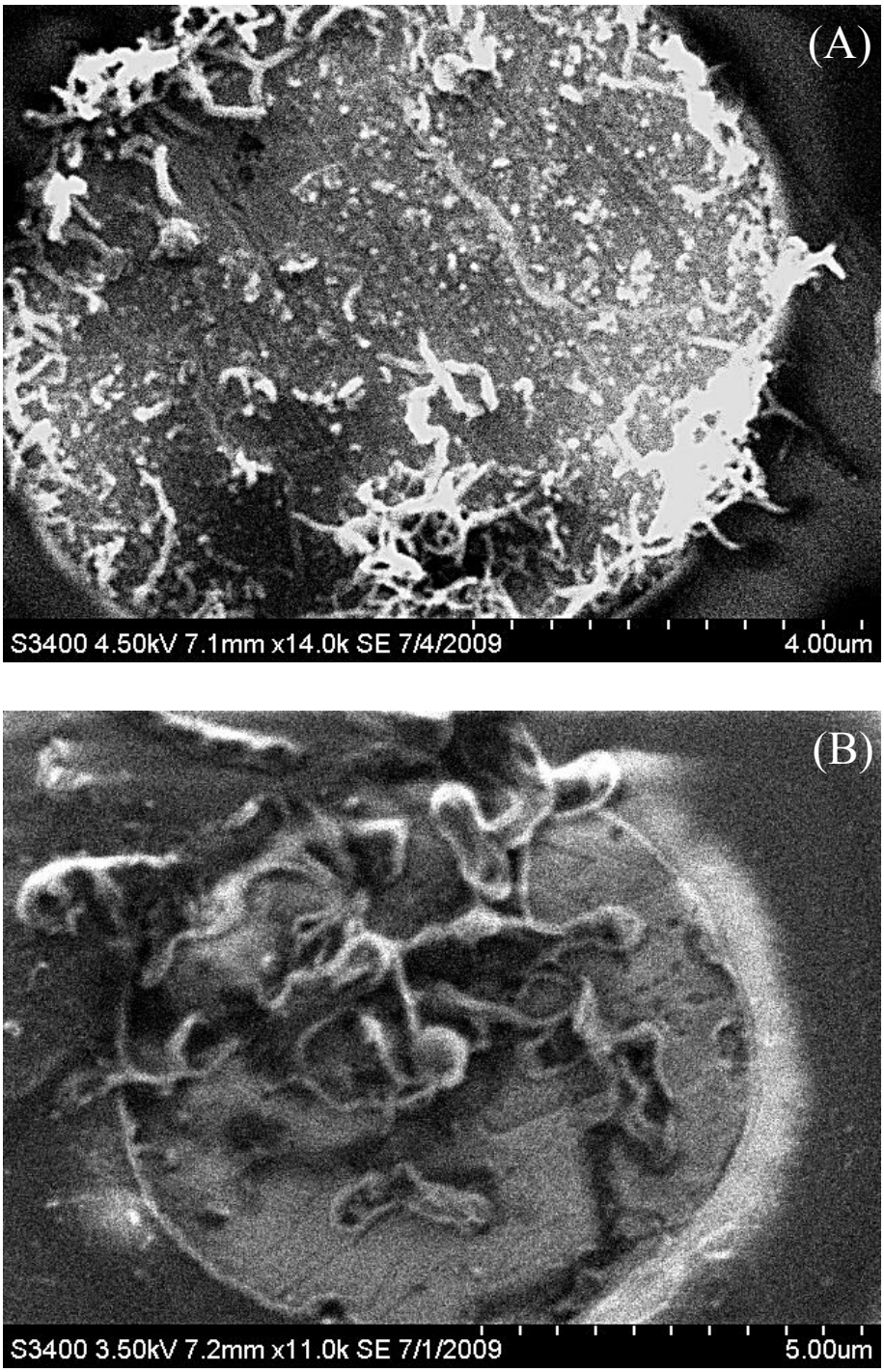

Figure 4.5 SEM images of electrodes coated with polypyrrole and glucose oxidase. In (A) the microelectrode (a = 3.7 μm) was prepared from a 0.3 M pyrrole/1000 UmL^{-1} GOx solution in 20 mM HEPES buffer by sweeping the potential twenty times between -0.2 V and 1.4 V. (B) The microelectrode (a = 5.4 μm) was prepared from a 0.05 M pyrrole/1000 UmL^{-1} GOx solution in aqueous 0.05 M KCl. The potential was held at 0.75 V *vs.* Ag/AgCl for two minutes. The scale, magnification and accelerating voltage are shown on the individual image.

The difficulties experienced in the pyrrole electropolymerization at GOx concentration ≥ 1000 UmL^{-1} might be overcome by reducing the enzyme concentration during that step. However, the loading of the enzyme might not be enough to ensure sensitive glucose detection as pointed out above. A two step polymerization strategy *i.e.*, preliminary covering of the platinum surface with a thin layer of polymer without enzyme, might also solve this problem.[45] However, the enzyme loading and its distance from the electrode surface is likely to reduce the detection sensitivity. Above all, the large background current (in the order of few nA) and the significant drift in the current before and after the glucose addition experienced during the sensor amperometric testing suggested a shifting towards other enzyme immobilization procedures.

4.3.2 Polyphenol/GOx Microsensors

The polymerization of phenol as described in Section 4.2.3.2 was carried on both inlaid disk (2.6 μm < a < 4.0 μm) and recessed (3.5 μm < a < 4.3 μm, 0.7 < H < 1.8) microelectrodes. Figure 4.6 shows the typical voltammograms during the potentiostatic polymerization of phenol. In Figure 4.6A, the UME was dipped into the solution mixture for twenty minutes prior the polymerization step. The presence of a broad peak on the first scan with an onset at ~ 0.35 V was similar to previous literature results for the phenols polymerization.[49,50] After the first sweep, the current decreases significantly which agrees with the insulating character of these films.[41,50-52] However, Figure 4.6B shows that, when the electrodes were kept into the solution for a longer time (~ 1.5 hours) before the polymerization step, the current in the first sweep was almost an order of magnitude smaller. This difference should not depend in the small differences in the radius and depth of the recess but it probably arises from the enzyme adsorption on the electrode. The adsorption would then decrease the available electrochemical active surface area giving rise to a lower current. This hypothesis might agree with the fact that the sensitivity of the sensors was higher when the time length of pre-polymerization step was longer. However, these conclusions have to be supported with a more detailed study and a larger sample of sensors.

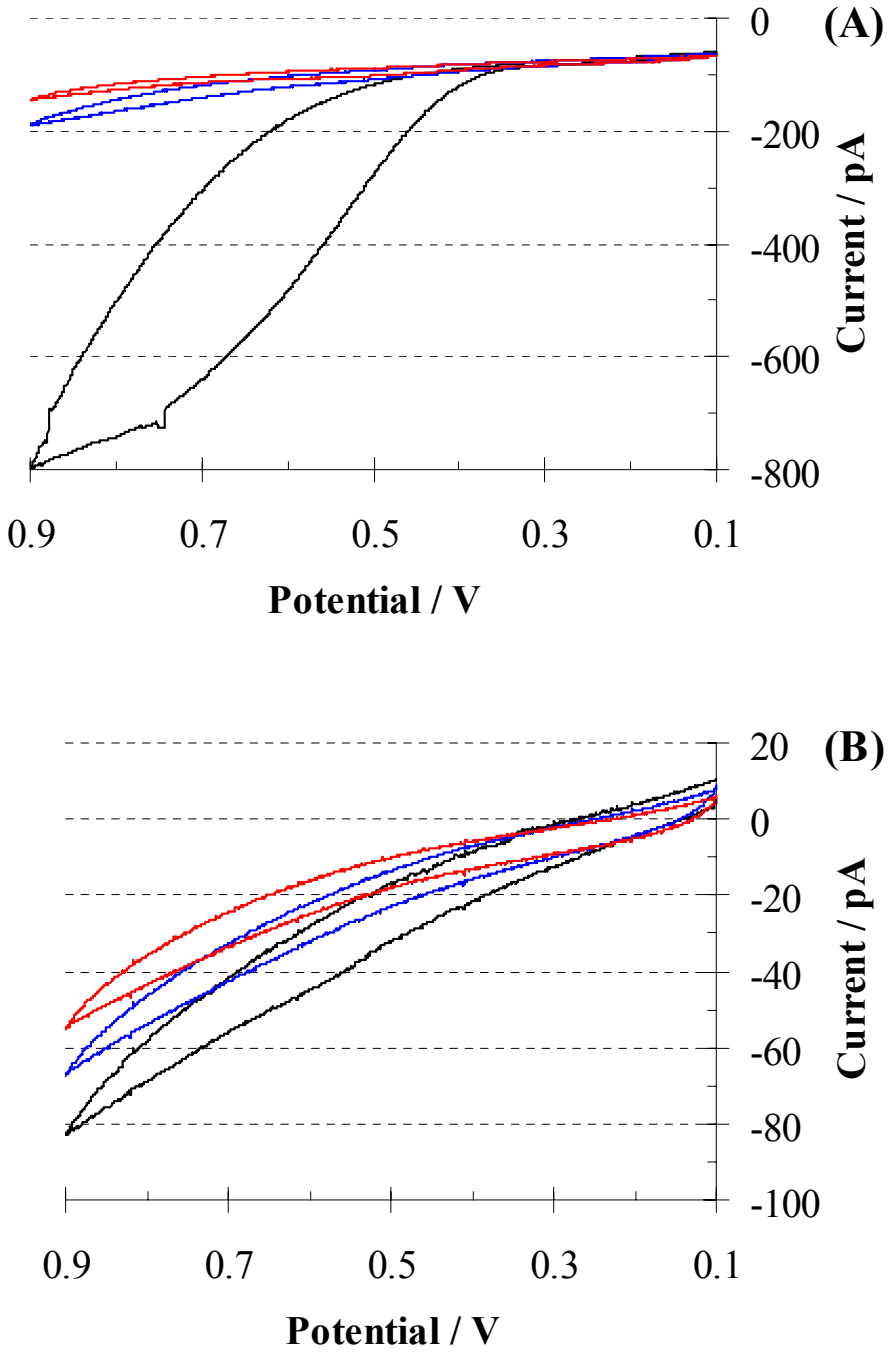

Figure 4.6 Potentiodynamic polymerization from a 60 mM phenol/ 150 mM allylphenol/ 3000 UmL^{-1} GOx solution in PBS buffer. In (A) the microelectrode (Pt-Et-PPh#2, a = 3.9 μm, H = 1.8) was left 20 minutes dipping into the solution prior to start the potential sweep while in (B) the probe (Pt-Et-PPh#4, a = 2.3 μm, H = 0.8) was left 1.5 hours. The potential was swept between 0.1 V and 0.9 V at a scan rate of 10 mVs^{-1}. The graphs show the (—) 1st, (—) 5th and (—) 10th sweeps.

SEM images did not show any physical detail of the polyphenol films coated on the electrode surface because the charging effects experienced during the imaging of the coated microelectrodes did not allow the achievement of a fine focus. These data suggest that a modification occurred and they might agree with the insulating nature of these films which is also supported by the voltammetry investigation using $[Fe(CN)_6]^{4-}$ as solution phase redox probe. The latter investigation gives an insight of the insulating and exclusion properties of these films as $[Fe(CN)_6]^{4-}$ can also partially mimic the behaviour of negatively charged interferents in a glucose sensor *e.g.*, ascorbic acid. Indeed, Figure 4.7 shows the voltammograms before and after the etching step and finally after the enzyme immobilization within the polyphenol layers. The first observation is that the current decreased in all cases after the etching step and again after the polymer coating, which agrees with the formation of a recess and the passivation of the electrode surface, respectively. However, the efficiency of the polyphenol coating was not completely reproducible as the ratio between the steady current before and after polyphenol coating ranged between 1.3 and 12.6. This aspect is very important in the discussion about the rejection of interferents, see after in this section.

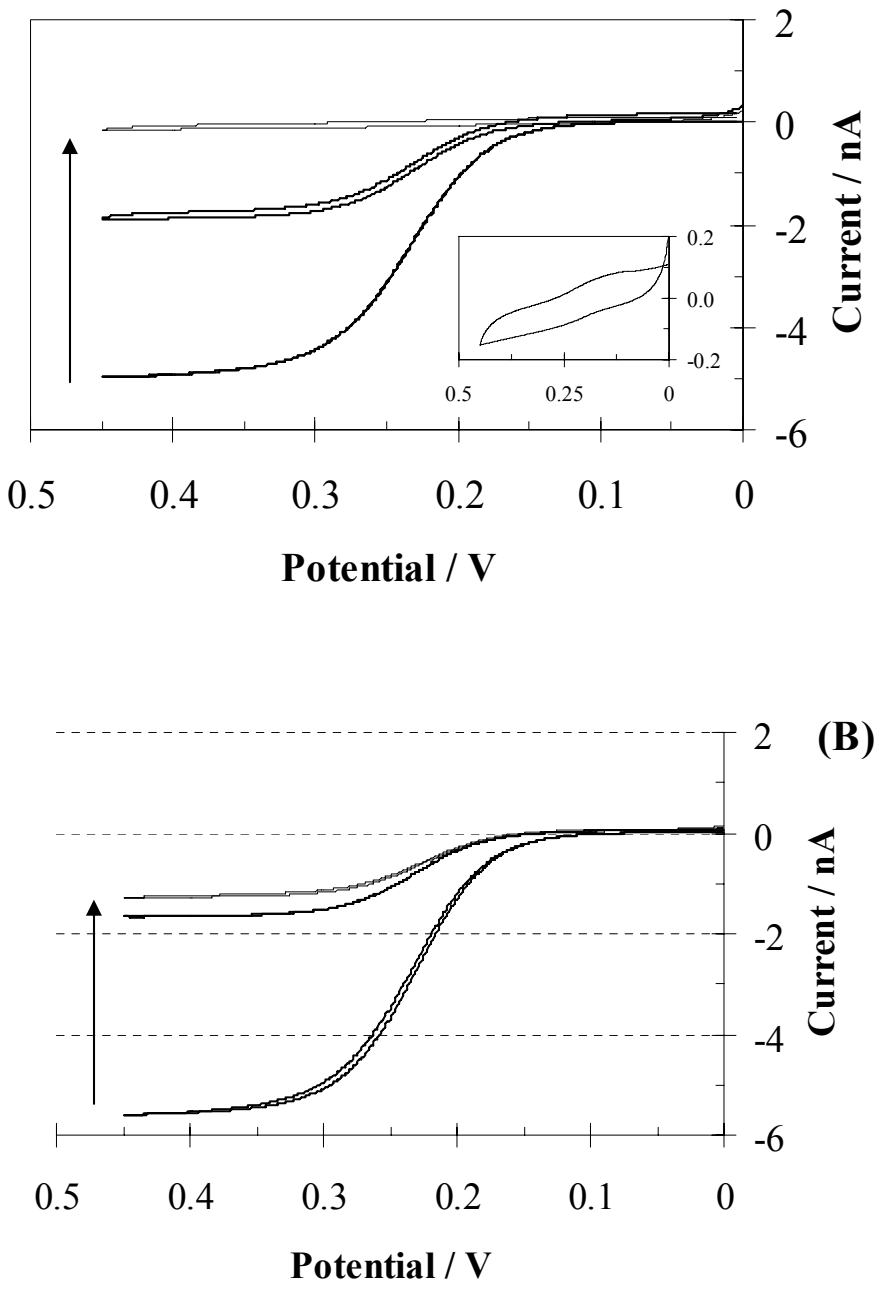

Figure 4.7 Comparison of the voltammograms using $[Fe(CN)_6]^{4-}$ as redox probe at (A) Pt-Et-PPh#3 (a = 3.5 μm, H = 1.4) and at (B) Pt-Et-PPh#2 (a = 3.9 μm, H = 1.8) before and after the etching step and after the polyphenol/GOx coating (as indicated by the direction of the arrows). The inset in (A) shows an enlargement of the voltammogram after the polyphenol coating step. The units of measure in the inset are the same as in the main figure. Potential was swept between 0 V and 0.45 V *vs.* Ag/AgCl. Voltammograms were acquired at a scan rate of 2 mVs^{-1} using a 5.5 mM $[Fe(CN)_6]^{4-}$ solution in aqueous 0.1 M KCl.

Figure 4.8A shows a typical plot of the current profile upon to multiple additions of 5 mM glucose into the electrochemical cell. The vertical lines in the figure are coinciding with the opening of the Faraday cage and with the injections of glucose solution which disturbed the recorded signal. It is apparent that the steady state after the glucose addition was reached very quickly (< 3 - 5 seconds) and was very stable. Indeed, no drift in the current was observed over 100 seconds which confirms the stability of the coating towards enzymatically generated H_2O_2. Figure 4.8B reports the plot of the amperometric signal due to oxidation of H_2O_2 as function of the glucose concentration for the same electrode in the former figure. The non linear regression gives R-squared value equal to 0.998 which supports the fact the enzyme sensors followed the Michaelis-Menten kinetics.

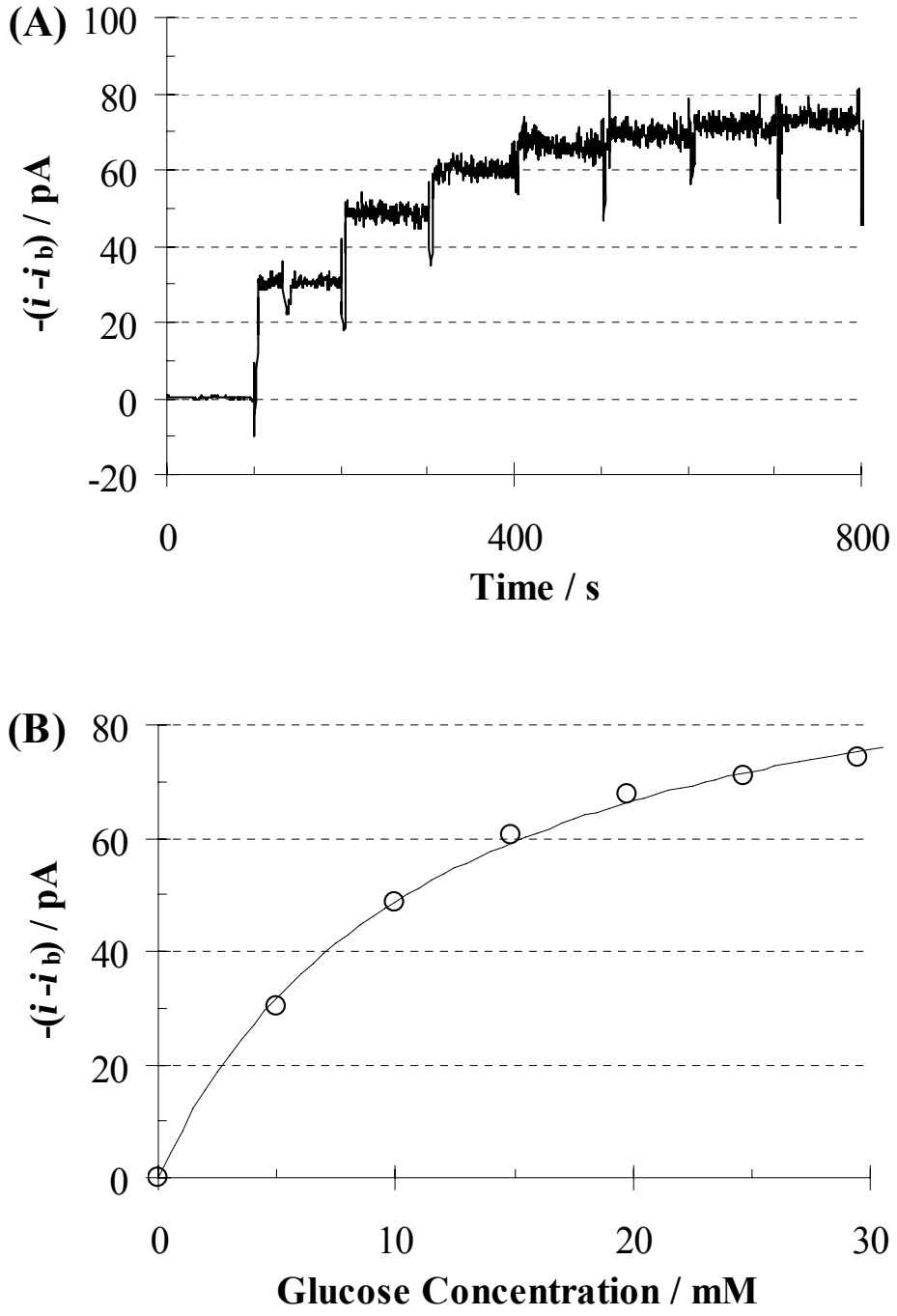

Figure 4.8 (A) Amperometric profile at Pt-Et-PPh#4 (a = 2.3 μm, H = 0.8) upon to the addition of 5 mM glucose at regular times (~ 100 seconds). (B) Current *vs.* glucose concentration plot for the same electrode in (A). The empty circles (○) represent the experimental data while the solid line (—) shows the best fitting assuming that Michaelis-Menten kinetics is followed. The electrode was fabricated from polymerization of phenols in presence of glucose oxidase as described in Section 4.2.3.2. i_b is the background current.

Table 4.2 reports the data obtained for the polyphenol/GOx sensors prepared in this work. It is apparent that with the polyphenol coated microelectrodes the background current was decreased by an order of magnitude compared to that found for the polypyrrole coated UMEs. The smaller background current agrees with the insulating properties and low dielectric of the polyphenol films. Hrapovic and co-workers[20] fabricated glucose sensors employing similar enzyme entrapment procedure and microelectrodes with radius ranging between 3 and 5 μm. The authors achieved sensitivities of ~ 50 $mAM^{-1}cm^{-2}$ which are in the same order of magnitude of the top ones in Table 4.2, *i.e.* ~ 20 $mAM^{-1}cm^{-2}$ normalizing the data for the geometric area. However, the authors reported background current which were at least an order of magnitude lower. In their work[20], phenol/allylphenol mixture was polymerized from methanol/water (pH = 9.2) solution in presence of GOx at 4 V for 15 minutes. The different conditions might be responsible for these differences. This conclusion is also confirmed by the fact that in this reference the enzyme saturation occurred for glucose concentration larger than 10 mM while in this work K_M^{app} values 2 – 3 times larger were found. Finally, Table 4.2 shows that disk-inlaid and recessed UMEs had similar K_M^{app} values which excludes a contribution of the recess in spanning the linear range differently from what stated elsewhere.[7] Though the data obtained for the polyphenol/GOx are satisfactory, the fabrication of submicrometer probes was not feasible with this immobilizing strategy because, with sensitivity in this order of magnitude, the amperometric signal due to the glucose would be small to be detected.

Table 4.2 Glucose sensor microelectrodes fabricated by entrapping glucose oxidase in polyphenol films grown under potentiodynamic control as described in Section 4.2.3.2. Δi_{max} and K_M^{app} values were calculated fitting the Δi_{ss} *vs.* C_{glu} plots by non linear regression and assuming Michaelis-Menten kinetics. i_b, A_m and Sens are the background current, the microscopic area of the electrode and the sensitivity, respectively. A_m was calculated from the charge passed under the platinum oxide reduction from a voltammogram in 1.0 M H_2SO_4 at 5 Vs^{-1} as explained in Section 1.3.6. The roughness factor of the disk inlaid UMEs is indicated in bracket besides the value of the microscopic area.

Electrode	$10^6 \times A_m$ / cm^2	i_b / pA	Δi_{max} / pA	K_M^{app} / mM	Sens / mAM^{-1}cm^{-2}
^Pt-PPh#1	1.88 (8.9)	174	95 ± 23	13.3 ± 5.9	2.31 ± 0.14
Pt-PPh#2	0.48 (1.1)	174	11 ± 2	26.4 ± 7.2	0.64 ± 0.06
Pt-Et-PPh#2	0.96	176	13 ± 1	36.7 ± 2.3	0.32 ± 0.04
Pt-Et-PPh#3	7.14	163	43 ± 1	24.0 ± 0.7	0.18 ± 0.02
^Pt-Et-PPh#4	1.74	170	105 ± 3	11.5 ± 0.9	2.84 ± 0.40
Pt-Et-PPh#7	6.75	174	11 ± 1	22.9 ± 3.0	0.48 ± 0.03

^These microsensors were left dipping in the solution for 1.5 hours prior to start the polymerization step.

Finally, the microelectrodes were tested against the common interferents present in a blood sample. Interferents chosen were: ascorbic acid, acetaminophen and urea at their maximum physiological concentration *i.e.*, 0.11 mM, 0.17 mM and 5 mM,[18] respectively. Addition of urea did not produce a detectable signal while ascorbic acid and acetaminophen additions had a measurable effect on the current as shown in Figure 4.9. Indeed, the sensor in this figure shows sensitivity towards ascorbic acid and acetaminophen of ~ 160 and ~ 90 mAM^{-1}cm^{-2} respectively which are larger than the highest glucose sensitivity reported in Table 4.2. Similar results were obtained with the other PPh/GOx microsensors. This result is again in contrast with what reported by Hrapovic and co-workers.[20] However, the different coating procedure might be responsible of the different membrane permselectivity.

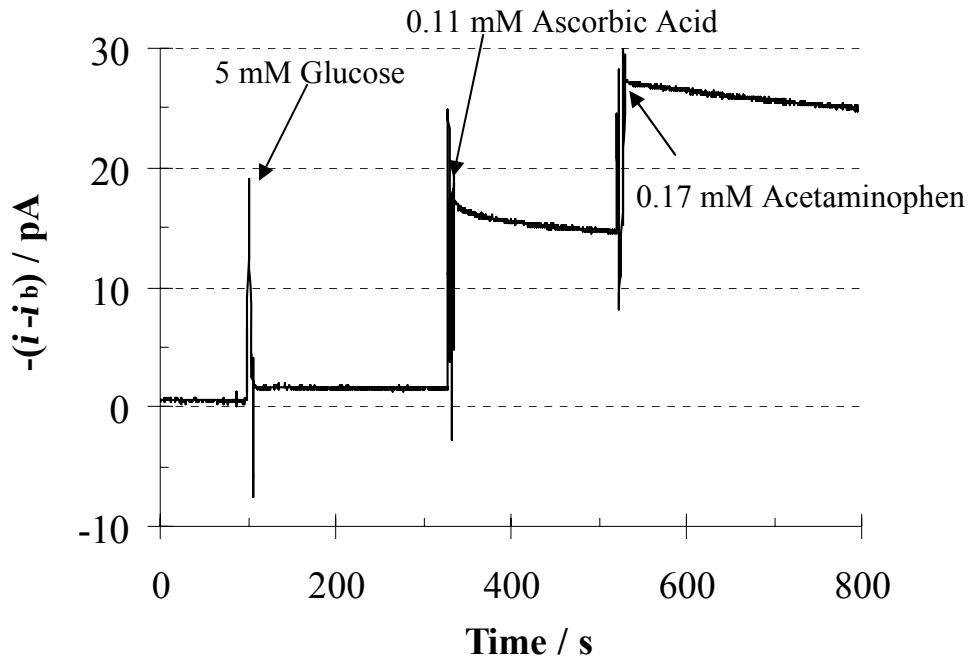

Figure 4.9 Amperometric profile at Pt-Et-PPh#7 (a = 2.7 μm, H = 4.9) upon to the addition of 5 mM glucose, 0.11 mM ascorbic acid and 0.17 mM acetaminophen at the time indicated by the arrows. The microsensor was fabricated as described in Section 4.2.3.2. i_b is the background current.

4.3.3 GOx Microsensors

Direct deposition of glucose oxidase, as demonstrated by Matsumoto *et al.*[43], enables a high loading of the enzyme to be achieved. Indeed, Chen *et al.*[53] combined the enzyme deposition with a post phenol polymerization and cross-linking steps. If the sensitivity of the sensors prepared by immobilization of the glucose oxidase within the polyphenol matrix is limited by the loading of the enzyme, a preliminary enzyme electrodeposition step might improve their performance.

The electrodeposition of GOx as described in Section 4.2.3.3 was performed on both inlaid disk (3.5 μm < a < 4.6 μm) and recessed microelectrodes (4.1 μm < a < 5.7 μm, 3.2 < H < 4.2). Glucose oxidase was electrodeposited at 1.3 V *vs.* Ag/AgCl which, according to Matsumoto and co-workers[43], should allow the thickest enzyme deposit (~ 500 nm). Figure 4.10 shows a typical amperometric profile during the enzyme electrodeposition. No correlation was found in this work between the electrodeposition

time and the sensors sensitivity towards glucose. Besides, SEM pictures of the inlaid disk UMEs after the electrodeposition step do not show any feature on the microelectrode surface associated with the GOx deposition. It must be concluded that the enzyme multilayer was thinner than the ~ 500 nm thick GOx film observed by Matsumoto and co-workers using similar experimental conditions.[43] Use of Triton X-100 reduced in this work instead than Triton X-100 like in reference [43] should not be responsible for this different behaviour. In fact, Triton X-100 is a non ionic detergent containing a benzene group while in the Triton X-100 reduced the benzene is replaced with a cyclohexane group but its properties as surfactant are claimed to be unchanged.

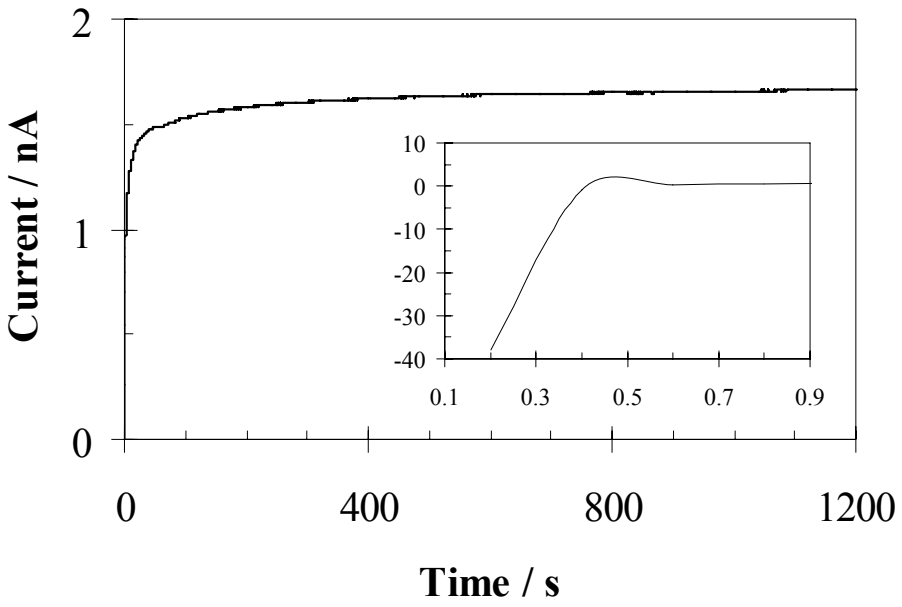

Figure 4.10 Amperometric profile at Pt-Et-GOx#3 (a = 5.5 μm, H = 4.1) during the enzyme deposition from 3000 UmL^{-1} GOx solution in PBS buffer. Potential was held at 1.3 V *vs.* Ag/AgCl. The inset shows an enlargement of the amperometric profile at short times. The units of measure in the inset are the same as in the main figure.

Figure 4.11A shows the typical sensor response upon to the injection of glucose into the electrochemical cell. Good stability of the signal before and after the injection was observed *i.e.*, no significant current drift can be seen in this figure. However, a certain delayed response can be noticed especially when compared to the PPh/GOx sensors as shown in Figure 4.8A. Indeed, after the glucose addition, 10 - 15 seconds were necessary to achieve the steady state value. The delay might arise from the formation of

a very compact enzyme layer on the electrode surface slowing the diffusion of the substrate and/or of the hydrogen peroxide enzymatically produced. Figure 4.11B reports the Δi_{ss} *vs.* C_{glu} plot for the same electrode tested in the previous figure and the non linear regression fitting the experimental data.

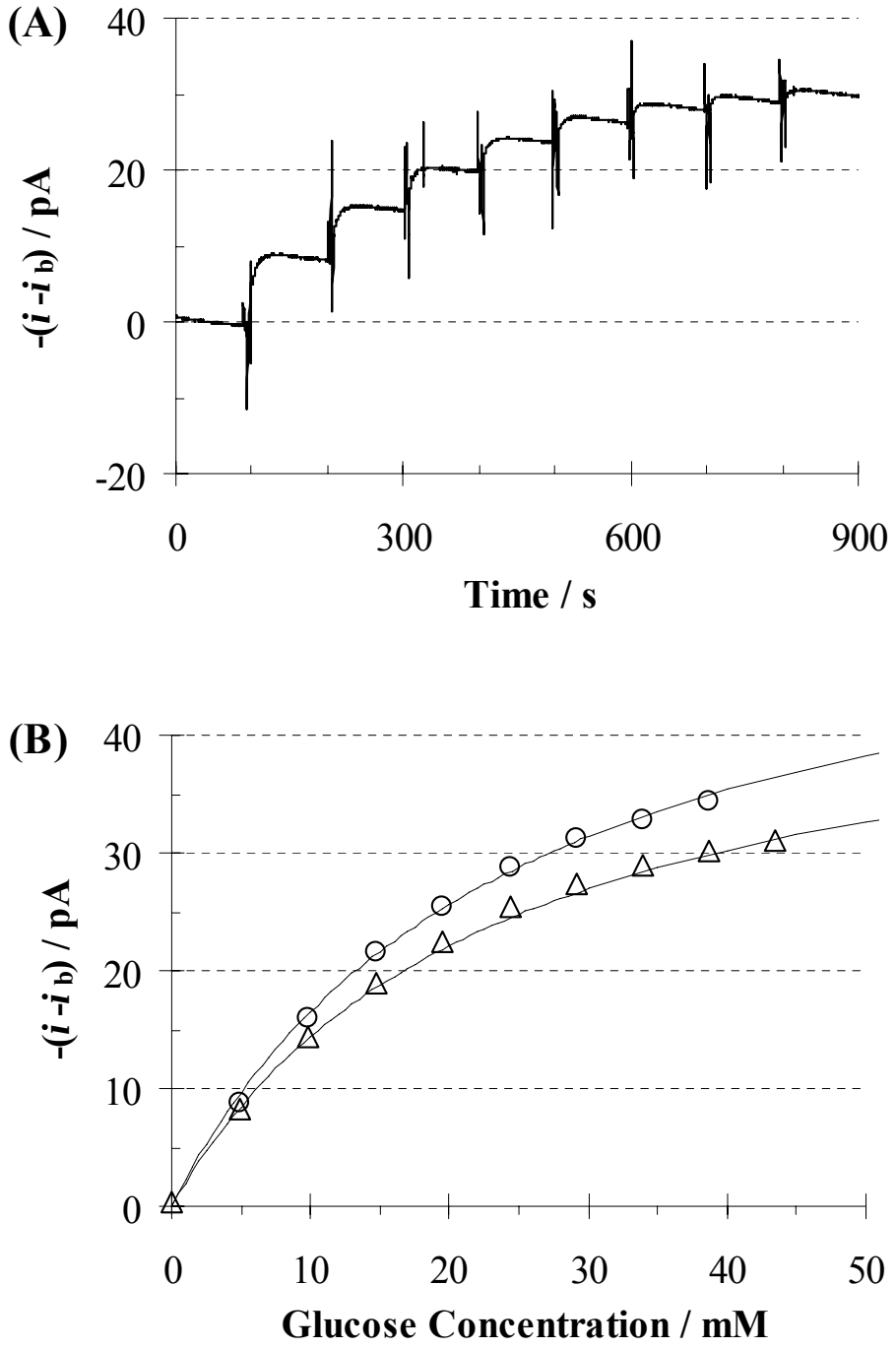

Figure 4.11 (A) Amperometric curve recorded at Pt-Et-GOx#4 (a = 4.1 μm, H = 9.7) fabricated as described in Section 4.2.3.3 upon to 5 mM glucose addition at regular times (~ 100 seconds). (B) Current *vs.* glucose concentration plot for the same electrode in (A) at different storage times: (○) t = 0 (stored in PBS buffer overnight at 4 °C after electrodeposition step) and (Δ) after that the electrode has been stored 3 days in PBS buffer at 4 °C. The solid lines (—) show the best fitting for the two series of data assuming that the Michaelis-Menten kinetics is followed.

Tables 4.3 and Table 4.4 summarize the data obtained with the GOx sensors. It was noticed that the recessed GOx sensors showed sensitivities between a factor 2 and ~ 50 larger than the disk-inlaid but reason of this behaviour is not fully understood. Background current and K_M^{app} values were not significant different from the PPh/GOx sensors. However, from Table 4.3 it is apparent that the GOx sensors showed top and an overall average sensitivity which were respectively a factor 2 and a factor 3 smaller than the ones obtained with the polyphenol/GOx sensors. It is important to note that some of the GOx sensors in Table 4.3 showed sensitivities in the order of ~ 1.0 $mAM^{-1}cm^{-2}$ which is practically the identical value reported by Chen and co-workers[53] using the enzyme electrodeposition procedure. It can be concluded that in the experimental conditions of this work the polyphenol matrix appeared to have a more porous structure (allowing faster response time) and that it appeared to be a milder immobilization enzyme mean (higher sensitivity) while electrodeposition might cause a partial denaturation of the glucose oxidase.

Finally, Table 4.4 gives the data of the two best performing sensors upon a time stability test. The changes in the i_b and K_M^{app} values observed after three days of storage in PBS buffer at 4 °C were not significant as within the standard deviation of these values. On the other hand, the changes in the sensitivity and Δi_{max} were larger, *i.e.* in the order of 10 – 40 % and 20 -30 % respectively and they probably arose from instability of the enzyme upon the storage conditions as previously observed in similar studies.[50,53]

Table 4.3 Glucose sensor microelectrodes fabricated by GOx electrodeposition as described in Section 4.2.3.3. Δi_{max} and K_M^{app} values were calculated fitting the Δi_{ss} *vs.* C_{glu} plots by non linear regression and assuming Michaelis-Menten kinetics. i_b, A_m and Sens are the background current, the microscopic area of the electrode and the sensitivity, respectively. A_m was calculated from the charge passed under the platinum oxide reduction from a voltammogram in 1.0 M H_2SO_4 at 5 Vs^{-1} as explained in Section 1.3.6. The roughness factor for the inlaid disk UMEs is indicated in bracket besides the value of the microscopic area.

Electrode	**$10^6 \times A_m$ / cm^2**	**i_b / pA**	**Δi_{max} / pA**	**K_M^{app} / mM**	**Sens / mAM^{-1}cm^{-2}**
Pt-GOx#4	9.52 (25)	166	12 ± 1	22.1 ± 2.0	0.031 ± 0.004
Pt-Et-GOx#1	1.57	174	38 ± 3	14.4 ± 2.3	1.01 ± 0.07
Pt-Et-GOx#4	0.97	169	57 ± 2	24.5 ± 1.4	1.70 ± 0.09
Pt-Et-GOx#5	4.52	174	12 ± 1	19.8 ± 0.8	0.093 ± 0.009

Table 4.4 Performance of two of the recessed glucose sensor microelectrodes reported in Table 4.3 after storage in PBS buffer for 3 days at 4 °C. Δi_{max} and K_M^{app} values were calculated fitting the Δi_{ss} *vs.* C_{glu} plots by non linear regression and assuming Michaelis-Menten kinetics. i_b and Sens are the background current and the sensitivity respectively. ΔSens is the per cent difference in the sensitivity compared to the initial value.

Electrode	**i_b / pA**	**Δi_{max} / pA**	**K_M^{app} / mM**	**Sens / mAM^{-1}cm^{-2}**	**ΔSens**
Pt-Et-GOx#1	178	33 ± 1	24.7 ± 0.8	0.62 ± 0.07	-38.6 %
Pt-Et-GOx#4	166	48 ± 1	23.2 ± 1.1	1.46 ± 0.11	-13.5 %

4.3.4 Ruthenium/GOx Microsensors

The fabrication of glucose sensors from sub-micrometer probes was not feasible with the immobilization techniques described above because the sensitivity values shown by the polyphenol/GOx and GOx UMEs would have not allowed a detectable current upon to the addition of glucose to be measured. Ruthenium metal electrodeposition in the presence of glucose oxidase might overcome this aspect providing a larger catalytic microscopic area with GOx dispersed and in intimate contact with the ruthenium conductive layers.

Inlaid disk electrodes (3.6 μm < a < 5 μm) were at first employed in the preparation of the sensors. Figures 4.12A and 4.12B show the voltammograms taken as soon as the microelectrode was dipped in the solution containing ruthenium(nitrosyl)nitrate and glucose oxidase and after the enzyme adsorption step. Indeed, in Figure 4.12B the second sweep seems to be conditioned by the longer time length of the adsorption step. Though the current passed in Figure 4.13 for the two UMEs was in the same order of magnitude, the electrodeposition amperometric curve after the longer adsorption time was more random and the resulting sensitivity lower. However, a larger sample of data is necessary in order to draw definitive conclusions on the effect of the enzyme adsorption step on the final properties of the sensors. Finally, employment of SEM does not show any microscopic feature on the microelectrodes after the coating step supporting the conclusion that the modification of the surface was at the nanoscale level (results not shown).

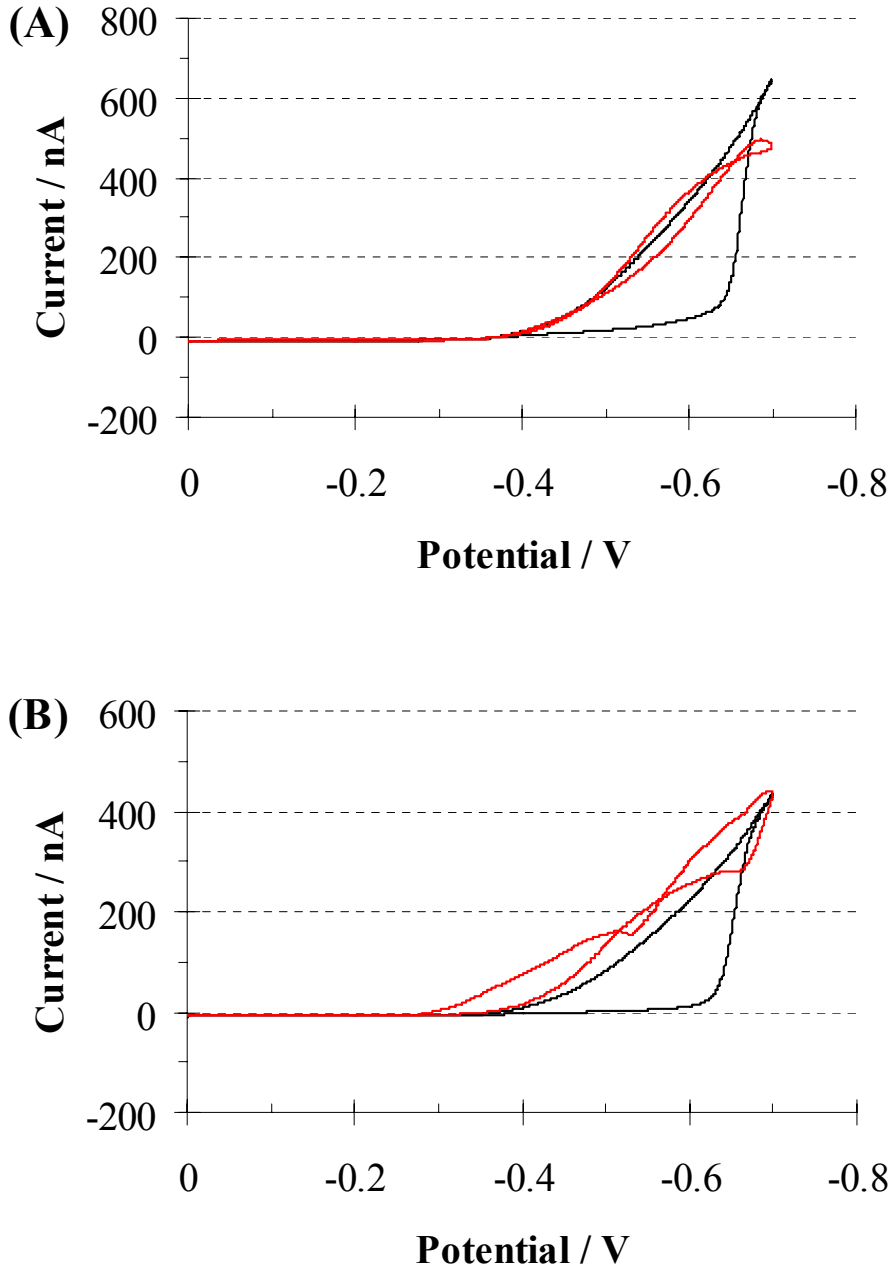

Figure 4.12 The voltammograms at (A) Pt-Ru#3 (a = 5.0 μm) and (B) Pt-Ru#4 (a = 3.7 μm) immersed in a solution of ruthenium nitrosyl nitrate/GOx prepared as described in Section 4.2.3.4. The solid black line (—) indicates the scan done at t = 0 both in (A) and in (B) while the solid red line (—) represents the sweep taken after the adsorption step which was 20 minutes in (A) and 1.5 hours in (B). Potential was swept between 0 and - 0.7 V with a scan rate of 50 mVs^{-1}.

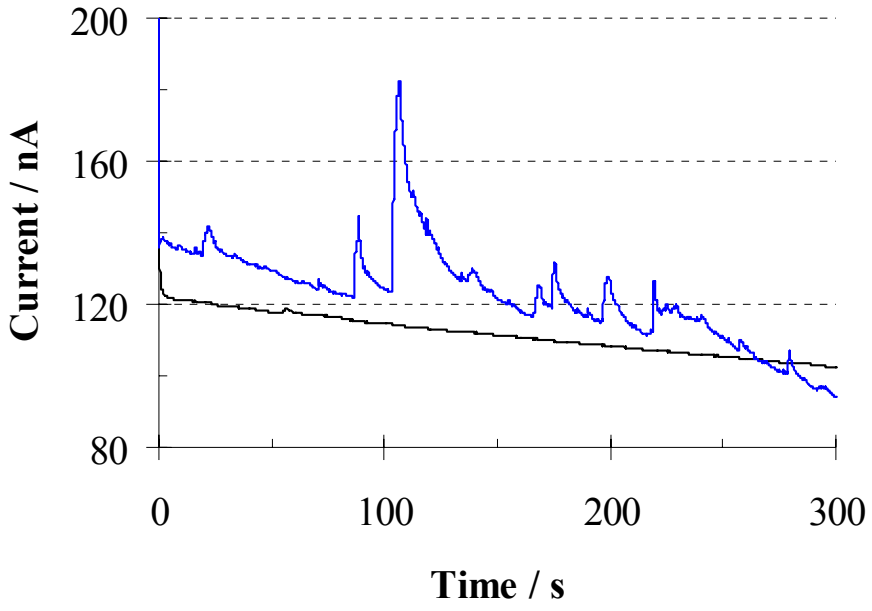

Figure 4.13 Chronoamperometric curve during the metal electrodeposition from the ruthenium nitrosyl nitrate/GOx solution prepared as explained in Section 4.2.3.4. The solid black line (—) is the chronoamperometric curve of the probe in Figure 4.13A where the adsorption step lasted 20 minutes while the solid blue line (—) is chronoamperometric curve for the probe in Figure 4.13B where the adsorption step lasted 1.5 hours. Potential was held at -0.5 V *vs.* Ag/AgCl in both cases.

Figures 4.14 shows the CVs in PBS buffer solution without glucose for one of the ruthenium/GOx coated inlaid disk microelectrodes. In the figure a peak with onset at ~ 0.45 V *vs.* Ag/AgCl is apparent which might correspond to the Ru(0)/Ru(IV) transition. Indeed, the $E°$ for the Ru(III)/Ru(IV) transition has been reported between ~ 0.2 – 0.3 V *vs.* Ag/AgCl depending on the pH of the solution.[54] This peak disappears in the second sweep in Figure 4.14 which might agree with the complete oxidation of the ruthenium film. It is important to note that the $E°$ of Ru(IV)/Ru(VI) transition $E°$ has been reported in the range 0.7 – 0.95 V *vs.* Ag/AgCl depending on the pH of the solution.[54] However, the understanding of the oxidation states of the ruthenium within the film and their role in catalysing the electron transfer between the hydrogen peroxide and the platinum support was beyond the scope of this thesis.

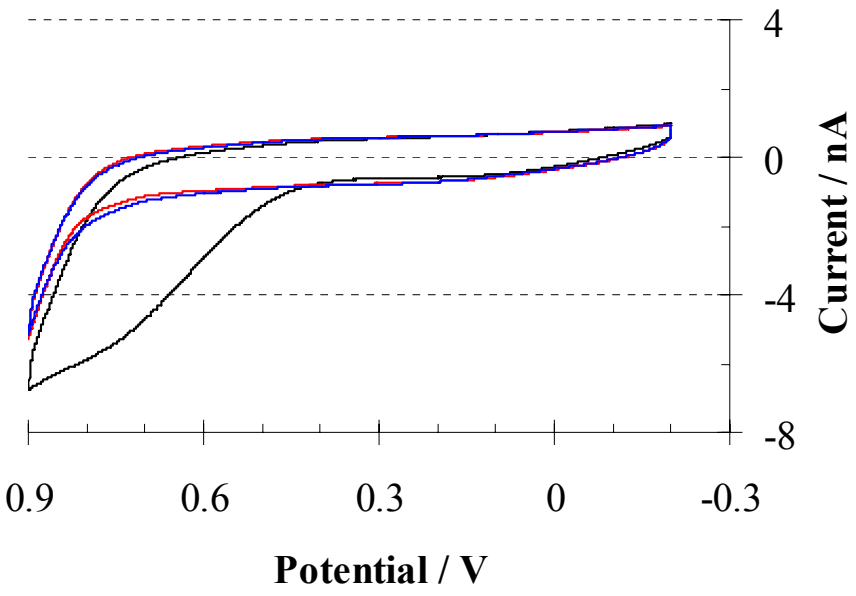

Figure 4.14 Voltammogram obtained cycling the potential of a Ru/GOx UME in PBS buffer (pH = 7.2) without glucose. The sensor, Pt-Ru#3 (a = 5.0 μm), was prepared from electrodeposition of ruthenium in presence of glucose oxidase as described in Section 4.2.3.4. The potential was swept between -0.2 V and 0.9 V at the scan rate of 50 mVs^{-1} for 5 times. The graph shows the (—) 1st, (—) 3rd and (—) 5th recorded sweep.

Figure 4.15A shows the typical sensor response upon to addition of glucose. From this figure a drift in the current is apparent and it should be correlated somehow with the enzymatically generated hydrogen peroxide because well established steady state current was observed before the glucose addition. At the moment, exact reasons of this behaviour are unknown. In order to use the data affected by this drift, it was decided to sample the signal 4 - 6 seconds after the glucose addition which corresponded to the largest difference in current. The thin line in Figure 4.15A represents the new current profile generated by the rectification of the drift. This approach was taken because the drift was not constant and the achievement of a steady state did not happen within the hundred seconds between two following glucose injections. Figure 4.15B shows the current profile against the glucose concentration obtained from Figure 4.15A after the drift correction. Figure 4.15B reports also the non linear fitting of the experimental data according to the Michaelis-Menten model. Despite the "rectification" of the current drift might significantly overestimate the sensitivity and Δi_{max} values, it should be noticed that the data fitted showed high R-squared values, *e.g.* 0.994 in case of Figure 4.15B. Indeed, Table 4.5 summarizes the data found with the Ru/GOx sensors for the amperometric response towards glucose after correction of the drift.

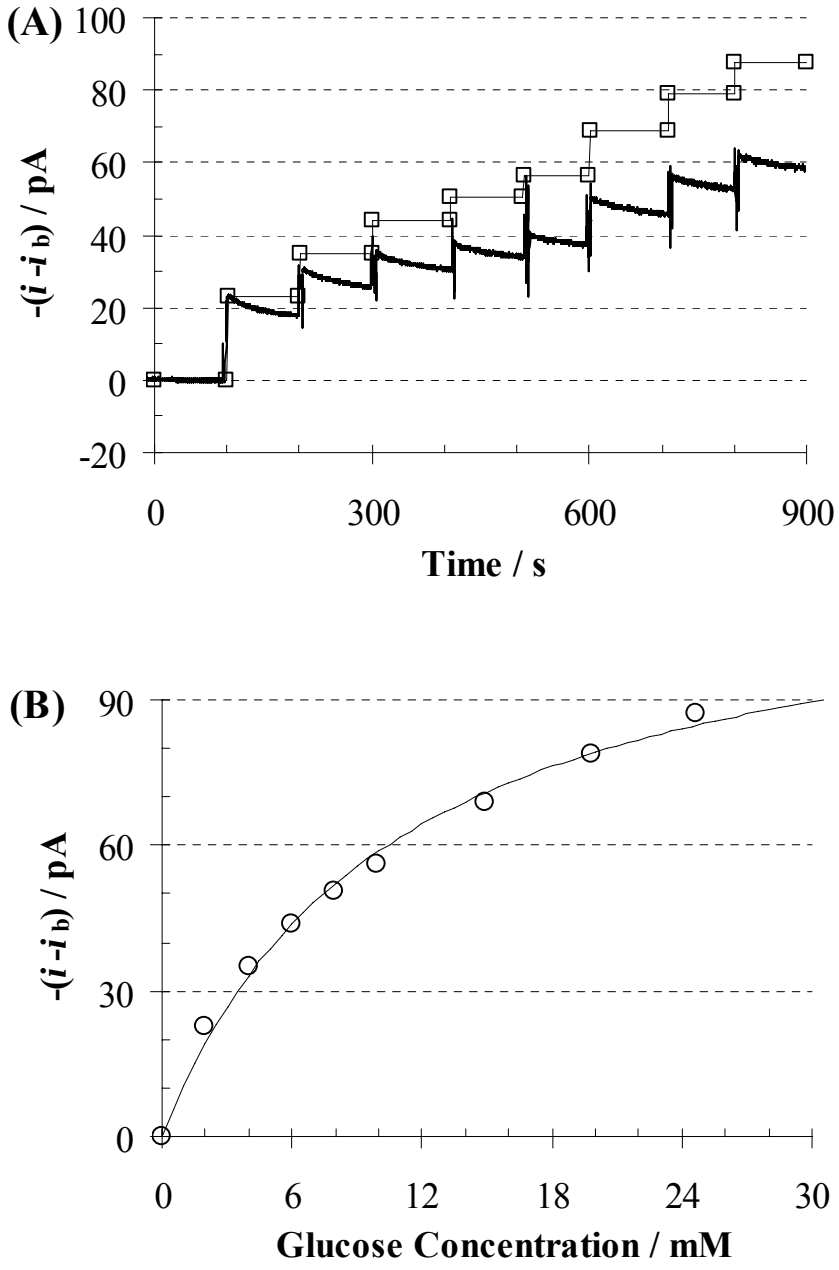

Figure 4.15 (A) The solid thick line (▬) is the amperometric curve recorded at one of the Ru/GOx sensor upon to the addition of glucose. The solid thin line (—) shows the amperometric profile once the drift is rectified using the Δi values observed after the glucose addition. The symbols (□) represent the new values of the current between two glucose injections. (B) Current *vs.* glucose concentration plotted for the same electrode in (A) using the "rectified" amperometric profile. The empty circles (○) represent the experimental data while the solid line (—) shows the best fitting assuming Michaelis-Menten kinetics is followed. The UME, Pt-Ru#3 (a = 5.0 μm), was fabricated by electrodeposition of ruthenium in presence of glucose oxidase.

Table 4.5 Glucose sensor microelectrodes fabricated by ruthenium electrodeposition in presence of glucose oxidase as described in Section 4.2.3.4. Δi_{max} and K_M^{app} values were calculated fitting the Δi_{ss} *vs.* C_{glu} plots by non linear regression and assuming Michaelis-Menten kinetics. i_b, A_m and Sens are the background current, the microscopic area of the electrode and the sensitivity, respectively. A_m was calculated from the charge passed under the platinum oxide reduction from a voltammogram in 1.0 M H_2SO_4 at 5 Vs^{-1} as explained in Section 1.3.6. The roughness factor for the disk inlaid UMEs is indicated in bracket besides the value of the microscopic area.

Electrode	$10^6 \times A_m$ / cm^2	i_b / pA	Δi_{max} / pA	K_M^{app} / mM	Sens / mAM^{-1}cm^{-2}
Pt-Ru#2	0.52 (0.7)	96	76 ± 4	7.7 ± 0.9	9.3 ± 2.1
Pt-Ru#3	0.54 (0.7)	172	121 ± 6	10.7 ± 1.1	16.3 ± 2.8
^Pt-Ru#4	0.52 (1.3)	167	93 ± 4	8.2 ± 0.9	15.2 ± 3.3
Pt-Et-Ru#2	0.810	139	13 ± 1	4.0 ± 0.3	1.1 ± 0.4
*Pt-Et-Ru#3	0.238	171 ± 1	6 ± 1	4.6 ± 3.3	3.7 ± 1.2

*i_b, Δi_{max}, K_M^{app} and Sens values were calculated averaging three independent measurements. ^This microelectrode was left dipping for 1.5 hours into the ruthenium nitrosyl nitrate/GOx solution prior to start the electrodeposition step instead than 20 minutes as for the others.

The most interesting aspect arising from Table 4.5 is that the values of the sensitivity obtained for the three inlaid disk microelectrodes were approximately an order of magnitude higher than the top results reported in Table 4.2 and 4.3 respectively for the PPh/GOx and the GOx UMEs. Indeed, with the latter sensors the best sensitivity was in the order of ~ 1 mAM^{-1}cm^{-2}. The enhanced sensitivity can be in part explained by an increase of the electrochemical surface area due to the ruthenium electrodeposition. Indeed, the metal electrodeposition might cause a parallel increase in the enzyme loading which agrees with the larger Δi_{max} values *i.e.* between 70 and 120 pA. On the other hand, it can be noticed that K_M^{app} values were 4 - 5 times smaller than the previous sections which should be associated with the different sensor design. Indeed, here the enzyme was "encapsulated" within a ruthenium conductive film and not within an

electrochemical inert matrix like done using polyphenol or enzyme direct electrodeposition. Oxygen supply at the enzyme layer might be responsible for such decrease.[10,55]

The high sensitivity shown by the ruthenium/GOx UMEs allowed recessed sensors to be prepared from submicrometer probes (0.60 μm < a < 0.66 μm, 3.4 < H < 6.5). Figure 4.16A shows the typical amperometric response of a recessed sensors upon to the addition of glucose. The response was affected by a drift in the current as above reported. Indeed, for the Ru/GOx recessed microelectrodes, glucose testing was repeated three times storing the microelectrode in PBS for an hour in between two following measurements. Figure 4.16A shows an increased noise in the signal repeating the glucose sensing test. Figure 4.16B gives the current-glucose concentration profile after the rectification of the drift and reports the non linear regression of the data assuming the Michaelis-Menten model.

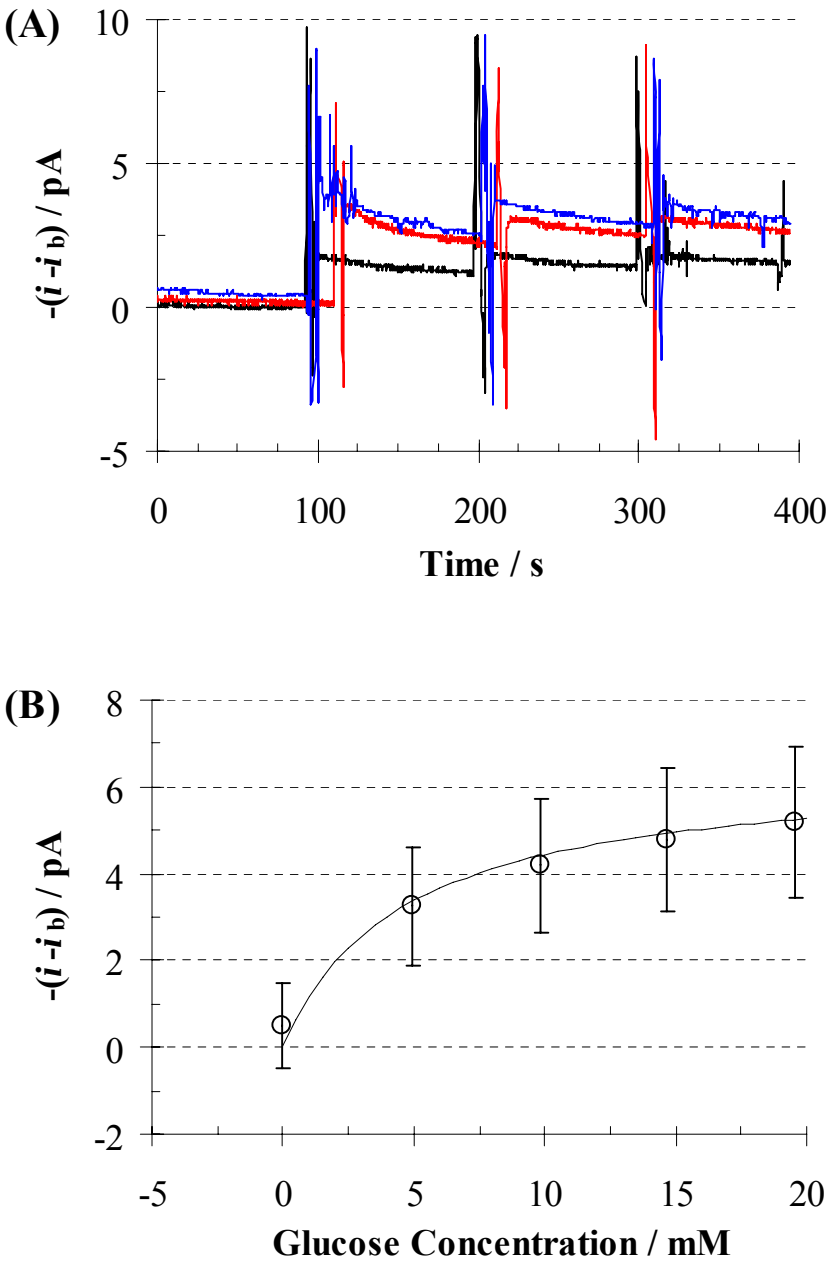

Figure 4.16 (A) Amperometric profile recorded at recessed Ru/GOx sensor upon to the addition of glucose at regular times. Pt-Et-Ru#4 (a = 597 nm, H = 3.4), was fabricated by electrodeposition of ruthenium in presence of glucose oxidase as described in Section 4.2.3.4. The solid lines represent the (—) 1st, (—) 2nd and (—) 3rd repeated measurement. (B) Current *vs.* glucose concentration plot for the same electrode in (A) after rectification of the current as explained above. The empty circles (○) represent the experimental data while the solid line (—) shows the best fitting assuming that Michaelis-Menten kinetics is followed. The electrode was stored in PBS buffer at room temperature between two following tests for at least one hour.

The main noticeable difference of the Ru/GOx sensors is that when they were prepared from recessed UMEs they showed values of Δi_{max} and sensitivities an order of magnitude smaller than when inlaid disk UMEs were employed. Reason of the latter behaviour should arise from lower current densities observed during the ruthenium electrodeposition for the recessed electrodes. Indeed, Figure 4.17A shows a typical chronoamperometric curve obtained during the metal electrodeposition at one of these recessed microelectrodes. From this figure it is apparent that the current was an order of magnitude smaller than what observed in Figure 4.13 where inlaid disk UMEs were employed. As the microscopic area of recessed and disk inlaid microelectrodes was in the same order of magnitude, it follows that the current density during the ruthenium electrodeposition was an order of magnitude smaller with the former electrodes. Therefore a lower amount of ruthenium was electrodeposited at the recessed UMEs. This hypothesis agrees also with voltammogram of the recessed Ru/GOx in PBS buffer without glucose reported in Figure 4.17B. In fact, in this figure the peak with onset at 0.45 V, which was assumed to be associated with the Ru(0)/Ru(IV) transition, was apparently less pronounced than in Figure 4.14. Thus, the smaller charge under that peak would suggest that a smaller content of ruthenium was electrodeposited in the recessed electrodes.

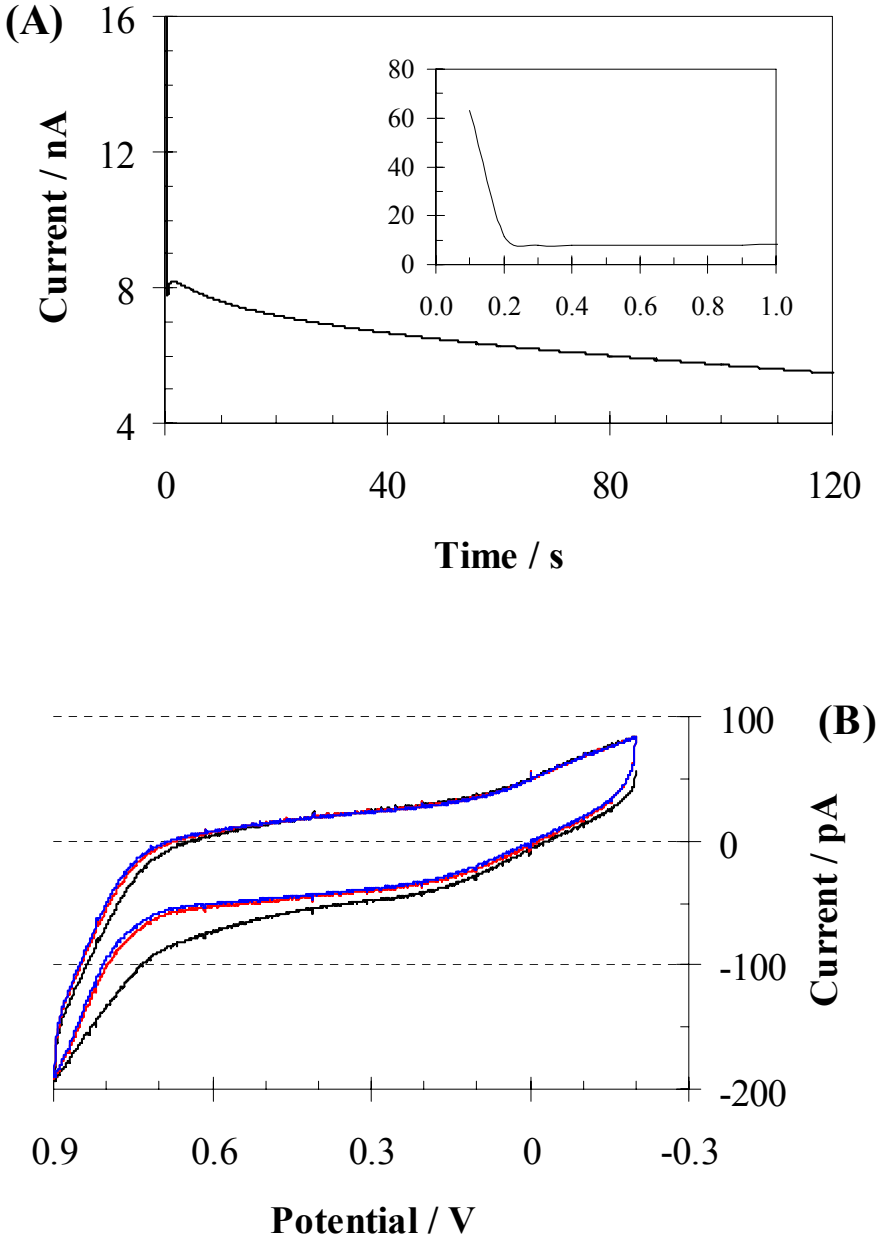

Figure 4.17 (A) Amperometric curve during the metal deposition at Pt-Et-Ru#3 (a = 669 nm, H = 6.5) from ruthenium nitrosyl nitrate/GOx solutions as described in Section 4.2.3.4. The potential was held at -0.5 V *vs.* Ag/AgCl. The inset shows an enlargement of the chronoamperometric profile at short times. The units of measure in the inset are the same as in the main figure. (B) Voltammogram in PBS buffer (pH = 7.2) without glucose obtained with the recessed ruthenium/GOx coated sensor prepared in (A). The potential was swept between -0.2 V and 0.9 V at the scan rate of 50 mVs^{-1} for 5 times. The solid lines show the (—) 1st, (—) 3rd and (—) 5th recorded sweep.

It is reasonable to consider at this stage that the sensitivity of the sensors depended on the amount of ruthenium electrodeposited which should be somehow proportional also to the amount of enzyme encapsulated during this step. Then from the charge passed and using the faradic law, it is possible to calculate the moles of ruthenium electrodeposited assuming that the only reaction occurring was the reduction from Ru(III) to Ru(0) and unitary efficiency for this process. Table 4.6 reports the charge passed during the electrodeposition, the weight and the weight density of the ruthenium films and finally the ratio, σ, between the moles of electrodeposited ruthenium, N_{Ru}, and the superficial platinum, N_{Pt}, (calculated from the charge under the reduction peak of the platinum oxide when the electrode potential was cycled in 1 M H_2SO_4 and assuming n = 2). Despite the fact that the values in Table 4.6 might not be correct because of the initial assumptions, these values can help in understanding the discrepancy of performance between disk-inlaid and recessed sensors. Indeed, comparing Tables 4.5 and 4.6 it seems that the sensitivity of the sensors was controlled in first approximation by the amount of the electrodeposited ruthenium (and then enzyme). In fact, in the inlaid disk UMEs σ was two orders of magnitude larger than in the recessed microelectrodes which, therefore, should correspond to a higher content of ruthenium and enzyme in the former sensors. It can be concluded that the Ru/GOx inlaid disk microelectrodes showed sensitivity an order of magnitude bigger than the correspondent Ru/GOx recessed sensors because of the smaller amount of ruthenium (and enzyme) electrodeposited.

Table 4.6 Glucose sensor microelectrodes fabricated by ruthenium electrodeposition in presence of glucose oxidase as described in Section 4.2.3.4. The table reports the charge passed during the electrodeposition step. It was assumed that the only electrochemical process occurring was the reduction from Ru(III) to Ru(0) and unitary efficiency. The weight and weight density of the electrodeposited ruthenium were then calculated using the faraday law and the data were normalized using the microscopic area reported in the previous table. The ratio between the moles of ruthenium deposited and the superficial platinum, N_{Ru}/N_{Pt} is also given. N_{Pt} was calculated from the charge passed under the platinum oxide reduction cycling the electrode potential in 1.0 M H_2SO_4 as done prior to the electrodeposition step and assuming $n = 2$.

Electrode	Charge / µC	Weight / ng	Weight / ngcm^{-2}	N_{Ru}/N_{Pt}
Pt-Ru#2	60.6	21.2	47.0	1.85×10^5
Pt-Ru#3	33.5	11.7	25.1	9.88×10^5
^Pt-Ru#4	36.8	12.8	24.5	1.12×10^5
Pt-Et-Ru#2	1.22	0.43	0.53	2.39×10^3
Pt-Et-Ru#3	0.775	0.27	1.27	5.74×10^3
Pt-Et-Ru#4	0.591	0.21	0.87	3.94×10^3

^This microelectrode was left dipping for 1.5 hours instead than 20 minutes as for the others into the solution prior to start the electrodeposition step.

Finally, the recessed microelectrodes were tested against ascorbic acid and acetaminophen. Figure 4.18 shows that these two compounds interfere with the monitoring of glucose. In fact, at the detection potential used and at their maximum physiological concentration, they generated a response two or three time larger than the one due to the oxidation of the enzymatically generated hydrogen peroxide. These results are in contradiction with the conclusions presented by Kohma and co-workers[12] employing a similar procedure but using carbon microfiber. Indeed, these authors found the response of some common electrochemical interferents was suppressed and argued that the ruthenium/GOx films might have some sieving/rejecting properties. On the other hand, the results agree partially with the conclusion by Wu and co-workers[56]

who showed that the oxidation of ascorbic acid was possible on screen-printing ruthenium dioxide electrodes. It must be concluded that, the amount of ruthenium electrodeposited and the enzyme loading control the morphology, *e.g.* porosity, of these films but a further investigation of these parameters in the characteristics of the RuOx/GOx film was not carried in this thesis. Despite the failure of the test shown in Figure 4.18, it is significant to note that the ratio of the signals between the glucose and the interferents was improved compared to what obtained with the polyphenol/GOx sensors and shown in Figure 4.9. In fact, the Ru/GOx coated sensors have sensitivity towards ascorbic acid and acetaminophen ~ 230 and ~ 280 $mAM^{-1}cm^{-2}$ but the ratio of the signals between glucose and interferents with the Ru/GOx sensors resulted improved of factor 4 and 3 for ascorbic acid and acetaminophen respectively compared to PPh/GOx sensors.

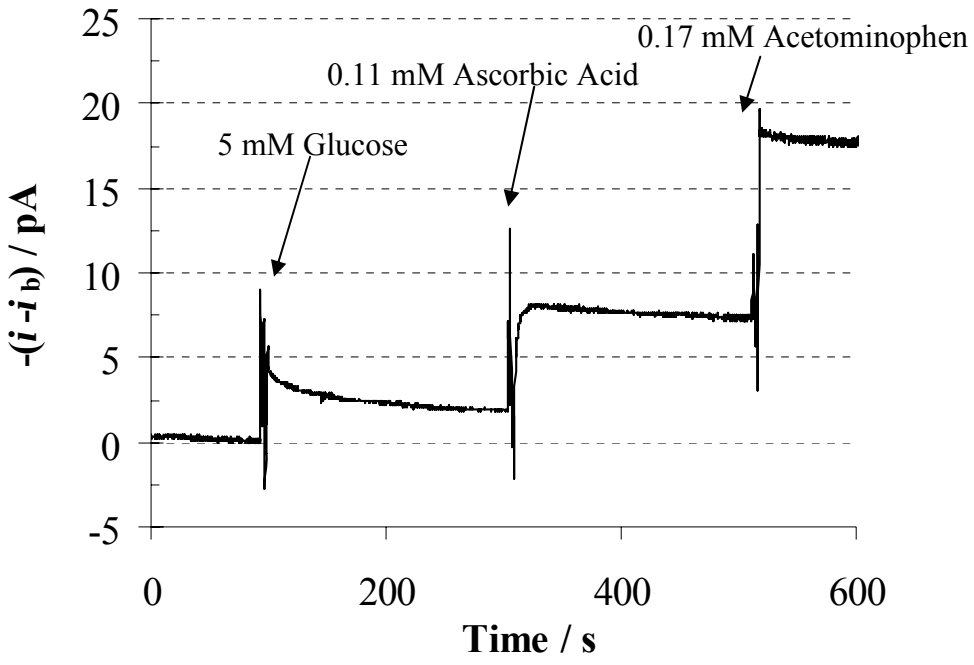

Figure 4.18 Amperometric profile at Pt-Et-Ru#4 (a = 0.597 nm, H = 3.4) upon to the addition of 5 mM glucose, 0.11 mM ascorbic acid and 0.17 mM acetaminophen at the time indicated by the arrows. The microsensor was fabricated as described in Section 4.2.3.4.

4.4 Conclusions

The investigation of some glucose oxidase immobilization procedures at platinum inlaid disk and recessed microelectrodes was carried in this chapter pursuing the fabrication of glucose micro- and nano- sensors. This work elucidates the difficulties to achieve an efficient entrapment of glucose oxidase within a polypyrrole film grown with a single polymerization step.

Better results were achieved entrapping the enzyme within a non conductive polyphenol film. Indeed, the latter sensors have a very fast response time (< 3 - 5 seconds). The nearly instantaneous response can be attributed to the intimate contact between the biocatalytic and electrocatalytic surface sites,[57] to the open porous surface structure,[9,20,50] to the absence of supporting membranes[19] and to the small electrode size (95 % of the steady state current for an uncoated 5 μm UME is reached in approximately 1 second).[29,32] The highest sensitivity shown by some of these microelectrodes was twice as larger as other polyphenol/GOx sensors prepared with similar method.[53] A very stable signal, before and after the glucose injection, was also observed. Besides, they showed large values of K_M^{app}, compatible with the glucose concentration range in the human blood as the sensor has to be operated in its linear region *i.e.*, $C_{glu} < K_M^{app}$.[57] However, the polyphenol films in these sensors were not completely able to reject interferents like ascorbic acid and acetaminophen. The latter aspect is very important for their use in medical monitoring, *e.g.*, point of care and subcutaneous implantable device and solutions are currently under investigation. Indeed, use of a second membrane with molecular weight cut-offs < 100 might solve this issue. Nevertheless, the microelectrodes fabricated in this work can have a significant role in the research where glucose has to be monitored with spatial and temporal resolution under controlled conditions.[14,15]

Direct electrodeposition of glucose oxidase on the microelectrode surface did not produce sensors showing larger sensitivity than the polyphenol/GOx ones. Besides, a certain delay (10 – 15 seconds) in the achievement of a steady state was also experienced. However, very recently, an extraordinary high sensitivity, ~ 6 $AM^{-1}cm^{-2}$, was achieved using the latter procedure depositing GOx in nanochannel created by means of AFM.[22]

Finally, encouraging results were obtained by electrodeposition of ruthenium in the presence of glucose oxidase. Indeed, sensitivities of the Ru/GOx sensors were ~ 15 $mAM^{-1}cm^{-2}$ which was an order of magnitude higher than the top one obtained with the polyphenol/GOx sensors of this work, *i.e.* ~ 1 $mAM^{-1}cm^{-2}$. Besides, these sensitivities are significantly higher than the ones reported in the literature using conductive polymers[53,58,59] or non conductive polymers.[53,58,59] The enhanced sensitivity might arise from the sensor design *i.e.* a larger amount of the enzyme could be encapsulated in a conductive ruthenium dioxide film. Significantly, with the latter procedure, the preparation of glucose sensors from submicrometer probes could be possible. However, the microelectrodes exhibited a significant drift in the current upon to the addition of glucose which hampers their use as glucose sensors at the moment. Moreover, these probes were not immune from interference due to ascorbic acid and acetaminophen differently from the conclusions stated by Kohma and co-workers[12] who employed similar procedures to coat 33 μm carbon fibers. Current work is addressed in understanding the reason of the drift, in finding opportune solutions for the latter and in the improvement of the ratio of the signals between the glucose and the interferents.

Despite the fact that the enzyme immobilization procedures in this work have been already employed in the literature, it is the first time that an extensive comparative study was undertaken using electrodes with radius < 5 μm. In further studies, working on the specific anisotropic orientation of the enzyme at the electrode surface, employing self assemble strategies and layer-by-layer deposition[1,57,60] to have highly ordered multilayer structures might be an interesting route in order to achieve a good amplification of the signal. However, in this prospective, particular care has to be taken to avoid the denaturation and suppression of the catalytic enzyme activity which would decrease the sensor sensitivity.[61]

4.5 References

(1) Schuhmann, W.; Bonsen, E. M. In *Biosensors;* Unwin, P. R., Ed.; Encyclopedia of Electrochemistry. Volume 3. Instrumentation and Electroanalytical Techniques; Wiley Ltd.: Federal Republic of Germany, 2003; pp 350.

(2) Ciobanu, M.; Taylor, D. E.; Wilburn, J. P.; Cliffel, D. E. *Anal. Chem.* **2008**, *80*, 2717.

(3) Masson, J.; Kranz, C.; Booksh, K. S.; Mizaikoff, B. *Biosensors and Bioelectronics* **2007**, *23*, 355-361.

(4) Quinto, M.; Losito, I.; Palmisano, F.; Zambonin, C. G. *Fresenius J. Anal. Chem.* **2000**, *367*, 692.

(5) McRipley, M. A.; Linsenmeier, R. A. *J. Electroanal. Chem.* **1996**, *414*, 235.

(6) Rong, Z.; Leitao, E.; Popplewell, J.; Alp, B.; Vadgama, P. *IEEE Sensors Journal* **2008**, *8*, 113.

(7) Csoregi, E.; Quinn, C. P.; Schmidtke, D. W.; Lindquist, S. E.; Pishko, M. V.; Ye, L.; Katakis, I.; Hubbell, J. A.; Heller, A. *Anal. Chem.* **1994**, *66*, 3131.

(8) Anderson, J. L.; Coury, L. A. J.; Leddy, J. *Anal. Chem.* **1998**, *70*, 519R.

(9) Poitry, S.; Poitry-Yamat, C.; Innocent, C.; Cosnier, S.; Tsacopoulos, M. *Electrochimica Acta* **1997**, *42*, 3217-3223.

(10) Schuvailo, O. M.; Soldatkin, O. O.; Lefebvre, A.; Cespuglio, R.; Soldatkin, A. P. *Anal. Chim. Acta* **2006**, *573-574*, 110-116.

(11) Cosnier, S.; Innocent, C.; Allien, L.; Poitry, S.; Tsacopoulos, M. *Anal. Chem.* **1997**, *69*, 968.

(12) Kohma, T.; Oyamatsu, D.; Kuwabata, S. *Electrochem. Comm.* **2007**, *9*, 1012-1016.

(13) Xin, Q.; Wightman, R. M. *Anal. Chim. Acta* **1997**, *341*, 43-51.

(14) Schulte, A. and Schuhmann, W. *Angew. Chem. Int. Ed.* **2007**, *46*, 8760.

(15) Sun, P.; Laforge, O.; Abeyweera, T. P.; Rotenberg, S. A.; Carpino, J.; Mirkin, M. *PNAS* **2008**, *105*, 443.

(16) Yang, Q.; Atanasov, P.; Wilkins, E. *Biosensors and Bioelectronics* **1999**, *14*, 203-210.

(17) Xie, H.; Tan, X. L.; Gao, Z. *Frontiers in Bioscience* **2005**, *10*, 1797.

(18) Bindra, D. S.; Zhang, Y.; Wilson, G. S.; Sternberg, R.; Thevenot, D. R.; Moatti, D.; Reach, G. *Anal. Chem.* **1991**, *63*, 1692.

(19) Wang, J. and Angnes, L. *Anal. Chem.* **1992**, *64*, 456.

(20) Hrapovic, S. and Luong, J.H.T. *Anal. Chem.* **2003**, *75*, 3308.

(21) Polsky, R.; Harper, J. C.; Wheeler, D. R.; Brozik, S. M. *Electroanalysis* **2008**, *20*, 671.

(22) Tsai, Y.; Ho, C.; Liao, S. *Electrochem. Comm.* **2009**, *11*, 1316-1319.

(23) Gooding, J. J.; Hall, E. A. H.; Hibbert, D. B. *Electroanalysis* **1998**, *10*, 1130.

(24) Choleau, C.; Klein, J. C.; Reach, G.; Aussedat, B.; Demaria-Pesce, V.; Wilson, G. S.; Gifford, R.; Ward, W. K. *Biosensors and Bioelectronics* **2002**, *17*, 647-654.

(25) Sakslund, H.; Wang, J.; Lu, F.; Hammerich, O. *J Electroanal Chem* **1995**, *397*, 149-155.

(26) Hall, S. B.; Khudaish, E. A.; Hart, A. L. *Electrochimica Acta* **1999**, *44*, 4573-4582.

(27) Hall, S. B.; Khudaish, E. A.; Hart, A. L. *Electrochimica Acta* **1998**, *43*, 2015-2024.

(28) Bond, A. M.; Luscombe, D.; Oldham, K. B.; Zoski, C. G. *J. Electroanal. Chem.* **1988**, *249*, 1.

(29) Bartlett, P. N.; Taylor, S. L. *J. Electroanal. Chem.* **1998**, *453*, 49-60.

(30) Lyons, M. E. G. *Sensors* **2003**, *3*, 19.

(31) Cannes, C.; Kanoufi, F.; Bard, A. J. *Langmuir* **2002**, *18*, 8134-8141.

(32) Bard, A. J.; Faulkner, L. R. In *Electrochemical Methods. Fundamentals and Applications.* Wiley Inc.: United States of America, 2001; , pp 833.

(33) Woo, D.; Kang, H.; Park, S. *Anal. Chem.* **2003**, *75*, 6732-6736.

(34) Sorensen, A. H.; Hvid, U.; Mortensen, M. W.; Morch, K. A. *Rev. Sci. Instrum.* **1999**, *70*, 3059.

(35) Paixao, T. R. L. C.; Lowinsohn, D.; Bertotti, M. *J. Agric. Food Chem.* **2006**, *54*, 3072.

(36) Anicet, N.; Bourdillon, C.; Moiroux, J.; Saveant, J. *J. Phys. Chem. B* **1998**, *102*, 9844-9849.

(37) Sun, P.; Mirkin, M. V. *J. Am. Chem. Soc.* **2008**, *130*, 8241-8250.

(38) Liu, H. Y.; Fan, F. R. F.; Lin, C. W.; Bard, A. J. *J. Am. Chem. Soc.* **1986**, *108*, 3838.

(39) Zhang, B.; Zhang, Y.; White, H. S. *Anal. Chem.* **2004**, *76*, 6229.

(40) Berg, J. M.; Tymoczko, J. L.; Stryer, L. In *Biochemistry;* Julet, M.: United States of America, 2002; , pp 974.

(41) Arrigan, D. W. M.; Bartlett, P. N. *Biosensors and Bioelectronics* **1998**, *13*, 293-304.

(42) Nien, P. C.; Huang, M. C.; Chang, F. Y.; Ho, K. C. *Electroanalysis* **2008**, *20*, 635.

(43) Matsumoto, N.; Chen, X.; Wilson, G. S. *Anal. Chem.* **2002**, *74*, 362.

(44) Bartlett, P. N.; Toh, C. S.; Calvo, E. J.; Flexer, V. In *Modelling Biosensor Responses;* Bartlett, P. N., Ed.; Bioelectrochemistry. Fundamentals, Experimental Techniques and Applications; Wiley Ltd: Great Britain, 2008; pp 267.

(45) Trojanowicz, M.; Krawczynski vel Krawczyk, T.; Geschke, O.; Cammann, K. *Sensors Actuators B: Chem.* **1995**, *28*, 191-199.

(46) Shin, M.; Kim, H. *Biosensors and Bioelectronics* **1996**, *11*, 161-169.

(47) Wallace, G. G.; Spinks, G. M.; Kane-Maguire, L. A. P.; Teasdale, P. R. In *Conductive Electroactive Polymers. Intelligent Polymer System;* Taylor & Francis Ltd: United States of America, 2008; Vol. 1, pp 270.

(48) Belanger, D.; Nadreau, J.; Fortier, G. *J. Electroanal. Chem.* **1989**, *274*, 143.

(49) Nagahara, L. A.; Thundat, T.; Lindsay, S. M. *Rev. Sci. Instrum.* **1989**, *60*, 3128.

(50) Zhang, Z.; Liu, H.; Deng, J. *Anal. Chem.* **1996**, *68*, 1632.

(51) Nakabayashi, Y.; Wakuda, M.; Imai, H. *Analytical Sciences* **1998**, *14*, 1069.

(52) Yuqing, M.; Jianrong, C.; Xiaohua, W. *Trends Biotechnol.* **2004**, *22*, 227-231.

(53) Chen, X.; Matsumoto, N.; Hu, Y.; Wilson, G. S. *Anal. Chem.* **2002**, *74*, 368.

(54) Kumar, A. S.; Chen, P.; Chien, S.; Zen, J. *Electroanalysis* **2005**, *17*, 211.

(55) Wang, J. *Chem. Rev.* **2008**, *108*, 814.

(56) Wu, J.; Suls, J.; Sansen, W. *Electrochem. Comm.* **2000**, *2*, 90-93.

(57) Rusling, J. F.; Wang, B.; Yun, S. In *Electrochemistry of Redox Enzyme;* Bartlett, P. N., Ed.; Bioelectrochemistry. Fundamentals, Experimental Techniques and Applications; Wiley Ltd.: Great Britain, 2008; pp 39.

(58) Nien, P. C.; Tung, T. S.; Ho, K. C. *Electroanalysis* **2006**, *18*, 1408.

(59) Wang, Z.; Liu, S.; Wu, P.; Cai, C. *Anal. Chem.* **2009**, *81*, 1638.

(60) Scheller, F. W.; Wollenberger, U. In *Enzyme Electrodes;* Wilson, G. S., Ed.; Encyclopedia of Electrochemistry. Volume 9. Bioelectrochemistry; Wiley-VCH: Federal Republic of Germany, 2002; pp 431.

(61) Yoon, H.C. and Kim, H.-S. *Anal. Chem.* **2000**, *72*, 922.

Chapter 5

Conclusions and Future Work

5 Conclusions and Future Work

This thesis has its focus in the biosensing field in conjunction with the use of nano- and micro- electrodes. Biosensors are promising devices which are convenient over traditional analytical techniques as they are highly specific, fast-response, portable and simple-to-operate analytical tools. Besides, they will have a pivotal role in the field of self-care or point-of-care in the next decade. From this perspective, micro- and especially nano- electrodes are favourite candidates in order to develop fast-response electrochemical biosensors as they achieved steady state response in short times and the charging of the double layer is extremely fast.

Chapter 2 has described the preparation of platinum nanometer sized electrodes as small as few nanometers with the help of a laser puller. For the first time, this procedure was also applied to fabricate of gold ultramicroelectrodes with radius > 500 nm. Optimisation of the procedure set for the gold should allow achieving smaller electrodes. Besides, this method can be employed in the preparation of other metal nanoelectrodes which might be an interesting option in several research fields. In this chapter, a wide range of techniques was employed for the characterisation of the probes in order to establish a standard procedure to identify defective electrodes. In the last part of the chapter, the features of a nanocavities array were imaged by SECM using a nanometer sized tip. This result is extremely significant for the electrochemical investigations at the sub-micrometer scales *e.g.*, measurements of metabolites in biological microenvironments with high spatial and temporal resolution.

Chapter 3 has evaluated a transducing principle based on the redox steady state current observed at a microelectrode for the development of an electrochemical immunosensor. Indeed, anti-hIgG labelled microspheres and hIgG coated UMEs were employed in this study. Upon the immuno reaction, the sphere should bind to the electrode surface blocking the diffusion of the redox species and then lowering the steady state current. The biochemical reaction is then transduced and amplified into an electrical signal. In particular, the investigation has demonstrated that more than a one sphere affected the signal and that electrostatic effects might produce false results. Decreasing the size of the electrodes and beads, use of beads with other shapes, *e.g.*, microdisc, and integration

of the immunosensor in a microfluidic device are interesting solutions for the above problems.

Finally, Chapter 4 has compared different procedures for the immobilisation of glucose oxidase in order to prepare glucose microsensors. Though the methods for the enzyme immobilisation were not novel, it is remarkable that they have been applied to fabricate enzyme based microelectrodes with radius < 5 μm. These small sensors will have a significant role in the "on the fly" analyte measurements for point-of-care applications and as SECM probes for biological investigations. Indeed, it has been shown that polyphenol/GOx films assured fast response time and good sensitivity though those sensors were not immune from common electrochemical interferents. Encouraging results in terms of sensitivity were obtained by ruthenium electrodeposition in presence of glucose oxidase but these sensors showed a significant drift in the amperometric signal which hampers their use at the moment. Further investigations should be addressed in the understanding the origin of the latter and in its removal.